High-Resolution Atmospheric Modelling and the Effects on the Prediction of Wave Characteristics

C. R. van Laerhoven

Delft University of Technology

TU Delft Delft University of Technology

Challenge the future

Front cover: *A Storm at Sea* – Artist Unknown

High-Resolution Atmospheric Modelling and the Effects on the Prediction of Wave Characteristics

by

C. R. van Laerhoven

in partial fulfilment of the requirements for the degree of

Master of Science

in Hydraulic Engineering

at the Delft University of Technology,

to be defended publicly on Thursday March 24, 2016 at 14:00.

Student number:	4186885	
Thesis committee:	Prof.dr.ir. A.J.H.M. Reniers (Chairman)	Delft University of Technology
	Dr. J. Groeneweg (Daily supervisor)	Deltares
	Dr.ir. G.Ph. van Vledder	Van Vledder Consulting
	Dr.ir. M. Zijlema	Delft University of Technology
	ir. H.J. Verhagen	Delft University of Technology

An electronic version of this thesis is available at `http://repository.tudelft.nl/`.
The data produced during this study is available at `http://datacentrum.3tu.nl/`.

TU Delft Delft University of Technology

Deltares Enabling Delta Life

ABSTRACT

Since their development in the 1970s, mesoscale atmospheric models have been used for a variety of meteorological applications. Over the years, the models have evolved and nowadays, state-of-the-art atmospheric models are capable of operating on spatial resolutions in the order of kilometres. In the hydraulic engineering community, atmospheric models are used for operational flood protection. HIRLAM is used in the Netherlands with typical spatial resolutions of 11 km. These scales are too coarse to correctly predict small scale effects such as squall-lines and convections cells. Furthermore, the resolution is too low to accurately capture the land-water boundary. The state-of-the-art models of today are capable of predicting small scale meteorological events that might be of interest for hydraulic engineers.

The goal of this study was to successfully use a state-of-the-art atmospheric model at high-spatial resolutions to investigate the possible added-value of these models for hydraulic engineering purposes. The problem that was addressed concerns wave growth at short fetch. This is specifically important for wave prediction on rivers, harbour basins, and small lakes. Deltares [2013] investigated the predictive capabilities of SWAN for short fetches (< 5000 m) at Lake IJssel. SWAN computations were performed for a selection of 20 cases and they found uncertainties in the model predictions for wave heights (H_{m0}; rbias = −15%, SI= −11%) and wave periods (T_{m-10}; rbias= −15%, SI= −11%). It is believed that this is partially due to inaccurate representation of the wind variability near the land-water transition.

A model of the atmosphere was set up using the non-hydrostatic state-of-the-art mesoscale model WRF. The model covers a total area of 3240 × 4050 km. Initial and boundary conditions were derived from ERA-Interim and using a series of five nests, a horizontal resolution of 500 m was realized for the area around the northwest of Lake IJssel. Two storms were hindcasted; storm 1 from January 3rd 2012 to January 7th 2012 and storm 2 from December 4th 2013 to December 8th 2013. The model was validated using wind and temperature observations from the KNMI and Rijkswaterstaat at Lake IJssel. Overall, the model is in good agreement with the observations. Statistical analyses of data, showed that the uncalibrated model performed well in terms of wind speed (around Lake IJssel; storm 1: rbias < 5%, SI ≈ 10%; storm 2: rbias 10%–20%, SI ≈ 20%) and wind direction (around Lake IJssel; storm 1: bias ≈ 3°, RMSE ≈ 10°; storm 2: bias 4°–15°, RMSE ≈ 20°). Large errors were found for the surface temperature of Lake IJssel. SST updates from ERA-interim do not represent the temperature of Lake IJssel, and were structurally over-predicted (storm 1: ∼ 2°C or ∼ 70%; storm 2: 2.5–3°C or 70%–75%).

A non-stationary SWAN model was set up using calibrated settings (WTI2011) to perform wave simulations at Lake IJssel. To use friction velocities (instead of the diagnostic 10-meter wind speed) in SWAN, an extra step was required. The friction velocities from WRF were transformed to 'pseudo winds' by using the drag relation from SWAN [Wu, 1980] inversely. The model was validated for the two storms using observations of wave height (H_{m0}), wave periods (T_p, T_{m01}, T_{m02}, T_{m-10}) and 1-D wave spectra. For wind directions along the shore normal (239°N±20°), negative biases were found for the wave heights (H_{m0}; storm 1: −13%, −21% for location FL48 and FL49 respectively; storm 2: −18%, and −11% for location FL48 and FL49 respectively) and wave periods (T_{m-10}; storm 1: 10%, 7% for location FL48 and FL49 respectively; storm 2: –7%, –4% for location FL48 and FL49 respectively). A part of the error was caused by the already existing errors in the wind data from WRF. 2-D wave spectra from SWAN predicted disturbances for the stations FL48 and FL49 during slanting fetch conditions. Alongshore propagating low-frequency wave components were predicted and the bended coastline enhanced the disturbances. No directional observations were available, but the qualitative agreement between the 1-D spectra suggests that the SWAN predictions are realistic and that the measuring locations FL48 and FL49 are disturbed by energy that is not aligned with the wind direction.

To investigate the effects of high spatial resolutions in WRF, both storms were simulated using five different horizontal resolutions of 2700, 1500, 900, 500, and 300 m. Analysis showed that only little differences between the simulations occur during calm periods. The simulations did react differently during periods of rapid variations in the wind field. Investigation of the origin of these rapid variations showed that these mainly occurred during periods of precipitation (often combined with passage of weather fronts). A particular event

with high velocities ($> 30\,\mathrm{m\,s^{-1}}$) was investigated. The specific event turned out to be a gust front coming from a convection cell. The simulations responded differently to the event; with increasing resolutions, higher velocities, precipitation rates, downward velocities, and other locations were found. Finally, for the highest resolution ($\Delta x = 300$ m) artificial disturbances in the atmospheric pressure were found, indicating limitations to the validity of the chosen model settings.

To assess the effects of the wind field resolution on SWAN, both storms were simulated using the 2700, 1500, 900 and 500 m wind fields. The same method, using pseudo wind speeds was applied for the use of the friction velocity in SWAN. However, for the specific purpose of dealing with wave growth at short fetches, problems were found near the land water boundary. Because the wind fields were relatively coarse compared the length scales associated with short fetches, wind field data did not accurately model the land-water boundary. Therefore, an extra preprocessing step was used to exclude land points from the WRF wind field, and to extrapolate water-based data to the land-water boundary. Time series of the results showed equal performance for all simulations, no differences due to the wind field resolution were found. Further investigation of the spatial variability of the wave field showed that the effects of the wind streaks were also shown in the SWAN results. This resulted in differences between the simulations up to 6% near the coast.

In conclusion, the results showed that the model was still able to produce results that were in agreement with observations, and simulations with other resolutions, without showing signs (in the variables: pressure, temperature, humidity, and wind) of instabilities. This suggests—in agreement with Hong and Dudhia [2012]—that the model indeed still produces reliable wind results for resolutions up to 500 m. A specific event was investigated that turned out to be a convection cell. The simulations clearly showed different results with increasing resolutions. Higher velocities (horizontally and vertically), higher precipitation rates, and different locations for the convection cell were found for the high resolution simulations. The coarser resolutions ($\Delta x = 2700$ m and $\Delta x = 1500$m) hardly showed any deviations in wind speed due the convection cell, while the higher resolutions showed strong surface winds of up to $32\,\mathrm{m\,s^{-1}}$.

Simulations with SWAN showed only little variation based on the resolution of the wind field. The added value of these models in relation to wave modelling can be found from the better representation of the surface features such as the land-water boundary, and land-use for the determination of the roughness, which allow for the prediction of wind above harbour basins and river, possibly leading to more accurate predictions of wave characteristics on these locations. Furthermore, the prediction of convective processes such as squall-lines and convection cells could be a valuable addition for operational wave (en wind) predictions.

PREFACE

The report that lies before you is the final result of my Master Thesis. The thesis concludes the Master of Science program at the Faculty of Civil Engineering and Geosciences, Delft University of Technology. The research was conducted at Deltares in Delft.

The study could not have been conducted without the guidance and support of other people. Therefore, I would like to thank a number of people. First of all, I would like to thank all the members of my graduation committee for their guidance and feedback during the past year. I especially want to thank Jacco Groeneweg and Gerbrant van Vledder for the time they invested in me and the discussions we had. They were always there to provide advice when that was needed.

Furthermore, I would like to thank Deltares for the opportunity they gave me to perform my research, and for the inspiring work/study environments they provided. I'd also like to thank Delft University of Technology for everything I learned in the short period I studied here. They are both highly regarded institutes; I am very grateful for all the things I learned and the inspiring people I met.

Finally, I would like to thank all my family and friends for their support during my entire study program. Special thanks to Margarita, who always encouraged and supported me during the past years.

C. R. van Laerhoven
Delft, March 2016

CONTENTS

LIST OF FIGURES

LIST OF TABLES

1

INTRODUCTION

1.1. BACKGROUND

Flood defences are designed to protect land from water during extreme circumstances. Analysis of the potential damage regarding casualties and economic loss due to the failure of flood defences has led to maximum allowable failure probabilities for flood defences in the Netherlands. Hydraulic boundary conditions—water levels, river discharges, and wave height—are among the most important factors determining the functional and structural requirements of these structures. Underestimating these hydraulic boundary conditions might lead to structural failure during extreme weather conditions. Overestimating the hydraulic boundary conditions might result in much too conservative designs or the unnecessary rejection of a hydraulic structure during the assessment of its functioning.

The extreme conditions associated with these maximum allowable failure probabilities have never been recorded. Wave models such as HISWA [Booij and Holthuijsen, 1985] or SWAN [Booij et al., 1999] are used to predict the wave properties based on wind forcing [DWW et al., 2007]. Statistical extrapolation of measured wind data is used to predict extreme wind conditions. However, most wind measurement stations are located on land. A Translation is made using the Wieringa-Rijkoort two-layer model [Wieringa and Rijkoort, 1983] to obtain the open-water wind conditions on the location of interest. This model imposes some drawbacks, the model only accounts for the roughness at the location of interest, and it thereby neglects roughness effects of the surrounding environment. Furthermore, for this particular model, unreliable results were found for extreme wind speeds [Caires et al., 2009]. Altogether, there is increasing demand for more advanced methods for predicting extreme conditions.

Nowadays, atmospheric models are capable of predicting wind fields with high spatial resolutions. Even though these models provide some great opportunities (e.g. Groeneweg et al. [2011]; van Vledder and Enet [2014]), they are not yet (widely) accepted in the hydraulic engineering community for purposes other than operational flood protection. With these high spatial resolutions, transitions in surface roughness can be captured more accurately. With a better representation of the wind field over a complex geometry, it is possible to make a more accurate prediction of the wind loads on ships, the flow of water, and the local generation of waves. These models can also provide extra insight into the response of water systems to particular atmospheric phenomena such as a meteotsunami. A third application of such a model is to generate entire wind climates in regions where measurements are scarce (e.g. [García-Díez et al., 2012]). Finally, these models are capable of predicting mesoscale phenomena such as sea-breezes (and mountain/valley winds); this might, for example, be of interest in morphological studies in which not only extreme conditions are governing (e.g. harbour siltation [Verhagen and Savov, 2000]).

1.2. PROBLEM STATEMENT

Hydraulic boundary conditions are determined for the design and assessment of hydraulic structures. The accurate predictions of governing wave characteristics are one step in the determination of the hydraulic boundary conditions. Determination of the wave characteristics is often done using the numerical (spectral) wave model SWAN.

In the determination of wave characteristics in harbour basins and rivers, SWAN is forced with a uniform wind field. The characteristics of this wind field are determined based on a statistical analysis of historical data. Most of the data collection takes place using land-based weather stations. However, it is well known that wind speeds are usually higher at open-water than on land. Wind speed and direction vary depending on the state of the atmospheric boundary layer or the surface roughness (e.g. Hsu [1980]; Taylor and Lee [1984]; Kudryavtsev et al. [2000]. Both change when passing the land-water boundary, creating differences in wind speed and direction. This results in higher open-water wind speeds than land-based wind speeds. Hence, in order to use statistic predictions for open-water locations, spatial interpolation, as well as, a conversion from land-based wind to open-water wind is needed. For this conversion, several methods are available (e.g. Hsu [1986]; Taylor and Lee [1984]; Lo et al. [1994]; Kudryavtsev et al. [2000]; Wieringa and Rijkoort [1983]). These methods have a limited field of application and do not always provide sufficiently accurate results.

Deltares is currently working on the determination of a new set of hydraulic boundary conditions, which will be used for the periodical assessment of the primary flood defences in the Netherlands. They found that at short-fetch ($F \sim$ 1–5 km) conditions, wave heights H_s, and wave periods T_{m-10} predicted by SWAN at Lake IJssel, were systematically under-predicted by 15 % and 11 % respectively [Deltares, 2013]. It is believed that this is partially due to inaccurate representation of the wind variability near the land-water transition.

Properly accounting for wind field variability near land-water boundaries might lead to better wave predictions for short-fetch conditions. This would be beneficial for wave prediction on small lakes, rivers, and around complex geometries (harbour basins, around locks). State-of-the-art atmospheric mesoscale models (e.g. HARMONIE and WRF), might offer a solution to this problem. However, these models are designed to operate on the typical mesoscales (10–1000 km). To provide accurate information on the variability of a wind field near the land-water transitions, the models need to use high spatial resolutions (<2.5 km). It is not clear whether these models are still able to provide physically correct results at these high resolutions.

1.3. AIM AND OBJECTIVES

A short description of the problem and the research area was given in the previous sections of this introduction. The problem addressed (wave growth at short fetches) might be just one of many hydraulic engineering problems that can benefit using atmospheric models. The aim of this study is to solve/ understand the problem that arises with wave prediction at these short fetches. Furthermore, this study is used to show the significance of the numerical weather prediction models in relation to hydraulic engineering. It is intended to provide an example of how the use of numerical weather prediction models can be used to the benefit of the hydraulic engineer.

In accordance with the aim of this study, the main objective is twofold. Firstly, to assess whether it is possible to use a mesoscale atmospheric model with high spatial resolutions (< 2.5 km), such that it still produces physically reliable results. It should become apparent that there is a significant difference between model results using these high resolutions and a model with less high resolutions regarding wind or wind-related phenomena. Second, to determine whether the outcome of these high-resolution models leads to a significant improvement in the prediction of the spatial evolution of wave at short fetches. It should become apparent that the structural errors in wave height and period are reduced by accounting for more realistic variation of the wind field. With these primary objectives, the question intended to be solved with the study is formulated as:

What is the added value of using high-resolution atmospheric models for forecasting wave characteristics?

1.4. SCOPE AND LIMITATIONS

High-resolution atmospheric models could be applied to investigate several problems in the field of hydraulic engineering, for example, the generation of wind climates in regions where no measurements are available, specific meteorological phenomena, or forces on ships in harbours. This study will only address the possible added value of these models for the prediction of wind wave generation in regions with short fetches, where the focus is on the differences in surface roughness.

Different types of atmospheric models are available for different ranges of applications. This study only considers the application of mesoscale model WRF [Skamarock et al., 2008] because it is open-source and has a large community.

WRF provides the opportunity to perform large-eddy simulations (LES). Although this is an interesting and promising technique to investigate the problems attended in this study, LES is computationally much more demanding and setting up the model will be harder since there are more (sensitive) parameters involved. Because of these reasons, LES is excluded from the study beforehand.

The study of the atmosphere is typically a subject for meteorologists and climatologists. The average hydraulic engineer mostly deals with the atmosphere as a predefined boundary condition (wind). Boundary layer winds (or boundary layer flow) in the atmosphere follow the same physical relations (Navier-Stokes equations, including the turbulent properties of wall flow) as boundary layer flow in water. Nevertheless, due to differences in the properties water and air (e.g. density, thermal inertia) the behaviour can be different. When reading this report, it should be kept in mind that, atmospheric (meteorological) processes are not part of the curriculum at the Faculty of Civil Engineering at Delft University of Technology (DUT), and that the author has no prior knowledge on these subjects.

The atmospheric model used in this study is WRF. There is no experience using this (or any other) NWP model at the Department of Environmental Fluid Mechanics at DUT, nor is there any at Deltares. Prior to the start of the (modelling part of the) study, an informal agreement was made to perform the necessary simulations with WRF under the guidance of a WRF expert at another institute. However, for practical reasons, the assistance was never established. Hence, getting acquainted with the model and learning how to use it (from documentation) has become an unforeseen and significant part of this study.

1.5. DEFINITION OF TERMS

Some terms used in this report require further explanation. These are terms that might not be everyday jargon of the civil engineer or terms that describe some properties in a relative manner and need to be put in the proper frame of reference.

Waves on the water surface vary from very long (e.g. tides and tsunamis) to very short (e.g. capillary waves). In this document the term **wave** is frequently used. Therefore, it is important to establish a precise definition of what is meant by a wave. In the context of this report, a wave refers to a 'wind-generated surface gravity wave'. These waves have typical periods between 0.25 and 30 seconds. The focus lies mainly on locally generated waves (i.e. wind sea), swell waves are not treated in this study.

Probably one of the most returning terms in this report is **high-resolution**, in relation to the atmospheric model. The use of high-resolution in relation to modelling atmosphere varies throughout the various books and publications; it seems to have changed along with the developments in atmospheric modelling. State-of-the-art mesoscale models are capable of operating on resolutions up to 2.5–10 km, which are generally considered to be high resolutions. However, in this study, the interest lies in even higher resolutions. For this reason, the definition adopted in this report considers high-resolutions (in relation to atmospheric modelling) to be resolutions higher than 2.5 km.

Another term that often returns is **short fetch**. As has been discussed by Deltares [2013], there are no formal definitions found for short fetches. Therefore, the same definition is adopted as was proposed by them. In an absolute sense, a short fetch is defined as a fetch with a distance less than 5 km.

There are several spatial and temporal scales (and sub-scales) known to meteorology, the three scales relevant to this study are the synoptic scale, the mesoscale, and the microscale. The **synoptic scale** contains meteorological phenomena with spatial scales roughly between 100 and 5000 km, and temporal scales of days to weeks. Typical examples of synoptic scale phenomena are high- and low-pressure systems, weather fronts, ridges and troughs, and hurricanes. **Mesoscales** contain phenomena that typically range spatially from 1 to 100 km and have temporal scales that varies between minutes and hours. Typical mesoscale phenomena are squall lines, convective clouds, tornadoes, sea-breezes, mountain and valley breezes. An even smaller scale is the **microscale**. Microscale phenomena have typical spatial scales smaller than 1 km and temporal scales in the order of minutes or less. Typical microscale phenomena are micro bursts, wind gusts, dust devils, and also turbulence.

Finally, meteorological parameters are frequently used throughout the report. An overview of these parameters is given in Appendix A, where also the definitions and short descriptions are included.

1.6. OUTLINE OF THE REPORT

The outline of this thesis is as follows. Chapter 2 gives an overview on the current state of knowledge on the topics to be treated. Chapter 3 provides a description of the methods used to solve the problem. Next, Chapter 4 and 5 treat the model set-up and validation of WRF and SWAN respectively. These chapters show the used model setting and also provide a reference for the performance of the models. Chapter 6 further investigates the effects of high spatial resolutions on the prediction of wind and wave characteristics, and discusses these results. Finally, Chapter 7 draws the main conclusion from the results in the report and gives further recommendations for future research on this topic.

2

LITERATURE REVIEW

2.1. INTRODUCTION

This chapter provides a review on the theory and recent studies relevant to the subjects treated in this thesis. The reader is expected to have basic knowledge of fluid mechanics—including topics as waves, turbulence, stratified flows, and oceanography. The chapter starts with a review of waves and the most common definitions. In the third section, wind and atmospheric parameters that influence wave growth are treated. After the basic theory regarding wind and waves is discussed. The fourth section shall consider atmospheric models and their limitations. Finally, the chapter ends with a summary of the main conclusions obtained from this literature study.

2.2. WAVES

This section treats some basic knowledge needed for understanding the different aspects in this report. It should be noted that no attempt is made to provide a complete overview of the comprehensive theory of waves. The topics that are treated are based on the book 'Waves in Oceanic and Coastal Waters' by Holthuijsen [2007]. A more elaborate description of the theory and methods described in this section (and more) can be found in this book.

2.2.1. AN INTRODUCTION TO WAVES

Considering a one-dimensional record of the surface elevation (η) (statistically stationary) with duration D, a wave can be distinguished as the profile between two zero-crossings. A single wave is characterized by a height (H), a period (T) (or frequency (f)), and a length (L). Figure 2.1 shows how a wave is defined from the time record of the surface elevation. The wave height for a single wave is determined as the distance between the crest and the through; the wave period is the time between two (downward) zero crossings; and the length of the wave is defined as the distance between two zero crossings.

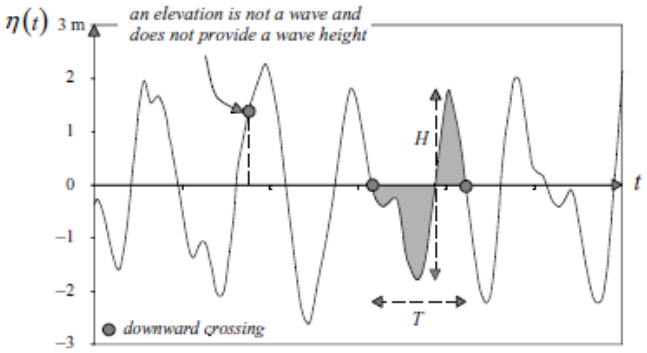

Figure 2.1: The definition of wave height and wave period in a time record of the surface elevation (the wave is defined with downward zero-crossings. Figure reproduced from Holthuijsen [2007].

A wave record is often described using average quantities of the individual waves. Equations (2.1) and (2.2) show how the significant wave height (H_s)—defined as the average height of the highest one-third of the waves—and the mean zero-crossing wave period ($\overline{T}_0$) are determined for a wave record of N waves.

$$H_s = H_{1/3} = \frac{1}{N/3}\sum_{i=1}^{N/3} H_i \tag{2.1}$$

$$\overline{T}_0 = \frac{1}{N}\sum_{i=1}^{N} T_{0,i} \tag{2.2}$$

where this time i is the rank of the wave (with i=1 is the largest and $i = N$ the smallest wave in the record).

2.2.2. SPECTRAL DESCRIPTION OF WAVES

Due to the turbulent character of the wind, a wave field is rather irregular, and the water surface varies rapidly in time. Statistically, wave parameters vary much slower in time. For periods short enough, these statistics are approximately stationary. A wave record can then be seen as one realization of a stochastic process (a stationary, Gaussian process).

A deterministic description of the sea surface is not always necessary. As an alternative one can use a wave spectrum instead. The wave spectrum describes the distribution of wave energy (variance) over the different wave frequencies for a particular period. Using this information, statistical quantities of the wave field can be obtained. Key in obtaining the spectrum of a wave field is the random-phase/amplitude model; this model describes the moving sea surface (η) as the summation of a large number of harmonic waves (a Fourier series):

$$\underline{\eta}(t) = \sum_{i=1}^{N} \underline{a}_i \cos\left(2\pi f_i t + \underline{\alpha}_i\right) \tag{2.3}$$

in which $a = H/2$ is the amplitude, α is the phase of the harmonic, and the underscore denotes the random character of the variables. Each of these harmonics has its own constant amplitude, period, and phase. The values of the amplitudes and the phases of the harmonic waves can be obtained from Fourier analysis. This principle is also illustrated in Figure 2.2. Using the relation between the wave amplitude and wave energy—known from linear wave theory—it can be shown that wave energy is proportional to the variance of the wave components ($\underline{a}_i^2/2$). Letting $E\{\ \}$ denote the expected value of a random variable; a variance density spectrum can then be obtained by:

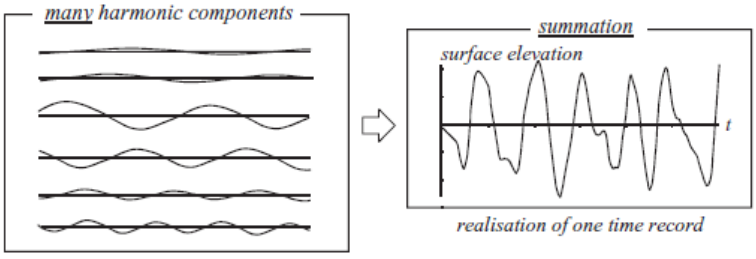

Figure 2.2: The summation of many harmonic waves, with constant amplitudes and phases, recreates a sea surface. Figure reproduced from Holthuijsen [2007].

$$E(f) = \lim_{\Delta f \to 0} \frac{1}{\Delta f} E\left\{\frac{1}{2}\underline{a}^2\right\} \tag{2.4}$$

in which E is the variance density and $\Delta f = 1/D$ is the spectral resolution. By taking into account the wave directions, a two-dimensional wave spectrum $E(f,\theta)$ can be obtained in a similar way. Wave parameters are estimated from the spectrum using the moments of the wave spectrum:

$$m_n = \int_0^{2\pi} \int_0^{\infty} f^n E(f,\theta)\, \mathrm{d}f \mathrm{d}\theta \tag{2.5}$$

in which m_n is the n-th order moment of the wave spectrum. Without giving any proof, some of the wave parameters that can be obtained from the spectral moments are:

$$H_{m0} = 4\sqrt{m_0} \tag{2.6a}$$
$$T_{m01} = \frac{m_0}{m_1} \tag{2.6b}$$
$$T_{m02} = \sqrt{\frac{m_0}{m_2}} \tag{2.6c}$$
$$T_{m-10} = \frac{m_{-1}}{m_0} \tag{2.6d}$$

in which H_{m0} is the spectral equivalent of the significant wave height, T_{m01} is the wave period corresponding to the mean period of the spectrum, T_{m02} is spectral equivalent of the mean zero-down-crossing period, and T_{m-10} is the energy wave period[1]. Another parameter that can be defined from the wave spectrum is the peak period T_p (or peak frequency: $f_p = 1/T_p$). The peak period is defined as the period associated with the main peak of the wave spectrum.

2.2.3. WAVE GROWTH

In the past, many theories have been developed for the generation of waves and wave growth. The initiation of wave development is still not well understood. Accepted theories on this subject are those by Phillips [1957] (wave generation) and Miles [1957] (wave growth). This section describes these theories based on the description by Holthuijsen [2007].

THEORETICAL APPROACH

According to Phillips [1957] wind induces a turbulent pressure on the flat water surface. The pressure field moves over the surface as a nearly frozen field and can be seen as a large sum of harmonic pressure waves. All oriented in different directions, but propagating in the wind direction. Resonance occurs if the pressure waves have the same wavelength, and travels at the same speed and in the same direction, as a surface gravity wave. Due to these resonance conditions, energy is exchanged between the wind and water surface. The energy exchange was estimated by Phillips to be constant in time, resulting in linear growth, see Equation (2.7).

$$S_{\text{in};1}(f,\theta) = \alpha \tag{2.7}$$

in which $S_{\text{in};1}(f,\theta)$ represents the source term due to wave generation, θ is the direction of the wave energy, θ_{wind} is the wind direction, and α is the constant that represents the energy exchange due to the theory of Phillips. A value for α can be determined by the expression of Cavaleri and Malanotte-Rizzoli [1981] (e.q. in SWAN):

$$\alpha = \begin{cases} C_\alpha \left[\mathbf{u}_* \cos(\theta - \theta_{\text{wind}})\right]^4 & \text{for } |\theta - \theta_{\text{wind}}| \leq 90° \text{ and } f \geq f_{\text{pm}} \\ 0 & \text{for other wave components} \end{cases} \tag{2.8}$$

[1] The name energy wave period originates from its use in the computation of wave power [WMO, 1998]

in which C_α is a tunable coefficient, $\mathbf{u}_*$ is the shear velocity, θ_{wind} is the wind direction and f_{pm} is the Pierson–Moskowitz peak frequency.

In 1957, Miles created a model for the transfer of energy from a shear flow to a surface wave. According to his findings, there is a feedback mechanism between waves and wind pressure. Waves modify the air flow in such a way that the maximum pressure occurs on the windward side of the wave, where water particles are moving downward. On the Leeward side of the wave a minimum air pressure occurs, allowing the water particles to move upward more quickly. The amount of energy transferred depends on the amplitude of the wave. The higher the amplitude, the more energy is exchanged. This implies that the effect becomes more efficient during the process. The process is, therefore, parameterized using an exponential growth term:

$$S_{\text{in;2}}(f,\theta) = \beta E(f,\theta) \tag{2.9}$$

in which $S_{\text{in;2}}(f,\theta)$ represents the source term due to wave growth, β is coefficient, and $E(f,\theta)$ is the energy density. Based on measurements it was found that the β can be determined with, for example, the formulation by Snyder et al. [1981], see Equation (2.10):

$$\beta = \epsilon \frac{\rho_{\text{a}}}{\rho_{\text{w}}} \left[28 \frac{\mathbf{u}_*}{c} \cos(\theta - \theta_{\text{wind}} - 1) \right]^2 2\pi f \tag{2.10}$$

in which ϵ is a tunable coefficient, ρ is density and c is the phase speed of the wave component. Combining 2.7 and 2.9 gives a general expression for wave growth:

$$S_{\text{in}}(f,\theta) = \alpha + \beta E(f,\theta) \tag{2.11}$$

It can be seen that the wind forcing in Equations (2.8) and (2.10) is represented by a shear stress in the form of the shear velocity $\mathbf{u}_*$, defined by:

$$\boldsymbol{\tau} = \rho_{\text{air}} {\mathbf{u}_*}^2 = \rho_{\text{air}} C_d \mathbf{u}_{10}^2 \tag{2.12}$$

in which $\boldsymbol{\tau}$ is the shear stress at the water surface and $\mathbf{u}_{10}$ is the wind velocity at a height of 10 meters and C_d is the drag coefficient. The determination of $\mathbf{u}_*$ will be discussed in Section 2.3.

EMPIRICAL GROWTH CURVES

Wave parameters, such as the significant wave height or peak period can also be determined using empirical relations known as growth curves. By studying the evolution of the wave spectrum for situations in with the wind blows perpendicular to the coast, many empirical relationships for wave growth have been found (e.g. Bretschneider [1958], Hurdle and Stive [1989], Kahma and Calkoen [1992b] and Breugem and Holthuijsen [2007]) . The foundation of these growth curves lies in the spectral similarity theory by Kitaigorodskii [1962]. Who introduced the following dimensionless parameters:

$$\widetilde{F} = \frac{gF}{\boldsymbol{u}_{10}^2} \tag{2.13}$$

$$\widetilde{H} = \frac{gH}{\boldsymbol{u}_{10}^2} \tag{2.14}$$

$$\widetilde{E} = \frac{g^2 E}{\boldsymbol{u}_{10}^4} \tag{2.15}$$

$$\widetilde{T} = \frac{gT}{\boldsymbol{u}_{10}} \tag{2.16}$$

where $\widetilde{F}$ is the dimensionless fetch, $\widetilde{H}$ the dimensionless wave height, $\widetilde{E}$ the dimensionless wave energy, and $\widetilde{T}$ the dimensionless wave period. Sometimes other variants of these parameters are used (e.g. instead of

using the 10-m wind speed, Kahma and Calkoen [1992b] also proposed to use the friction velocity $\mathbf{u}_*$). The growth curves are derived for ideal circumstances (long straight coastline, constant wind, and deep water), which are rarely encountered. Thus it necessary to take in account deviations from these ideal conditions. This results in effective parameters that account for the irregular behaviour of the corresponding normal parameters. Some examples are an effective fetch [TAW, 1985; WMO, 1998], effective wind speed [Perrie and Toulany, 1995], or effective depth [Hurdle and Stive, 1989].

2.2.4. SCALING ISSUES FOR SHORT FETCHES

From 2007 onward, a large wind and wave measurements campaign is being conducted by Rijkswaterstaat (RWS) (see [Bottema, 2007]). Deltares [2013, 2015] studied the data set and found that there is still a considerable amount of scatter in the data for short fetches when compared to the growth curves. Furthermore, for the stations closest to the shore (FL49~ 850 m and FL48~ 1650 m), the measured data were structurally higher than the growth curves predicted. They believe that the variability in the data indicates that there are other processes involved that are currently not being accounted for with the standard growth curves.

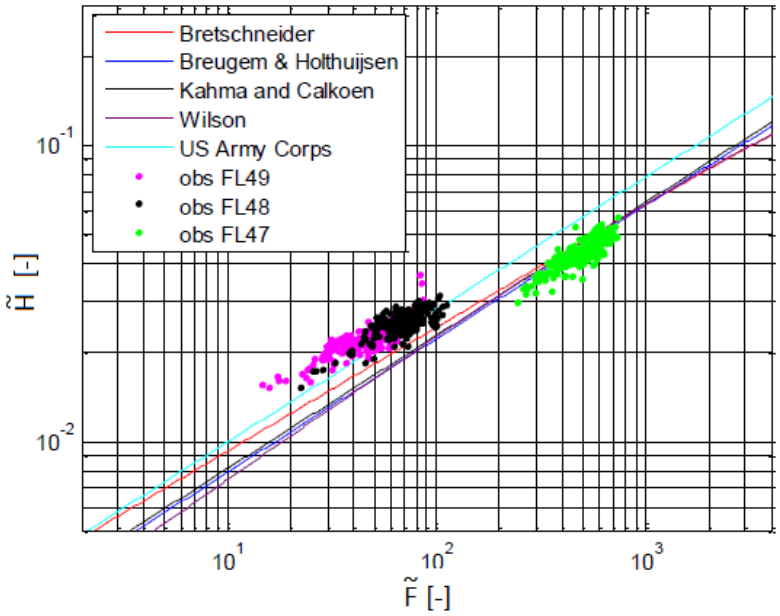

Figure 2.3: Lake IJssel data (measurement stations FL47, FL48, and FL49) plotted alongside a number of empirical growth curves. Only for data where $\boldsymbol{u}_{10} > 10\,\mathrm{m\,s^{-1}}$, θ_{wind} 240°N ± 20°, and H_{m0} larger than threshold (0.80 m, 0.5 m, 0.3 m for FL47, FL48, FL49, respectively). Figure reproduced from Deltares [2015].

In their study, [Deltares, 2015] investigate a number of processes that were identified by Babanin and Makin [2008] as possible mechanisms affecting wave growth. Their analysis indicates that wave steepness and gustiness of the wind contribute to the variability of the data.

2.2.5. SLANTING-FETCH CONDITIONS

Special attention is required when studying waves under slanting-fetch conditions near the coast when the wind blows obliquely from the shore (e.g. Pettersson [2004]; Ardhuin et al. [2006]; Bottema and van Vledder [2007]). Deviations between the wind direction and the mean wave direction have been observed for waves under slanting-fetch conditions. [Bottema and van Vledder, 2007]. Low-frequency components, associated with alongshore transportation of wave energy, dominate the higher components that travel in the same direction as the wind. This effect becomes specifically noticeable for very short fetches < 3 km [Bottema and van Vledder, 2007] and for wind directions that deviate more than 20°–30° with the shore normal [Ardhuin et al., 2006].

2.3. WIND

The Wind is the basic force driving ocean waves. Consequently, understanding the behaviour of the wind is important for the prediction of waves. Flow in the atmosphere is primarily driven by pressure differences and influenced by several other forces. The most important secondary forces affecting wind are Coriolis and friction. Throughout this document the wind $\mathbf{u} = [u, v, z]$ is denoted in several ways, most used is the 10-meter wind speed $\mathbf{u}_{10} = [u_{10}, v_{10}]$, which is defined as de vector of the horizontal wind at a height of 10 m.

In the upper part of the troposphere, the wind is almost completely geostrophic (i.e. there is an equilibrium between the Coriolis force and pressure force). Due to the influence of Coriolis, the wind flows perpendicular to the direction of the pressure gradient (i.e. parallel to the isobars; to the right in the Northern Hemisphere and the left in Southern Hemisphere). Closer to the earth's surface wind is dominated by friction, and a boundary layer is formed (the atmospheric or planetary boundary layer). This is illustrated in Figure 2.4. The direction of the wind is being altered in the atmospheric boundary layer (ABL) due to the influence of friction. The atmosphere above the ABL is often referred to as the free atmosphere.

Since wind processes relevant for the growth of waves occur inside the atmospheric boundary layer, the primary focus of this section is on the behaviour of the wind within the atmospheric boundary layer. Topics such as the generation of the wind and global circulation will not be treated, more information on these topics can, for example, be found in Barry and Chorley [2003].

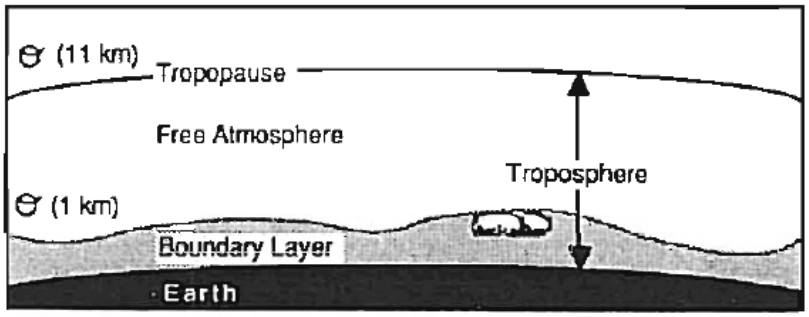

Figure 2.4: Division of the troposphere into two parts: the atmospheric boundary layer and the free atmosphere. Figure reproduced from Stull [1988].

2.3.1. ATMOSPHERIC BOUNDARY LAYER

This section describes the general behaviour and characteristics of the ABL. For this purpose extensive use is made of the book 'Boundary Layer Meteorology' by Stull [1988]. For more information on the subject, the reader is referred to the original book. The atmospheric boundary layer is defined by Stull [1988] as:

'the part of the troposphere that is directly influenced by the presence of the earth's surface, and that responds to the surface forcing with a timescale of about an hour'.

The ABL differs from the free atmosphere due to the influence of turbulence. Friction imposed by the earth's surface creates shear stresses, which results in the generation of mechanical turbulence. Furthermore, heating of the atmosphere by the earth's surface causes thermals to rise, forming large eddies.

Another difference is that the direction of the wind in the atmospheric boundary layer differs from the wind direction in the free atmosphere. The influence of friction, in combination with Coriolis and pressure differences, cause an Ekman spiral to form. Along the height of the boundary layer wind changes direction (towards the direction of the pressure force). This region is, therefore, called the Ekman layer. In the lowest part of the ABL, turbulent fluxes vary less than 10% and they are often assumed to be constant is this region. The assumptions underlying the Ekman spiral do not hold in this layer (the eddy viscosity is no longer constant). This region is known as the surface layer (or constant flux layer) which will be discussed later in this chapter.

The thickness of the ABL changes in time and space and varies roughly between 100 and 3000 m. Above the open ocean, changes are relatively slow in space and time, and they are primarily influenced by synoptic and mesoscale processes. There is more variation of the ABL over land; the ABL is thinner in high-pressure areas

due to the subsidence of air from upper layers to lower layers and the horizontal divergence of air in the lower atmosphere. In low-pressure areas the opposite happens, the ABL grows higher due to the uprising air and horizontal convergence of air at the lower levels.

The state of the boundary layer is substantially influenced by the stability of the atmosphere. During the diurnal cycle, heating and cooling of the surface alternates; also resulting in three typical phases of the ABL: the mixed layer (or convective boundary layer), the residual layer, and the stable (or nocturnal) boundary layer.

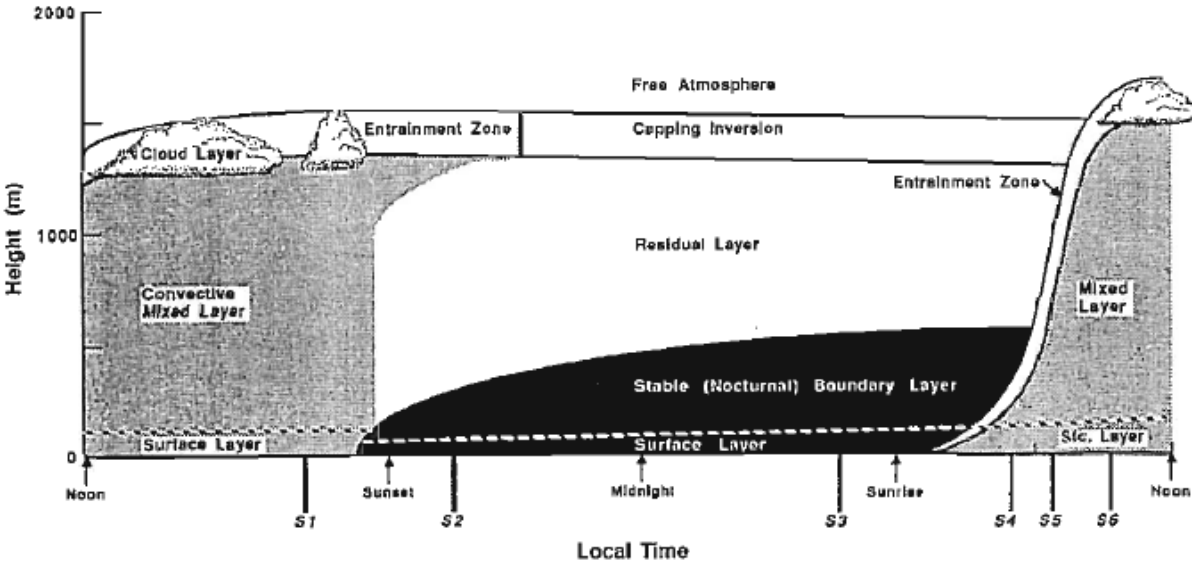

Figure 2.5: The different boundary layer regimes. Figure reproduced from Stull [1988].

Mixed Layer The mixed layer is characterized by intense mixing of heat, moisture, and momentum, this is primarily due to convection-driven turbulence. Sources of convection are the transfer of heat from a warm ground surface or cooling from a cloud top. The warm ground surface, heated by radiation from the sun, heats the air near the ground; this creates a buoyancy-driven upward motion of air resulting unstable stratification. The opposite can happen due to cooling of the air from a cloud layer. The now denser, colder air sinks towards the ground creating vertical motions, also resulting in unstable stratification. The wind speed in the mixed layer follows a logarithmic profile in the vertical direction; starting from zero at the ground to a more or less constant value in the middle of the mixing layer.

The growth of the mixing layer starts about half an hour after sunrise and reaches its maximum depth in the late afternoon. The mixing layer grows through entrainment of less turbulent air above it. The layer in which this happens is called the entrainment zone. The entrainment zone forms a stable layer on top of the mixing layer. This causes it to function as a lid for the rising thermals, restraining the domain of turbulence. The growth in depth of the mixing layer might cause rising thermals to reach their lifting condensation levels, creating fair weather clouds.

The mixed layer can occur in two states, depending on the dominant origin of the turbulence in the layer. A state of free convection occurs when the turbulence is (mostly) caused by buoyant convective processes (in this case, the mixed layer is often referred to as the convective layer). A state of forced convection; that occurs when mechanical processes dominate the production of turbulence (in which the atmosphere is neutrally stratified).

Residual Layer After sunset, the absence of solar radiation causes the turbulence in the mixing layer to decay, this results in the residual layer. The initial state of the residual layer is equal to that of the mixing layer. The base of the residual layer lies on top of the nocturnal layer. Because of the absence of turbulent transport of surface-related properties, the residual layer does not follow the previously mentioned definition of ABL.

Table 2.1: Stability classes based on the Obukhov length (L_b), reproduced from Gryning et al. [2007].

Interval of the Obukhov length [m]					Stability Class
10	≤	L_b	<	50	Very stable
50	≤	L_b	<	200	Stable
200	≤	L_b	<	500	Near stable
|500|	≤	L_b			Neutral
-500	≤	L_b	<	-200	Near unstable
-200	≤	L_b	<	-100	Unstable
-100	≤	L_b	<	-50	Very unstable

Stable boundary layer A stable boundary layer forms when the surface temperature is lower than the temperatures in the layer above it. This is characteristic for the boundary layer at night (which is then referred to as a nocturnal boundary layer). After sunset, the nocturnal layer forms under the residual layer. Turbulence intensity in this layer is usually very small. At night, winds along the surface become calm. Turbulence in the stable boundary layer is suppressed due to the stable conditions. There can be bursts of turbulence due to the nocturnal jets (winds higher in the stable boundary layer might accelerate to super-geostrophic winds).

The top of the stable boundary layer is poorly defined. There is a smooth transition between the stable boundary layer and the residual layer. The top of the ABL is defined by the fraction of turbulence compared to the turbulence level at the surface.

Surface layer The surface layer (sometimes also referred to as the constant flux layer) consists of the bottom part of the boundary layer. It is defined as the part of the ABL where the momentum flux varies less than 10%; this is roughly the lowest 10% of the ABL.

2.3.2. WIND PROFILE

The vertical wind profile in the ABL has two boundary conditions; the no-slip condition at the surface ($\mathbf{u} = 0$), and the wind in the free atmosphere at the top of the ABL. The profile in between these boundaries is further influenced by the stability of the atmosphere. Several approaches can be used to determine the stability, two of which are described here; one using Obukhov length, and one using the (bulk) Richardson number.

The first method uses the Obukhov length (L_b) [Obukhov, 1971], which is commonly used in atmospheric sciences. The Obukhov length was defined by Obukhov in 1946 (translated to English in 1971), and it represents a length scale that estimates the height at which convection driven turbulence starts to dominate over shear produced turbulence [Stull, 1988]:

$$L = -\frac{\theta_v {\mathbf{u}_*}^3}{g\kappa \overline{w'\theta'_v}} \tag{2.17}$$

in which θ_v is the virtual potential temperature, and g is the gravitational acceleration. Several different interpretations of the Obukhov length with respect to the stability classes are found in literature (e.g. [Hsu, 1992], [Gryning et al., 2007], [Sathe and Bierbooms, 2007]). As an indication, the classes defined by Gryning et al. [2007] are shown in Table 2.1. The Obukhov length is often used in an dimensionless form $\zeta = z/L_b$ as a scaling parameter for boundary layer processes.

An alternative is the Richardson number. The Richardson number is a dimensionless quantity that represents the ratio of buoyancy over shear-induced turbulence. A practical form of the Richardson number is the bulk Richardson number [Stull, 1988]:

$$Ri_b = \frac{\frac{g}{\theta_v}\frac{\Delta\theta_v}{\Delta z}}{\left[\left(\frac{\Delta u}{\Delta z}\right)^2 + \left(\frac{\Delta v}{\Delta z}\right)^2\right]} \tag{2.18}$$

Table 2.2: Stability classes based on the Richardson number, based on Stull [1988].

Richardson number [-]					stability class
		Ri_b	$<$	0	Unstable (Convective turbulence)
		Ri_b	$=$	0	Neutral
0	$<$	Ri_b	$<$	$Ri_c \approx 0.21$–0.25	Stable (Mechanical turbulence)
$Ri_c \approx 0.21$–0.25	$<$	Ri_b		1	Transition
1	$<$	Ri_b			Stable (Laminar flow)

An overview of the stability regimes is given in Table 2.2. The bulk Richardson number provides a simpler manner for determining the stability of the atmosphere. However, the stability parameter (ζ) is often used in boundary layer meteorology. Several methods have been proposed to determine ζ based on the Ri_b, for example Hsu [1989]; Grachev and Fairall [1996].

NEUTRAL CONDITIONS

Flow in the ABL can be schematized as flow along a wall know from basic fluid mechanics. For simplicity, it is assumed that the wind moves in the x-direction so that $v = 0$. The surface flux layer can be divided into three regions: the viscous sub-layer, the buffer layer, and the inner layer. In the laminar sub-layer viscosity dominates and the shear stress is determined by $\boldsymbol{\tau} = \nu_m \partial_z(u)$, where ν_m is the molecular viscosity. The inner layer is dominated by turbulence, and the turbulent shear stress (or Reynolds stress) is defined as:

$$\boldsymbol{\tau}_t = \boldsymbol{\tau}_{xz} = -\rho \overline{u'w'} \tag{2.19}$$

in which ρ is the density. The prime ($'$) denotes turbulent fluctuations and the bar $\overline{(\,)}$ denotes ensemble averaging. The buffer layer is the region between the viscous sub-layer, and the inner layer. Both viscous and turbulent stress are important in the buffer layer. In the region close to the wall, the shear stress does not vary much. Moreover, it can be assumed that the shear stress in the lowest part of the boundary layer is constant [Stull, 1988].

$$\frac{\partial \overline{u'w'}}{\partial z} = 0 \quad \Rightarrow \quad \boldsymbol{\tau} = -\rho \overline{u'w'} = \rho \boldsymbol{u}_*^2 = \text{constant} \tag{2.20}$$

where $\boldsymbol{u}_* = \sqrt{\boldsymbol{\tau}/\rho}$ is the friction velocity. This assumption of a constant momentum flux in the surface boundary layer together with Prandtl's well-known mixing-length hypothesis allows for the derivation of the characteristic logarithmic velocity profile. Prandtl's mixing length theorem states that the velocity that characterizes turbulent fluctuations, scales with the velocity difference in the mean flow over a distance l_m. In the case of wall flow, l_m is often taken as proportional to the distance from the wall $l_m = \kappa z$ [Uijttewaal, 2014]. So that:

$$\boldsymbol{u}_* = l_m \left| \frac{\partial \overline{u}}{\partial z} \right| = \kappa z \left| \frac{\partial \overline{u}}{\partial z} \right| \tag{2.21}$$

in which κ is the von Karman constant. Solving the differential equation gives the well-know logarithmic velocity profile for neutral conditions:

$$\overline{u}(z) = \frac{\boldsymbol{u}_*}{\kappa} \ln \frac{z}{z_0} \tag{2.22}$$

where z_0 is the aerodynamic roughness length.

NON-NEUTRAL CONDITIONS

In the previous section, the logarithmic velocity profile for neutral conditions was derived using physical arguments. The same logarithmic velocity profile could also be obtained using similarity theory[2]. This section

[2] In similarity theory, groups of dimensionless constants are formed. Relationships between these dimensionless groups are found based on empirical research, leading to an expression [Stull, 1988].

also includes the effect of atmospheric stability into the wind profile.

Monin and Obukhov [1954; cited by Stull [1988]] investigated the velocity structure in a stratified surface layer. They included the Obukhov length [Obukhov, 1971] as an extra variable in their analysis. This resulted in their well-known similarity theory (only the relation for momentum is shown):

$$\frac{\partial \overline{u}}{\partial z} = \frac{\boldsymbol{u}_*}{\kappa z}\phi_m(\zeta) \tag{2.23}$$

in which, ϕ_m is a stability function for momentum, and $\zeta = z/L_b$ is the boundary layer scaling parameter. The stability functions ϕ_m is undefined in their theory. The Monin-Obukhov theory has been widely used. However, it has two limitations. First, it is only valid in the case winds are not weak (i.e. $\mathbf{u}_*$ should not be 0). Second, the theory is not correct in neutral conditions since the Obukhov length becomes infinite in these circumstances [Stull, 1988].

Based on empirical research both Bussinger and Dyer came to similar relations for the stability function ϕ_m. Hence, the relation is called the Businger-Dyer relation Stull [1988](only the equations for momentum are shown):

$$\phi_m = \begin{cases} 1 + (4.7\zeta) & \text{for } \zeta > 0 \quad \text{(stable conditions)} \\ 1 & \text{for } \zeta = 0 \quad \text{(neutral conditions)} \\ [1 - (15\zeta)]^{-1/4} & \text{for } \zeta < 0 \quad \text{(unstable conditions)} \end{cases} \tag{2.24}$$

Integration of the equation for momentum then leads to an alternative expression for the wind profile:

$$\overline{u}(z) = \frac{\boldsymbol{u}_*}{\kappa}\left[\ln\left(\frac{z}{z_0}\right) + \Psi_m(\zeta)\right] \tag{2.25}$$

in which Ψ_m is a new stability function for momentum. Several expressions for Ψ_m are known. A commonly used expression is the one suggested by Paulson [1970], shown in Equation (2.26):

$$\Psi_m(\zeta) = \begin{cases} 4.7\zeta & \text{for } \zeta > 0 \quad \text{(stable)} \\ -2\ln\left[\frac{(1+x)}{2}\right] - \ln\left[\frac{(1+x^2)}{2}\right] + 2\tan^{-1}(x) - \frac{\pi}{2} & \text{for } \zeta < 0 \quad \text{(unstable)} \end{cases} \tag{2.26}$$

in which $x = [1 - 15\zeta]^{1/4}$.

2.3.3. AERODYNAMIC ROUGHNESS LENGTH

The aerodynamic roughness length is a parameter that represents the height at which the logarithmic velocity profile becomes zero. Although not the same, the roughness height is related to the length scale of surface roughness elements near the ground. The value for the roughness length can be established based on measured data (at least two heights). Typical values for the roughness length have been derived for different types of vegetation and surfaces; some examples are shown in Table 2.3.

As with other surfaces, waves also impose a certain surface roughness to the air flow. However, waves differ from other surfaces since they move and react to pressure differences. These interactions between waves and wind, make the determination of the roughness of waves less trivial than for other surfaces.

Charnock [1955] studied the wind profile under the influence of waves. He used measurements to establish a generalized wind profile over a wave field. In analogy with the logarithmic profile described above, this resulted in an expression for the roughness height z_0. This expression is known as Charnock relation:

$$z_0 = \alpha\frac{\boldsymbol{u}_*^2}{g} \quad \text{or} \quad z_{0*} \equiv \frac{g z_0}{\boldsymbol{u}_*^2} = \alpha \tag{2.27}$$

Table 2.3: Terrain classification in terms of the aerodynamic roughness length, x is a typical upwind obstacle distance and H is the height of the corresponding major obstacles. Table reproduced from WMO [2008].

Terrain Description	z_0 [m]
Open sea, fetch at least 5 km	0.0002
Mud flats, snow; no vegetation, no obstacles	0.005
Open flat terrain; grass, few isolated obstacles	0.03
Low crops, occasional large obstacles; $x/h > 20$	0.10
High crops, scattered obstacles, $15 < x/h < 20$	0.25
Parkland, bushes, numerous obstacles, $x/h \approx 10$	0.50
Regular large obstacle coverage (suburb, forest)	1.0
City centre with high- and low-rise buildings	≥ 2

in which α is a constant, known as the Charnock constant. The relation highlights the proportionality of the surface roughness with the wind stress. Studies by Garratt [1977], Wu [1982] confirmed the validity of Charnock relation in different situations by comparison with measured data. The values of the Charnock coefficient found in different measurements vary. Charnock [1955] found $\alpha = 0.012$, Smith [1980] $\alpha = 0.011$ Garratt [1977] $\alpha = 0.0144$ and Wu [1980] found $\alpha = 0.0185$. According to Smith [1980] these differences are due to the differed measurement conditions. He states that prior to 1980 most $\mathbf{u}_*$ measurements were taken at depth and fetch limited places. As a result, these measurements consist mainly of coastal observations with relatively young wave fields.

It is known that the roughness of a wave field also depends on the sea state (commonly defined by the wave age or a wave steepness). Donelan [1990; cited by Maat et al. [1991]] reasons that waves become longer with age due to the energy transfer from high frequencies to low frequencies. Long waves travel faster, and when these velocities approach the wind speed, these waves no longer contribute as much to the roughness. Therefore, young waves tend to impose a higher roughness than mature waves.

No characteristics of the wave field are included in Charnock's relation. This implies the assumption of an entirely saturated wave field, in equilibrium with the wind forcing [Maat et al., 1991]. In one of the earlier studies on this subject, Hsu [1974] suggested that the roughness length should be a function of the wave steepness s, defined as $s = (H_s/L)$; in which H_s is the significant wave height and L is the wave length. Based on dimensional considerations he stated that $z_0 \propto (H/L)(\boldsymbol{u}_*^2/g)$, which is in line with the findings of Charnock, only now using a variable coefficient depending on the wave steepness. By using $\boldsymbol{c} \propto \sqrt{(gL)/(2\pi)}$ he rewrote this into Equation (2.28), where he found a^* to be in the order of 1.

$$z_0 = \frac{a^*}{2\pi}\left[\frac{H}{(\boldsymbol{c}/\boldsymbol{u}_*)^2}\right] \tag{2.28}$$

Maat et al. [1991] included the wave age, defined as $\boldsymbol{c}_p/\boldsymbol{u}_*$ (were $\boldsymbol{c}_p$ is the phase velocity at the spectral peak), in the assumed relation for the wave roughness. They found:

$$z_{0*} \equiv \frac{g z_0}{\boldsymbol{u}_*^2} = \mu\left(\frac{\boldsymbol{c}_p}{\boldsymbol{u}_*}\right) \quad \text{or} \quad z_0 = \mu\left(\frac{\boldsymbol{u}_*^3}{g\boldsymbol{c}_p}\right) \tag{2.29}$$

in which μ is a constant. Smith et al. [1992] later found that $\mu = 0.48$. The relation clearly shows the analogy with Charnock's relation, only the constant is replaced with a power function that depends on the wave age. Similar relations for the surface roughness based on wave age were found by Donelan [1993]. By comparison of different types of data set he found:

$$\frac{z_0}{\sigma} = 6.7 \cdot 10^{-4}\left(\frac{\boldsymbol{u}_{10}}{\boldsymbol{c}_p}\right)^{2.6} \tag{2.30}$$

with

$$\sigma = 0.0055\left(\frac{\boldsymbol{u}_{10}^2}{g}\right)\left(\frac{\boldsymbol{u}_{10}}{c_p}\right)^{-1.7} \tag{2.31}$$

Taylor and Yelland [2000] used the wave steepness as a scaling parameter for the surface roughness. The general form of their expression is given by Equation (2.32). They used $A_1 = 1200$ and $B_1 = 4.5$.

$$\frac{z_0}{H_s} = A_1\left(\frac{H_s}{L_p}\right)^{B_1} \tag{2.32}$$

Oost et al. [2002] derived an equation for the surface roughness based on the wave age and the wavelength.

$$\frac{z_0}{L_p} = A_2\left(\frac{\boldsymbol{u}_*}{\boldsymbol{c}_p}\right)^{B_2} \tag{2.33}$$

with $A_2 = 50$ and $B_2 = 4.5$.

Drennan et al. [2003] used the inverse wave age end the wave height for the surface roughness based on the theory by Donelan [1993].

$$\frac{z_0}{\sigma} = A_3\left(\frac{\boldsymbol{u}_*}{\boldsymbol{c}_p}\right)^{B_3} \Longleftrightarrow \frac{z_0}{H_s} = \frac{A_3}{4}\left(\frac{\boldsymbol{u}_*}{\boldsymbol{c}_p}\right)^{B_3} \tag{2.34}$$

with $A_3 = 13.4$ and $B_3 = 3.4$.

Olabarrieta et al. [2012] studied the effect of the last three parameterizations in the applications of the Coupled Ocean–Atmosphere–Wave–Sediment Transport (COAWST) Model [Warner et al., 2010]. The subject of their study was hurricane Ida and the storm that evolved from Hurricane Ida: Nor'Ida. They found that the spatial and temporal patterns of surface roughness were similar. They did found that the model by Oost et al. [2002] showed more intense spatial gradients and produced higher roughness values than the others, this led to better results regarding RMSE and model skill with the method by Oost et al. [2002] than with the other two models.

For very high velocities ($> 30\ \mathrm{m\,s^{-1}}$) other processes become important, and the standard Charnock relation for the wave surface roughness does not hold anymore (also see section 2.3.5). Makin [2005] proposed an alternative expression for the surface roughness during these conditions, which accounts for the effects of a so-called suspension layer above the surface.

$$z_0 = c_l^{1-1/\omega}\alpha^{1/\omega}\frac{\boldsymbol{u}_*^2}{g} \tag{2.35}$$

where $\omega = \boldsymbol{a}/\kappa\boldsymbol{u}_*$, with $\boldsymbol{a}$ is the fall velocity of the droplets. Note that the expression reduces to Charnock's equation for $\omega = 1$ (no spray effect).

2.3.4. SPATIAL VARIATION

As already described in section 2.3.2, the wind profile is influenced by the surface roughness and the atmospheric stability. This section describes the evolution of the wind profile as it adapts to new surface conditions.

When a wind profile, in equilibrium with the surface conditions, encounters a change in surface conditions it starts to adjust to these circumstances beginning from the lowest part of the ABL. Due to these modifications, a separate boundary layer begins to form within the ABL, the internal boundary layer (IBL). In case the changes in surface conditions are caused by thermal properties, it is called the thermal internal boundary layer (TIBL).

VARIATION IN ROUGHNESS

As the distance from this transition or border increases, changes in the wind profile will further modify the flow in higher levels. Above the IBL, the conditions are not yet adapted to the new boundary conditions; this region still has the same properties as upstream of the boundary. The growth of the IBL is often expressed in the form of a power function depending on the fetch [Stull, 1988]:

$$\frac{\delta}{z_{0;1}} = a_{\text{ibl}} \cdot \left(\frac{x}{z_{0;1}} \right)^{b_{\text{ibl}}} \tag{2.36}$$

in which δ is the depth of the internal boundary layer, x is the fetch, and a_{ibl} and b_{ibl} are constants. The constant b_{ibl} is about equal to 0.8 for neutral conditions, 0.6 to 0.7 for stable conditions and 0.8 to 1.0 for unstable conditions. The constant a_{ibl} has a value between 0 and 0.8 and is sometimes determined by a function of both the roughness lengths [Stull, 1988]:

$$a_{\text{ibl}} = 0.75 + 0.03 \ln \left(\frac{z_{0;2}}{z_{0;1}} \right) \tag{2.37}$$

If the roughness becomes less after the transitions ($z_{0;1} < z_{0;2}$) the flow accelerates. In the opposite situation, the flow decelerates; this is associated with convergence and divergence of air and creates extra vertical motions in the IBL. There are two main regions found in the IBL. The first is inner or equilibrium layer; this is the layer near the surface in which the profile has adapted to the new equilibrium conditions. The transition between the equilibrium layer and the conditions outside the IBL is called the bending layer [Garratt, 1990].

VARIATION IN THERMAL PROPERTIES

If air encounters a transition between a cool surface to a warmer surface, a thermal internal boundary layer (TIBL) forms, for example, with land-water transitions. Two states of TIBL can be distinguished according to the stability properties: a convective TIBL and a stable TIBL. A convective TIBL forms when the air moves from a colder to a warmer surface. As with the mixed layer in ABL, the convective TIBL contains much turbulence. Moving further away from the boundary, the temperature difference between the air and the surface decreases; this leads to a reduced heat flux and with that, to a reduction in turbulence. Eventually, the temperature difference vanishes and the air temperature is in equilibrium with the surface temperature. The growth of convective TIBL can be parameterized in terms of the fetch; Venkatram [1977] suggested:

$$\delta = \left[\frac{2C_d \left| \overline{\theta}_{\text{land}} - \overline{\theta}_{\text{sea}} \right| x}{\gamma(1 - 2A_R)} \right]^{1/2} \tag{2.38}$$

in which γ is the vertical gradient in potential temperature directly above the TIBL, and A_R is an entrainment coefficient ranging from 0 to 0.22.

A stable TIBL forms when the wind flows from a warm to a colder surface. This layer has the same properties as the stable ABL. Right after the boundary turbulence is still present in the TIBL, but this decreases when moving further away from the boundary since the turbulence is suppressed by the stable stratification. The height of the stable TIBL can be estimated with the parameterization by Garratt [1987]):

$$\delta = 0.014 \boldsymbol{u} \left(\frac{x\overline{\theta}}{g\Delta\overline{\theta}} \right)^{1/2} \tag{2.39}$$

in which $\Delta\theta$ is the initial temperature difference between the air and the new surface.

MODELS FOR WIND VARIATION OVER THE LAND-SEA BOUNDARY

During the years, several models have been developed to account for the spatial variation of the wind over the land-water boundary. Some of these models are discussed here.

Taylor and Lee [1984] give guidelines on how to account for spatial variation of roughness in neutral conditions. Their approach assumes the development of an IBL with a logarithmic velocity profile. In the layer above the IBL, a logarithmic velocity profile based on the upwind roughness is assumed:

$$\frac{\delta}{z_{0;2}} = 0.75\left(\frac{x}{z_{0;2}}\right)^{0.8} \tag{2.40}$$

in which $z_{0;2}$ is the downstream value of the roughness length.

Based on the assumption of a logarithmic velocity profile for both the IBL and the region above the IBL, it follows that the velocity difference due to the roughness differences can be described by Equation (2.41):

$$\Delta u(x,z) = u_2(x,z) - u_1(z) = \left(\frac{\ln(z/z_{0;1})\cdot\ln(\delta/z_{0;2})}{\ln(\delta/z_{0;1})\cdot\ln(z/z_{0;2})} - 1\right)u_1(z) \tag{2.41}$$

Note that this is only valid inside the IBL (i.e. if $z < \delta$).

In the Netherlands the Wieringa-Rijkoort two-layer model [Wieringa and Rijkoort, 1983] is used for the determination of local wind conditions based on measurements. The model distinguishes two layers, the surface layer, and the Ekman layer. The fundamental idea behind the model is as follows. Based on the wind conditions at a location, the wind speed at a height of 60 m is determined. Assuming that the wind at this height is not influenced by the changes in surface roughness, the same value is valid for a second location in that region. Accounting for the different roughness at that location that local wind speed can be determined using the wind speed at 60 m.

However, it has been shown that the model produces inaccurate results for extreme wind speeds when compared to measurements [Caires et al., 2009]; this problem has been named the curvature-problem. Due to this problem, the current method for determining local wind conditions is reconsidered, and alternatives are investigated.

An more advanced model is proposed by Kudryavtsev et al. [2000]. They developed a model using the IBL approach which accounts for changes in both atmospheric stability and surface roughness. The model distinguishes two regimes. In the first regime, the small scale growth of the IBL within the surface layer is considered. The second regime considers the growth of the IBL above the surface layer. Therefore, the model is valid for both small scale and mesoscale evolution of IBL. A description of the model in terms of equations is rather elaborate and, therefore, not given in this document.

2.3.5. WIND DRAG RELATIONS

It is often easier to express the wind-induced shear stress on the water surface ($\mathbf{u}_*$) using a drag coefficient, as was done in Equation (2.12). In the previous section, the relation between wind speed, temperature, and the aerodynamic roughness was shown; this resulted in a velocity profile depending on the state of the boundary layer and the aerodynamic roughness. In practice, the wind velocity at a certain height is often known (or more easy to determine than the friction velocity). The wind velocity profile is then used to determine the friction velocity $\mathbf{u}_*$.

The determination of the friction velocity based on the wind speed (often at 10 meters, $\boldsymbol{u}_{10}$) can pose some problems. First of all, it is not always straightforward since the Obukhov length contains both the friction velocity and the surface heat flux in its definition. The set of equations, therefore, needs to be solved simultaneously [Stull, 1988]. Furthermore, the conditions for deriving the logarithmic velocity profile (i.e. a more or less constant momentum flux) need to be valid; this means that the surface layer should be deeper than 10 m, and this might not be the case for weak winds [Komen et al., 1996].

In practice, a bulk coefficient for the transfer of momentum from the surface to the atmosphere is often used to determine the friction velocity. This coefficient is known as the drag coefficient.

$$\boldsymbol{\tau} = \rho \boldsymbol{u}_*^2 = \rho_{air} C_d \boldsymbol{u}_{10}^2 \tag{2.42}$$

Using the logarithmic velocity profile, it follows that:

$$C_d = \frac{\kappa^2}{[\ln(z/z_0) + \Psi(z/L)]^2} \tag{2.43}$$

Although relations for C_d are mainly determined based on empirical research, this clearly shows the dependence of C_d on the observation height, roughness height, and the atmospheric stability. It also highlights the dependence of C_d on the existence of the constant flux layer. It can also be seen from Equation (2.43) that differences in atmospheric stability effect influence the drag coefficient. Neglecting stability in the determination of $\mathbf{u}_*$ can lead to deviating values, this can cause large errors in the prediction of wave heights when the stability regime is used [Young, 1998].

Using Charnock's relation, Equation (2.43) can be further expanded. This was first done by Wu [1969] (for neutral stratification), see Equation (2.44). Later Wu [1980] showed that the curve obtained from plotting C_d as a function of the Froude number (Fr), could be very well approached by a linear function.

$$C_d = \left[\kappa \ln^{-1}\left(\frac{1}{\alpha C_d \mathrm{Fr}^2}\right)\right]^2 \quad \text{with} \quad \mathrm{Fr} = \frac{\overline{\boldsymbol{u}}(z)}{\sqrt{gz}} \tag{2.44}$$

Both Garratt [1977] and Wu [1982] provided simple linear relations to express the roughness of properties of the sea surface in the form of a drag coefficient as a function of the wind speed (u_{10}). These relations are very much alike. The relationship by Wu [1982], Equation (2.45), is still often used in numerical models including SWAN.

$$C_d = (0.8 + 0.065\boldsymbol{u}_{10}) \cdot 10^{-3} \tag{2.45}$$

The previously mentioned relations for the drag coefficient only use the wind speed in their formulation. As already mentioned, the relation for the drag coefficient is also a function of the roughness and the atmospheric stability. Geernaert et al. [1987] proposed a drag coefficient as a function of the wave age.

$$C_d = a\left(\frac{\boldsymbol{c}_p}{\boldsymbol{u}_*}\right)^b \tag{2.46}$$

Based on measurements on the North Sea they found that $a \approx 0.012$ and $b \approx -2/3$. For extreme conditions (wind speeds ($> 30\ \mathrm{m\,s^{-1}}$)) Powell et al. [2003] found a maximum value for the drag coefficient, after which the maximum value of C_d decreased. Similar results where obtained by Holthuijsen et al. [2012].

Donelan et al. [2004] investigated this phenomenon in a laboratory setting. He found a maximum drag coefficient for a wind speed of $33\ \mathrm{m\,s^{-1}}$ and higher. He suggests that separation of airflow for the breaking crests could be a possible explanation.

Another possible mechanism for the saturation of the surface drag coefficient is given by Makin [2005]. He believes that the reduced surface drag is the consequence of wave breaking (white capping). During extreme wind conditions, the lowest part of the surface layer is filled with small water particles, forming the so-called suspension layer. The particles are kept in suspension by an upward force caused by turbulent stresses. The presence of this suspension layer changes the dynamics of the airflow and causes a reduction of the drag coefficient.

Zijlema et al. [2012] found a second order polynomial based on different data sets (including both low and high velocities). This resulted in Equation (2.47). Compared to other parameterizations of C_d this equation predicts lower values for the range 15 to $32.6\ \mathrm{m\,s^{-1}}$. Compared to the expression by 2.45 [Wu, 1982] values are 10% to 30% lower. Similar results where found by Hwang [2011] and Zweers et al. [2010].

$$C_d = \left(0.55 + 2.97\widetilde{\boldsymbol{u}} - 1.49\widetilde{\boldsymbol{u}}^2\right) \cdot 10^{-3} \tag{2.47}$$

with $\widetilde{\boldsymbol{u}} = \boldsymbol{u}_{10}/\boldsymbol{u}_{ref}$ and $\boldsymbol{u}_{ref} = 31.5\ \mathrm{m\,s^{-1}}$.

2.4. MODELLING OF ATMOSPHERE

This section investigates the possibilities of modelling processes in the atmospheric boundary layer for the application on hydraulic engineering related problems. An earlier study on this subject by Baas [2014] shows that increasing horizontal resolution in numerical atmospheric models results in a better prediction of wind velocities near coasts and an improvement of the prediction of storm surge levels.

2.4.1. INTRODUCTION

Atmospheric models use balance equations for mass, momentum, heat and moisture in combination with parameterizations of physical processes to simulate the behaviour of the atmosphere. Physical processes associated with the atmosphere are the formation of clouds, precipitation, surface fluxes, ABL processes (turbulence and diffusion) and radiation. These models can be divided into several sub-categories, depending on the aim of the model (weather prediction models or climate models), depending on the scale of the model (global or regional). Based on purpose, timescales, and spatial scales, a general subdivision of atmospheric models can be made:

- General Circulation Models (GCMs)
- Regional Climate Models (RCMs)
- Numerical Weather Prediction (NWP) Models
- Cloud-Resolving Models (CRMs)

General Circulation models (or global climate models) are used to acquire a better understanding of the global climate and the way it develops. GCMs simulate the processes of the atmosphere and oceans (including the effects of sea ice and interactions with land) for periods varying from months to decades. The models use three-dimensional spherical grid over the globe, with resolutions in the order of 3° × 3° to 0.5° × 0.5° [Rasch, 2012].

Regional climate models simulate the local climate of geographic regions varying from few thousand square kilometres to a continent. They are often used for the downscaling of General Circulation models to obtain higher resolutions (~ 50 km). Regional climate models are also used to study local climate processes [Rasch, 2012].

Weather prediction models have been optimized to provide information about the atmosphere over a relatively short time (few days to a week). Weather prediction is typically an initial value problem (where climate modelling is a boundary value problem). To produce accurate results, data assimilation is used to incorporate observations into the model [Rasch, 2012]. The models operate typically on region scales (mesoscale). However, there are also global weather predictions models (e.g. Global Forecast System used by NOAA).

Cloud-resolving models are defined as models that are capable of explicitly simulating individual clouds. This is accomplished by using high spatial resolutions (50 m to 4 km). They are mostly used to study shallow and deep convection, to test cumulus parameterization schemes and advanced studies of cloud systems [Randall et al., 2003].

In this study, the Weather Research and Forecasting (WRF) model [Skamarock et al., 2008] is used (see Appendix B). WRF is a mesoscale numerical weather prediction model designed for both research and operational purposes.

2.4.2. MESOSCALE NUMERICAL WEATHER PREDICTION MODELS

This section gives a description of the capabilities of a state-of-the-art mesoscale NWP model (WRF is taken as an example). An NWP model uses a set of governing equations to predict flows and transport in the atmosphere. These equations are discretized in order to be solved numerically. Parameterizations are added to represent physical processes that could not be described by the governing equations. The discretized equations and parameterizations are applied to a certain domain and integrated using appropriate initial and boundary conditions.

A mesoscale NWP model is an NWP model capable of working at sufficiently high resolutions to forecast mesoscale weather phenomena. Mesoscale meteorology is the study of weather systems with typical scales ranging from 1 km to 1000 km. Atmospheric phenomena in this range include thunderstorms, squall lines, fronts, precipitation bands in tropical and extratropical cyclones, and topographically generated weather systems such as mountain waves and sea and land breezes [Society, 2015]. Typical horizontal spatial resolutions used in these models range from of 2.5 km to 15 km.

The governing equations consist of balance equations for mass (air and moisture), momentum (Navier-Stokes or Euler equations) and energy (first law of thermodynamics) and an equation of state (ideal gas law). With these equations, the model can describe flow and temperature distributions in the atmosphere.

Parameterizations are used to describe processes that are too small (in relation to the computation grid) or too complex to be resolved explicitly. These parameterizations should not be considered individually because the different schemes interact with each other. An overview of the interaction between the physics parameterizations is given in Figure 2.6. Examples of parameterized processes in mesoscale NWP models are:

- Microphysics: The microphysics parameterization scheme describes cloud and precipitation processes. This includes phase changes of moisture and the associated latent heat transport, evolution and interaction of water and ice particle, and fall-out of precipitating particle [Dudhia, 2014].
- Cumulus convection: the cumulus parameterization is responsible for the sub-grid scale effects of vertical latent heat driven transport by updrafts and downdrafts within convective clouds (sometimes also shallow clouds).
- Surface layer physics: the surface layer models determine the friction velocities, moisture fluxes and heat fluxes related to vegetation and snow cover, and possibly urban areas. (WRF uses two parameterizations for this step, the surface layer model and the land-surface model)
- Planetary boundary layer physics: the planetary boundary layer parameterization accounts for vertical sub-grid-scale fluxes due to transport by turbulent eddies in the whole atmospheric column (not only in the boundary layer).
- Radiative physics: the radiation parameterization handles heating of the atmosphere, and soil layers due to short and long wave radiation.

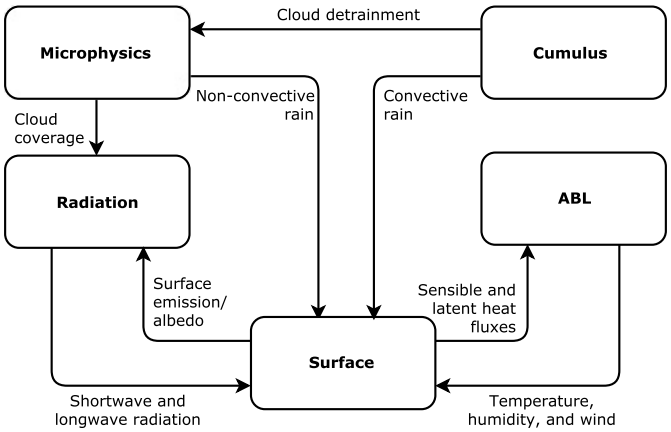

Figure 2.6: Schematic of parameterized physics and their interactions within a typical NWP model. Figure reproduced from Dudhia [2014].

The domain used to compute the governing equations, and the parameterized physics can be in 2-D as well as in 3-D, depending on the purpose of the model. In the horizontal directions, the domain is discretized into a grid. Depending on the model, different types of grids can be used (e.q. WRF uses a (structured) Arakawa-C staggered grid while, MPAS [Heinzeller et al., 2016] uses an unstructured grid using Voronoi tessellations). The vertical direction is divided into layers, for which also different options are available (η-layers, σ-layers). Local refinements can be made in models with structured grids by using nesting. A finer domain is then nested in a coarser domain, in order to obtain the wanted resolutions, without increasing the computational costs too much.

A mesoscale model is driven by the imposed initial and boundary conditions. In numerical weather prediction, it is important to impose accurate initial conditions. Using data assimilation, the models are often updated during the model runs to match most recent conditions. The initial condition and the boundary conditions for a mesoscale model are obtained from larger scale models (e.g. global models such as the Global Forecasting System by NOAA or EMCWF data).

2.4.3. LIMITATIONS OF MESOSCALE MODELS

This section discusses the limitations of mesoscale models (such as WRF). A model is a simplified representation of some part of the real world, for a particular purpose. This definition shows that model is limited in several ways.

An important limitation on the capabilities of these models has always been computational power. A refinement of a horizontal grid with a factor 3 means 3^2 more grid points and a reduction of the time step with at least factor 3; this increases computational cost a factor 27 (even neglecting a possible necessary increment of the vertical resolution). The first mesoscale NWP models—40 years ago—used horizontal spatial resolutions in the order of 100 km and just a few vertical layers. Current mesoscale NWP models are capable of performing computations on spatial resolutions up 1 km [Dudhia, 2014]. During the development of these models much changed, the governing equations (from hydrostatic to non-hydrostatic), the numerical methods (increased stability, efficiency and accuracy) and the parameterizations changed in order to obtain more accurate and reliable results.

Second, these models are designed for specific fields of application. The form of the governing equations and parameterizations of the model are chosen or designed to function within this field of application, and therefore, have limits to their validity, and might produce results that are inaccurate if these limits are exceeded. Increasing the computational power of computers nowadays makes it possible to use these models at very high resolutions. However, limitations are imposed by the validity of parameterization schemes in these models.

Since the some of the parameterization represent (partially) unresolved processes, the validity of parameterization is in some cases linked to the spatial resolutions. These boundaries are not well defined, which implies that there is a grey area in which processes will be partially solved explicitly and partially by the parameterization. According to Dudhia and Wang [2014], parameterizations with such grey areas are:

- planetary boundary layer models, which represent vertical mixing (turbulence)
- cumulus models
- microphysics models

A first problem is related to the resolving capabilities of turbulence in high-resolution models. The planetary boundary layer scheme is used to determine the vertical sub-grid-scale turbulent fluxes in the atmospheric column. The largest turbulent eddies in the atmospheric boundary layer have a typical length scale l in the same order of magnitude as the height of the ABL (~1 km). Until now most models used spatial resolutions (Δ) much larger than the length related to the largest turbulent eddies ($\Delta \gg l$). With the increasing spatial resolutions of mesoscale models, an area is reached in which $\Delta \sim l$; this area is referred to by Wyngaard [2004] as 'terra incognita'. In this grey area, mesoscale models are starting to resolve turbulence explicitly, but the spatial resolutions are still too coarse for large eddy simulations. Based on an international workshop on numerical weather prediction, Hong and Dudhia [2012] state that this is not a practical problem yet. They say that the planetary boundary layer schemes still function adequately at grid resolutions of less than 1 km and possibly less than 500 m. For even higher resolutions (~ 100 m) large eddy simulations are needed.

A second problem arises with cumulus parameterization. On coarse grids, cumulus parameterizations are used to account for sub-grid-scale effects of convective and shallow clouds. The schemes represent the vertical fluxes that are formed by the (unresolved) updraft, downdraft and compensating motions outside the clouds; newer schemes also give cloud and precipitation field tendencies [Skamarock et al., 2008]. These schemes are initially developed for coarse resolutions (32 to 48 km [Arakawa, 2004]).

The problem is formed by the fact that the convective processes are partially resolved and partly determined by sub-grid models in a mesoscale model [Wang and Seaman, 1997; Arakawa, 2004]. This subject has been investigated in many studies over the past years, see for example Weisman et al. [1997], Wang and Seaman [1997] Gilliland and Rowe [2007] and Bryan et al. [2003]. Weisman et al. [1997] studied the effects of grid

resolution on convective processes using a non-hydrostatic cloud model to help clarify the capabilities and limitations of using explicit physics to resolve convection in mesoscale models. They concluded that cumulus parameterizations are not necessary for grid resolutions of 4 km. The study of Gilliland and Rowe [2007] agrees with these finding. However, they found that real-case simulations of a summertime convection case (without significant synoptic forcing), with no cumulus parameterization, and grid resolutions of 4 km, did not produce the expected results. Moreover, they found that a cumulus parameterization scheme was needed to trigger convection and precipitation. Another study by Bryan et al. [2003] concludes that resolutions in the order of 100 m are necessary to fully resolve convective processes.

Resolving convection explicitly also affects the microphysics schemes. Microphysics schemes are responsible for the formation, growth, and sedimentation of water particles in the atmosphere. A scheme with at least six classes (water vapour, cloud water, rain, cloud ice, snow, and graupel) is needed to distinguish the snow from denser ice particles (graupel/hail) formed through mixed-phase interactions (riming) that are associated with resolved vertical motions [Dudhia, 2014].

Finally, Skamarock [2004] investigated the possibilities of model verification based on the kinetic energy spectra, based on earlier work by Nastrom and Gage [1985]. Nastrom and Gage [1985] studied wind and temperature data collected over more than 6900 flights. They showed that there is a clear k^{-3} dependence of the energy in the atmosphere for low wave numbers (spatial scales larger than 5000 km) and a $k^{-5/3}$ dependence for high wave numbers (spatial scales smaller than 5000 km). Skamarock [2004] compared kinetic energy spectra produced by WRF with observed spectra of Nastrom and Gage [1985]. He found that the WRF spectra reproduced the observed spectra well, Indicating correct performance of WRF. However, the energy density was under-predicted for wavelengths between $7\Delta x$ and $2\Delta x$. He suggested that the under-prediction of the model at these spatial scales was due the parameterized dissipation in the model. He suggest an effective resolution of $7\Delta x$ (also see Figure 2.7) to account for these .

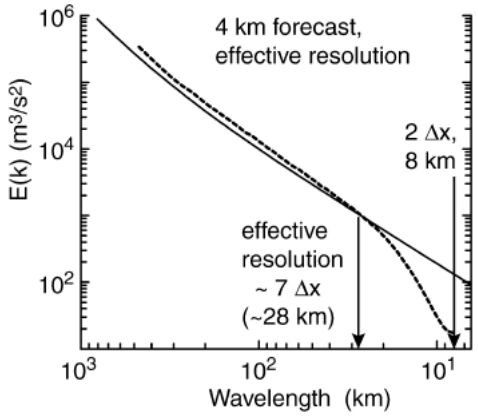

Figure 2.7: Effective resolution determined from forecast-derived spectra for the BAMEX-configured WRF model at 4-km horizontal grid spacing; Dotted line representes model results. Figure reproduced from Skamarock [2004].

2.5. CONCLUSIONS

The purpose of this literature review was to provide insight into the physical processes associated with wave growth, and the wind in the atmospheric boundary layer. Furthermore, as part of the main research objective, numerical modelling of the atmosphere was investigated in an attempt to provide an overview of the possible limitations of mesoscale NWP models regarding spatial resolutions.

2.5.1. WIND-WAVE INTERACTION

The most important factor driving wave growth is the wind. Specifically surface layer winds are important. Characterised by turbulence, the wind in the surface layer is described through the well-known logarithmic profile. The velocity of the wind depends on the surface roughness (z_0), friction velocity ($\mathbf{u}_*$), and the stability of the atmosphere (Ψ_m). The friction velocity $\mathbf{u}_*$ represent a shear stress, and is often used as a coupling parameter for the transfer of energy from wind to waves. The same logarithmic wind profile is also used for the determination of the friction velocity (if the wind speed is known). Waves also influence the wind profile

through the variable surface roughness they impose. The roughness of the water surface depends amongst other on friction velocity, making wind and waves are interdependent processes.

The dependence of the wind on the wave surface makes the determination of $\mathbf{u}_*$ less trivial than for other surfaces. Different methods have been treated in this chapter. It is common to use a drag coefficient for this purpose. The drag coefficient relates the wind speed directly the friction velocity. The properties of the logarithmic velocity profile are then all put together in one bulk coefficient. A drawback of these methods is the limited validity of these coefficients since they are derived from particular observations. A more fundamental approach is, therefore, preferable.

A second parameter that influences the velocity profile of the wind is the stability of the atmosphere, commonly measured by the Obukhov length (L_b) or bulk Richardson number (Ri_b). Due to a difference in temperature, the atmosphere can be stable (cold air below warm air), unstable (warm air below cold air), or neutral (no temperature difference or a high wind speed). The stability changes the velocity profile of the wind given a certain wind speed in the surface layer—creating higher friction velocities for unstable conditions and lower friction velocities for stable conditions; this has a direct impact on wave growth.

Despite the waves, the water surface is much smoother than land surfaces; this causes winds to increase their velocity when they move offshore, and the decrease their velocity when they move onshore. Throughout the years, many relations have been established to calculate the open-water wind speed from a land-based wind speed. Most of these relations (or models) use the assumption of an internal boundary layer that develops inside the ABL due to differences in roughness or temperature.

Altogether, it can be seen that the interaction between wind and waves is quite complex. The dependence of the surface roughness on the wind and the dependence of atmospheric stability on the water temperature makes coupled approaches between models attractive option (e.g. Warner et al. [2010],). Otherwise, the use of advanced parameterizations—including stability, and wind speed depended on roughness lengths—for the determination of $\boldsymbol{u}_*$ are preferred.

2.5.2. LIMITATIONS OF ATMOSPHERIC MODELLING

The atmospheric models available nowadays, provide advanced methods to simulate the wind and other atmospheric processes using high spatial resolutions. Operational models already go as high as resolutions of 2.5 km. However, several studies indicate that higher resolutions are possible, keeping in mind the limitations of the model. Limitations of these mesoscale NWP models related to high resolutions are found in the planetary boundary layer parameterization, the cumulus parameterization, and the microphysics parameterization.

- Turbulent fluctuations are removed from the governing equations by Reynolds averaging. The PBL scheme parametrizes vertical sub-grid-scale fluxes due to transport by these turbulent fluctuations. The parameterization should be used for resolutions lower than ~ 1000 m. No PBL scheme should be used for resolutions higher than ~ 100 m. The range in between is a grey area; it is questionable whether or not the model produces physically reliable results for this range.
- The cumulus parameterization is used for the determination of sub-grid-scale convective processes. The parameterization should be used for resolution lower than ~ 4km. The convective processes are fully resolved for resolutions higher than ~ 100 m. The area in between is a grey area, and the reliability depends on the particular situation. However, it is advised to turn of the parameterization for resolutions higher than ~ 4km.
- Once convection permitting resolutions are reached, microphysics schemes should be able to distinguish the snow from denser ice particles (graupel/hail) formed through mixed-phase interactions (riming) that are associated with resolved vertical motions of order 10 m s-1 or more. The scheme would otherwise underestimate the fall speeds precipitation rates near convective cores.

In conclusion, there are theoretical objections to high-resolutions, mainly because turbulence will be resolved both implicitly—by the planetary boundary layer scheme—and explicitly by resolving large eddies with the model. However, the consequences do not do not have to be problematic. Studies have shown that models still function adequately for resolutions higher than one kilometre.

3

METHODOLOGY

3.1. INTRODUCTION

This chapter provides an overview of the steps that were necessary to answer the research question and to accomplish the objectives of the study. First, a general description of the study is given. This section describes the primary activities of the study and the intended results. The study focuses on a specific location. The choice of the location is described in Section 3.3. Furthermore, during the study two storms were hindcasted; Section 3.4 describes the chosen storms. Finally, the last section of this chapter gives the techniques that were used to analyse the data.

3.2. OVERALL APPROACH

To obtain an answer to the main research question, two types of numerical models were used; an atmospheric model, to hindcast the wind fields during the two storms; and a wave model, to hindcast the waves during these storms. For the atmospheric simulations WRF ARW V3.6.1 [Skamarock et al., 2008], a state-of-the-art non-hydrostatic NWP model for atmospheric simulations was used. Wave simulations were carried out using SWAN 40.72ABCDE [Booij et al., 1999], a state-of-the-art third-generation spectral wave model. General descriptions of these models are given in Appendices B and C for WRF and SWAN respectively. All data processing was performed off-line using MATLAB [The MathWorks Inc., 2014].

First, the WRF model set-up had to be determined. Since there was no experience with WRF, the model settings and input were determined based on literature and earlier studies. To analyse the results, tools for post-processing were developed using MATLAB. With the chosen settings, an assessment was made of the ability of WRF to reproduce the wind conditions during the two storms. The validation consisted of an analysis of both the synoptic scale (qualitatively) performance and the mesoscale performance. Furthermore, some of the settings were varied to investigate the models sensitivity to this configuration. These simulations were used as a reference in the later analysis.

Second, the SWAN model was set up using the calibrated settings that were also used in simulations by Deltares [2013]. As with WRF, reference simulations with SWAN were performed and analysed to assess the quality of the model prediction for the two storms. Again, post-processing tools were developed using MATLAB. Analysis of the results provided an overview of the predictive capabilities of SWAN using the WRF wind field.

Third, to test the performance of WRF at high spatial resolutions, the two storms were hindcasted using spatial resolutions of 2.7 km, 1.5 km, 900 m, 500 m and 300 m. An analysis of the results and observations indicated the performance of WRF at these resolutions and the possible limitations.

Finally, a preprocessing method was developed to overcome some problems with the input for SWAN. Simulations were then performed with SWAN using the different wind field resolutions. The simulations were analysed to investigate the added value of the high-resolution wind fields.

3.3. LOCATION

The chosen location is at the north-west of Lake IJssel (see Figure 3.1); this is not a location where short-fetch waves are part of the governing hydraulic conditions (which would be the case in e.g. harbours or rivers), but it does provide an enclosed environment that excludes swell waves from the measurements. This simplifies the comparison between the simulations and the measurements. The same location was used in previous studies by Deltares [2013, 2015]. They valued this location for three reasons. First, because the measuring locations lay in a straight line perpendicular to the shore (about 59°N). Second, the prevailing wind conditions at this location are south westerly. Third, the first two measuring locations are close to the shore; this makes it possible to validate and investigate the wave growth at short fetches.

Figure 3.1: Lake IJssel, area of interest (red rectangle). Green dots represent measuring locations.

3.4. CHOICE TEST-STORMS

Given the limited time available for this study, the same storms were used as in the study by Deltares [2015]. The underlying idea was that using the same storms has several advantages. The storms are already modelled and analysed in an earlier study by Deltares [2015] using WRF, HARMONIE, and HIRLAM; this provided reference material that could be used for assessing the added value of higher resolutions.

The periods were used:

- storm 1: 3–6 January 2012

- storm 2: 3–7 December 2013

In the following sections a qualitative description is given of these storms based on reports of the 'stormvloedwaarschuwingsdienst' (SVSD, formerly StormVloedSeinDienst), a Dutch warning service for flood risks.

Storm 1 The period between January 3rd and 6th actually consisted of two storms. The first storm was caused by a strong depression that moved from Scotland to South-Norway on January 3rd, 2012. At the southwest side of the depression, a strong storm field caused winds to reach speeds op 10 to 11 Bft. Early in the afternoon on January 3rd, a cold front passed the Dutch coast. After the passage of the front, wind directions veered to the west-southwest. The wind near the coast varied from 8 to 9 Bft. In the morning of January 4th, winds veered to west-northwest and increased in speed. Towards the afternoon, a second depression moved in, causing the winds to lie down. [SVSD, 2012a]

[h]

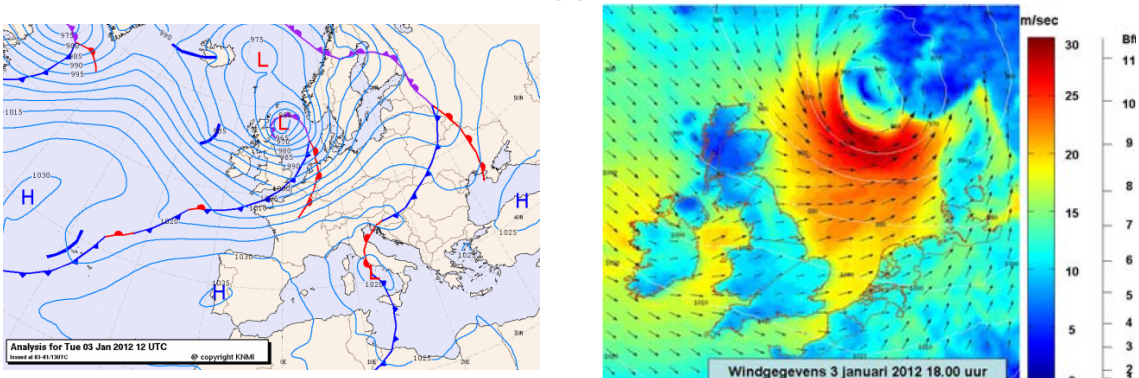

(a) **(b)**

Figure 3.2: Left: a) Weather map during the storm at January 3rd 2012, 13:00 UTC+1 [SVSD, 2012a]. Right: b) Wind and air pressure at January 3rd 2012, 18:00 UTC+1 [SVSD, 2012a].

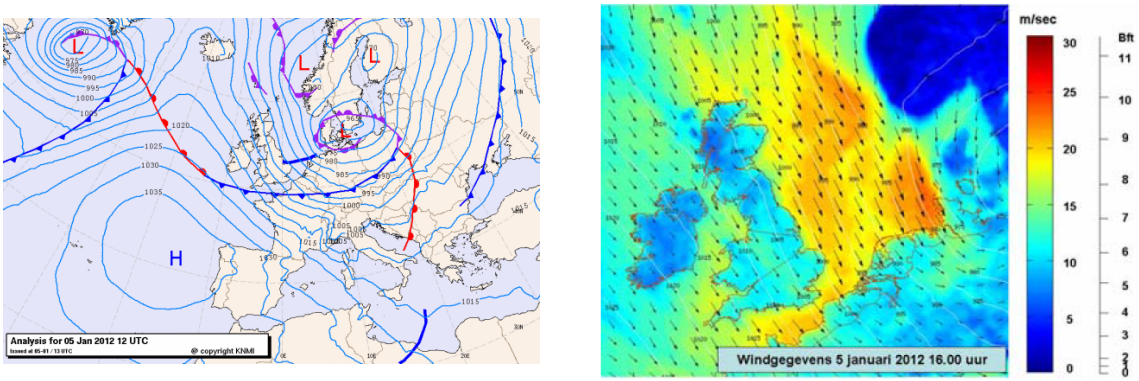

(a) **(b)**

Figure 3.3: Left: a) Weather map during the storm at January 5th 2012, 13:00 UTC+1 [SVSD, 2012b]. Right: b) Wind and air pressure at January 5th 2012, 16:00 UTC+1 [SVSD, 2012b].

The second storm in this period was caused by a low-pressure system (975 hPa) that was positioned south of Iceland in the afternoon of January 4th. The depression moved in the southeast direction until it reached the south of Sweden in the afternoon of January 5th. During the morning of January 5th, a cold front associated with (thunder)storms, hail and strong wind gusts passed from north to south of the Netherlands. After the passage of the cold front, the wind direction veered from southwest to west-northwest. The wind decreased in strength from severe gale to moderate gale conditions. In the afternoon, a trough reached the northern coast, after which the wind veered to northwest. Wind speed increased again to gale–severe gale conditions. In the afternoon of January 5th, the cold depression moved on towards the east and winds over the North Sea

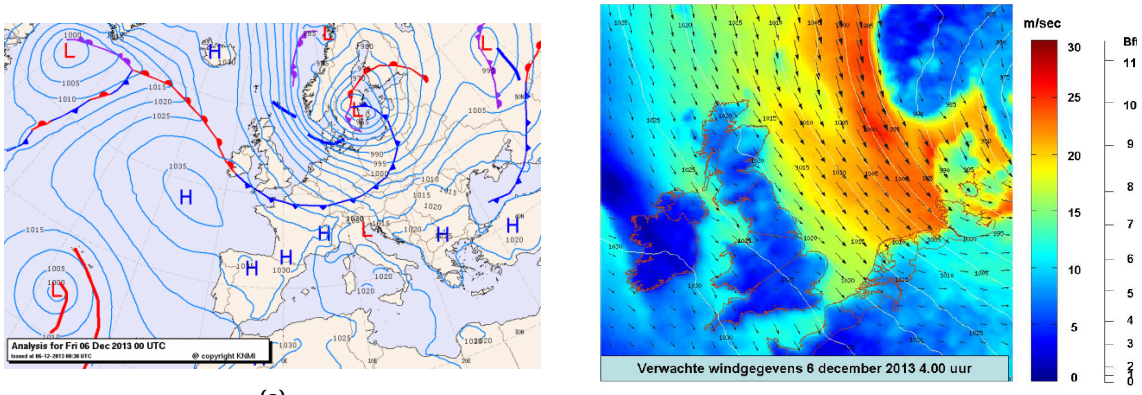

(a) **(b)**

Figure 3.4: a) Weather map during the storm at December 5th 2013, 01:00 UTC+1 [SVSD, 2013]. b) Wind and air pressure at December 6 2013, 04:00 UTC+1 [SVSD, 2013].

reached speeds of 8–9 Bft. In the morning of January 6th, a ridge approached from the west causing the wind to decrease to 6–7 Bft. [SVSD, 2012b]

Storm 2 At December 5th, 2013 an active low-pressure system (970 hPa) moved from Scotland to the Baltic sea. At the west side of this low-pressure system, there was a storm field. During the afternoon, a cold front passed the Netherlands, followed by a back-bent occlusion. During the passage of the back-bent occlusion, winds increased rapidly in strength reaching 10 Bft. After the cold front had passed, the wind decreased in speed to 9 Bft and veered to northwest. The wind remained fairly strong near the coast during that night and the next day (7–8 Bft), but decreased during the evening on Friday, December 6th to 6 Bft. [SVSD, 2013]

3.5. DATA COLLECTION

This section gives a description of the available data from measurements and the relevant specifications of the instruments with which the measurements were performed. Mainly two data sets were used during this study, these are:

- KNMI Stations
- Rijkswaterstaat (RWS) wind and wave measurements at Lake IJssel.

3.5.1. KNMI STATIONS

The network of measuring stations of the KNMI exists of about 55 stations. Most stations are land based (see Figure 3.5). The stations automatically register a number of variables. A list of some of these variables is given below. However, not every station measures all these variables and the availability of data also varies in time.

- Temperature (at various heights above the ground or sea surface)
- atmospheric pressure or air pressure
- humidity or relative humidity, dew point temperature
- wind speed and direction
- precipitation (amount and duration), snow cover
- clouds (type, sort, and height) and degree of coverage

For this study, the most relevant parameters are wind speed and wind direction. These are measured at a height of 10 m above a flat surface, usually a grass or water surface. Obstacles are placed at a minimal distance of ten times the height of the object, to make sure the observations are not disturbed. The measurements are said to be representative for an area within a radius of 30 km from the measuring location.

Wind speed measurements were carried out with cup anemometers. These are operational within the region between 0.5–50 $\mathrm{m\,s^{-1}}$ and are accurate up to 0.5 $\mathrm{m\,s^{-1}}$. The instrument provides a resolution of 0.1 $\mathrm{m\,s^{-1}}$. The sampling frequency is 1 Hz. Wind speed measurements are reported as hourly averaged values, the average of the last ten minutes of an hour and the maximum gust per hour (3-second average).

Wind directions were measured using wind vanes; these measure the wind direction in a range of 360°. They are operational for wind speeds > 2 $m s^{-1}$. Measurements are accurate up to 3°, and the instrument provides a resolution of 1°; the sampling frequency is 1 Hz. Wind direction data were reported as the average of the last ten minutes of each hour. For information on the other measurement equipment used by the KNMI, the reader is referred to KNMI [2001].

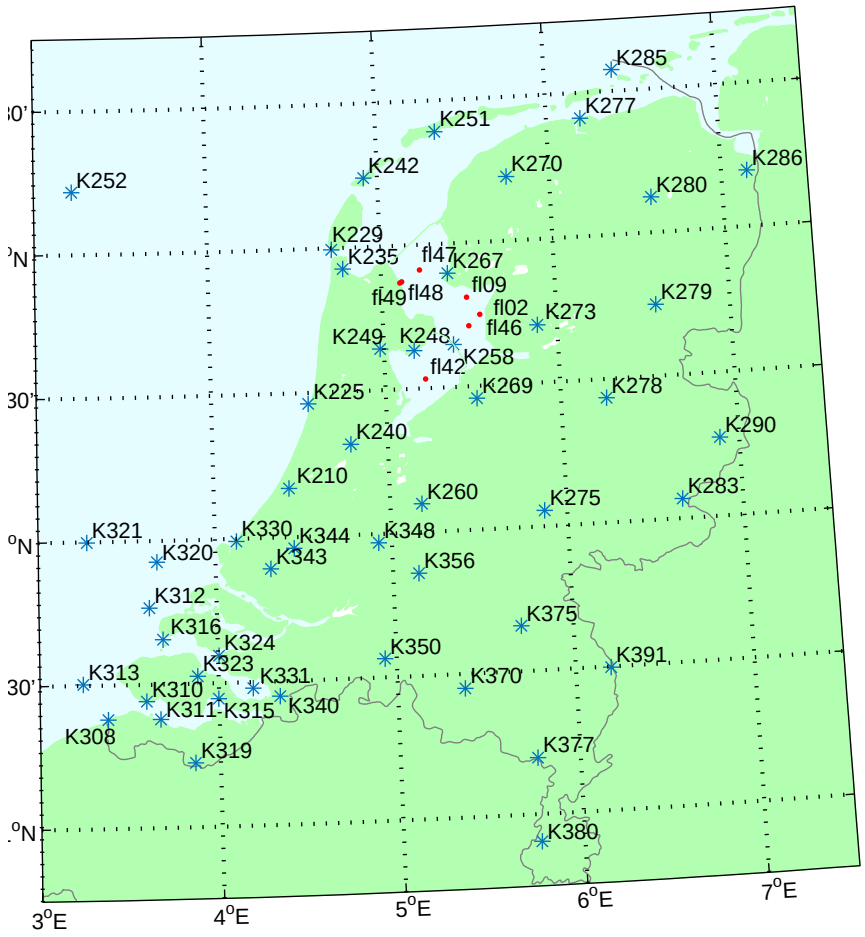

Figure 3.5: An overview of measuring stations, blue stars denote KNMI stations and red dots denote RWS stations.

3.5.2. WIND AND WAVE MEASURING CAMPAIGN RIJKSWATERSTAAT

In 1997, Rijkswaterstaat (RWS) started a large wind and wave measuring campaign on Lake IJssel and Lake Sloten [Bottema, 2007]. Initially, the campaign would continue until 2007, but it was extended and is currently still ongoing. The information presented in this section is mainly based on the description of Bottema [2007]; Baas [2014]; Deltares [2015]. Figure 3.5 shows the locations of measuring stations in Lake IJssel. Besides the wind and wave data also air and water temperatures are collected.

Wave data were collected using Etrometa step gauges and capacitance probes. The step gauges are of the Marine-300-11 type. The step gauges are 3 m long and contain 60 sensors, providing a resolution of 0.05 m. The sampling frequency of the wave gauges is 4 Hz. The orientation of all the step gauges is southwest. The capacitance probes are of the Multicap DC 11 type. The capacitance probes are 3 or 5 m long and have a sampling frequency of 4 Hz (except for station FL25, that has a sampling frequency of 8 Hz). The orientation of

all the step gauges is southwest. It should be noted that these measurements are not without errors. Deltares [2015] mentions that wave observations at these measuring stations are likely to be over predicted by 5–10% for directions around 240°N.

Wind speed is measured with cup anemometers of type 403 (in some cases type 018) produced by Mierij Meteo. The cup anemometers start to function from wind speed of 0.5 $\mathrm{m\,s^{-1}}$. Wind direction is measured using wind vanes of type 508 produced by Mierij Meteo. The resolution of these wind vanes is 1.4°. For both the wind speed and direction, sampling frequencies of 1 Hz are used.

3.6. DATA ANALYSIS

This section describes the proposed method for the analysis of the results. The data from both models (WRF and SWAN) is analysed both visually and numerically. All data processing was performed off-line using the software package MATLAB [The MathWorks Inc., 2014].

Error statistics used here are the Root-mean-square error (scatter index), bias (relative bias), the standard deviation of the error, and correlation coefficient. An overview of the definitions of the statistical parameters used in this report can be found in Appendix E.

The bias or mean error (ME) is an indicator that measures structural errors in data. The bias is positive if the model structurally over-estimates the parameter, and negative if it structurally underestimated the parameter. As an alternative, also the relative bias is included, in with the bias is normalized using the average of the observation.

The standard deviation of the error σ_{p-o} gives the spread of the error, which can be used as a measure of the performance. The value of the standard deviation is larger or equal to zero, where zero is a perfect score. The standard deviation of the error is insensitive to structural errors.

The root-mean-square error (RMSE) is a measure of the overall error in the model. By squaring the errors, only positive terms are produced. Squaring the errors also punishes larger errors more than small errors, making it sensitive to outlines. As an alternative also the Scatter Index (SI) is included, which is defined as the RMSE normalized by the mean of the observations.

The correlation coefficient (r) measures the linear correlation between two variables. The correlation coefficient is an indicator of how well two patterns coincide. However, the correlation coefficient is not sensitive to structural errors. The correlation coefficient ranges from -1 to 1, where |1| indicates a perfect correlation and 0 indicates no correlation.

Some general examples of errors and the behaviour of the statistical parameters are shown in Figure 3.6. Note that is was not intended to provide a full overview of all possible types of errors. It can be show that $\mathrm{RMSE}^2 = \mathrm{BIAS}^2 + \sigma_{p-o}^2$. This can be a helpful feature in determining the type of error that was found (structural or non-structural).

3.6.1. WIND

Early inspections of model results were done visually (2-D plots, 1-D plot, scatter plots). For the verification of the wind data, the following parameters were assessed: temperature, wind speed (u_{10}), friction velocity (u_*) and wind direction (θ_{wind}).

Measured data were reported in hourly averaged (KNMI), and 10-minute averaged (RWS) values. For both data sets, wind speed and wind directions were reported separately. Modelled data were requested in time series at certain points and for the whole domain. The diagnostic 10-m wind values were reported in vector form, at every time step for the time series and every 10 minutes for all grid points. For each vector, the magnitude and the direction were determined. Afterwards, data were averaged to 10-minute and hourly values so that they could be compared to the observed data.

For the verification, values at a height of 10 m were used. Most land-based stations measure winds at a height of 10 m. This is not always the case for water-based stations. The stations that did not meet these requirements were corrected. The KNMI in the Netherlands uses the Benschop correction [Benschop, 1996] to convert wind speeds from non-standard heights to 10 m heights. The Benschop method assumes a logarithmic velocity profile in neutral conditions. The neutral stratification assumptions make it questionable to use this method. Baas [2014] investigated the use of the Benschop method in non-neutral conditions. He states that

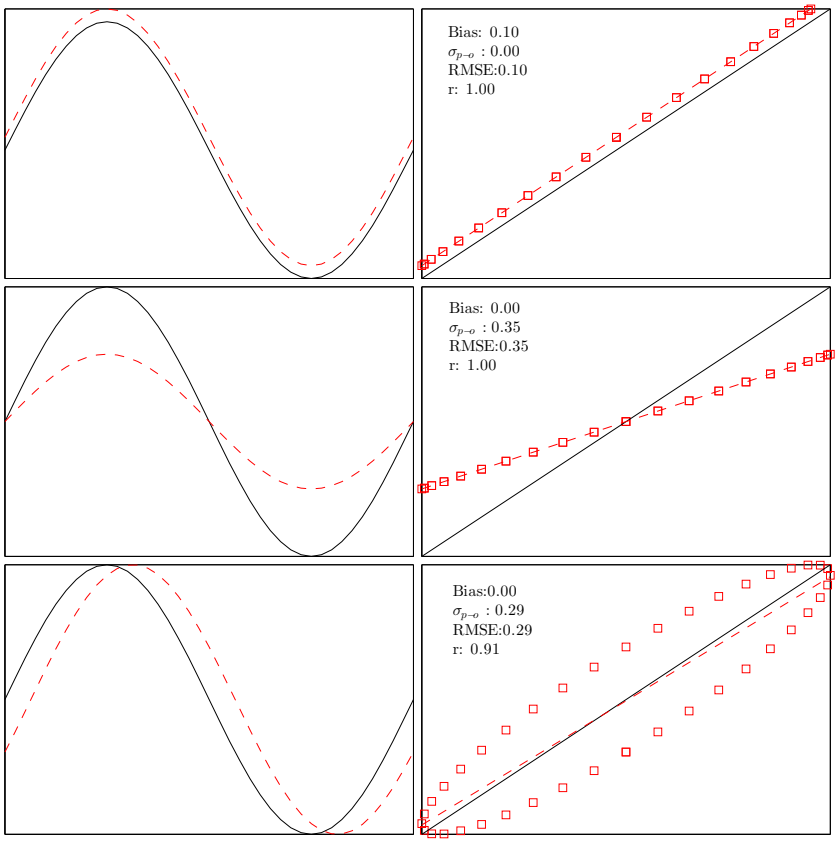

[h]

Figure 3.6: Examples of different types of errors and the behaviour of the statistical parameters. Left: Function of a arbitrary variable, right: the corresponding scatter plot

the errors are in the same order of magnitude as the error in the observations and that the application of the Benschop correction is justified.

Modelled data were assessed visually by comparing 2-D plots, scatter plots and box plots with measurements. Finally, a more quantitative representation of the quality of the forecast is given using statistical quantities: RMS error, bias, relative bias, scatter index, the standard deviation of the error, and correlation coefficient.

3.6.2. WAVES

For the verification of the wave data, the following parameters were assessed: significant wave height (H_{m0}), and wave periods (T_p, T_{m01}, T_{m02}, and T_{m-10} T_{m02}). The wave parameters were determined according to Equations 2.5–2.6. The measured wave spectra had ranged from 0.08 Hz to 1.5 Hz. To match the observations, wave parameters from SWAN were also determined using this range of frequencies.

Modelled data were compared visually with measurements using graphs, 2-D plots, and scatter plots. Once it seems that the model is reproducing the measured data, statistical tools are used to gain insight into the quality of these predictions. Finally, a more quantitative representation of the quality of the forecast is given using statistical quantities: RMS error, bias, relative bias, scatter index, the standard deviation of the error, and correlation coefficient.

4

MODELLING OF THE ATMOSPHERE

4.1. INTRODUCTION

In this chapter, a model set-up is described for the atmospheric NWP model WRF. An overview of the WRF model is given in Appendix B, but for a detailed description the reader is referred to Skamarock et al. [2008]. The set-up of the model was determined using tutorials, rules of thumb, and other literature. The model was validated for its performance to predict the wind, by evaluating the spatial and temporal evaluation of the boundary layer variables, and comparing them to measurements. This analysis is a baseline measurement for the remainder of the study. Some alternative settings are discussed at the end of the chapter.

4.2. MODEL SET-UP

WRF is a mesoscale numerical weather prediction system designed for both research and operational purposes. The model consists of two dynamical cores, the Advanced Research WRF (ARW) developed by MMM Division of NCAR [Skamarock et al., 2008], and the Nonhydrostatic Mesoscale Model (NMM) developed by The NOAA/NCEP and the Developmental Testbed Center (DTC) [Janjic et al., 2010]. The main differences between these cores are the grid definitions and the integration methods. The NMM is primarily used for operational weather forecasting, and the ARW is also used for research purposes. ARW also provides the opportunity to study idealized cases, which is not possible with NMM. This study uses the ARW core of WRF version 3.6.1.

4.2.1. INITIAL AND BOUNDARY CONDITIONS

The initial and lateral boundary conditions were provided by the ERA-interim reanalysis dataset [Dee et al., 2011]. ERA-Interim is a global atmospheric reanalysis produced by the European Center for Medium-Range Weather Forecasts (ECMWF). The dataset covers a period from 1979 onward and is updated every month. The atmospheric model of ERA-interim uses cycle 31r2 of the ECMWF's Integrated forecasting system (IFS) [ECMWF, 2007]. This system uses a four-dimensional variation analysis (4D-VAR) to included observations in the analysis. The model uses 60 levels in the vertical, and the model top is located at 0.1 hPa. The model uses a T255 spectral grid, which corresponds to a resolution of approximately 79 km [Berrisford et al., 2011]. The atmospheric model is coupled to a wave model. The wave model implemented in the IFS is based on WAM [WAMDI Group, 1988]. With a resolution of 110 km, wave spectra are discretized using 24 directions and 30 frequencies. For more information, the reader is referred to Dee et al. [2011].

The specific dataset that was used to provide the initial and lateral boundary conditions for WRF was sampled with a spatial resolution of 0.75° × 0.75° and a temporal resolution of 6 hours. In the vertical, meteorological variables were given at 38 levels.

Era-Interim is distributed in several files; static variables, surface level variables, and 3-D variables are stored separately. Furthermore, relative humidity—a variable required by WRF—is not available in the ERA-Interim data set. Because of this, implementation of ERA-Interim in WRF was not trivial. A method was found in which several parts of the data set are pre-processed by WPS (WRF Preprocessing System) individually. Because ERA-interim contains the specific humidity—and not the required relative humidity—a modification

of the variable table was needed solved this issue. Finally, the sea surface temperature (SST) were included in WRF from ERA-Interim.

A additional test was also conducted using the FNL dataset from NCEP [NCEP et al., 2000], see Section 4.4. The performance of this dataset was similar to the performance of ERA-Interim.

4.2.2. GRID CONFIGURATION AND DOMAIN

Domains in WRF can be configured using four types of projections: the Lambert conformal, polar stereographic, Mercator, and latitude-longitude projections. Depending on the location, the most suitable projection is chosen. A Lambert projection was chosen for this study since it is most suitable for domains around mid-latitudes [Skamarock et al., 2008]. The true latitudes of the projection (i.e. the latitudes where the projection intersects the surface of the earth) were 49°N and 55°N, and the domain was centred around 56°N, 2°W. Furthermore, the WRF domains were defined parallel to the 2°W meridian.

HORIZONTAL DISCRETIZATION

For the purpose of this study high horizontal resolutions (~ 300–2,500 m) were needed. Furthermore, the domain needed to be large enough (~2,000 × 2,000 km) to capture synoptic scale processes [Gill and Pyle, 2012]. Covering a domain of this size with a high-resolution grid would computationally be very demanding. To overcome this problem, WRF provides the possibility of dynamically downscaling the model, using nests with different resolutions. With nests, the resolution of a domain can be refined multiple times and communication between nests can be both in one or two-way. As a rule of thumb, it is advised to keep the ratios between these nests and the outer domain a factor 3 [Dudhia and Wang, 2014]. Since the model needs to adapt the variables to the new grid resolutions, it should be kept in mind that results near the border of the nest are inaccurate. The minimum distance between the nest's boundary and the parent boundary is four grid cells. However, this is insufficient as a buffer zone between those nests.

Courser grids are computationally less demanding, recall the example given in Section 2.4, a refined of the horizontal grid with a factor 3 leads to an increase of the computation time by at least a factor 27. The finest grid is most demanding, and the courser grid is relatively 'cheap'. It is not unreasonable to use a course grid with three times the dimensions of the fine grid. In general no less than 100 × 100 grid points should be used. The number of grid points in the outer domain should not be less than the number of grid points in the inner domain [Gill and Pyle, 2012].

The domains were defined working from the inside out (i.e. from the finest domain to the coarsest domain). For this 'reference' set-up a resolution of 500 m (domain 5) was tested near the area of interest (Lake IJssel). This domain consisted of 100 × 100 grid points, and the domain was positioned such that the larger part of the domain lies in the upwind direction (southwest) of Lake IJssel; this was done to obtain a good representation of the land-induced surface roughness. Domain 4 had a resolution of 1,500 m and also consisted of 100 × 100 grid points. As for domain five, domain four was also positioned such that the largest part lay southwest of the domain 5. Similar reasoning was used to create domain 3, which also had 100 × 100 grid point and a resolution of 4,500 m. Domain 2 had a resolution of 13,500 m and was positioned in such a way that the United Kingdom lay within the domain. Domain one was the largest domain using a resolution of 40.5 km and 100 × 80 grid points it covered an area of 4,050 km × 3,240 km. An overview of the domain configuration is given in Figure 4.1 and 4.2. All domains were two-way nested (i.e. there was feedback between the domains).

Limited-area models are very sensitive to the lateral boundary conditions imposed [Warner, 2011], and it is advised to investigate the sensitivity of the model to the location and size of the domain. To this extend additional tests were performed using different positions of the computational domain; these are discussed in Section 4.4.

VERTICAL DISCRETIZATION

In general at least 30 vertical levels, with a model top at 50 hPa (~20 km) are recommended [Skamarock et al., 2008]. The distance between these layers should not be larger than 1000 m [Wang, 2015]. Dudhia and Wang [2014] advice to keep $\Delta z < \Delta x$, not doing so might lead to significant noise at the top of the model.

Keeping these recommendations in mind, 40 vertical layers were used, with the model top at 50 hPa. Figure 4.3 shows the distribution of these layers with height. It can be seen that the layers are non-equidistantly

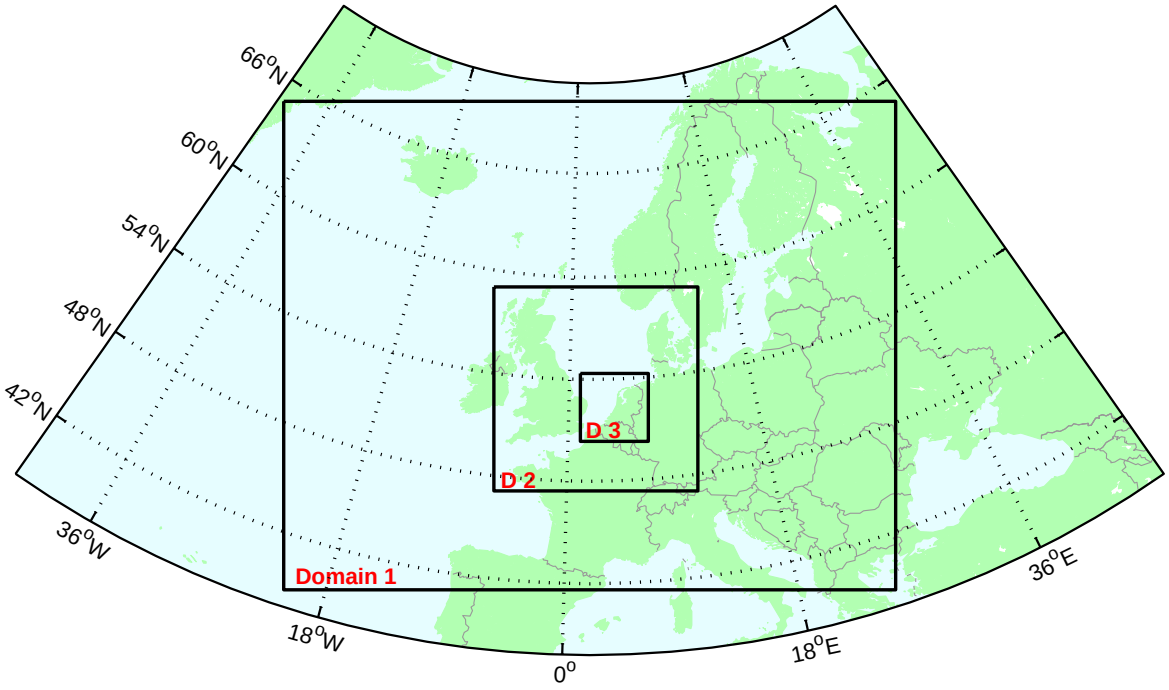

Figure 4.1: Projection of Europe showing domain 1 ($\Delta x = 40,500$ m), domain 2($\Delta x = 13,500$ m), and domain 3 ($\Delta x = 4,500$ m)

spaced, creating a higher resolution near the bottom of the domain. This is specifically done to capture the large gradients of parameters in the boundary layer.

4.2.3. RUN TIME

The duration of the simulations consists of the required spin-up time and the duration of the storm. Because initial conditions are usually much coarser than the computational grid, only large-scale structures are present in the model initially. WRF needs some time to spin up for the correct representation of small-scale structures Skamarock [2004] in the model. The amount of spin-up time that is required for this varies in literature. Baas [2014]; van der Brink et al. [2013] state that these small scale structures need 5–10 hours to develop. Other, studies use longer spin-up times up to 24 hours [Hawkins, 2012; Kleczek et al., 2014].

For this study 6 hours of spin-up time were used. The duration of both storms was four days, resulting in a total simulation time of 4.5 days.

4.2.4. TIME STEP

The chosen horizontal resolution and the numerical schemes that were used for the simulations, impose constrains on the maximum allowable time step. The time step (Δt) of the model should be small enough to prevent any numerical instabilities.

The combination of the 5$^{\text{th}}$ order convection scheme and 3$^{\text{rd}}$ order Runge-Kutta (RK3) scheme gives the following requirement:

$$C_{\text{cr}} = \frac{\mathbf{u}\Delta t}{\Delta x} < \frac{1.42}{\sqrt{3}} \tag{4.1}$$

in which C_{cr} is the Courant number, Δx ($= \Delta y$) is the horizontal resolution, and Δt is the temporal resolution. Note that the original Courant number is reduced with a factor of $\sqrt{3}$ to account for the three dimensions [Skamarock et al., 2008]. The only remaining unknown is the maximum velocity. As a rule of thumb, Skamarock et al. [2008] advices a time step (in seconds) smaller than six times the horizontal resolution in kilometres.

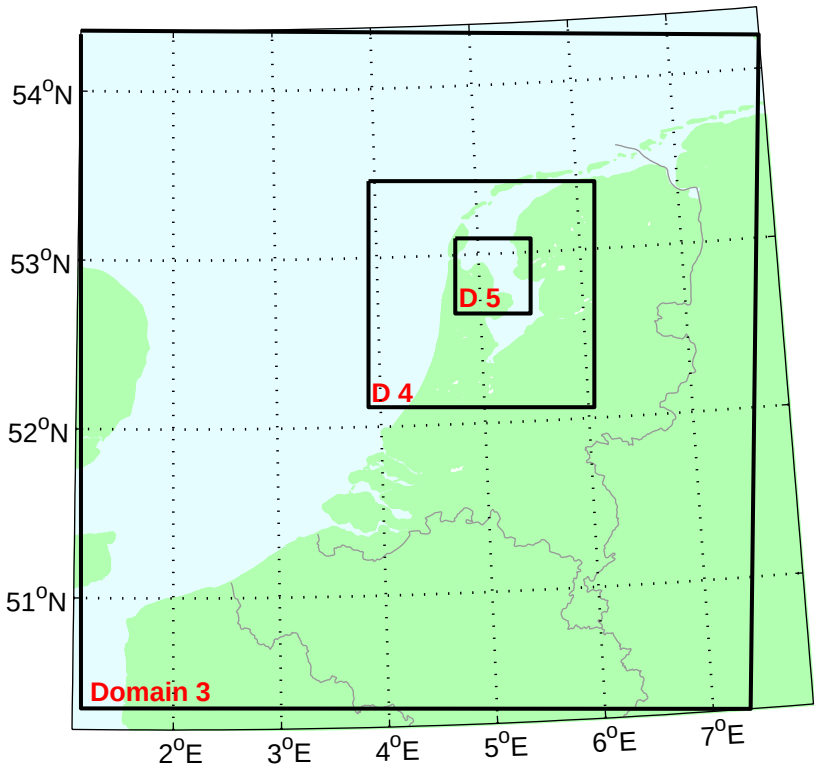

Figure 4.2: Projection of the Netherlands showing domain 3 ($\Delta x = 4,500$ m), domain 4($\Delta x = 1,500$ m), and domain 5 ($\Delta x = 500$ m)

Table 4.1: Horizontal resolutions and time steps used in WRF simulations. * 166 × 166 grid points instead of 100 × 100

Domain	Δx [m]	Δt [s]
1	40,500	180
2	13,500	60
3	4,500	20
4	1,500	6.67
5	500	2.22

Time steps were chosen for each domain, taking into account these requirements. The time steps were round off in order to be able to generate the model output at a convenient interval.

4.2.5. GEOPHYSICAL DATA

Land elevation data from the Shuttle Radar Topography Mission (SRTM) by NASA and NGA [2015] was used. NASA used interferometry to determine the surface height. The SRTM collected data of most land surfaces between 60°N and 54°S and has a resolution of 30 arcseconds (~ 900 m).

Two data sets are available for land-use data: the USGS data set containing 24 categories and the IGBP MODIS data set containing 20 categories. By default, the USGS land-use maps are used in WRF. The IGBP MODIS maps are only used in combination with the Noah land surface layer model. IGBP MODIS data are available with resolutions up to 15 arcseconds (~ 500 m), whereas the highest resolution of the USGS data is 30 arcseconds. Since WRF was required to model storms at high resolutions (even smaller than 500 m), a high resolution of the land-use data was preferred. Therefore, IGBP MODIS with a resolution of 15 arcseconds was chosen.

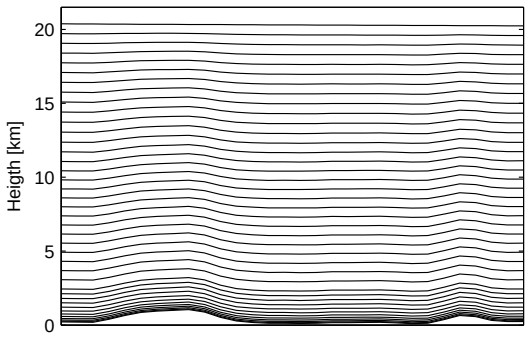

Figure 4.3: Vertical cross-section showing the distribution of vertical layers.

4.2.6. PHYSICS

WRF uses several physics parameterizations. For each type of parameterization, several options are available, varying from simple models to more advanced models.

Microphysics The microphysics parameterization scheme describes cloud and precipitation processes. This includes phase changes of moisture and the associated latent heat transport, evolution and interaction of water and ice particles, and fall-out of precipitating particles. A total of 21 microphysics schemes are available in WRF. The Eta scheme (or Ferrier scheme) [Rogers et al., 2012] was selected for this study because it was designed for high-resolution operational forecasts [MMM and NCAR, 2015].

Cumulus Parameterization The cumulus parameterization handles the sub-grid scale effects of vertical latent heat driven transport by updrafts and downdrafts within convective clouds (or sometimes also shallow clouds). A total of 11 cumulus schemes are available in WRF. The Kain-Fritsch scheme [Kain, 2003] was used (default) for domains 1 and 2. The resolutions of the other domains were high enough to explicitly resolve convective processes so that the cumulus scheme could be turned off (see Section 2.4.3).

Planetary Boundary Layer The planetary boundary layer parameterization accounts for vertical sub-grid-scale fluxes due to transport by turbulent eddies in the whole atmospheric column (not only in the boundary layer). A total of 13 PBL schemes are available in WRF. Two schemes are generally recommended [Hawkins, 2012], Mellor-Yamanda-Janjic (MYJ) scheme [Janjic, 1994], and the Yonsei State University (YSU) [Hong et al., 2006]. For this study, the Yonsei University scheme (YSU) [Hong et al., 2006] was selected.

Surface Layer The surface layer determines friction velocities and exchange coefficients that are used in the land-surface models and planetary boundary layer scheme for the determination of the surface fluxes. Except for water surfaces, where the scheme calculates the fluxes itself. A total of 8 surface-layer schemes are available in WRF. The revised MM5 similarity theory [Jimenez et al., 2012] was selected for this study. This parameterization had to be used together with the MRF or YSU PBL scheme.

Land-Surface Model The land-surface models used information, from all other physics parameterizations to determine surface fluxes. A total of four Land-surface models are available in WRF. The unified Noah land-surface model Tewari et al. was selected for this study. This model is only compatible with the IGBP MODIS data and it must be used with either the YSU or MRF PBL scheme.

Atmospheric Radiation The radiation parameterization handles heating of the atmosphere, and soil layers due to short and longwave radiation.

- Longwave-radiation includes infrared or thermal radiation absorbed and emitted by gasses and surfaces. A total of seven longwave-radiation schemes are available in WRF. The Rapid Radiative Transfer Model (RRTM) [Mlawer et al., 1997] was selected (default) for this study.
- Short-wave radiation parameterization includes visible and surrounding wavelengths that make up the solar spectrum. A total of seven shortwave-radiation schemes are available in WRF. The Dudhia scheme [Dudhia, 1989] was selected (default) for this study.

Because the radiation schemes are computationally demanding, it is advised not to call the radiation parameterization every time step. Instead, it is advised [MMM and NCAR, 2015] to related the time step between the calls to domain resolution, by using time steps of one minute per kilometre grid size. This value should be equal for all domains in case of two-way nesting. Hence, a time step of 0.5 minutes was used between the calls of the radiation schemes.

4.2.7. NUMERICS

WRF provides several options for the numerical schemes used by the solver of the model. Time marching is done with a time-split approach, in which high and low-frequency modes are treated separately. This is especially done to prevent unnecessary small time steps based on acoustic modes (which are insignificant). For both modes, Runge-Kutta 3 (RK3) is used for the integration.

The advective terms of the equations can be integrated using 2^{nd} to 6^{th} order schemes. The even-order schemes are spatially centred, and the odd-order schemes are upwind schemes, making them diffusive.

The 5^{th} order scheme was selected for the horizontal terms and the 3^{rd} order scheme was selected for the vertical terms as was recommended by Skamarock et al. [2008].

4.3. MODEL VALIDATION

To validate the performance of the model, reference simulations were made for both storms using the model settings described in the previous section. This section describes the validation procedure and the results.

4.3.1. EVALUATIONS STRATEGY

The model results were validated on two scales, synoptic (qualitatively) and a mesoscale level. The synoptic validation of the model primarily concerned the position and strength of pressure centres and the position of weather fronts. The pressure systems are the driving force of the boundary layer winds and are thus crucial for the correct prediction of the wind fields. Weather fronts are responsible for rapid changes in the wind field. Hence, incorrect prediction of the frontal areas leads to temporal errors in the wind records. Furthermore, fronts are often associated (depending on the type of front) with precipitation and convective processes. The mesoscale performance of the model was determined by comparing several boundary layer variables (the wind, temperature, and humidity) with observations. This gave insight into the quality of the modelled wind fields.

SYNOPTIC SCALE

For the qualitative validation of the synoptic scale performance of the model weather charts of the KNMI were used. The weather charts were produced based on analysis using HIRLAM. The charts were produced every six hours and contain atmospheric pressure reduced to mean sea level (MSLP) and weather fronts. No digital data were available of these weather maps. Therefore, the analysis is only qualitatively. The charts were compared with WRF predictions for Domain 1 (Δx=40.5 km).

A full synoptic weather analysis of the WRF prediction was not made since this was beyond the scope of the study (and it would require a meteorologist). Instead, using the available parameters from the WRF hindcast, charts were made of the equivalent potential temperature (theta-e (θ_e)) at a height of approximately 700 hPa, mean sea level pressure (MSLP), and 10-m wind. Theta-e gives a good overview of the movement of different air masses since it combines temperature and humidity in one parameter. Because of this, it is also a good indicator of weather fronts. Since weather fronts are often associated with rapid changes in wind direction, winds are a good second indicator. The variables theta-e and MSLP are no standard output variables of WRF. The methods used to determine these variables are described in Appendix A.

MESOSCALE

The mesoscale evaluation consisted of the comparison of predicted boundary layer variables with observed variables. The variables considered were wind and temperature. The output of WRF data was requested every 12 minutes for all grid points in the domain. In addition, also times series were requested at the specific points where measurements were taken. For these points, all time steps were recorded. WRF will automatically interpolate by means of nearest-neighbour approach. Although this is not ideal, there are no other ways of interpolation available in WRF for this. The domain used for this evaluation is domain 3 (Δx = 4.5 km), because this domain covers the whole Netherlands.

The wind and temperature were evaluated. Measured variables came from measurement stations of the KNMI and RWS (only wind). The predicted values were treated in the same way as the observed values, i.e. average over the same period. Measurements of wind speed and direction were reported by the KNMI as the average of the last ten minutes of the hour, and for the wind speed also as hourly average values. The temperature was reported as the instantaneous measurement at each hour. WRF variables are treated in the same way.

WRF data was compared to point measurements. According to Baas [2014], the use of grid box averaged roughness length in the model causes a deviation from the local values within the grid box. Since measurement stations are placed in relatively smooth regions (open grass fields), this causes modelled wind speeds to be lower than the measured values. A second problem described by Baas [2014] occurs near the land-water boundary. Stations near the land-water boundary might behave either as a land-based station or as a water-based station, depending the direction of the wind (upstream roughness). To overcome these problems, he proposes a correction of the measured results based on the wind direction. The procedure consists of determining an observed roughness, which is done using the standard deviation of the wind and the observed wind speeds (see e.g. [Verkaik, 2000]), and physical downscaling (e.g. [Rooy and Kok, 2004]) is used to correct the prediction using the 'observed roughness'. However, standard deviations needed to determine the observed, direction-depended roughness are not publicly available. Therefore, the method could not be used. The problems mentioned should be kept in mind when evaluating the results.

4.3.2. SYNOPTIC SCALE EVALUATION

At the start of the simulations, WRF predictions were almost identical to the weather charts. The high and low-pressure systems were predicted at the right locations with the correct MSLP values. Furthermore, it can be seen from the theta-e contours and the wind direction that the warm and cold fronts were also predicted correctly. Occulted fronts and troughs could not be identified from these WRF plots. See Figures 4.4 and 4.5 for an impression of the synoptic predictions by WRF.

In both storms it seemed that the pressure systems and fronts remain predicted well, however, small deviations did become visible. Although it cannot be seen at this scale, some errors were found due to temporal differences of the passage of fronts. Looking at time series of the wind direction during the storm, the passage of cold fronts can be observed from the rapid changes in wind direction. Figure 4.6 to 4.9 give time series of both the storms for station FL48. The passing cold and warm fronts are indicated using vertical lines. It can be seen that at the beginning of both storms, the model is about an hour ahead of the observations. During the second day of the simulations, these errors faded away. However, at least for the first storm, at the end of the simulation, there was once again a temporal difference at the synoptic scales.

These errors affected mostly the wind direction; the wind speed did not give a directly noticeable reaction to the passage of fronts. What should be kept in mind is that difference in directions can also lead to different upstream aerodynamic roughness. So there might still be some second order influences noticeable.

4.3.3. MESOSCALE EVALUATION

OBSERVATIONS

This section gives a detailed description of the wind behaviour during the two storms. The station FL48 at Lake IJssel is used as a reference. Figure 4.6 to 4.9 show time series of the wind speed and wind direction.

Storm 1: January 2012 Early on January 3rd, 2012, a moderate south-southwest breeze (around 10 $\mathrm{m\,s^{-1}}$) blew over Lake IJssel. During the night and the next morning, wind speeds increased steadily to strong gale wind speeds (20–22 $\mathrm{m\,s^{-1}}$). After the passage of the cold front (around 14:00), winds veered to west-southwest and wind speeds dropped rapidly to moderate breeze conditions. The cold front was followed by a trough around 18:00. In the following hours wind speeds rose again to a maximum of about 17 $\mathrm{m\,s^{-1}}$ (around 20:00). During the evening, wind speeds gradually decreased again to 13–14 $\mathrm{m\,s^{-1}}$. At about 04:00 the second trough passages the Netherlands and wind veered rapidly to west. The passage of the trough has no noticeable influence on the wind speed. During the morning of January 4th, the wind direction gradually backed to west-southwest. In the evening, the wind gained speed and rose to near-gale conditions (about 16 $\mathrm{m\,s^{-1}}$). Around 01:00 (January 5th) a warm front passed the Netherlands, followed by a cold front about three hours later. The passage of the cold font caused the wind to veer west (even west-northwest for a short period)

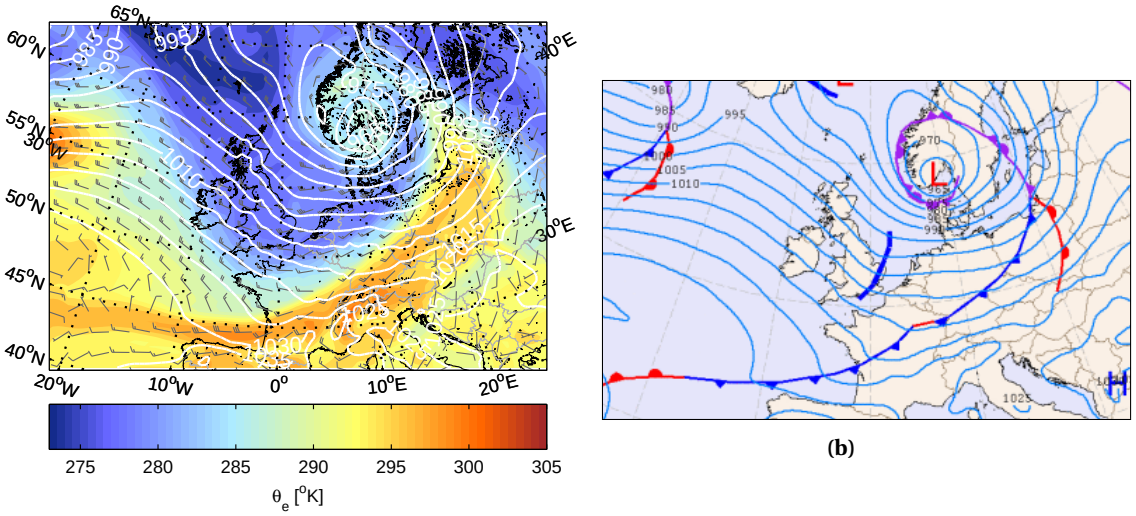

Figure 4.4: Synoptic weather conditions at January 4rd 2012, 01:00 UTC+1. (a) WRF predictions showing theta-e [°K] at 700 hPa, MSLP [hPa] (white contours) , and 10-m winds (half barb equals 2.5 $m\,s^{-1}$, full barb 5 $m\,s^{-1}$, and triangle 25 $m\,s^{-1}$). (b) Weather chart KNMI

and it temporarily weakened to a strong breeze. During the rest of the morning and the afternoon, wind speeds kept a near-gale strength and veered (west-northwest around 18:00). The trough that passed in the afternoon (around 14:00) did not have a noticeable influence on the wind conditions. After midnight, another trough passed with no notable effect on the wind speed. In the moving of January 6th, the wind backed and decreased to a gentle breeze in the evening.

Storm 2: December 2013 During December 4th, 2013, wind conditions where mild (moderate breeze). Winds started of blowing from west-southwest. During the morning winds start veering. Around 12:00 a cold front passes the Netherlands, causing the wind to shift (almost instantly) to north-northwest. A change in wind speeds during this event was barely noticeable. The wind gradually backed to west-southwest after the cold front had passed. During the night of December 5th, winds rapidly gained speed, reaching severe gale speeds around noon (+20 $m\,s^{-1}$). These high wind speeds remained until a cold front arrived, and winds shifted to west-northwest. Wind speeds fell back to about 15 $m\,s^{-1}$, but rose again to gale/ near-gale conditions, after the event. These conditions remained during the night. Around the afternoon on December 6th, winds gradually weakened, and during the night on December 7th, winds started backing. In the morning, the wind had turned to south-southwest, and wind speeds were less than 5 $m\,s^{-1}$. During the afternoon, around 13:00, a warm front passed the Netherlands, veering the wind to west-southwest and causing wind speeds to increase slightly.

WIND DISTRIBUTION

To obtain a general impression of the performance of WRF spatial distributions of the predicted wind speed and direction are plotted against the observed distributions during the same storms. Figure 4.10 and 4.11 show these distributions. It can be seen that WRF underestimates the lower wind speeds (between 0–7.5 $m\,s^{-1}$ for storm 1, and 0–4 $m\,s^{-1}$ for storm 2). The mid-range velocities were over-predicted by WRF. High velocities were represented well by the model. It should be noted that there were only a few measurements (2952 for storm 1 and 3936 for storm 2) in total. Furthermore, only two storms were reviewed; the winds in both storms were predominately south-westerly to northwesterly. Thus, biases might be specifically related to these wind directions and do possibly not indicate the performance of WRF for other circumstances.

Looking at the distributions of the wind directions it stands out that WRF winds are oriented more towards the west than the observed winds. Especially the wind directions predicted in the first storm mostly cover a narrow band between 250°N and 280°N. During the second storm wind conditions are more spread out between 240°N and 310°N. No specific reasons for these biases have been found.

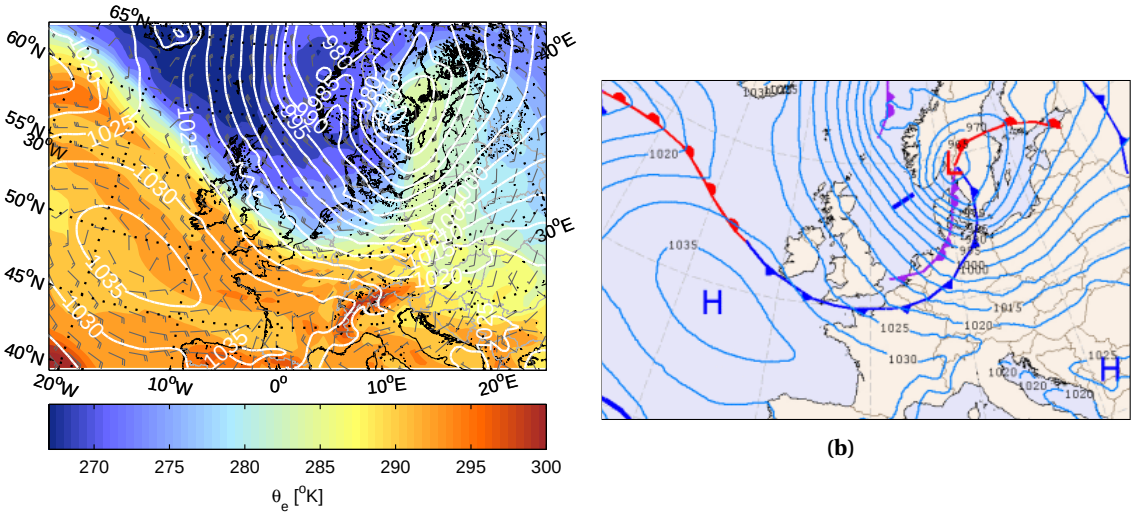

(a) (b)

Figure 4.5: Synoptic weather conditions at December 5rd 2013, 01:00 UTC+1. (a) WRF predictions showing theta-e [°K] at 700 hPa, MSLP [hPa] (white contours) , and 10-m winds (half barb equals 2.5 ms^{-1}, full barb 5 ms^{-1}, and triangle 25 ms^{-1}). (b) Weather chart KNMI

STABILITY

The correct prediction of wind conditions in non-neutral conditions is a challenge for atmospheric models [Hawkins, 2012]. Atmospheric stability can cause deviations in the estimation of the friction velocity (u_*), which translates into the incorrect prediction of the wind in the surface layer. An obvious choice to assess the stability would have been the bulk Richardson number. However, the bulk Richardson requires observations of wind and temperature at equal height. This is not the case in the present situation. Correcting wind or temperature profiles to other heights—especially in non-neutral conditions, and maybe more important, this close to the surface —is not trivial due to the interdependencies of these variables.

The data of the surface temperature and air temperature is shown in Figures 4.12 and 4.13. It should be mentioned that WRF did not predict water temperatures itself. The SST data were updated from the ERA-Interim reanalysis and interpolated to the WRF grid. This means that temperatures for Lake IJssel were determined based on sea surface temperatures.

It stands out from the figures that the surface temperature shows relatively large errors for both storms (~ 2° for storm 1 and ~ 2.5° for storm 2). The surface temperatures from WRF were structurally higher than those observed.

Air temperature measurements correspond to different heights (WRF at 2 m and the RWS measurements at 5 m). This makes the comparison between of the measurements harder. It was not possible to make a height correction for either one of these, without introducing further errors.

Comparing the differences between surface and air temperatures, it can be seen that there is only a small difference between the surface temperature and the air temperature for WRF. Except for a short period around noon January 3rd, both temperatures varied around 7 °C for storm 1. This indicates little to no heat flux. For storm 2, differences between air and surface temperature varied between 0 °C and 0.5 °C, where surface temperature was higher. The observations showed larger differences. For the first storm, air temperatures were about 2 °C higher than the surface temperature. The differences for the second storm were smaller, varying from 0 °C to 0.5 °C, where air temperatures were higher.

Based on the small temperature difference in the WRF data for the first storm, it is safe to assume that wind profile in WRF was predicted according to (near-)neutral conditions. The temperature difference shown by the observations indicates a tendency to more stable conditions. For the second storm, WRF predictions showed that surface temperatures are somewhat higher than the air temperature (most of the time). The difference indicates a tendency to unstable conditions. Observations showed the opposite for the second storm, with a tendency to stable conditions.

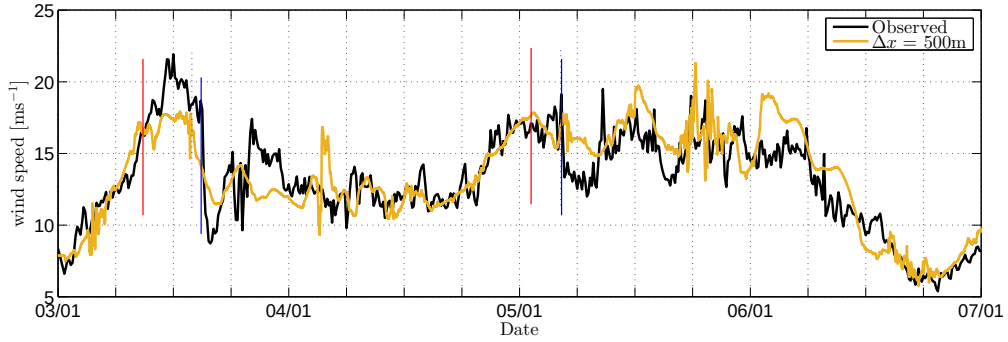

Figure 4.6: Storm 1: Wind speed for station FL48, vertical lines indicate passage of a weather front. (Blue: cold front, Red: warm front, Purple: occulted Front — Solid line: Observations, dotted line:WRF).

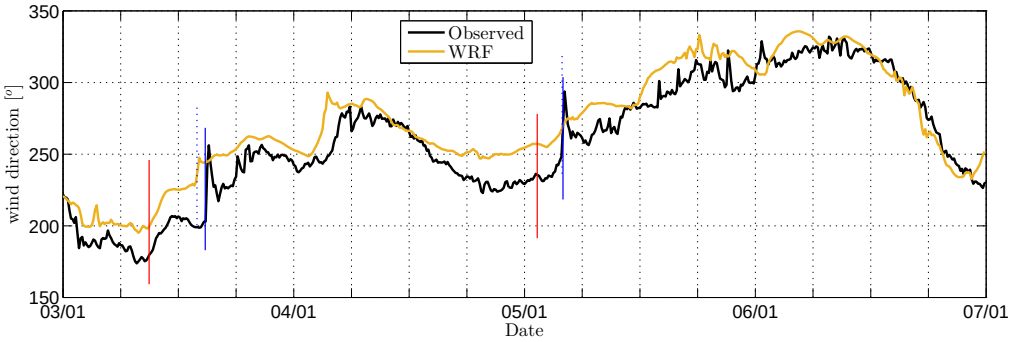

Figure 4.7: Storm 1: Wind direction for station FL48, vertical lines indicate passage of a weather front. (Blue: cold front, Red: warm front, Purple: occulted front — Solid line: observations, Dotted line: WRF).

SPATIAL AND TEMPORAL EVOLUTION

This section discusses the spatial and temporal trends for the boundary layer parameters. The analysis mainly consists of the evaluation of statistical parameters. Several figures show statistics for locations of the measuring stations. The figures shown in this sections only show the bias, RMSE, and the correlation coefficient of storm 1. In Appendix F a complete overview is given of all statistical parameters for both storms.

Wind speed The statistical parameters of the wind speed for storm 1 are shown in Figure 4.14. It can be seen that there is a small (~5%) negative bias for the stations near the coast (Figure 4.14a). Moving land inwards, the bias becomes positive and increases to value around 1.5–2.0 $\mathrm{m\,s^{-1}}$ (~10–20%), indicating an over-prediction by WRF. There are some stations (K240 Schiphol and K225 IJmuiden) that show biases that clearly deviate from the surrounding stations. Figure 4.14b shows that the standard deviation of the errors is more or less the same for all stations and roughly varies between 1.5 and 2.5 $\mathrm{m\,s^{-1}}$. Except for the stations that showed high biases, the RMSE varies roughly between 1.5 and 2.5 $\mathrm{m\,s^{-1}}$. The SI does show a clear spatial trend in which the stations near the coast show lower values (10–20%) and the stations inland higher values (30–50%). The measuring stations in and around Lake IJssel follow the general trend and show only little bias for storm 1 ($\pm$ 0.5 $\mathrm{m\,s^{-1}}$ or < 4%). Figure 4.14d shows that the correlation coefficients vary roughly between 0.7 and 0.8. WRF shows more or less the same patterns for the second storm. The bias is slightly higher, especially for the station in Lake IJssel (1.5–2 $\mathrm{m\,s^{-1}}$ or 10–20%). The RMSE varies roughly between 1.5 and 2.5 $\mathrm{m\,s^{-1}}$. The SI also shows the same pattern, with lower values at the coast (10–20%) and higher values inland (40–50%). The correlation coefficient varies around 0.9.

The model predicted wind speeds rather well, even though de model was not calibrated. For some stations, in particular, K240 Schiphol and K225 IJmuiden, high biases were found. This is likely caused by the error associated with comparing between grid-cell-averaged quantities and point measurements. The higher land-inward biases are associated with lower wind speeds; this is in correspondence with the finding of the previous section, where was found that low velocities are overestimated by WRF. These lower inland wind speeds also explain the spatial trends that were seen for the relative parameters (relative bias and SI).

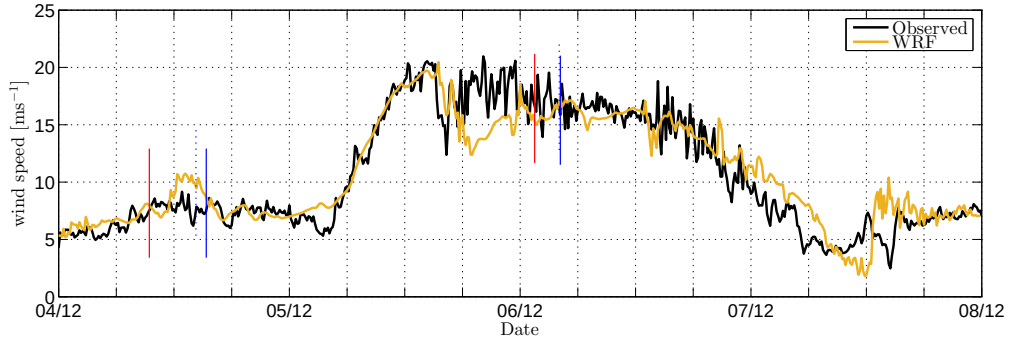

Figure 4.8: Storm 2: Wind speed for station FL48, vertical lines indicate passage of a weather front. (Blue: cold front, Red: warm front, Purple: occulted Front — Solid line: Observations, Dotted line:WRF).

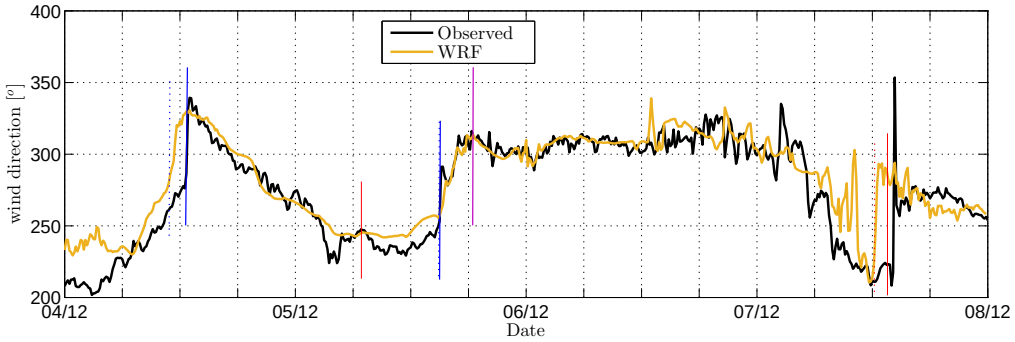

Figure 4.9: Storm 2: Wind direction for station FL48, vertical lines indicate passage of a weather front. (Blue: cold front, Red: warm front, Purple: occulted front — Solid line: observations, Dotted line: WRF).

Wind direction Statistical parameter of the wind direction for storm 1 are shown in Figure 4.15, note that directional statistics are used here, see Appendix E. Station FL49 is excluded from the dataset because it showed only one constant value. It can be seen from Figure 4.15a that the bias varies roughly between 2° and 12°, predicted wind speeds are shifted clockwise relative to the observations. The wind direction turns from 264° at the northwest of the Netherlands to 240° at the southeast of the Netherlands. The bias shows this same pattern, but also shows some high values in southwest of the Netherlands. High value are shown for stations FL48 and FL02. Figure 4.15b shows that the standard deviations vary roughly between 8° to 11°, moving from the nothwest to southeast. High values were found for station FL02. The resulting RMSE error, show in Figure 4.15c, follows the same spatial trend with values around 9° in the northwest and roughly 13° in the southeast. The high values for station FL48 and FL02 are about 20°, twice as high as the surrounding stations. Figure 4.15d shows high correlations coefficients throughout the domain (most stations > 0.95). The results for the second storm seem much poorer than for the first storm. Biases near the coast (including FL48 and FL49) in the northwest and west are comparable with those stations in the first storm, but in other regions (including station FL47) the biases are much higher (roughly between 10° and 15°). The standard deviations also give high values over the whole domain (~20°), resulting also in high RMSEs. Correlation coefficients were high, about 0.9.

The results of the first storm were reasonably good; especially the correlation coefficients were very high; indicating a good temporal representation. Some deviating values were found for two stations in Lake IJssel—FL48 and FL02. FL48 only showed a deviation in the bias, indicating a structural error. Station FL02 showed large values for both the bias and the standard deviation, indicating both large structural and large incidental errors. The second storm showed overall both large biases and large standard deviations.

Temperature Statistical parameter of the air temperature for storm 1 are shown in Figure 4.16. It should be noted that temperature are measured by the KNMI at a heigth of 1.5 m, while predicted temperature by WRF are given at a height of 2 m. Therefore, some bias is expected due to the difference in height. The magnitude of the bias depend on the atmospheric stability. The potential temperature is constant trough out the boundary

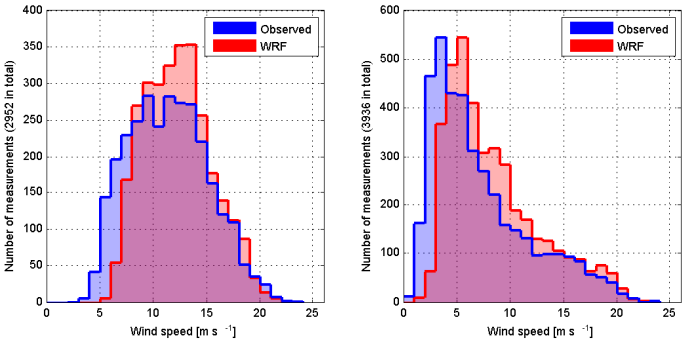

(a) **(b)**

Figure 4.10: Distribution of modelled and observed 10-m wind speed [$\mathrm{m\,s^{-1}}$] for all stations in bins of 1 $\mathrm{m\,s^{-1}}$. (a) Storm 1, (b) Storm 2.

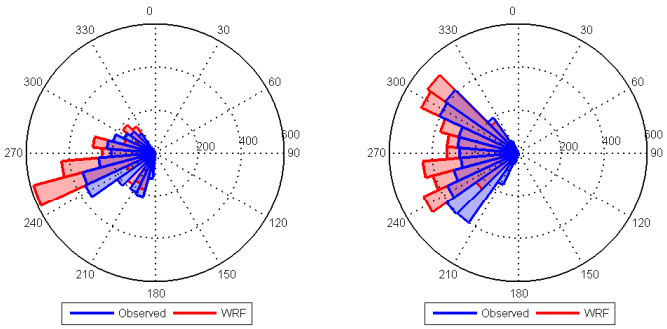

(a) **(b)**

Figure 4.11: Distribution of modelled and observed 10-m wind direction [°N] for all stations in bins of 10°; (a) storm 1, (b) storm 2.

layer during neutral conditions, so in that case comparison between 1.5-m and 2-m temperature is justified. During stable conditions it is expected that the 1.5-m temperature is slightly lower than the 2-m temperature. The opposite is expected during unstable conditions.

During the first storm, temperatures varied roughly between 8°C in the southeast of the Netherlands to about 6°C in the northwest of the Netherlands. WRF predictions also showed the same spatial pattern, with higher temperatures in the southwest and lower temperatures in the southeast. Figure 4.16a shows that biases at the northwest of the Netherlands were slightly positive (~ 0.2°C or <0.05%). More land-inward, temperature biases decreased and became negative (~-0.4 °C, about -10%). The RMSE values varied around 1°C; no spatial trends were noticeable. The correlation coefficient was poor at the northwest of the Netherlands ($r = 0.5$) but became better towards the southeast ($r = 0.9$).

During the second storm, temperatures varied roughly between 6.5°C in the west of the Netherlands, to 3°C in the east of the Netherlands. WRF predictions also showed the same spatial pattern, with higher temperatures in the west and lower temperatures in the east. Figure 4.16a shows that biases at the north of the Netherlands were positive (~ 1°C or 10%–20%). Towards the south, temperature biases decreased and became negative (~-0.7 °C, about -10%). The RMSE values varied roughly between 1–2°C, no spatial trends were noticeable. The correlation coefficient varied between 0.6 and 0.9, with no distinct pattern.

WIND FIELD VARIABILITY

Some spatial plots and cross sections were made to obtain an impression of the variability of the wind field produced by WRF. The plots of one timestep are shown in Figure 4.17 as an impression. WRF uses an Arakawa-C grid causing the 3-D variable (i.e. not the diagnostic 10-m variables that have been used so far) to staggered. Because of this, they were not available at the same grid points. The u and v-velocity components were unstaggered by linearly interpolating them to the mass grid points. For the cross sections, a nearest-neighbour approach was used.

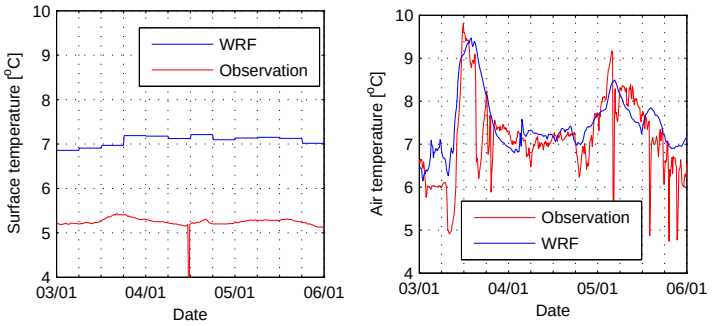

(a) **(b)**

Figure 4.12: Temperature [°C] during storm 1 for station FL47; (a) water temperature, (b) air temperature (observation at a height 5 m, WRF output at a height 2 m).

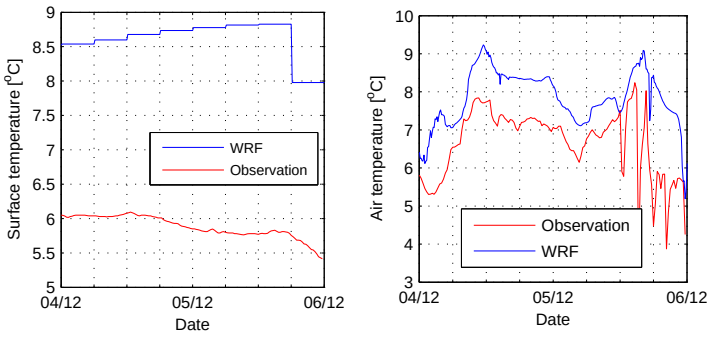

(a) **(b)**

Figure 4.13: Temperature [°C] during storm 2 for station FL47; (a) water temperature, (b) air temperature (measurement at 5 m, WRF output at 2m).

Figure 4.17a show the 10-meter wind speed in space. It can be seen that there is much variability in the wind field due to differences in roughness. Clear wind streaks are visible, indicating that the differences in surface roughness are still noticeable far downstream (tens of kilometers after the change in surface roughness). The wind steaks indicated little lateral exchange of momentum.

It is questionable whether these winds streaks are real, or just a numerical result of the boundary/ surface layer parameterization. Kudryavtsev and Makin [1996] mention that strong jet-like surface winds of tens of kilometres can develop a thermal boundary layer due to strong pressure gradients. However, this is not likely the cause of the wind streaks observed in these simulations since surface temperatures vary only very little (about 0.2°C for the example of Figure 4.17a). Another article also mentions these wind streaks in WRF. Dörenkämper et al. [2015] investigated boundary layer winds in relation to an offshore wind farm near the coast of Denmark. They also used WRF at high spatial resolutions (700 m). They found that these wind streaks disappear during unstable conditions, due to the extra vertical mixing.

Figure 4.17b shows the wind speed along the cross section in the vertical. The position where the cross section was taken is shown in Figure 4.17c. It is quite clear that there are some vertical variations in the wind speed. The vertical discretization is too coarse to be able to witness variations due the differences in surface roughness (the lowest layer lies at a height of about 25 meters), even when zoomed in on the lower part of the boundary layer.

Taking a closer look at the velocity differences between the measuring stations gives some interesting insight. Figure 4.18 shows the ratio of the wind speeds of FL48 of FL47, and the wind speeds ratio of FL49 over FL48 respectively. It can be seen that the ratio of the predicted values by WRF is generally close to 1. Indicating that there was little difference in wind speed between the two stations. The observed wind speeds had more variation between the stations FL48 and FL49, as the ratio varies roughly between 0.85 and 1.05. For the ratio

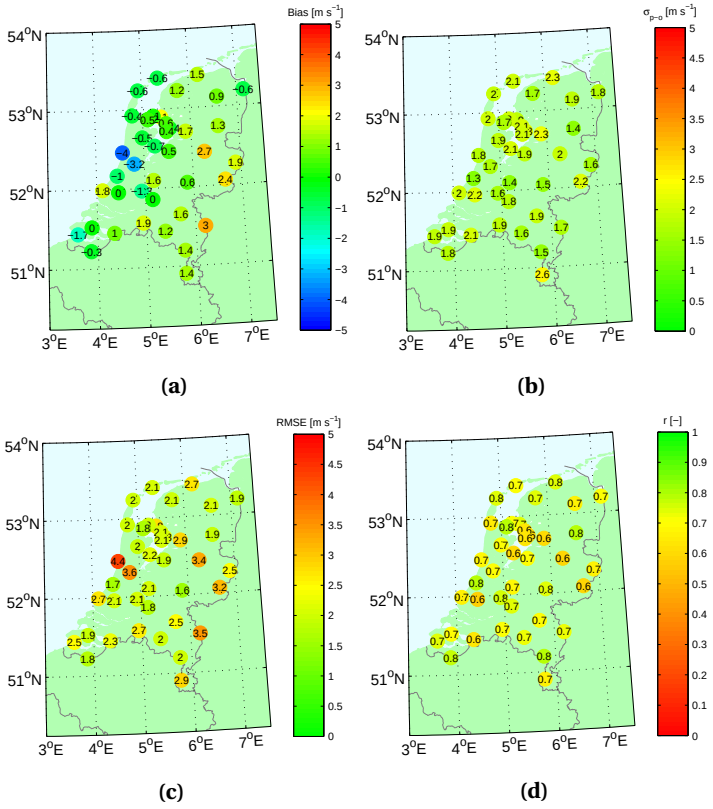

Figure 4.14: Statistical scores per station during storm 1 for wind speed [ms^{-1}]. (a) Bias, (b) root-mean-square error, (c) standard deviation of error, and (d) correlation coefficient.

of station FL48 over FL47, the observed and predicted variance between the data was more alike and varied roughly between 0.7 and 1.1.

An interesting observation can be made from these scatter plots. Looking at the ratio for wind direction around the 320°N, one can see that the ratio between FL49 and FL48 suddenly decreases to a value of about 0.85. A very distinct reason for this is the predicted sheltering of station FL49 due to upstream land-roughness effect, whereas this is not the case for FL48. The large difference between the station is line with the gradient of the predicted wind streaks. The absence of this in the observations suggests that the wind-sheltering, in reality, is much less (or, at least, the gradients are less steep).

4.4. SENSITIVITY TO MODEL SETTING

The performance of the model depends on the representation of the physical processes, the boundary conditions, and the model parameters. Ideally, one would like to know the effects of the different model configurations, so that the optimal setting for a specific situation can be used. WRF contains many parameterizations, and even more individual parameters; a full assessment of al used parameters was not a realistic objective for this study.

The model was set up using rules-of-thumb and findings from other studies. Some of the settings that were used in the model were kept their default values. In order to get familiar with the model, some different configurations have been tested. Analysis of the output was mainly based on statistics for the wind, and temperature. The results of these tests are briefly discussed in this section.

4.4.1. MODEL HEIGHT

Atmospheric models such as WRF quickly become computationally very costly. An attractive way of reducing the computation times would be by excluding unnecessary high layers from the model. Three different model top heights have been assessed, all other settings were unchanged, as described in Section 5.2:

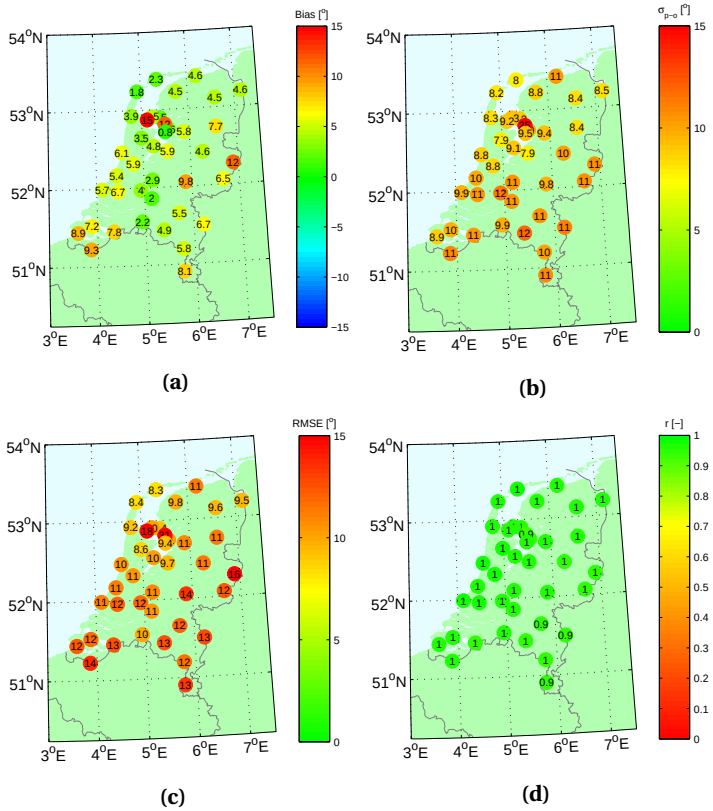

Figure 4.15: Statistical scores per station during storm 1 for wind direction [°N]. (a) Bias, (b) root-mean-square error, (c) standard deviation of error, and (d) correlation coefficient.

- 50 hPa (~ 20 km)
- 200 hPa (~ 12 km)
- 500 hPa (~ 5.5 km)

The results showed little to no difference between the 50 hPa and 200 hPa simulations for wind speed, wind direction, and temperature. The overall performance of those simulations was equal. The 500 hPa simulation showed large errors and low correlation for all variables.

4.4.2. NUMBER OF VERTICAL LAYERS

The number of vertical layers also a parameter that quickly increases computational costs, yet it is a crucial parameter for the correct prediction of wind. To see how the number of layer influences the outcome of the model runs, three different setting were compared:

- 30 layers
- 40 layers
- 50 layers

The results showed little to no difference in the wind speed, wind direction, and temperature in terms of bias, RMSE, and linear correlation. Spatial plots of the 10-m wind speed also did not show differences between the simulations. Vertical plots of the wind speed did show disturbances at the top of the model (chequerboard pattern) for the simulation with 30 vertical layers. The model with 40 vertical layers was the best choice.

4.4.3. DOMAIN POSITION

The position of the domain determines the boundaries at which information is passed over from the global model to the limited-area model (LAM). According to Warner [2011], LAMs are notoriously sensitive to the position of the lateral boundaries. Therefore, five different positions for domain 1 have been tested. These

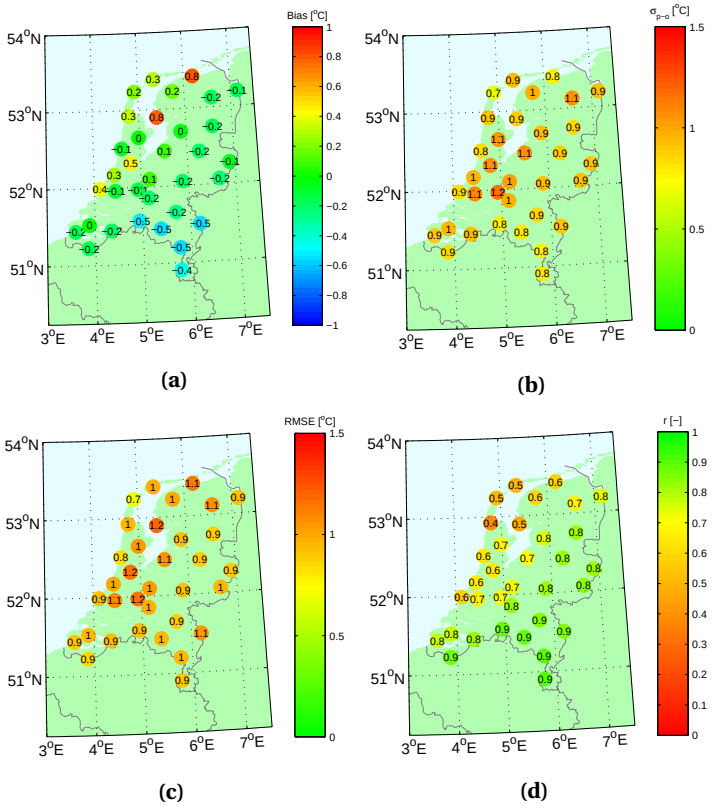

Figure 4.16: Statistical scores per station during storm 1 for temperature [°K]. (a) Bias, (b) root-mean-square error, (c) standard deviation of error, and (d) correlation coefficient.

are shown in Figure 4.19.

Results from the simulations show little to no difference in the wind speed, wind direction, and temperature in terms of bias, RMSE, and linear correlation. Spatial plots of the 10-m wind speed also did not show differences between the simulations.

4.4.4. DOMAIN SIZE

The effect of the size (in the number of grid points) of the domain becomes an important factor when different resolutions are required. Reaching the wanted resolution while keeping the lateral boundary conditions at the same position can only be done by changing the amount of grid points in the domain. To assess the effects of the domain size, three simulations are performed using different size of domain 5:

- 100 × 100 grid points
- 125 × 125 grid points
- 150 × 150 grid points

Results from the simulations show little to no difference for the wind speed, wind direction, and temperature in terms of bias, RMSE, and linear correlation. Spatial plots of the 10-m wind speed also did not show differences between the simulations.

4.4.5. NESTING RATIOS

The main objective of this study concerns the modelling of atmosphere art different resolutions. To reach these resolutions, series of nests were constructed. The nesting ratios between domain are advised to be kept at a value of 3, and maybe 5 Dudhia and Wang [2014]. In order to reach different resolutions near the area of interest, it was necessary to vary these ratios. Two tests were performed to assess two type of nest constructions. In the first test nests ratio of 5 were allow, for the second test, all ratios were kept at a ratio of 3. This resulted in the following nest configurations:

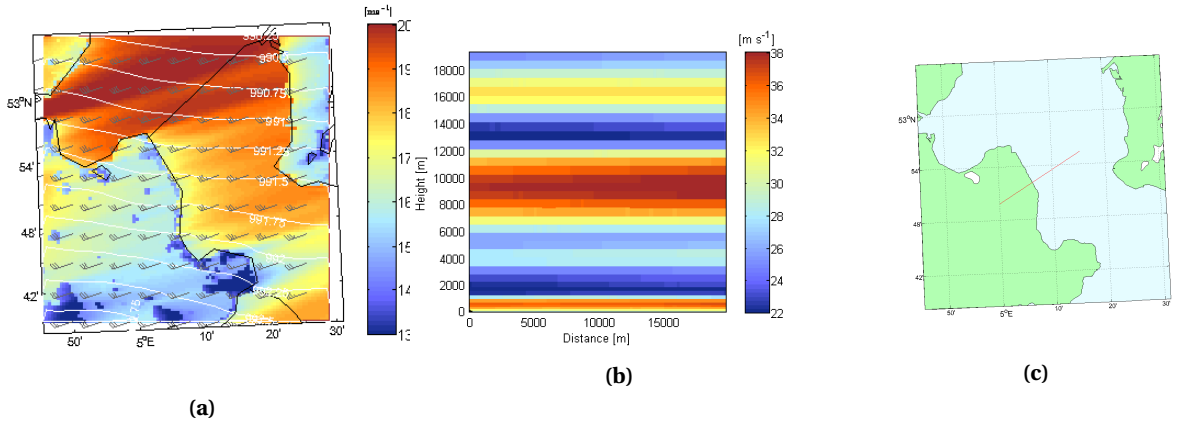

(a) (b) (c)

Figure 4.17: Wind field January 5th 2012 00:24; (a) 10-m wind field, (b) velocity along the cross section, (c) position of the cross section.

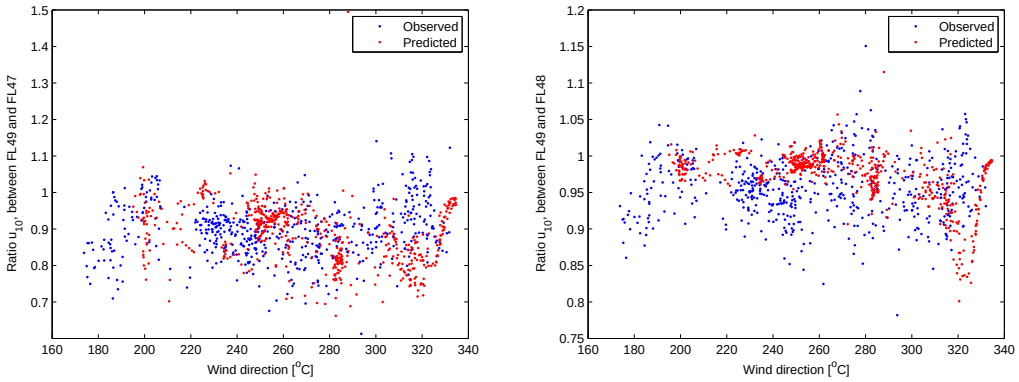

(a) (b)

Figure 4.18: Storm 1: wind speed ratio as a function of the wind direction; (a) Wind speed ratio of FL49 over FL47, and (b) Wind speed ratio of FL49 over FL48.

- 40.5 km–13.5 km–4.5 km–1.5 km–0.3 km
- 24.3 km–8.1 km–2.7 km–0.9 km–0.3 km

Results from the simulations show little to no difference for the wind speed, wind direction, and temperature in terms of bias, RMSE, and linear correlation. Spatial plots of the 10-m wind speed showed a few occasional differences. The first configuration showed more resembles the model set-up described in the previous sections. Furthermore, distributions of the wind speeds for al stations showed that the wind climate during the first storm changed for the second configuration. In comparison to the validated model settings, it can be seen that less high wind speeds (16–22 $\mathrm{m\,s^{-1}}$) were predicted, and more moderate wind speeds (8–13 $\mathrm{m\,s^{-1}}$). This causes the distribution to be poorer than the other simulation, which was comparable to the validated model.

While performing these test, a bug in the model was found. When using a nest with a ration of 5, WRF misplaces the inner grid by one grid point. The problem is shown in Figure 4.20. The different grid types of grid points (m-, u-, and v-points) react slightly different. The shift in on the m-grid is both in latitude and longitude, the shift on the u-grid is only in latitudinal direction, and the shift on the v-grid is only in longitudinal direction. The bug was only observed in the grid generated by `wrf.exe`; all other subprograms (see Appendix B) worked correctly.

This does not seem to have any influence on the results of the simulations, since the grid points of the nest are used for the results, and because the points at the boundary (where the information is exchanged between the two domains) are positioned correctly. UCAR has been contacted, and they currently address the problem.

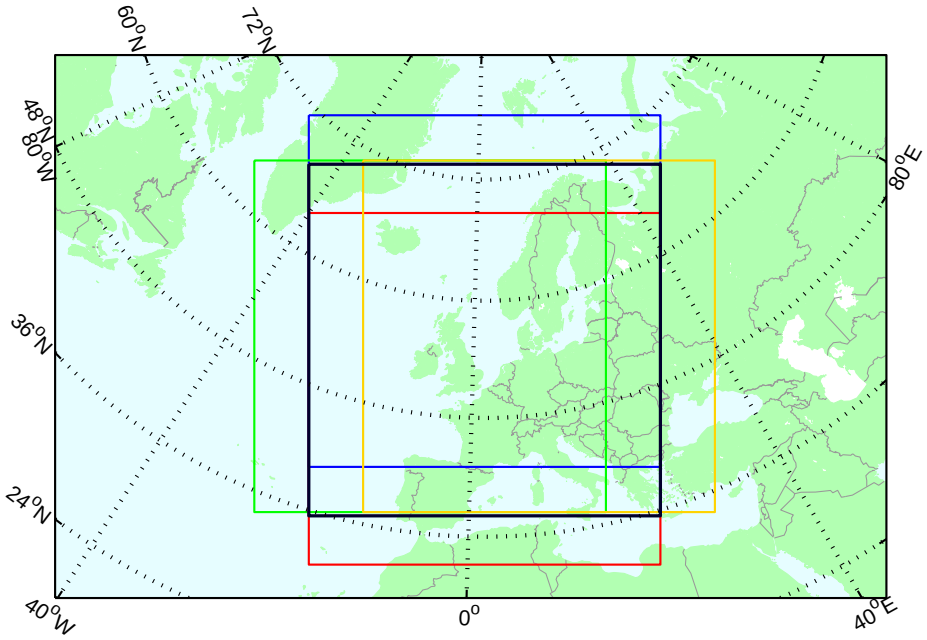

Figure 4.19: Five different positions of the outer domain; the original domain is shown in black

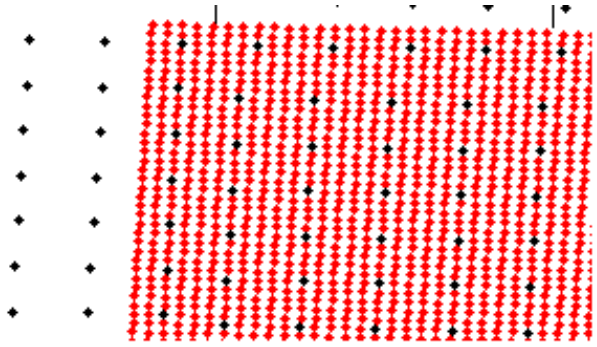

Figure 4.20: Bug in WRF, grid points of the parent grid are shifted under the nest

4.4.6. ONE-WAY VS TWO-WAY NESTING

The effect of feedback between the domains was assessed by a simulation using one-way feedback and a simulation using two-way feedback. Results from the simulations show little to no difference for the wind speed, wind direction, and temperature in terms of bias, RMSE, and linear correlation. Spatial plots of the 10-m wind speed also did not show differences between the simulations.

4.4.7. BOUNDARY CONDITIONS

Errors in the model that were described in the previous section might well be caused by errors in the boundary conditions. Besides ERA-Interim, also other global data set are available, such as GFS [NCEP et al., 2000]. To see whether the results of the model deviate from these other boundary conditions, an extra simulation was performed using data from GFS.

Results from the simulations show little to no difference in the wind speed and wind direction regarding bias, RMSE, and linear correlation. Differences were found for temperature. For stations near the coast, temperature biases were about 1°C higher than they were for the validated model. Moving land inward, biases remained higher, but the difference became less (about 0.1–0.2°C). The poorer performance was also shown in RMSEs; which was roughly 0.5°C higher near the coast and 0.2°C inland.

4.4.8. ADDITIONAL SETTINGS

Even tough this study focusses on high resolutions, much of sub-grid variations are not taken into account by the model; for example the Afsluitdijk, a 32 km long dam separating Lake IJssel from the Wadden Sea. Because the dam is relatively thin, compared to the dimension of the grid cells, it is not noticed by WRF at all. Another example is the sub-grid variation in land-use. Roughness lengths are determined by the model by using the largest type of land-use in the grid cell and neglecting others. To overcome these types of modelling issues, two extra types of parameterizations were tested.

The first setting is `topo_wind`, this setting activates a parameterization that includes the sub-grid variance of orography in the model. The second is `sf_surface_mosaic`, this parameterization allows the user to specify the number of different land-use fraction that should be taken into account per grid cell.

The `topo_wind` parameterization decreases the overall wind speed bias of the model; improving the predictions in some places, but at other placed the performance was poorer. This was also observed from the wind distribution of all stations; wind speed became lower. Correlation coefficients for the wind speed also became less, indicating larger temporal errors. The directional bias of the wind improved significantly. Biases of the whole domain were improved, but especially land inwards, where biases went down from 6–8°to 0.5–1.5°. The positive effect was not found from the RMSEs; these remained more or less equal. The overall temperature bias became smaller (negative for most stations; thus poorer); this was also shown by RMSEs, which increased slightly for the station inland.

Results from the `sf_surface_mosaic` simulations show little to no difference in the wind speed, wind direction, and temperature regarding bias, RMSE, and linear correlation.

4.5. CONCLUSION: THE PERFORMANCE OF WRF

A set-up for WRF has been determined using references from literature and rules-of-thumb from the WRF experts. The model covers an area of 3240 × 4050 km, and initial, and boundary conditions are derived from the ERA-Interim reanalysis. Using five nests, a resolution of 500 × 500 m is realized over Lake IJssel.

Validation of the model showed that WRF consequently under-predicts the lowest wind speeds (the range between 4–7 m s^{-1} for storm 1 and 2–4 m s^{-1} for storm 2), and over-predicts the mid-range (the range between 9–15 m s^{-1} for storm 1 and 5–15 m s^{-1} for storm 2). Furthermore, WRF prediction showed structural errors on the wind direction. WRF has predicted substantially more winds in the direction of 250°N–320°N than were observed while it predicted fewer winds from the directions 200°N–240°N than were observed.

Statistical analyses of model data, showed that the uncalibrated model performed quite well in terms of wind speed (around Lake IJssel; storm 1: rbias < 5%, SI ≈ 10%; storm 2: rbias 10%–20%, SI ≈ 20%) and wind direction (around Lake IJssel; storm 1: bias ≈ 3°, RMSE ≈ 10°; storm 2: bias 4°–15°, RMSE ≈ 20°). Furthermore, the wind vane at station FL49 did not function during the first storm, and station FL48 showed a structural bias in wind direction of 18°. Since all the surrounding stations show a smaller bias, this is most likely caused by errors in the measurements. Additionally, some temporal errors were found for the wind direction, as a consequence of the inaccuracies in the synoptic scale predictions. The errors were largest around the time that the cold fronts pass by, and the winds rapidly changed direction. Even though this is not directly noticeable in the wind speeds, it might lead to significant differences in fetch when predicting waves.

Analyses of air and surface temperatures showed that there might be some deviations in the observed and predicted stability regimes. Surface temperatures in WRF are directly taken from the ERA-Interim data-set. The SST temperatures in ERA-interim are not representative for the temperatures in Lake IJssel (since it is an enclosed basin), and were structurally over-predicted (storm 1: ~ 2°C or ~ 70%; storm 2: 2.5–3°C or 70%–75%). It is advised to investigate the possibilities of reducing bias. A possible solution might be the coupling of a lake model that is implemented in de most recent versions of WRF.

The spatial evolution of the wind speed along a profile perpendicular to the coast showed that there is a large gradient in wind speeds when the wind moves of the land-water boundary. This was expected according to the theory. However, the gradient predicted by WRF seems too large if one compares the spreading of the wind speed between the two stations closest to the coast. The WRF results show little variation between the two stations while this is significantly more for the observed values. This indicates that the wind speeds in WRF reached the higher velocities too soon after the transition.

An interesting feature of the model results is the spatial variation in wind speed. Due to differences in surface roughness, distinct wind streaks were observed from the model data that extended tens of kilometres of the coast. These streaks indicate little horizontal exchange of momentum in the wind field. It is questionable whether these wind streaks also occur in reality. Only two references to these wind streaks were found in literature [Kudryavtsev and Makin, 1996; Dörenkämper et al., 2015]. They both mention these wind streaks in relation to stable conditions when turbulence is suppressed. This was not the case in these simulations (little to no difference between air and surface temperature). Furthermore, the observed ratios in wind speed between the stations FL48 and FL49 showed no sheltering from the wind for wind directions of 320°N, while this was very clearly seen in the WRF results as a consequence of such a wind streak. Because of these uncertainties further investigation on this subject is advised.

To obtain different spatial resolutions of the wind field near Lake IJssel, nesting ratios needed to be varied. An inevitable problem that occurs is the necessary modification of other model settings that might also influence the results (e.g. a higher resolution changes also the number of grid points in the domain if the size of the domain were to be kept equal; vice versa, keeping the same amount of grid points would lead to a smaller domain). To this end, tests were conducted to assess the effects of the amount of grid points (domain size), and the nesting ratio on the predicted wind speed and wind direction. The tests showed that comparable results could be obtained while changing the amount of grid points in the domain (tests ranged from 100×100 grid points to 150×150 grid points). The nesting ratio can be changed from 3 to 5 without influencing the results significantly. However, the coarser domains (especially domain 1) should remain untouched as much as possible. Otherwise, this leads to larger deviations in the results.

5

MODELLING OF WAVES

5.1. INTRODUCTION

In this chapter, a model set-up is described for the spectral wave model SWAN. An overview of the SWAN model is given in Appendix C, but for a detailed description the reader is referred to Booij et al. [1999]. The model settings are described and validated for the two storms creating a reference for the remainder of the study.

5.2. MODEL SET-UP

This section describes the settings that were used for the experiments with the spectral wave model SWAN [Booij et al., 1999]. The version of SWAN that was used during the study is version 40.72ABCDE. A description of this model is included in Appendix C. The model was set up using the calibrated settings that Deltares used for the determination of the hydraulic boundary conditions on Lake IJssel for the WTI2011 project [Deltares, 2013].

5.2.1. DOMAIN AND COMPUTATIONAL GRID

In order to be able to capture the wave growth at very short fetches correctly, a fine computational grid was required. Sufficient points were required between the coast and the first observation point (FL49) to correctly predict the transfer of energy from wind to waves within this short distance. Sensitivity analysis by Deltares [2013] had already shown that a spatial resolution of 20 × 20 m was sufficient. They found that a higher resolution did not further improve the results. Furthermore, to be able to capture the high-frequency energy associated with young waves, high frequencies should also be present in the model. Therefore, a large spectral domain was used that extended up to frequencies of 4 Hz.

The high-resolution grid and the broad frequency domain were computationally very demanding, especially considering the number of time steps that were needed per simulation. Therefore, simulations were performed on two different domains. The first domain covered Lake IJssel entirely. This domain was used for the reference simulations, and for simulations that required the full length of the lake, e.g. to assess the effects of the passing squall line during the second storm. The domain is shown in Figure 5.1 and shall be referred to as domain A.

The domain was discretized into 1049 × 1853 grid points, giving it a slightly coarser resolution of 40 × 40 m. The spectral domain had a directional coverage of 360° and contained frequencies ranging from 0.08 to 4 Hz. The spectral domain was discretized into 42 logarithmically spaced grid points and 36 directions ($\Delta\theta$ = 10°). The resulting SWAN input-line was:

```
CGRID   XPC=172490 YPC=487160 ALPC=41.0 XLENC=41920.0 YLENC=74080.0
        MXC=1048 MYC=1852 CIRCLE MDC=36 FLOW=.08 FHIGH=4.0
```

The second domain was specifically used for the simulations assessing the effects of wave growth at short fetches. Since this was the only interest for this domain, it was unnecessary to model the entire lake. Instead,

a smaller part of the lake was modelled, which also provided the opportunity to use higher resolution spatial, and spectral discretization then could have been used if the entire lake was modelled. The domain is shown in Figure 5.1 and shall be referred to as domain B.

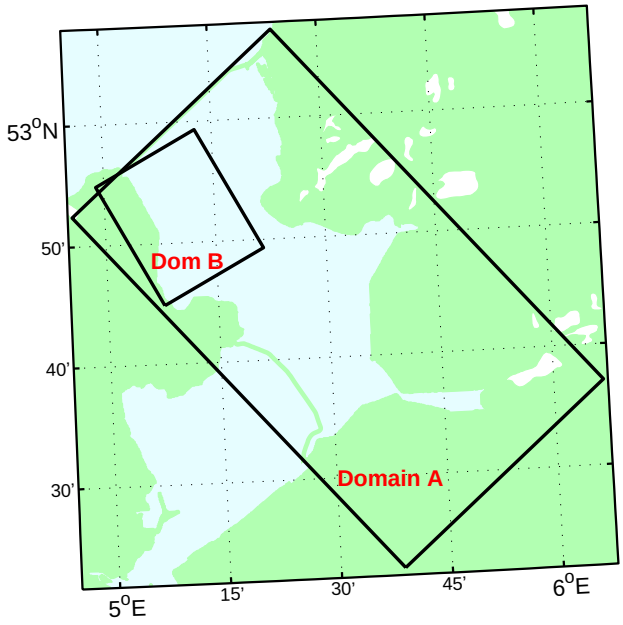

Figure 5.1: Boundary of the computational domain used in SWAN

The domain was discretized into 875 × 1050 grid points giving the computational grid a resolution of 20 × 20 m. The spectral domain had a directional coverage of 360° and contained frequencies ranging from 0.08 to 4 Hz. The spectral domain was discretized into 42 logarithmically spaced grid points and 36 directions ($\Delta\theta$ = 10°). The resulting SWAN input-line was:

```
CGRID   XPC=137500 YPC=529000 ALPC=27.8 XLENC=17500.0 YLENC=21000.0
        MXC=875 MYC=1050 CIRCLE MDC=36 FLOW=.08 FHIGH=4.0
```

5.2.2. INITIAL AND BOUNDARY CONDITIONS

INITIAL CONDITIONS

The main focus of this study was mainly on the response of waves to wind forcing. This required the model to be fully spun-up, and initial conditions were not specifically important (initial conditions only determined the time needed for the model to spin-up). In SWAN, the default initial conditions for non-stationary simulations are given by a JONSWAP spectrum with a $\cos^2\theta$ directional spreading centred around the local wind direction and a peak enhancement parameter γ = 3.3. These initial conditions were also used during this study.

BATHYMETRY

The bathymetry of Lake IJssel that was used during this study is shown in Figure 5.2; this is the same bathymetry file that was used by Deltares for the WTI2011 computations (G1U14S022S01.bot, see Deltares [2013]). The bathymetry has a spatial resolution of 40 × 40 m, covers the entire lake, and is representative for the periods treated in this study.

WATER LEVEL

During both storms there were much of variation in the water levels (between NAP −0.2 m and NAP +0.35 m during storm 1, and between NAP −0.8 m and NAP −0.35 m during storm 2). Water levels are important for the correct prediction of waves since these are influenced by the local water depth (friction, depth-induced

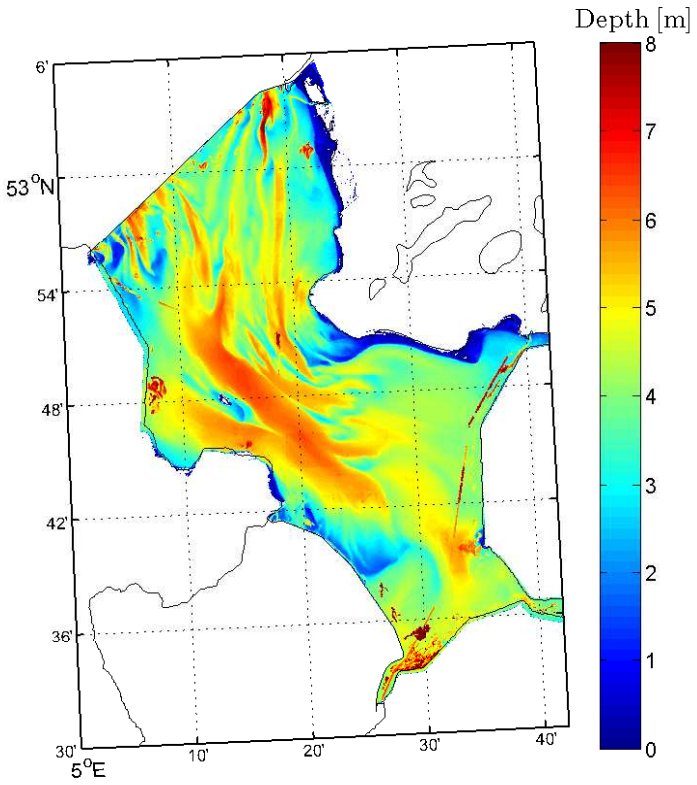

Figure 5.2: Bathymetry Lake IJssel with a resolution of 40 × 40 m [Deltares, 2013].

breaking). However, for the case of assessing wave growth at short fetches, the young waves will be small relative to the depth and no significant influence is expected. With this in mind, the water levels of FL48 were used as input for SWAN with an update frequency of 20 minutes. The water levels of station FL48 were chosen because they represented more or less the average water level of the three stations.

WIND FIELD

The most important factor influencing wave growth is the wind. WRF wind fields were used for this purpose. In WRF, $\mathbf{u}_*$ is determined by the surface layer parameterization. This parameterization determines the friction velocity using the wind speed of the lowest model level (also including a vertical sub-grid scale velocity and a convective velocity) through a logarithmic velocity profile, see Equation (5.1):

$$\mathbf{u}_*^t = 0.5\mathbf{u}_*^{t-1} + 0.5\frac{\kappa \mathbf{u}_{\eta=1}^t}{\ln\left(\frac{z+z_0}{z_0}\right) + \Psi_m\left(\frac{z}{L_b^t}\right)} \tag{5.1}$$

in which superscript denotes the modelled time step and η denotes the index of the model layer. The friction velocity is averaged with the friction velocity of the previous time step to prevent numerical oscillations. Subsequently, using $\mathbf{u}_*$ and the logarithmic velocity profile, the diagnostic variable $\mathbf{u}_{10}$ is determined.

The output of WRF could have been used in two ways. The most trivial way would have been by simply imposing the $\mathbf{u}_{10}$ values at every time step in SWAN. SWAN converts $\mathbf{u}_{10}$ to $\mathbf{u}_*$ using the relation by Wu [1982] (Equation (2.45)), which is only valid for neutral conditions. It is known that the assumption of a neutral wind profile during non-neutral conditions can lead to errors in the prediction of waves (e.g. Young [1998]). Because of this, it is preferred to use $\mathbf{u}_*$ directly, since stability effects are already accounted for.

Direct forcing with $\mathbf{u}_*$ is not an option in SWAN. Therefore, the approach, described by Deltares [2015], using 'pseudo wind speeds', has been was used. Pseudo winds speeds $\mathbf{u}_{10;p}$ were derived at water grid points in from the WRF data from $\mathbf{u}_*$. This was done in an iterative way, using the inverse of drag relation in SWAN.

By applying these pseudo wind speeds, SWAN converted them back the right values of friction velocity. An schematic overview of the method is shown in Figure 5.3. The direction of the pseudo wind was kept equal to the direction of the regular WRF winds.

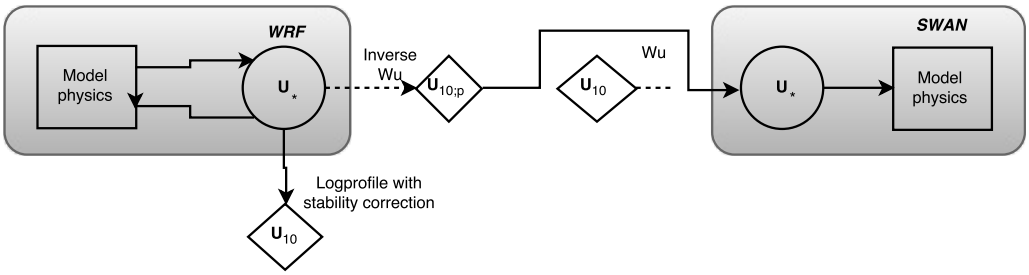

Figure 5.3: Schematization of the method using pseudo wind.

WAVES BOUNDARY

Because Lake IJssel is a closed basin, no wave boundary conditions were needed for domain A. No wave boundaries were used for domain B either since the main interest lay on short fetch wave growth. In order to assess the validity of this domain, some tests were performed, these will be treated later in this section.

5.2.3. PHYSICS

The physical parameterizations were set to the calibrated WTI2011 settings [Deltares, 2013]. Wind input in the spectrum was determined using an exponential growth term, see Equation (2.11). The friction velocity was determined with the drag relation by Wu [1982]. The linear growth term was not used, and the exponential growth term was determined with the expression by Yan [1987]. Whitecapping was determined via the parameterization of van der Westhuysen et al. [2007]. Quadruplet wave-wave interactions were modelled using the Discrete Interaction Approximation (DIA) of Hasselmann et al. [1985]. Triad wave-wave interactions ware modelled with the Lumped Triad Approximation (LTA) of Eldeberky [1996]. The bottom friction was modelled using the JONSWAP formulation of Hasselmann et al. [1973]. Depth-induced breaking was determined using the formulation of van der Westhuysen [2010]. Summarizing, the following settings were applied:

```
GEN3 WESTH
WCAP WESTH cds2=5.0e-5 br=0.00175 p0=4.0 powk=0.0 nldisp = 0.0 cds3=0.8 powfsh=1.0
QUAD iquad=2 lambda=0.25 cnl4=3.0e+07
BREAKING WESTH alpha=0.96 pown=2.50 bref=-1.3963 shfac=500.0
FRIC JONSWAP cfjon=0.038
TRIAD trfac=0.1 cutfr=2.5
LIMITER ursell=10.0 qb=1.0
```

5.2.4. PERIOD AND TIME STEP

SWAN was used in the non-stationary mode to assess the effects of temporal changes in the wind field. Therefore, the length of each simulation was equal to the duration of the storm. The time step used in SWAN for non-stationary computations is advised to be $\Delta t \leq 10$ minutes. Furthermore, it was important that the temporal variation of the boundary conditions could be resolved adequately. Simulations were performed using time steps equal to the update frequency of the wind field, i.e. ten minutes. Preferably, time steps would have been smaller, but in combination with the already computationally demanding domain settings this, would have been too time-consuming.

5.2.5. NUMERICS

The numerical schemes available in SWAN for non-stationary computations are the Stelling and Leendertse scheme (S&L, the default for non-stationary computations) and the BSBT-scheme. Both schemes are implicit and unconditionally stable. The BSBT scheme was used in this study because it is computationally less demanding than the S&L scheme. The BSBT-scheme does enhance some extra numerical diffusion of wave

action; this becomes noticeable over long distances and near steep gradients. This was not a problem since the main interest lay with local wave features (the direct response to the wind forcing).

The maximum number of iterations was kept at a high value (`mxitns=50`) to make sure the model converges. Depending on the variation of the wind speed, the number of iterations varied (roughly between 4 to 8 iterations); quickly varying winds resulted in more iterations. By using this number of iterations, a spin-up time of two hours was sufficient. The resulting SWAN input lines were:

```
PROP BSBT
NUM STOPC dabs=0.00 drel=0.02 curvat=0.002 npnts=99.  NONSTAT mxitns=50
```

5.3. MODEL VALIDATION

This section describes the validation of the SWAN predictions in comparison with observations. For this purpose, reference simulations were conducted using domain A—covering Lake IJssel as a whole—for both storms. The reference simulations are used to obtain a general impression of the performance of SWAN for these two storms. It should be kept in mind that deviations between observations and predictions might not only be the result of incorrect predictions by SWAN, but it might also be due to differences in simulated and observed wind speeds or wind directions. Furthermore, as was already indicated in Chapter 3, the measurements might also contain errors. According to Deltares [2015] it is likely that observation overestimate wave heights roughly by 5–10%. Also, comparison of wind directions between the different measuring stations—during the validation of WRF—the average observed wind direction was roughly 10° lower than expected. This is most likely due to an error related to the measuring equipment.

5.3.1. OBSERVATIONS

To obtain an impression of the observed response of the waves during the storms. First, a short analysis of the observations is made in relation to the wind forcing.

STORM 1

During the first storm, no wave observations were available for station FL47 and no directional data of the wind was available for FL49. In the following sections, it is assumed that the wind direction from station FL47 is representative for the wind direction of FL49.

In the early morning of January 3rd, wave heights (0.2 m near the coast), as well as the wave period (T_{m01} ≈1.3 s to 1.5 s) started out small. The one-dimensional wave spectrum was broad and the higher frequencies contained a substantial part of the total energy in the spectrum. For both stations, no JONSWAP spectrum was recognizable, and for station FL49 no distinct peak was observed. As the wind speed increased, so did the wave heights and wave periods. The wave heights near the coast were at their maximum around January 3rd, 12:00 and they were about 1 m high. Wave periods had their maximum ($T_{m01} \approx 2.6$ s for FL49 and $T_{m01} \approx 2.9$ s for FL48) earlier, between 09:00 and 10:00. The reason for the earlier decay of the wave periods, was found in the shape of the spectrum. The spectrum shows—first at FL49 and than also at FL48—a second peak at a higher frequency. This peak grew larger as the wind was veering. When the wind direction was nearly 205°N, that second peak became larger than the first peak, which caused a shift in the peak frequency. When the cold front passed— the wind dropped and shifted to 245°N—wave heights, and periods also dropped, almost instantly. During the remainder of the storm, wave heights followed the pattern of the wind speed, direct correlation between (effective) fetch and wave heights seemed weak. Wave periods also followed the similar pattern of the wind speeds, but also showed more direct influence of the (effective) fetch.

STORM 2

During December 4th, wave heights and periods were relatively low ($H_{m0} \approx 0.15$ m to 0.5 m and $T_{m10} \approx 1.3$ s to 1.5 s) due to the low winds speeds. The peak period fluctuated due to the lack of a well-defined peak in the spectrum at these low wind velocities. Wave heights and periods at the stations closest to the coast, reacted to the change in wind direction that was caused by the passing cold front in the afternoon of December 4th, even though there was barely a change of the wind speed. Especially at station FL49 where wave heights doubled to almost 0.3 m. As the wind speed reached its maximum of the storm (December 5th, around noon), so did the wave heights (0.6 m to 1.4 m). At that moment the wave periods for the station FL47 had their maximum ($T_{m01} \approx 3.5$ s). Maximum wave periods for the stations FL48 and FL49, followed later that day, at a moment at which the wind had turned to west-northwest. The difference in wind direction relates to a difference in the

Figure 5.4: Storm 1: Significant Wave height (H_{m0}), (Pseudo) Wind Speeds ($u_{10;p}$), Wind direction (θ_{wind}), and the Effective fetch (F_e)

(effective) fetch, which again illustrates the stronger correlation between wave periods and fetch than wave height and fetch.

5.3.2. RESULTS SIMULATIONS

Reference simulations were conducted for both storms using de 500 m wind field from WRF. These simulations provide an impression of the performance of SWAN for each storm. Furthermore, the reference was used to assess the validity of the smaller domain—domain B. A statistical overview of the performance of SWAN is shown in Tables 5.1 and 5.2.

TIME SERIES

At first sight, SWAN seemed to perform moderately in predicting wave heights and the different wave periods. Nevertheless, most errors were related to the errors in the prediction of wind speed, which can clearly be seen from Figure 5.6. It stands out that the error in the predictions of wave heights and wave periods also depends on the wind direction. In the direction of the shore normal, wave heights were under-predicted. For wind directions that deviate from the shore normal, the errors positive. By comparing the differences between the stations FL48 and FL49, it can be seen that the wave height differences between the two stations are small.

The ratio of the observed significant wave height for FL49 and FL48 varied roughly between 0.85 and 1.1, with no specific dependency on the wind direction. The difference between the two stations from the SWAN predictions varied even less, and the ratio was mostly close to 1. However, the SWAN results did show a clear dependency of the wave height ratio with the wind direction. The ratio became much smaller for winds from 320°N, which is almost along the direction of the coast. As was already mentioned in Chapter 4, the wind from this direction showed a large gradient in the speeds due to upstream differences in aerodynamic roughness,

Figure 5.5: Storm 2: Significant Wave height (H_{m0}), (Pseudo) Wind Speeds ($u_{10;p}$), Wind direction (θ_{wind}), and the Effective fetch (F_e)

between the two stations. Station FL49 was sheltered from the wind.

SPECTRA

As was already noted in the previous section, the observed spectra for the stations near the coast often showed more than one peak. The one-dimensional spectra produced by SWAN showed a similar behaviour. The spectra associated with the wind direction smaller than 190°N corresponded well to the observations in terms of peak frequency and energy distribution The two-dimensional spectrum of SWAN showed that the wave energy for these directions was mainly directed along the shore (in the direction of north-northwest), and the peak directions were approximately 160°N.

As the wind veered to a direction of 195°N, a second peak appears in the observed spectra at a higher frequency; first for FL49, and then also for FL48. The high frequency started to dominate the spectrum for wind directions larger than approximately 200°N. In SWAN, the second peak only started to show when wind directions had veered to more than 220°N, and it was not until the wind shifted more than 235°, that this second peak started to dominate the spectrum. Two-dimensional SWAN spectra showed that the wave energy associated with the second peak, travelled in the direction of the shore normal.

Even when wind directions were almost completely in line with the shore normal, the observed spectrum of FL49 still showed a small shoulder at the frequency associated with the low frequency. More surprising is that this low frequency remained predicted by SWAN even for wind directions up to 254°. This showed that there was still wave energy moving along the coast, slightly against the direction of the wind. This is shown as an example in Figure 5.8. It can be seen from from Figure 5.9 (note that this is another time), that there is large directional spreading near the locations FL48 and FL49. As wind directions increased even more, the peak in the energy density spectrum shifted towards the lower frequencies again.

Table 5.1: Statistical quantities for the stations in Lake IJssel, during storm 1

Parameter	Station	All directions							239°N ± 40°							239°N ± 20°						
		N	$\overline{o}$	$\overline{p}$	r	Bias	σ_{p-o}	RMSE	N	$\overline{o}$	$\overline{p}$	r	Bias	σ_{p-o}	RMSE	N	$\overline{o}$	$\overline{p}$	r	Bias	σ_{p-o}	RMSE
H_{m0} [m]	FL47	No data							No data							No data						
	FL48	270	0.57	0.57	0.7	0	0.13	0.13	130	0.6	0.51	0.79	-0.09	0.11	0.14	77	0.61	0.48	0.94	-0.13	0.09	0.16
	FL49	270	0.44	0.5	0.69	0.06	0.13	0.14	129	0.46	0.42	0.82	-0.04	0.09	0.1	75	0.46	0.39	0.94	-0.07	0.08	0.11
T_{m01} [s]	FL47	No data							No data							No data						
	FL48	270	2.19	2.14	0.79	-0.05	0.2	0.21	130	2.17	1.98	0.83	-0.18	0.17	0.25	77	2.14	1.9	0.94	-0.23	0.13	0.26
	FL49	270	2.03	2.01	0.88	-0.01	0.17	0.17	129	1.88	1.8	0.88	-0.09	0.14	0.16	75	1.82	1.7	0.94	-0.13	0.1	0.16
T_{m02} [s]	FL47	No data							No data							No data						
	FL48	270	2.05	1.99	0.75	-0.06	0.19	0.2	130	2.04	1.86	0.8	-0.18	0.16	0.24	77	2.02	1.79	0.93	-0.23	0.13	0.26
	FL49	270	1.9	1.87	0.87	-0.02	0.16	0.16	129	1.78	1.69	0.85	-0.09	0.13	0.16	75	1.73	1.6	0.93	-0.13	0.1	0.17
T_{m-10} [s]	FL47	No data							No data							No data						
	FL48	270	2.42	2.38	0.83	-0.05	0.21	0.22	130	2.37	2.19	0.88	-0.18	0.17	0.25	77	2.33	2.09	0.95	-0.23	0.12	0.26
	FL49	270	2.26	2.25	0.9	-0.01	0.18	0.18	129	2.08	1.99	0.92	-0.09	0.14	0.17	75	2	1.87	0.95	-0.13	0.09	0.16
T_p [s]	FL47	No data							No data							No data						
	FL48	270	2.75	2.84	0.85	0.09	0.29	0.3	130	2.6	2.57	0.86	-0.03	0.27	0.27	77	2.47	2.41	0.79	-0.06	0.28	0.28
	FL49	270	2.53	2.69	0.81	0.16	0.38	0.41	129	2.24	2.33	0.77	0.08	0.39	0.4	75	2.04	2.13	0.61	0.09	0.42	0.43

Table 5.2: Statistical quantities for the stations in Lake IJssel, during storm 2

Parameter	Station	All directions							239°N ± 40°							239°N ± 20°						
		N	$\overline{o}$	$\overline{p}$	r	Bias	σ_{p-o}	RMSE	N	$\overline{o}$	$\overline{p}$	r	Bias	σ_{p-o}	RMSE	N	$\overline{o}$	$\overline{p}$	r	Bias	σ_{p-o}	RMSE
H_{m0} [m]	FL47	270	0.64	0.69	0.93	0.06	0.17	0.17	40	0.91	0.85	0.97	-0.06	0.2	0.21	37	0.91	0.84	0.99	-0.07	0.21	0.22
	FL48	270	0.38	0.44	0.89	0.06	0.1	0.12	29	0.64	0.54	0.9	-0.1	0.1	0.14	27	0.65	0.53	0.98	-0.11	0.08	0.14
	FL49	269	0.3	0.38	0.89	0.08	0.08	0.12	29	0.48	0.44	0.9	-0.04	0.07	0.08	27	0.48	0.43	0.98	-0.05	0.05	0.07
T_{m01} [s]	FL47	270	2.42	2.45	0.9	0.03	0.41	0.41	40	2.79	2.66	0.98	-0.13	0.4	0.41	37	2.76	2.65	0.99	-0.12	0.41	0.42
	FL48	270	1.82	1.91	0.9	0.09	0.21	0.23	29	2.14	1.94	0.92	-0.2	0.17	0.26	27	2.13	1.93	0.96	-0.2	0.16	0.26
	FL49	269	1.73	1.8	0.91	0.07	0.2	0.21	29	1.83	1.72	0.93	-0.1	0.13	0.16	27	1.81	1.71	0.96	-0.11	0.13	0.16
T_{m02} [s]	FL47	270	2.24	2.26	0.89	0.01	0.39	0.39	40	2.57	2.43	0.98	-0.14	0.37	0.39	37	2.55	2.42	0.99	-0.13	0.38	0.4
	FL48	270	1.7	1.79	0.89	0.08	0.21	0.22	29	2.03	1.82	0.91	-0.21	0.17	0.27	27	2.03	1.81	0.96	-0.22	0.16	0.27
	FL49	269	1.62	1.68	0.9	0.07	0.19	0.2	29	1.74	1.62	0.92	-0.12	0.13	0.17	27	1.73	1.61	0.96	-0.12	0.13	0.17
T_{m-10} [s]	FL47	270	2.7	2.74	0.92	0.03	0.41	0.41	40	3.09	3	0.98	-0.1	0.42	0.42	37	3.07	2.98	0.99	-0.09	0.43	0.43
	FL48	270	2.07	2.12	0.9	0.04	0.2	0.2	29	2.3	2.14	0.93	-0.16	0.16	0.22	27	2.29	2.12	0.96	-0.17	0.15	0.22
	FL49	269	2.03	2	0.9	-0.03	0.19	0.19	29	1.98	1.89	0.93	-0.08	0.12	0.15	27	1.96	1.88	0.96	-0.08	0.11	0.14
T_p [s]	FL47	270	3.1	3.28	0.92	0.18	0.36	0.4	40	3.5	3.68	0.97	0.18	0.33	0.38	37	3.46	3.64	0.98	0.18	0.34	0.38
	FL48	270	2.32	2.46	0.89	0.14	0.31	0.34	29	2.45	2.42	0.9	-0.02	0.14	0.14	27	2.43	2.39	0.95	-0.04	0.11	0.11
	FL49	269	2.22	2.36	0.8	0.15	0.41	0.44	29	2.09	2.07	0.94	-0.02	0.1	0.1	27	2.06	2.04	0.95	-0.02	0.08	0.08

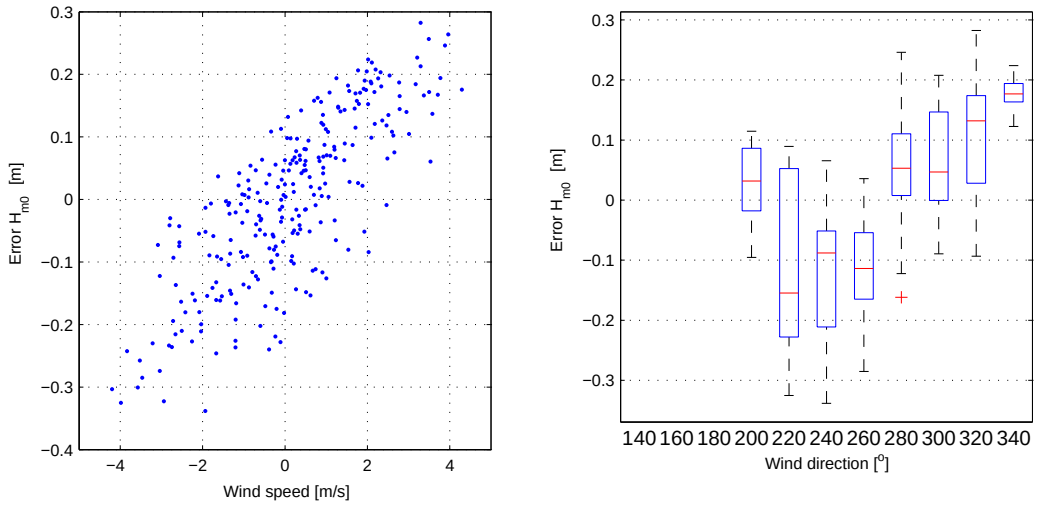

(a) **(b)**

Figure 5.6: Storm 1: (a) Error in significant wave height (H_{m0}) [m] vs error in wind speed (u_{10}) [m s^{-1}], (b) Error in wave height (H_{m0}) [m] vs wind direction (θ_{wind}) [°N]

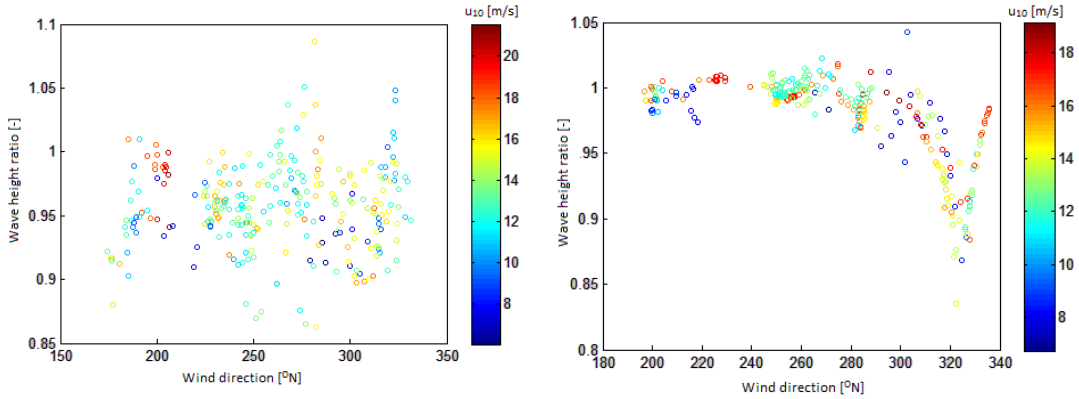

(a) **(b)**

Figure 5.7: Ratio in wave height between FL49 and FL48; (a) observed, (b) predicted

Finally, for wind directions near 300°N, predictions by SWAN severely over-predicted the wave height and periods. The spectra for these wind directions showed a mismatch in the position of the spectral peak, which caused SWAN to overestimate the wave energy at the low frequencies significantly.

LIMITATIONS OF DOMAIN B

To assess the performance of the smaller domain, comparisons were made between the above-described reference simulations (covering the entire lake) and simulations using the smaller domain B. Since the reference simulation used a coarser grid (40 m × 40 m) than the small domain (20 m × 20 m), an additional simulation using the small domain with a coarse resolution was set up. This would indicate the consequences of using a smaller domain. For practical reasons only the second storm was used for these comparisons.

The results of the simulations are also shown in Figure 5.5. It can be seen that the smaller domain performs more or less equal to the full domain, except when the wind directions deviate too much from shore normal. The undefined boundaries at the other ends of the domain give lower wave heights and lower wave periods. From these results, it could be seen that for correct model forecasts, wind directions needed to be smaller than 275°N for FL47 and smaller than 300°N for FL48 and FL49. For the other angles during these storms, it was safe to conclude that the small domain reproduced the performance of the entire domain.

LIMITATIONS OF THE TEMPORAL RESOLUTION

The non-stationary SWAN computations are unconditionally stable due to the implicit nature of the used discretization in the model. The accuracy, however, is still affected by the chosen time step (Δt). As already mentioned in section 5.2, the time step should be sufficiently small in order to be able to follow the temporal changes in the boundary conditions (the wind, waves, water levels, etc.). The time steps chosen for the simulations used in this study were 10 minutes, and this was because the wind fields were given every ten minutes.

Using this time step, SWAN still needed a number of iterations each time step, to converge the solution. Depending on the temporal gradient in the boundary conditions, the number of time steps varied on average between 3 to 8. This indicated that the boundary conditions might have been varying too rapidly for SWAN, and that the accuracy of the model predictions was possibly influenced by this. In order to assess these possible inaccuracies with a time step of 10 minutes, extra WRF simulations were carried out in order to produce wind fields every minute. Using these wind fields, extra SWAN simulations were carried out using time steps of $\Delta t = 2$ minutes and $\Delta t = 5$ minutes. Figure 5.10 shows the simulation results of storm 2, using the three different time step.

The results show that differences between the simulations due to the temporal resolution are small. Small differences are found near the local maxima and minima of the signal. The small time step causes the signal to have slightly larger maxima and slightly smaller minima. The largest difference in wave height found was around 0.02 m. Furthermore, the differences due to the smaller time steps did not lead to a better representation of the observed values.

From these results, it is safe to conclude that even though small inaccuracies arise from the time step of 10 minutes, increasing the time step does not significantly improve the results. A time step of 10 minutes is sufficiently small for the purpose of this study.

5.3.3. DISCUSSION OF THE RESULTS

GENERAL INTERPRETATION OF THE RESULTS

The results of the SWAN simulations show a moderate performance of SWAN to reproduce the wave conditions that were observed. For wind directions along the shore normal, wave heights and periods were negatively biased which was expected due to the systematic errors in the observations for this direction.

The performance is significantly influenced by prediction of the wind field. Although there is still a substantial amount of scatter, it was shown that errors in the wind speed prediction correlate with errors in wave height. An error of $\pm$ 4 m s^{-1} roughly results in an error of approximately 0.3 m in wave height. The observed wave height ratio of location FL49 over FL48 shows that waves at FL48 are roughly a factor 0.9–1 higher than at location FL49. The ratio of the predicted wave heights shows much less variation, and also shows that the ratio becomes more than 10% smaller for wind directions just above 320°. It is the same pattern as observed for the wind predictions in the previous chapter. The sheltering from the of location FL49 results in a wave height difference between the stations.

Both the observed and predicted wave spectra show that the wave spectrum near the coast deviates from the JONSWAP spectrum, which is normally expected for growing seas. The one-dimensional SWAN spectra show qualitatively the same behaviour as the observed spectra. According to the SWAN computations, the two peaks in the spectra are associated with alongshore and cross-shore propagation of wave energy. The energy directed alongshore is associated with lower frequencies that correspond to the larger fetch of the alongshore component of the wind. The effect is most clear for station FL49, and becomes less distinct for station FL48, indicating that the effect rapidly decreases for larger distances from the coast. These phenomena—related the wave growth in slating-fetch conditions—were also described by Ardhuin et al. [2006]; Bottema and van Vledder [2007].

The 2-D spectra from SWAN do show asymmetric behaviour. For winds veering from south to west-southwest the spectrum shows a second quickly rising peak while the transition from west to south-west is more gradual. The difference most likely caused by the geometry of the coastline in that area. Due to the bend in the coastline, raw fetches increase from to less than 3 km to 14 km if the direction of the wind backs more than 172°N with respect to station FL49 while the fetch for the other slanting directions decreases more gradual. Much wave energy is moving in from this direction and it a large directional spreading of wave energy in that area.

Unfortunately, there is no directional data from the observations to verify the 2-D spectra of SWAN. However, the qualitatively similar behaviour for the observed spectra and the SWAN does suggests that the low-frequency peak is associated with the alongshore propagation of the wave energy during slanting fetch conditions. This would explain the lower correlation of the wave parameters with a general formulation of the effective fetch. Furthermore, since the spectrum contains more energy (the alongshore component) than it would have been expected following the empirical growth curves, this could well explain why the observations of these locations were positioned structurally above the growth curves (see Figure 2.3) as was found by Deltares [2013]. It is recommend to investigate the alongshore transport of wave energy for slanting fetches because this could for example play a role in the prediction of waves on rivers—where the fetches perpendicular to the coast line are small compared to the fetches parallel to the coast line.

LIMITATIONS OF DOMAIN B

By comparing the results of the two domains only, small errors were found for the wind directions larger than approximately 300°N. No lower wind direction boundary for the validity of the domain B was found, indicating that domain B behaves similar to domain A, when the wind direction is smaller that 300°N.

LIMITATIONS OF THE TEMPORAL RESOLUTION

The number of the iterations that SWAN needs each time step made it questionable whether the results were sufficiently accurate. The simulations using the different time steps indicate that the 20 minute averaged values of the wave parameters are only slightly affected by the higher temporal resolutions. The time step of ten minutes is, therefore, considered to be sufficiently accurate for these simulations.

5.4. CONCLUSION: THE PERFORMANCE OF SWAN FORCED BY WRF

A non-stationary SWAN model was set up using the calibrated setting from the WTI project to perform wave simulations at Lake IJssel. Friction velocities, determined by WRF, were converted to wind speeds using the drag relation from SWAN backwards. These pseudo wind fields were used to force SWAN. The non-stationary simulations were performed using a time step of 10 minutes.

The model results were validated using observed data from the two storms. At first sight, SWAN results seemed to perform moderately well. For wind directions along the shore normal (239°N±20°), negative biases were found for the wave heights (H_{m0}; storm 1: −13%, −21% for location FL48 and FL49 respectively; storm 2: −18%, and −11% for location FL48 and FL49 respectively) and wave periods (T_{m-10}; storm 1: 10%, 7% for location FL48 and FL49 respectively; storm 2: –7%, –4% for location FL48 and FL49 respectively). A part of the error was caused by the errors already in the wind field.

The 1-D wave spectra showed deviations from the JONSWAP spectrum for the stations close to the coast. In correspondence with the finding of Bottema and van Vledder [2007], the spectra show two peaks. The observed and predicted spectra correspond well regarding the frequencies associated with these peaks. However, there are differences in the magnitude of the peaks. Especially in the SWAN spectra, the low-frequency peak contain a significant part of the wave energy, even for wind in the shore normal direction.

2-D SWAN spectra indicate that the low-frequency peak is associated with the alongshore transport of wave energy and the high-frequency peak with the cross-shore transport of wave energy. The qualitative agreement between the observed and predicted spectra suggests that this also happens in reality. However, no direction data of the wave observations are available, so this cannot be verified. The additional along shore directed energy would explain why the data for these short fetches no longer behaves according to the empirical growth curves. The effects seem to be amplified by the bend in the coastline. Even for wind directions completely along the normal, wave energy is moving in from approximately 170°, causing a large directional spreading in the area of the measuring locations. Directional data is necessary to provide verification of the results from SWAN.

Ideal locations for investigating wave growth consists of long straight coast lines so that disturbance of the measurement are minimized. If the findings from SWAN are realistic, the locations FL48 and FL49 are disturbed by al the influence of the bend; this would make the location inappropriate for investigation of wave growth (under idealized conditions). It is advised to further investigate the influences of the coastline on the measurements.

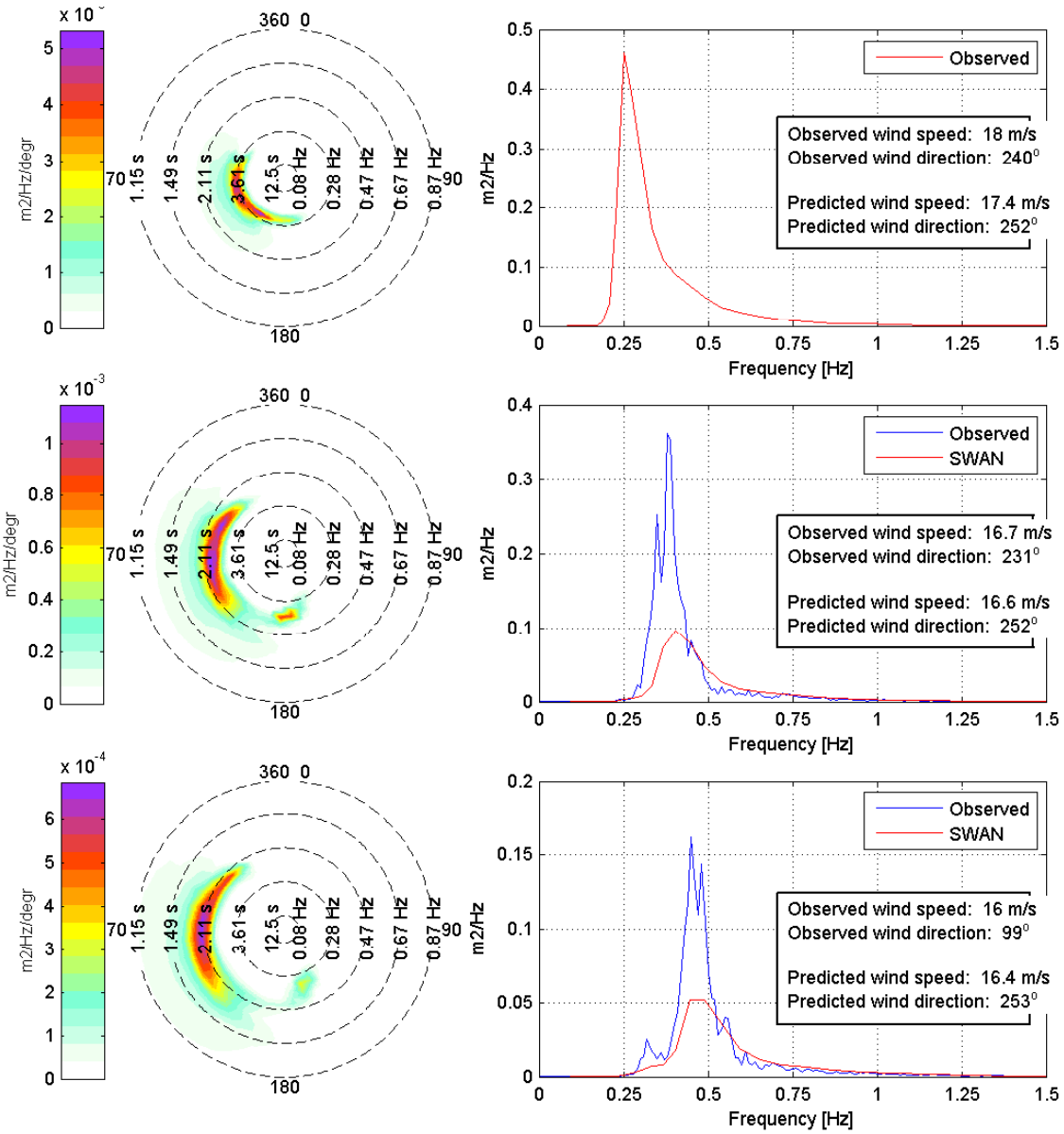

Figure 5.8: Storm 1, January 4th 23:20 UTC+1: Spectra of observed and predicted wave fields. Left: two-dimensional SWAN spectra, Right: one-dimensional spectra.

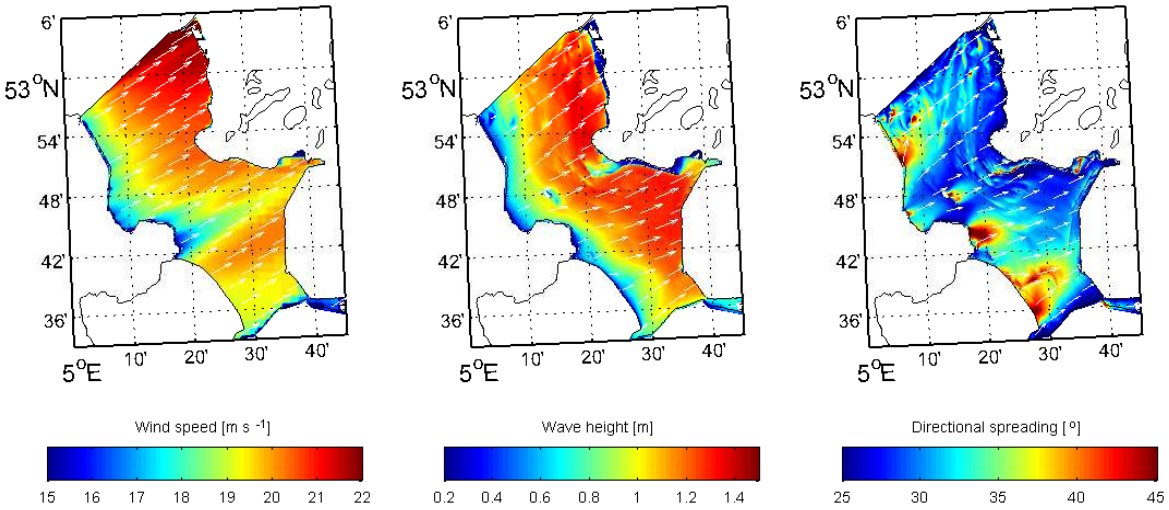

Figure 5.9: Storm 2, December 5th 11:20 UTC+1: 2-D plots of the wind speed (left), significant wave height (middle), and directional spreading (right).

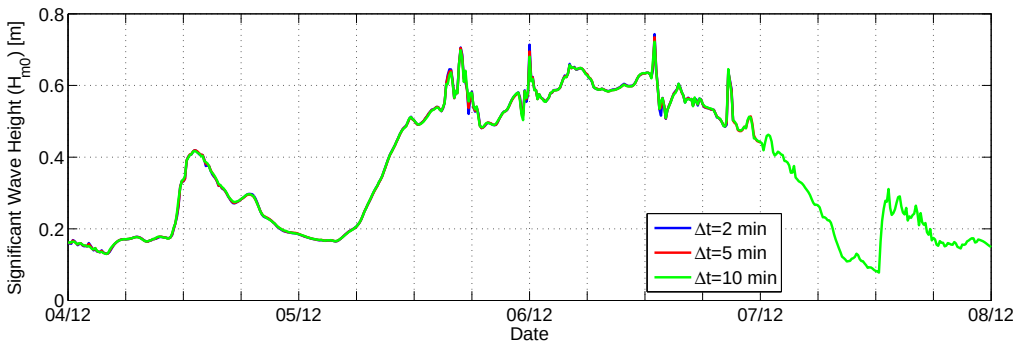

Figure 5.10: Storm 2: Significant wave height (H_{m0}) at station FL49 for three different time steps in SWAN)

6

EFFECT OF WIND FIELD RESOLUTION

6.1. INTRODUCTION

In the previous sections, the model set-up and the performance for both WRF and SWAN were discussed. This chapter looks further into the effects of different spatial resolutions in WRF, and the effects it has on the wave predictions. First, the effects of using the different resolutions in WRF are investigated. Several high-resolution simulations are performed and the impact on the results is discussed. Then SWAN computations are performed using these different wind fields to assess whether the higher resolutions have an an added value for the prediction of wave characteristics.

6.2. DIFFERENT RESOLUTIONS IN WRF

One of the main objectives of this study is to assess the performance of WRF in combination with high spatial resolutions (higher than the model was designed for). In this section, an analysis is made of the differences between five different spatial resolutions ranging from 2700 m to 300 m. The primary concern is to see whether there is a significant difference (in wind field variability) between the different resolutions and to assess whether WRF is capable of producing physically reliable results with these high spatial resolutions. To determine the physical reliability, WRF the wind fields with different resolutions are compared to each other, observations, and theory.

6.2.1. EXPERIMENTAL SET-UP

The same model set-up was used as described in the Section 4.2 to simulate both storms. The only adjustments made were the horizontal resolutions, the time steps, and the number of grid points (for some domains). The time steps were changed for the purpose of numerical stability, and the number of grid points were modified to keep the domains of the same size. An overview of the simulations, the associated resolutions, and time steps is shown in Table 6.1.

6.2.2. RESULTS AND DISCUSSION

TIME SERIES

A first assessment of the differences between the resolutions was made based on time series. Output was generated by WRF on the locations FL47, FL48, and FL49 based on the nearest-neighbour approach. . For the readability of this report, not all complete time series are shown here. This section only gives an analysis of the findings. Graphs of all simulations and for all stations can be found in Appendix G.

For all stations, the simulations followed the measured data reasonably well. No significant difference in the qualitative behaviour of the simulations was seen. In all simulations, periods of slowly varying wind speeds, and periods with fluctuations could be distinguished. During these calm periods, the differences between the simulations were generally smaller than 1 $\mathrm{m\,s^{-1}}$, sometimes even as little as 0.2 $\mathrm{m\,s^{-1}}$. During periods in which the velocity varied quickly, larger differences occurred. These differences were both in magnitude and in time. Figure 6.1a illustrates a calm period, and a period with fluctuations. The fluctuations for this specific case were caused by a passing occluded front, together with convection cells with high precipitation

Table 6.1: Horizontal resolutions and time steps used in WRF simulations. * 166x166 grid points instead of 100x100

	Run	Horizontal resolution [m]					Time step [s]				
		d5	d4	d3	d2	d1	d5	d4	d3	d2	d1
Storm 1											
	1			2700*	13500	40500			12	60	180
	2		1500	4500	13500	40500		6.67	20	60	180
	3		900*	4500	13500	40500		4	20	60	180
	4	500	1500	4500	13500	40500	2.22	6.67	20	60	180
	5	300*	1500	4500	13500	40500	1.33	6.67	20	60	180
Storm 2											
	6			2700	13500	40500			12	60	180
	7		1500	4500	13500	40500		6.67	20	60	180
	8		900*	4500	13500	40500		4	20	60	180
	9	500	1500	4500	13500	40500	2.22	6.67	20	60	180
	10	300*	1500	4500	13500	40500	1.33	6.67	20	60	180

rates. The graphs show that higher velocities are found for the simulations with high resolutions. Due to the higher resolutions, the microphysics scheme is better able to explicitly resolve convective processes. Which, in theory, should lead to better results. In this case, it caused to differences in wind speed up to 7.5 $\mathrm{m\,s^{-1}}$. Figure 6.1b shows another example of such fluctuations. Also for this case, the fluctuations are caused by precipitation. This example better illustrates the differences in the signals of the different resolutions. Again, the high resolutions predicted larger precipitations rates, which resulted in greater wind speed fluctuations and also in steeper gradients. Throughout both storms fluctuations of the velocity signal were observed due to precipitation and the passage of fronts. However, with the currently available data, it is not possible to verify whether or not these fluctuations are physically correct.

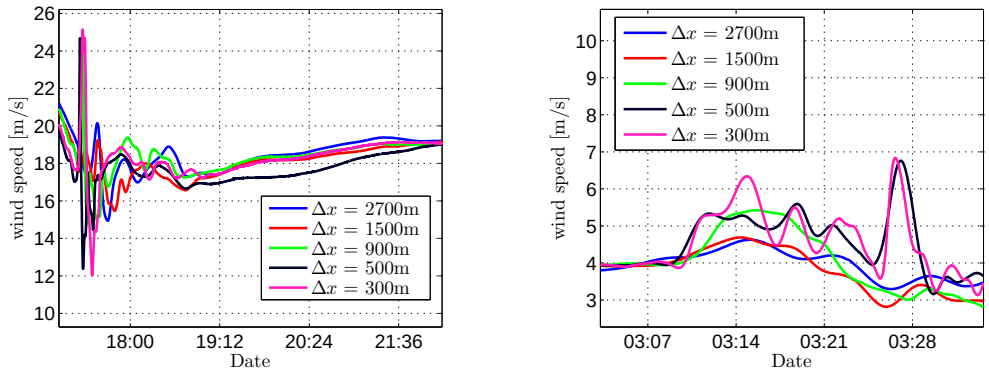

(a) **(b)**

Figure 6.1: (a) Transition from fluctuating to slow varying velocity (instantaneous 10-m wind velocity station FL 47 on December 5th 2013 UTC+1). (b) Close up of some fluctuations (u component of the instantaneous 10-m wind velocity station FL 47 on January 3rd 2012 UTC+1)

The WRF time series were averaged in time every ten minutes so that the data could be compared with the RWS measurements (which are also 10-minute average values). The statistical analysis of the data also confirms that the simulations perform more or less equally well. For reasons of readability of the report, tables with these statistical quantities are not shown in the main text, but can be found in Appendix G.

To specifically assess the influence of the difference in roughness due to land-water boundary only winds along the shore normal (239°N ± 20°) are considered. For these periods, both observed and predicted values showed the expected increasing wind velocities with increasing fetch. On average, observed differences between FL47 and FL48 were 0.88 $\mathrm{m\,s^{-1}}$ for storm 1 and 0.31 $\mathrm{m\,s^{-1}}$ for storm 2. The differences between FL48 and FL49 were 0.56 $\mathrm{m\,s^{-1}}$ for storm 1 and 1.37 $\mathrm{m\,s^{-1}}$ for storm 2.

Predicted mean velocities showed some bias as was also seen during the validation. The biases for the stations FL47 and FL48 were more or less the same for all simulations. The bias for station FL49 showed a clear trend, the bias decreased from 0.71 ms^{-1} (Δx = 2700) to 0.35 ms^{-1} (Δx = 300) for storm 1 and from 1.33 ms^{-1} (Δx = 2700) to 0.87 ms^{-1} (Δx = 300) for storm 2. Compared to the observed mean differences between the stations, this is quite an improvement. Other statistical parameters such as the RMSE, correlation coefficient, and the scatter index shows no further differences between the simulations related to the resolutions.

SPATIAL PATTERNS

The second part of the performance assessment of WRF for high resolutions is based on the spatial variation of the wind field. Comparison of the results in space also showed the periods of slow varying wind and periods of fluctuations. During the slowly varying periods, the overall performance of the different simulations was more or less equal. An example of such a moment is shown in Figure 6.2. For this particular moment in time, the wind speed above Lake IJssel varies between 12 to 18 ms^{-1}. All simulations showed slower wind speeds near the upstream coast due to the change in surface roughness. Except for the simulation with the coarsest resolution (Δx = 2700 m), all simulations showed the distinct wind streaks along the coast due to variation in roughness over land. The wind streaks tend to extend further over Lake IJssel for the finer resolution than for the coarser resolutions. Local differences in the representation of these wind streaks caused differences in wind velocity up to 1 ms^{-1}. According to Dörenkämper et al. [2015] these wind streaks are specifically found during periods of stable stratification. They found that the influence of the variable upstream surface roughness became less distinct during unstable conditions. The extra vertical mixing caused by the unstable stratification also enhances the horizontal mixing, thus reducing the wind streaks.

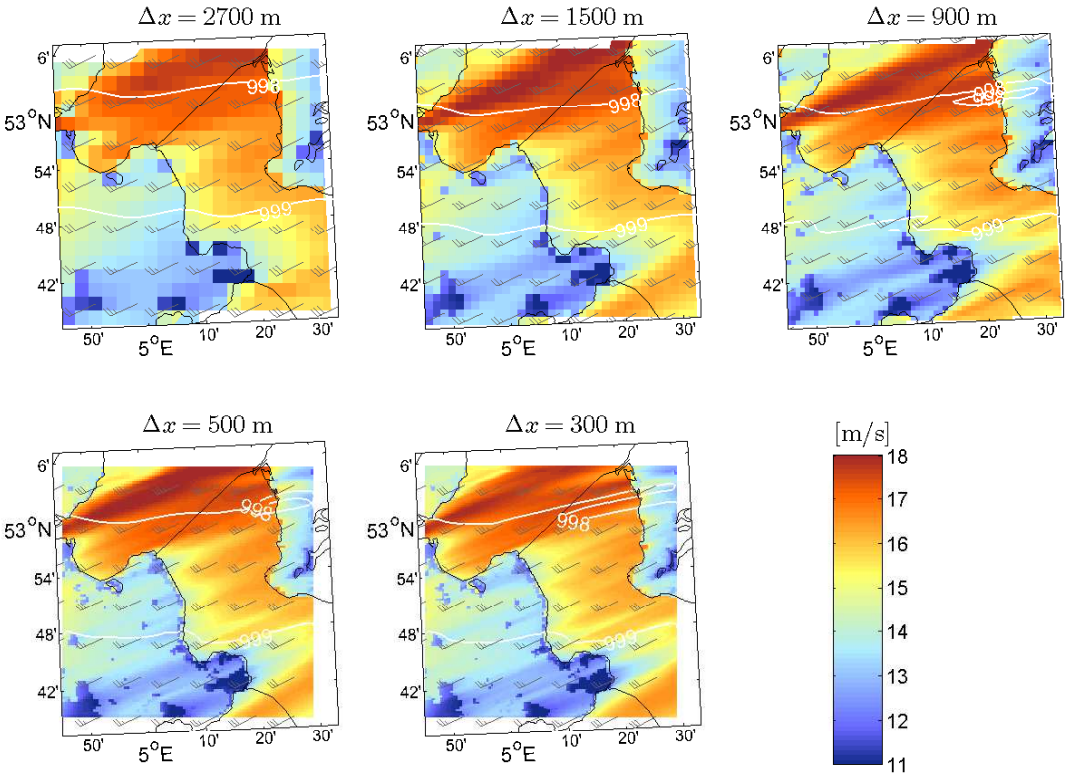

Figure 6.2: Storm 1 January 4th 21:00 UTC+1: 10-m wind speed (half barb equals 2.5 ms^{-1}, full barb 5 ms^{-1}, and triangle 25 ms^{-1}). White contour lines show mean sea level pressure (hPa).

Larger differences were found by looking at the periods where the winds speeds were quickly changing. Most of the time this happened, it was due to a passing front (especially cold fronts) and/or precipitation. The spatial images showed much variation in the wind field when this happened and velocities varied up to 15 ms^{-1} over a length of less than one kilometre. One of the more extreme situations (of these two storms) is shown in Figure 6.3. At first glance, two things stand out, first there is a difference in the position of the maximum velocities, and second, maximum velocities are higher (differences up to 15 ms^{-1}) for the simulations with

the high resolutions.

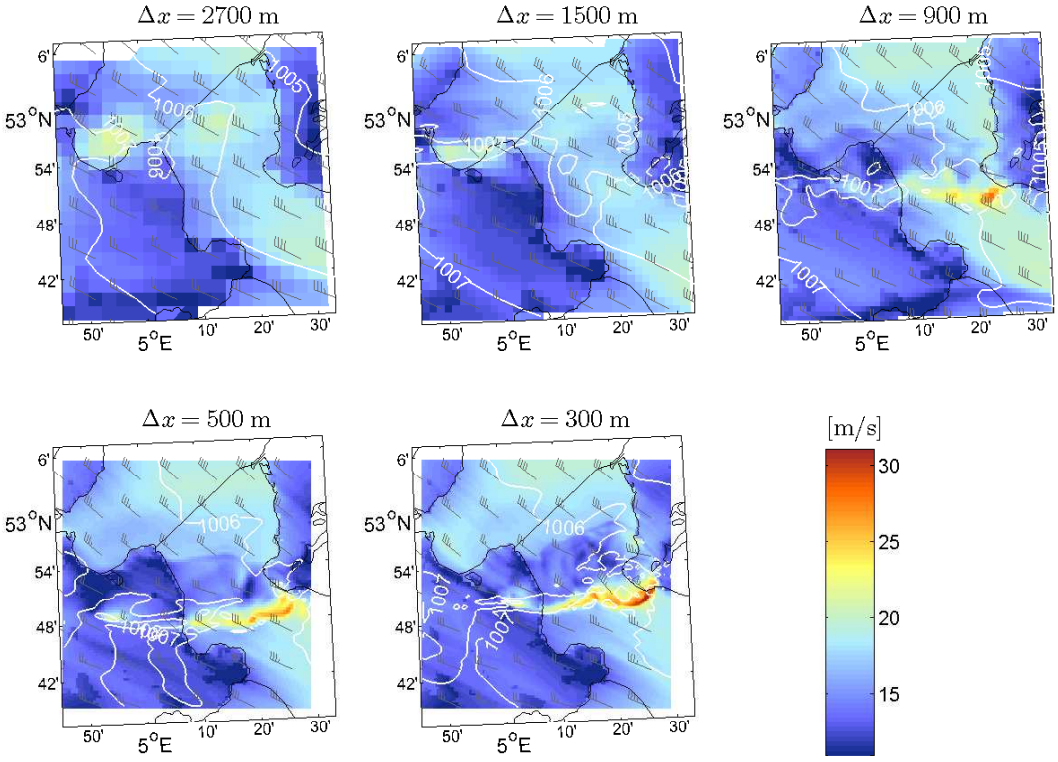

Figure 6.3: Storm 2 December 5th 17:30 UTC+1: 10-m wind speed (half barb equals 2.5 $\mathrm{m\,s^{-1}}$, full barb 5 $\mathrm{m\,s^{-1}}$, and triangle 25 $\mathrm{m\,s^{-1}}$). White contour lines show mean sea level pressure (hPa).

Further investigation of this particular situation shows that this is a gust front, caused by the downdraft of a convection cell. The convection cell reached a height of about 10 kilometers (according to the simulation for Δx = 300 m). Figure 6.4, shows the total precipitation fallen in the preceding 10 minutes (the difference between two model output fields, since WRF, gives the accumulated amount of precipitation). The differences between the simulations were significant. Not only were there substantial differences in the amount of rainfall, but also the location differed. For the three highest resolutions, the convection cell was positioned above Lake IJssel for the other two simulations this was above the tidal inlet between the mainland and Texel (northwest of the domain). Note that the shape of the convection cells is stretched (Figure 6.4) in the direction of the wind because the figure shows the rainfall accumulated over the previous ten minutes. As was already mentioned previously the fine resolutions show higher precipitation rates and larger gradients in precipitation.

Looking at the origin of the convection cell it was seen that it was triggered by WRF at different locations for each simulation. In the region of the convection cell, surface temperatures dropped about 5°C, which created large gradients in temperature (not shown). Furthermore, large vertical velocities, over 5 $\mathrm{m\,s^{-1}}$ (upward as well as downward) at a height of 1 km were predicted by WRF near the boundary of the convection cell (also see Figure 6.7 and 6.8). Both explain the large horizontal velocities (the gust front) at the surface. Comparison of the predicted precipitation with satellite observations from the KNMI (see Figure 6.5) shows that there were indeed several rainfall events near the area of Lake IJssel, and even near the location where WRF predicted the convection cell. However, precipitation rates shown on the radar images are much lower than those predicted by WRF. Maximum precipitation rates of about 3 $\mathrm{mm\,h^{-1}}$ were measured, where WRF predicted that about 3 mm falls within ten minutes.

Precipitation is explicitly resolved and triggered by the microphysics scheme (since CU scheme is absent). Theoretically, the higher resolutions are better able to resolve the convective processes explicitly. In a previous studies Dudhia [2014] noted that there are difficulties in predicting correctly the triggering of precipitation with WRF due to the absence of the cumulus scheme. Cassola et al. [2015] investigated the differences

between microphysics schemes in WRF and found that especially the ETA Ferrier scheme (the scheme used in this study) predicts many different individual structures (of precipitation), and that the scheme overestimates the amount of precipitation. Although this is in line with what was seen in this study, it could not be verified.

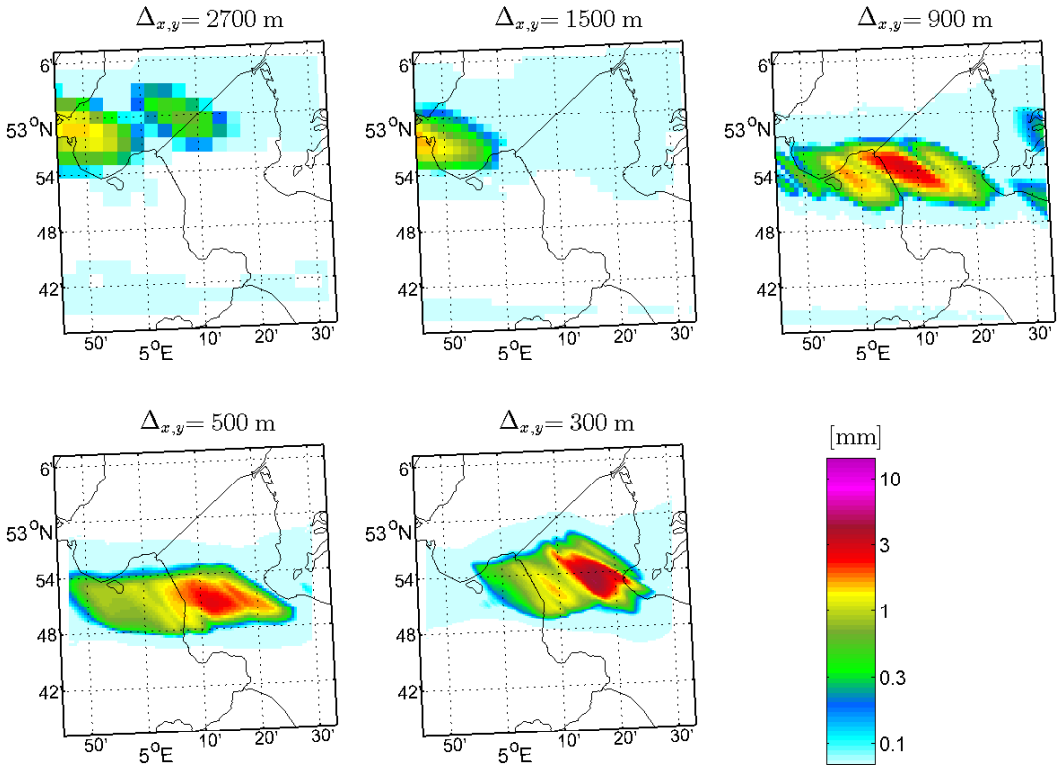

Figure 6.4: Storm 2 December 5th 17:30 UTC+1: precipitation accumulated over the foregoing ten minutes for all resolutions.

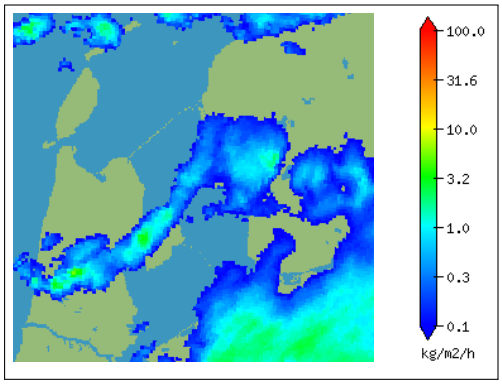

Figure 6.5: Storm 2 December 5th 17:30 UTC+1: Visualization of the KNMI precipitation radar, above the Netherlands. Image obtained with the ADAGUC WMS service of the KNMI precipitation radar.

The simulations used for assessing the influence of the domain size on the wind, during the model verifications also showed that the predictions of precipitation are sensitive to the size of the domain (and with that the position of the lateral boundaries). In Figure 6.6 the precipitation accumulated over 12 minutes of three simulations is shown. The size of the most inner domain (domain 5) varies between these simulations: 100 × 100, 125 × 125, and 150 × 150 grid points. All three simulations have resolutions of 500 m, giving them a size of respectively 50 × 50 km, 62.5 × 62.5 km, 75 × 75 km. Except for the size of the most inner domain, all settings are equal. The figure clearly illustrates the sensitivity of precipitation to the domain size and the position of the lateral boundary. In this case, the differences in the domain size were only 12.5 km (25 grid

points), while differences between domain 3 (2700 m run) and domain 5 (500 m and 300 m runs) are 400 km. This indicates that the results of the previously described simulations were also influenced by the size of the domain and the position of the lateral boundaries. It should be noted that this is an extreme example and that most of the time, differences between these simulations are minimal.

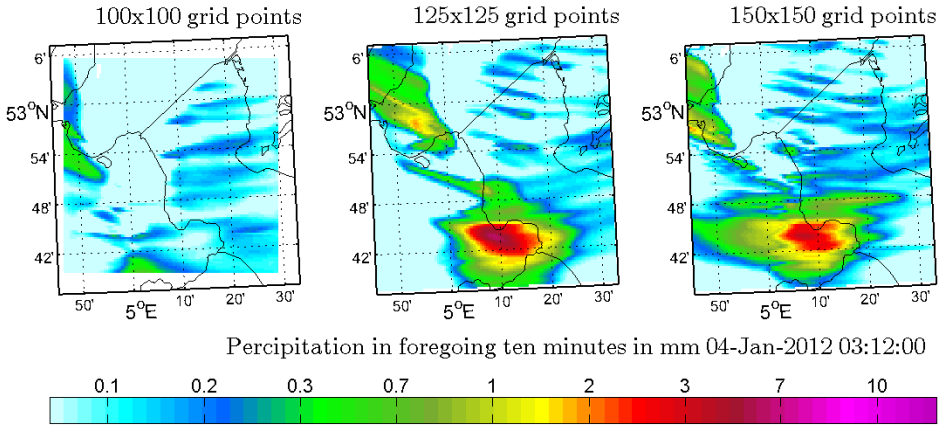

Figure 6.6: Storm 1 January 12th 03:12 UTC+1: precipitation accumulated over the foregoing twelve minutes for different size of the most inner domain. (a) 100 × 100 grid points, (b) 125 × 125 grid points, and (c) 150 × 150 grid points

Concluding, this convection cell illustrates the origin of the differences in wind speeds between the different simulations. The 10-m wind fields are influenced by processes that are much more difficult to predict (precipitation) than the wind itself. Other events causing substantial spatial variation and other fluctuations of the wind speed are less extreme than this one, but for both storms they were associated with the passage of fronts and/or precipitation.

U10 PROFILES

Profiles showing the 10-m wind speed perpendicular to the coast give a better view of the change in wind speed after the land-water boundary. Figure 6.9a shows the locations where the profiles are taken. This is exactly across the three measuring locations.

The general trend was the same for all simulation. For the comparison with the theory, it was interesting to investigate periods in which the flow behaves more or less stationary (or slowly varying over time). Furthermore, for the periods that showed much fluctuations in wind speed, no distinct profiles were found. Two moments in time have been chosen to illustrate the behaviour of WRF for the different resolutions; these are shown in Figure 6.9, The figures also show the HARMONIE results, the measurements by RWS (10-minute average), and the theoretical profile by Taylor and Lee [1984] (also see 2.3.4).

For the theoretical profile by Taylor and Lee [1984] Equation (2.45) was used to estimate u_*. For the aerodynamic roughness on land $z_0 = 0.01$ m was used, this is about the same as WRF used for this area (the exact roughness WRF uses is calculated by the NAOH land surface model). Furthermore, the Charnock relation (Equation (2.27)) with $\alpha = 0.0185$ was used (same as WRF uses) for the determination of the open water roughness.

The first figure, Figure 6.9b, shows quite a good comparison with the theoretical profile. The wind speed started at about 13.4 $\mathrm{m\,s^{-1}}$ and the spread between the different resolutions on land was 1 $\mathrm{m\,s^{-1}}$. Depending on the position of the grid point closest to the land-water boundary, a large jump in wind speed of about 1 to 1.5 $\mathrm{m\,s^{-1}}$ occurred. After the transition wind speeds gradually kept increasing, while the rate at which this happened decreased. Near the transition, the spread of the wind speed between the different resolutions was about 2 $\mathrm{m\,s^{-1}}$. Further downstream of the transition, the spread reduced to about 0.5 $\mathrm{m\,s^{-1}}$. The WRF predictions were in good agreement with the theoretical profile. The same behaviour was seen from the HARMONIE data. The velocity over land from the HARMONIE run was about 1 to 1.5 $\mathrm{m\,s^{-1}}$ higher than the WRF data. After the transition, the velocity increased in two steps of about 1.5 to 2 $\mathrm{m\,s^{-1}}$, after which it remained stable at about 18 to 18.2 $\mathrm{m\,s^{-1}}$. Both HARMONIE and WRF results showed milder gradients after the change in roughness than the theoretical profile.

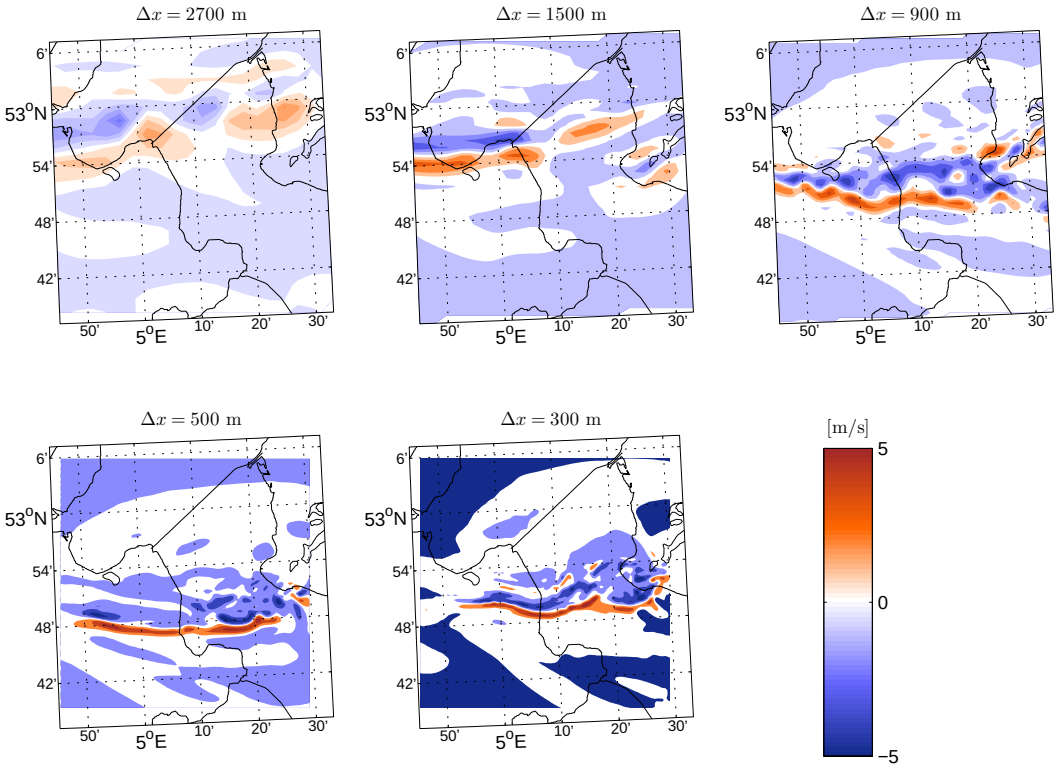

Figure 6.7: Storm 2 December 5th 17:30 UTC+1: vertical velocities at a height of approximately 900 m for all resolutions.

The second figure shows accelerating speeds. Before the land-water boundary, there was very little difference between the different WRF resolutions, the spread was about 0.2 $\mathrm{m\,s^{-1}}$. Near the land-water boundary, there was a jump of about 2 $\mathrm{m\,s^{-1}}$. After the transition, wind speeds kept increasing at the same rate. The spread between the different runs was about 0.5 to 1 $\mathrm{m\,s^{-1}}$. The absolute magnitude and the spatial gradient of the wind speed in the WRF runs were in good agreement with the HARMONIE run.

Even though results from HARMONIE and WRF showed differences in magnitude, they showed the same behaviour after the change in surface roughness. The two examples also illustrate that there are deviations from the theoretical profile. In some cases, the change of wind speed after the transition is barely noticeable. This illustrates the potential added value of using a numerical model instead of the simplified theoretical relations.

ANOMALIES IN THE RESULTS

Except for the types of differences (due to fronts and precipitation) shown previously, only one other noticeable difference between the simulations was found. Between December 3rd, 2013 20:10 (which is still during the spin up period) and December 5th 05:40 numerical instabilities in the surface level pressure were visible for the de highest resolution (Δx = 300m), this is shown in Figure 6.10. The oscillations had an amplitude of about 0.3 hPa and were found all over the domain. The origin of these oscillations is unclear. Further investigation shows that these oscillations extend to the top of the atmosphere. At higher altitudes, the amplitudes of these oscillations are larger, up to 5 hPa. Other meteorological parameters: humidity, temperature, and the wind do not show these oscillations.

6.3. CONCLUSION REGARDING SPATIAL RESOLUTIONS WRF

Both the storms were simulated with WRF for resolutions of 2700, 1500, 900, 500, and 300 meters. The general performance, i.e. the performance during most of the time (no disturbing influences due to fronts and precipitation) and for the greatest part of the domain, of the simulations based on the time series in comparison with the observations and the HARMONIE data are more or less equal. Near the transition from land to water differences of up to 2 $\mathrm{m\,s^{-1}}$ were found. Statistical analysis showed that higher resolutions resulted in a lower

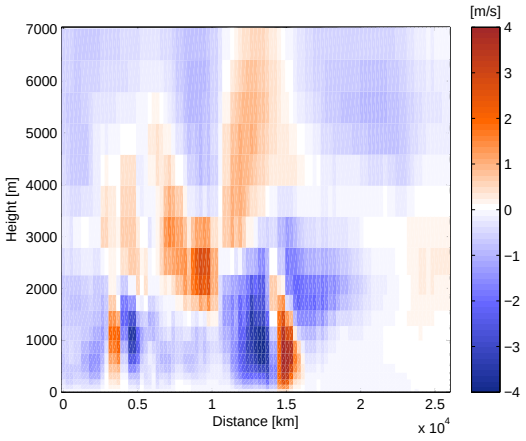

Figure 6.8: Storm 2 December 5th 17:30 UTC+1: cross section of the convection cell (northwest to southeast) predicted by the simulation with a resolutions of 300 m showing the vertical velocities. Upward is positive.

bias for location FL49, this implicates that higher resolutions wind fields result in a better representation of the land-water boundary.

During slowly varying conditions, similar results were found for the different resolutions. Wind streaks show the influence of the differences in land roughness, these wind streaks are especially clear for the highest resolutions (500 and 300 meters). Differences between the 300 m and 500 m resolutions are small, but this also due to the resolution of the land-use data ($\sim$ 500 m). Coarser resolutions smear out the gradients in wind speeds and also the wind streaks become less distinct and less long. For the coarsest resolutions, most of the wind structure of the domain have become unclear. The presence of the wind streaks over Lake IJssel clearly shows that the effects due to differences in upstream aerodynamic roughness are noticeable far after the transition. However, as has been mentioned with the validation of WRF, it uncertain whether these wind streaks real.

In both storms, periods were seen in which there was much spatial variation in wind speed. This was caused by the passing of fronts and precipitation. During these periods, differences between the simulations were found in both magnitude, time, and place. In some cases, this led to differences in wind speed up to 15 m s^{-1}. The general trend for these differences shows that higher resolutions have higher maximum velocities than the coarser resolutions. The reason for the differences in wind speed is mainly the difference in predicted precipitation.

Even thought the results of the 300 m resolution (in terms of wind) are comparable to the other resolutions, a numerical instability in the surface pressure field has been found for one of the storms. This indicates that there are some numerical issues associated the high resolution. The instabilities were not found for the other parameters that WRF determines. Furthermore, wind results were in good agreement with the other simulations and the measurements. However, it can not be said that WRF produces physically reliable results at this resolution, in combination with the used settings. It is therefore that the 500 m resolution is considered more reliable than the 300 m resolution. It is possible that another combination of parameterizations does not give these instabilities at this resolution. Although there is no obvious link the parameterizations that were expected to cause problems (Chapter 2), it is agreement with the general recommendation to keep resolutions lower than 1000 m.

6.4. WAVE RESPONSE TO HIGH-RESOLUTION WIND FIELDS

In the previous section, WRF experiments have been carried out using wind fields with different resolutions, ranging from 2700 m to 300 m. In this section, the effect of the wind field resolution on SWAN predictions is investigated.

6.4.1. EXPERIMENTAL SET-UP

The same model set-up was used as described in Chapter 5, using the small, high-resolution domain B. Initially, the only changes for the simulations in this section were the wind boundary conditions. It became

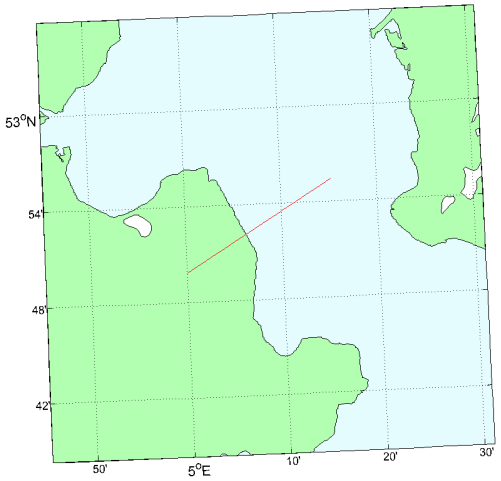

(a)

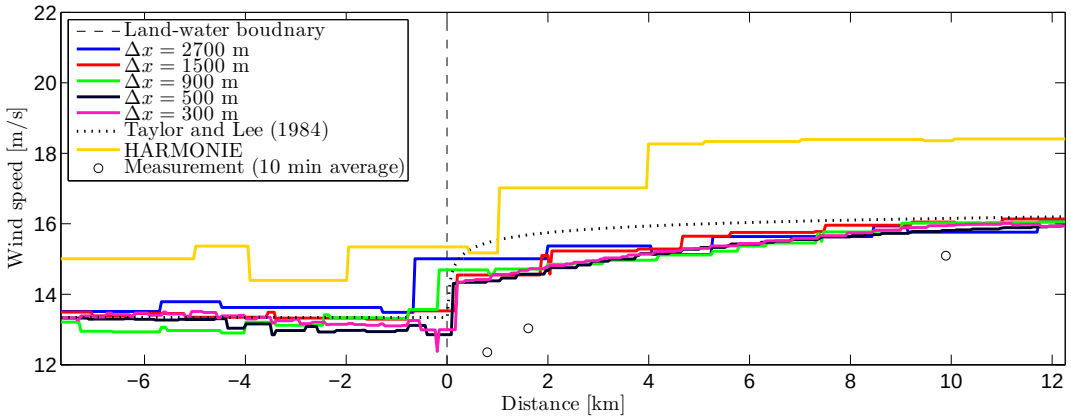

(b)

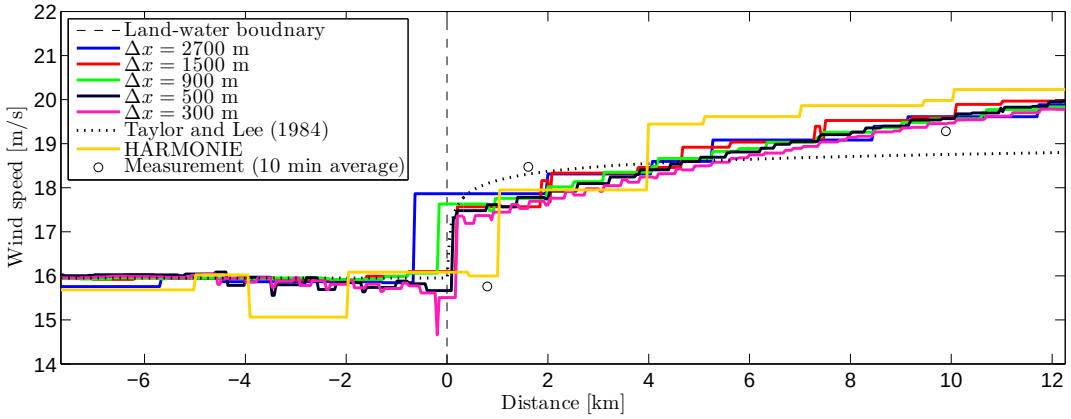

(c)

Figure 6.9: 10-m wind speed profile perpendicular to the coastline for all resolutions based on the closest grid point. HARMONIE results and a theoretic profile by Taylor and Lee [1984] have been added for extra comparison. (b) Storm 1:January 4th 21:00 UTC+1 (c) Storm 2: December 5th 11:00 UTC+1. Note that the diagonal crossing of the grid in combination with a closest grid point interpolation sometimes leads to short difference in wind speed on a smaller scale the grid resolution

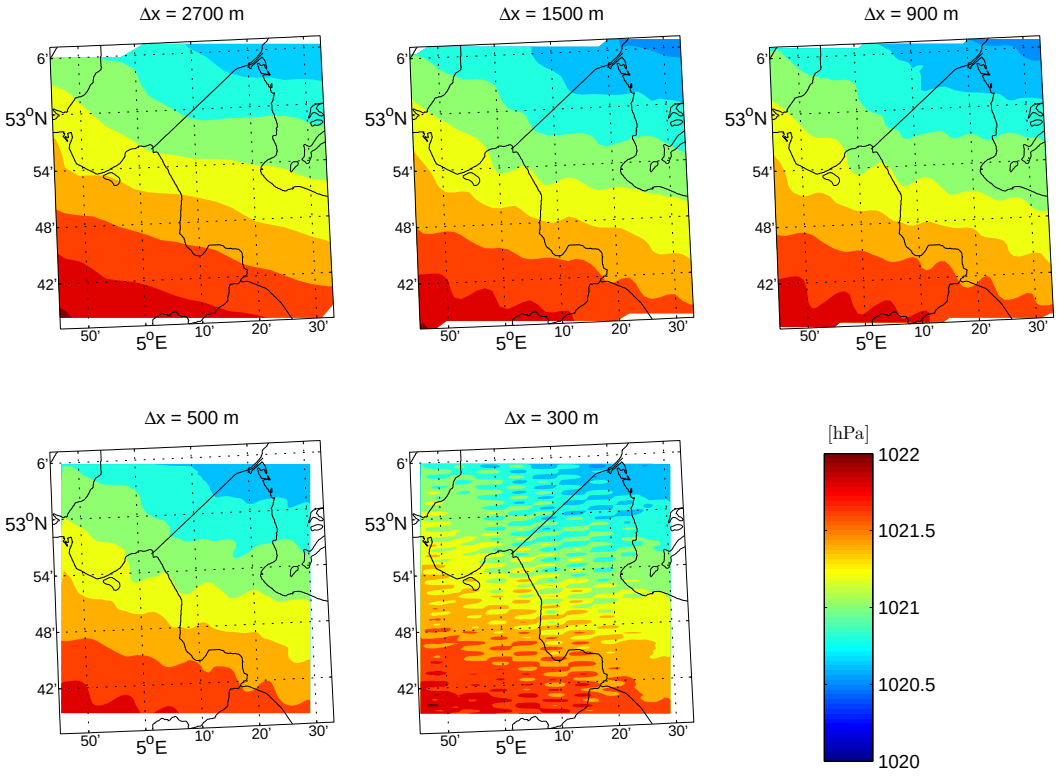

Figure 6.10: Storm 2 December 5th 17:30 UTC+1: surface level pressure.

clear in the previous section that the WRF results for a resolution of 300 m show indications that there are numerical instabilities. Therefore, the 300 m resolution wind field is not taken into account in this section. Simulations with SWAN were carried out using the wind fields with the four remaining resolutions. These simulations showed significant distortion of the wind field near the coast, due to the interpolation of the wind data between land and water grid points. A prepossessing step was implemented to exclude the land points of the WRF grid from the interpolation and to extrapolate the remaining grid points up to the land-water boundary.

6.4.2. A PREPROCESSING METHOD TO REDUCE INTERPOLATION ERRORS NEAR THE COAST

The initial simulations that were carried out showed that the results were biased due to the different positions of the grid points in WRF this made is difficult to compare the different simulations with each other. Moreover, the interpolation method by SWAN does not discriminate between land or water points in the wind field. This caused the large gradient (step, since it is actually the friction velocity) in wind speed near the land-water boundary to flatten. Two figure are included to illustrate this, Figure 6.11 and 6.13. Both figures clearly show the difference in the wind speed between the wind field resolutions. Especially the coarser resolutions are affected by this.

Both figures show that the behaviour near the land-water boundary clearly deviates from the behaviour seen from the WRF results. This problem was also observed by [Deltares, 2015], and they suggested and interpolation method that excluded land points from WRF. A more or less similar approach is used here.

A preprocessing step was performed in which land-points are excluded from the WRF wind field. The remaining points are then bi-linearly interpolated to a grid with a resolution of 100×100 m[1] to estimate the wind speeds between the points. Afterwards, the interpolated field is smoothed, which causes it to follow the general trends in the wind field without discontinuities. This is especially beneficial for the extrapolation up to the land-water boundary.

The whole procedure is preformed using MATLAB routine 'GridFitt' [D'Errico, 2010]. It stretched that due

[1] The wind data was not directly interpolated to the SWAN grid in order to keep processing time within an expectable range.

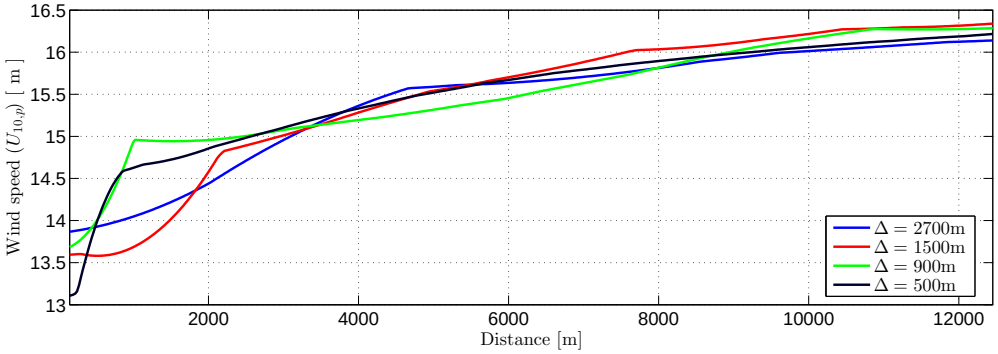

Figure 6.11: Shore normal profile: Pseudo wind speed at January 4th, 21:00, with regular interpolation by SWAN

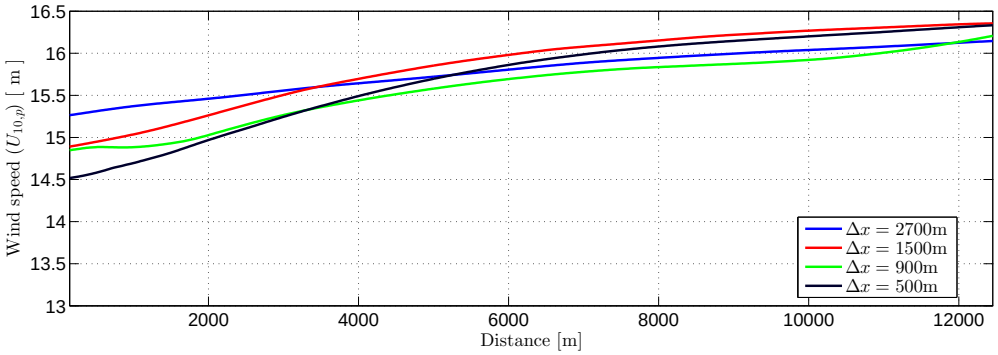

Figure 6.12: Shore normal profile: Pseudo wind speed at January 4th, 21:00, using improved interpolation method

to the smoothing, this is not a pure interpolation procedure, but more (as the name 'GridFitt' suggests) a surface fitting procedure. The smoothing of the surface causes small differences between the interpolated and original wind field. The performance has been assessed to make sure that these errors remain within acceptable limits (< 1%.

Figures 6.11 to 6.14 give two examples of the results of the preprocessing method. It can be seen that the land-based wind speeds no longer contaminate the SWAN domain. The wind speeds along the coast increased to a value that is nearer to the WRF results for open-water wind speeds. The 2-D plots do still show some signs of disturbances due to the grid point positions along the coastline. Even though the method is not faultless, it still significantly improves the implementation of the wind field in SWAN.

6.4.3. RESULTS AND DISCUSSION

For this analysis, only short fetch conditions were considered. Wave spectra of the reference simulations showed that there are larger differences between the observed spectra and the SWAN spectra for wind speeds lower than approximately $8\,\mathrm{m\,s^{-1}}$. For this reason, only results for wind speeds higher than $10\,\mathrm{m\,s^{-1}}$ were used. Furthermore, the time series were filtered based on the predicted wind direction. It was preferable only to consider wind direction between 239°N ± 20° since the wave spectra seemed to be very sensitive to wind direction (low-frequency energy). However, because only two storms were hindcasted, only a very small part of the results could be used for the analysis. Hence, also a broader range was considered (239°N ± 40°), keeping in mind the limitations the processes predicted by SWAN for these locations. The time series and tables with statistics are available in Appendix G.

TIME SERIES

The time series for the stations all showed the same behaviour as was seen during the validation of SWAN. The differences resulting from the different wind fields resolution were very small and ranged from 1 cm during steady weather, to 8 cm during rainfall events. Wave periods also varied little, differences in predicted T_{m10} ranged from less than 0.01 s to 0.02 s. The results for the other wave periods were comparable.

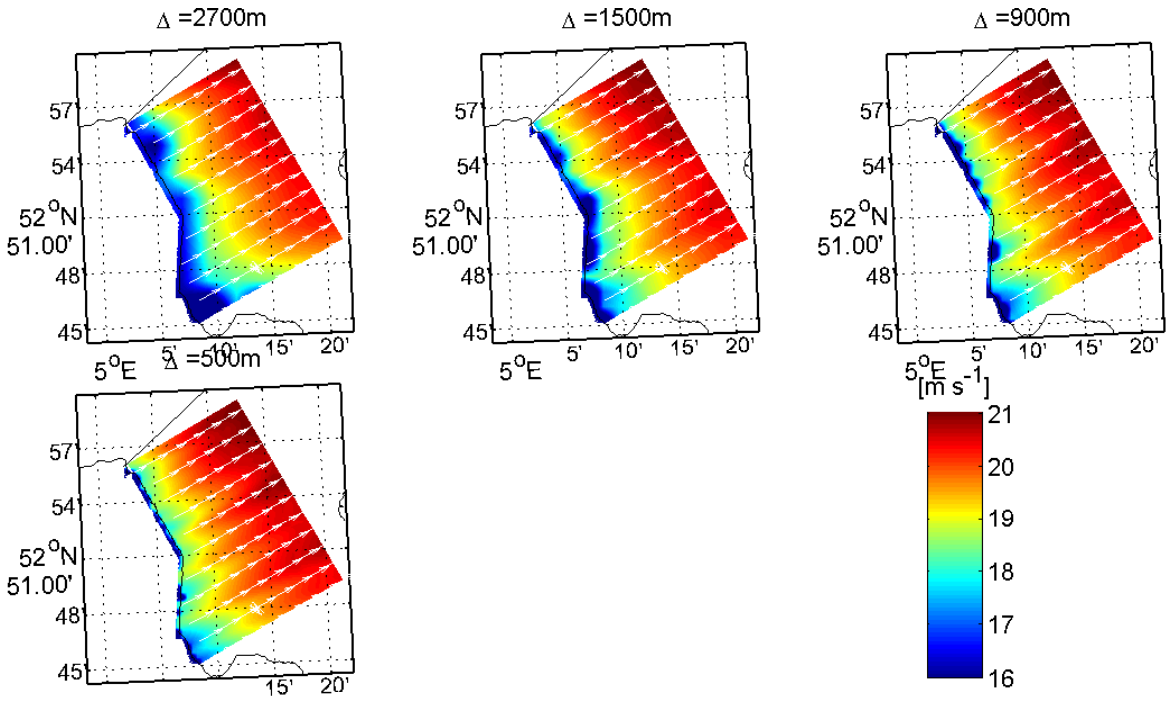

Figure 6.13: 2-D Plots: Pseudo wind fields interpolated by SWAN at December 5th, 12:00.

An overview of the statical analysis is given in Tables 6.2 and 5.2. The results show little to no difference between the simulations for both the directional ranges. The bias for the directions between 239°N ± 20°(for H_{m0} –18% and –13% for stations FL48 an FL49 respectively) is slightly larger than for the direction between 239°N ± 40° (for H_{m0} –15% and –4% for stations FL48 an FL49 respectively). As was also mentioned with the validation of the model, offshore directed winds had a slight negative bias which is partially due to errors in the observation for this direction. The wider spread of the direction clearly influences the correlation coefficient for all parameters, indicating a temporal mismatch between the time series. All statistical quantities are more or less equal for all simulations, indication little to no sensitivity to the wind field resolution at these locations.

SPATIAL PATTERNS

The spatial variation of the wind profile shows that land induced roughness effects are still visible offshore for tens of kilometres. To investigate the effects of these wind streak on wave height spatial patterns are investigated.

Figure 6.15 show the wave height for the same moment of as the wind speed was given in Figure 6.14. Wind speed were high, severe gale conditions. It is not immediately clear from figure whether these wind streaks results in differences in wave height (or periods). The differences in wave heights provide more insight. Figure 6.16 shows the difference between the wave heights of the 500 m wind field resolution and the other simulations (the simulation with the 500 m wind field subtracted from the other). Looking at these differences is can be seen that the pattern of the wind streaks are also noticeable in the wave field predicted by SWAN. The largest differences are seen form the 2700 m resolution, were wave height are locally up to 0.02 m smaller and larger (±6%) than the for the 500 m resolution. For the other simulations differences in wave height were smaller ($\Delta x = 1500$: ±4%; $\Delta x = 900$: ±3%). These differences are mainly found close to the coast. Further away from the coast, the differences were minimal

Additionally alongshore profiles of wave parameters and wind were compared. The wind clearly shows more variation then the wave field. Appendix G.4 also show cross section of the wind and wave field. Furthermore, they only highlight the finding from the two dimensional plots,

Finally, some extra simulations have been performed to asses the reaction of the water surface to the convections cell that was found. Because the speed at which the convection cell moved varies faster then the time

Table 6.2: Statistical quantities of the significant wave height [m] for the stations in lake IJssel, during storm 1

	Δx_{wind}	239°N ± 40°							239°N ± 20°						
	[m]	N [-]	$\overline{o}$ [m]	$\overline{p}$ [m]	r [-]	Bias [m]	σ_{p-o} [m]	RMSE [m]	N [-]	$\overline{o}$ [m]	$\overline{p}$ [m]	r [-]	Bias [m]	σ_{p-o} [m]	RMSE [m]
Fl47	2700	0							0						
	1500	0				No data			0				No data		
	900	0							0						
	500	0							0						
Fl48	2700	129	0.59	0.52	0.8	-0.08	0.11	0.13	76	0.61	0.5	0.94	-0.11	0.09	0.14
	1500	130	0.6	0.52	0.8	-0.08	0.11	0.14	76	0.61	0.49	0.94	-0.12	0.09	0.15
	900	126	0.59	0.51	0.79	-0.09	0.11	0.14	77	0.61	0.49	0.94	-0.12	0.09	0.15
	500	129	0.6	0.51	0.79	-0.09	0.11	0.14	77	0.61	0.49	0.93	-0.12	0.09	0.15
Fl49	2700	127	0.45	0.43	0.82	-0.02	0.09	0.09	75	0.46	0.41	0.94	-0.05	0.08	0.09
	1500	130	0.46	0.43	0.82	-0.02	0.09	0.1	76	0.46	0.4	0.94	-0.06	0.08	0.1
	900	128	0.46	0.43	0.82	-0.02	0.09	0.1	74	0.46	0.4	0.94	-0.06	0.08	0.1
	500	129	0.46	0.43	0.82	-0.03	0.09	0.1	75	0.46	0.4	0.94	-0.06	0.08	0.1

Table 6.3: Statistical quantities of the significant wave height [m] for the stations in lake IJssel, during storm 2

	Δx_{wind}	239°N ± 40°							239°N ± 20°						
	[m]	N [-]	$\overline{o}$ [m]	$\overline{p}$ [m]	r [-]	Bias [m]	σ_{p-o} [m]	RMSE [m]	N [-]	$\overline{o}$ [m]	$\overline{p}$ [m]	r [-]	Bias [m]	σ_{p-o} [m]	RMSE [m]
Fl47	2700	40	0.9	0.84	0.99	-0.06	0.2	0.21	36	0.92	0.85	0.99	-0.08	0.2	0.22
	1500	40	0.91	0.85	0.97	-0.06	0.2	0.21	37	0.91	0.84	0.99	-0.07	0.21	0.21
	900	41	0.9	0.85	0.98	-0.06	0.2	0.21	37	0.91	0.84	0.99	-0.07	0.2	0.21
	500	40	0.91	0.86	0.97	-0.06	0.2	0.21	37	0.91	0.84	0.99	-0.07	0.21	0.21
Fl48	2700	31	0.62	0.54	0.92	-0.08	0.1	0.12	29	0.62	0.53	0.99	-0.09	0.09	0.12
	1500	30	0.63	0.54	0.91	-0.09	0.1	0.13	28	0.63	0.53	0.99	-0.1	0.08	0.13
	900	30	0.63	0.54	0.91	-0.09	0.1	0.13	28	0.63	0.53	0.99	-0.1	0.08	0.13
	500	30	0.63	0.54	0.91	-0.09	0.1	0.13	28	0.63	0.53	0.99	-0.1	0.08	0.13
Fl49	2700	30	0.47	0.45	0.91	-0.02	0.07	0.07	28	0.47	0.44	0.98	-0.03	0.05	0.06
	1500	29	0.48	0.45	0.89	-0.02	0.07	0.07	27	0.48	0.44	0.98	-0.04	0.05	0.06
	900	29	0.48	0.45	0.89	-0.02	0.07	0.07	27	0.48	0.44	0.98	-0.04	0.05	0.06
	500	29	0.48	0.45	0.9	-0.03	0.07	0.07	27	0.48	0.44	0.98	-0.04	0.05	0.07

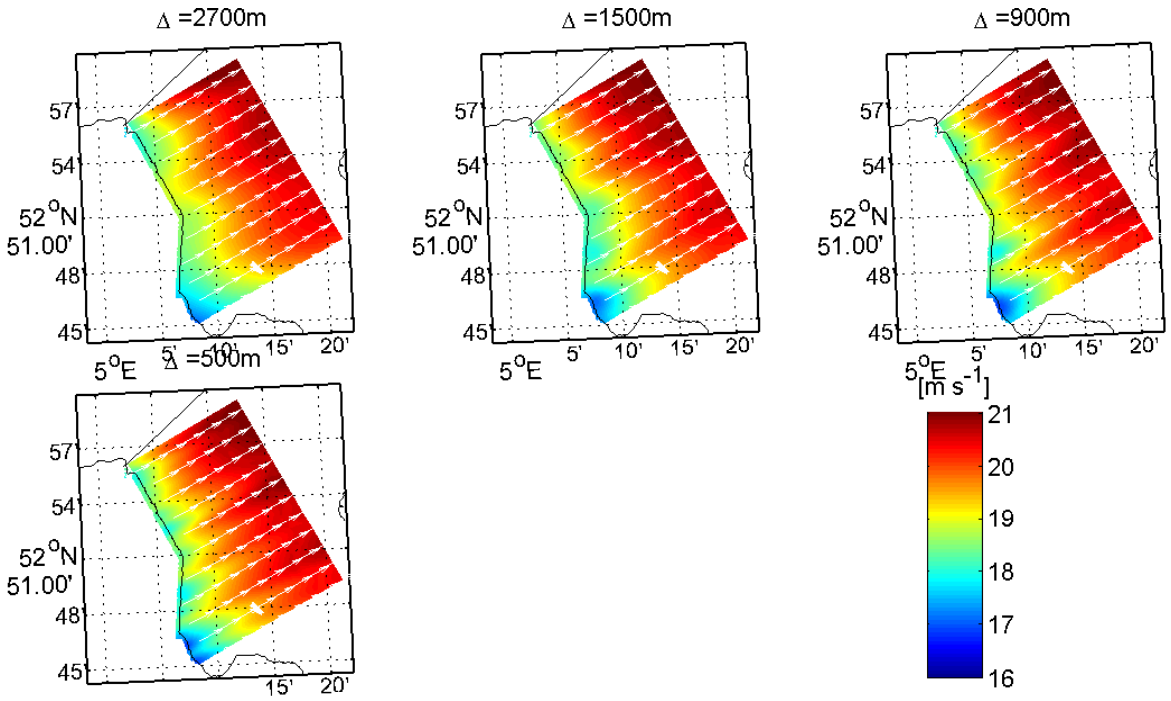

Figure 6.14: 2-D Plots: Pseudo wind fields preprocessed and interpolated by SWAN at December 5th, 12:00.

scales at which the wind varied, the time step in SWAN was reduced to 2 minutes (using wind fields updated every two minutes). Because of the uncertainties that come from these assumptions, the results were not included in the report.

6.5. CONCLUSION: THE EFFECT OF DIFFERENT SPATIAL RESOLUTIONS FOR THE CASE LAKE IJSSEL

Both storms were simulated with SWAN using (pseudo) wind fields produced by WRF. The wind fields had resolutions of 2700, 1500, 900, and 500 m. First simulations carried out by SWAN showed many disturbances along the coast due to interpolation of the land-based wind speeds by SWAN. This was especially noticeable for the coarser resolutions. By including a preprocessing step, the majority of these disturbances were reduced. The simulations using the prepossessing step all showed similar behaviour for wave height and periods, and are comparable to the results found during the validation of SWAN.

Based on statistics analyses, no differences were found between in the reaction of SWAN to the wind field resolutions. Biases of –17% and –11% were found for stations for FL48 and FL49.

The wave field did showed some influence of the upstream roughness. The largest influences were found near the coast and differences between the simulated wave fields were largest for the 2700 m resolution. During strong wind (about 21 $m s^{-1}$) differences of 6%, 4%, and 3% were found between the wind field resolutions of 500 m wind field resolutions of 2700, 1500, and 900 m respectively.

In conclusion, no differences were found between the performance of the SWAN with the different resolution wind fields for the measuring locations in Lake IJssel. At other locations differences (although small) were found. However, roughness differences were small. The results indicate little influence of the wind field variability in the SWAN results.

In conclusion, the high-resolution wind fields due give a better representation of the land-water transition. Apart from this, no added value of the high-resolution wind fields was found. It was shown that the simulations using the 2700 m wind field produce more or less the same (averaged) results as the 500 m wind field while using the preprocessing method. Considering the difference in computation time (approximately a factor 6 to 8 longer) this makes it an attractive alternative.

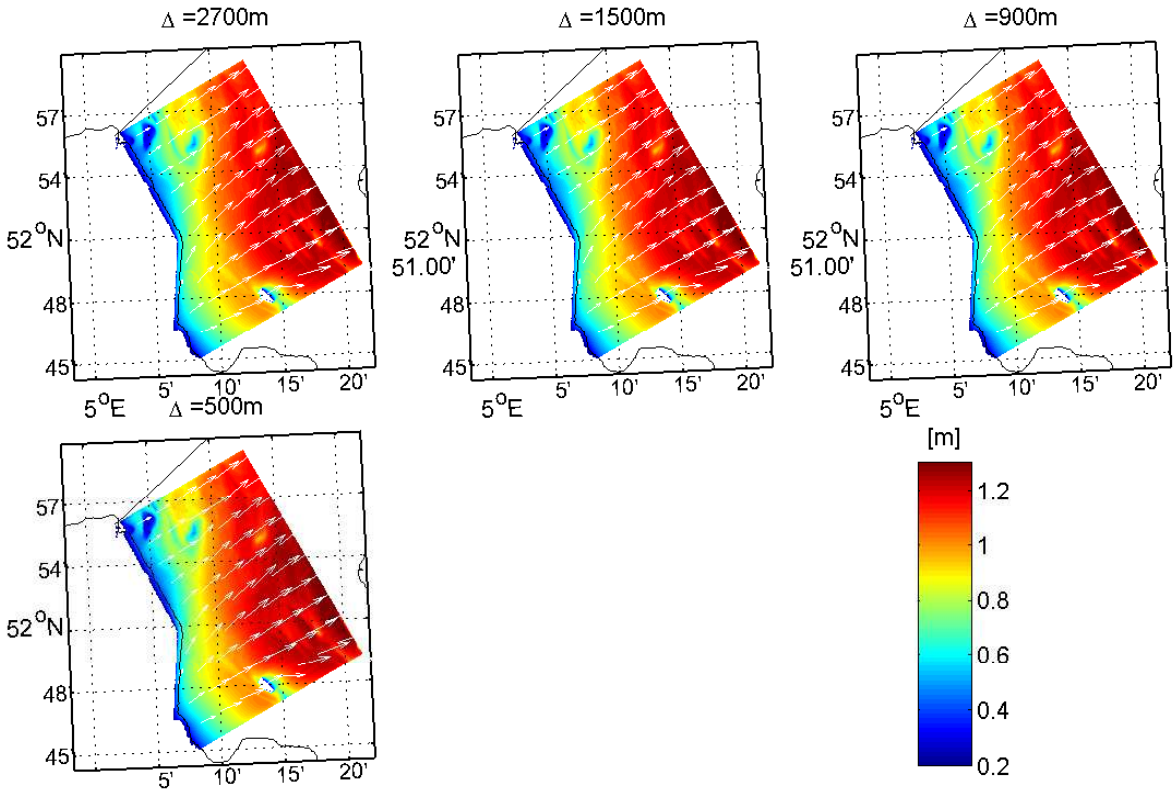

Figure 6.15: Significant wave height (H_{m0}) at December 5th, 12:00.

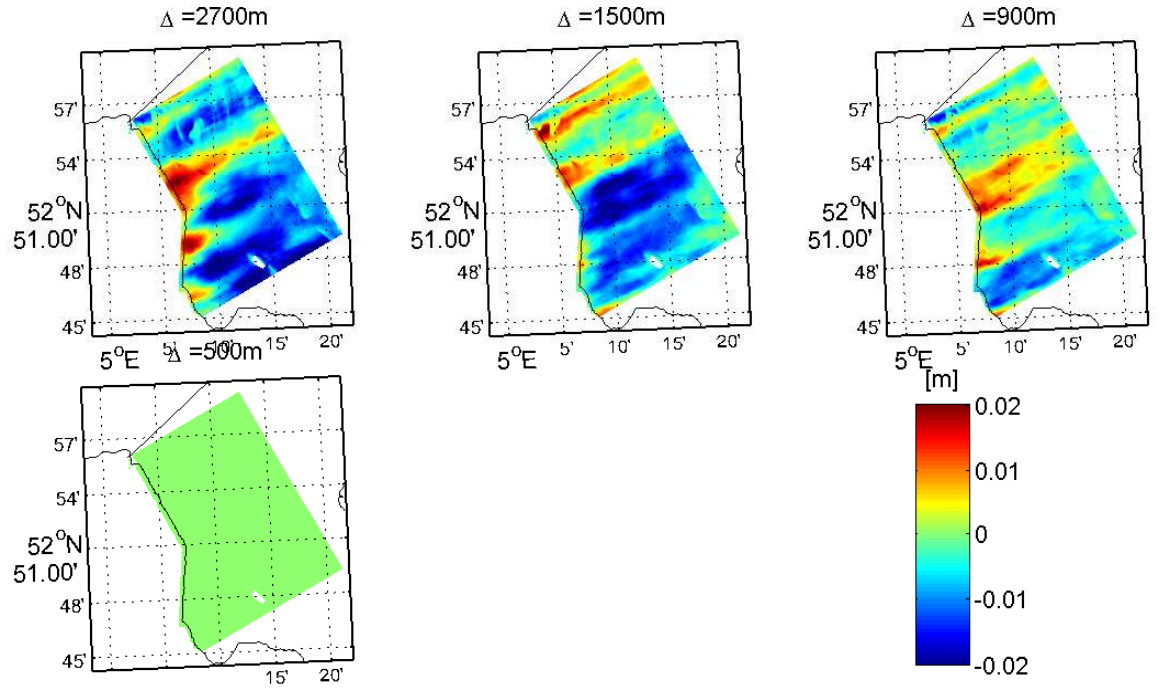

Figure 6.16: Difference in significant wave height Significant wave height (H_{m0}) at December 5th, 12:00 (Significant wave height – significant wave heigth 500-m wind field simulation).

7

CONCLUSION AND RECOMMENDATIONS

7.1. INTRODUCTION

This thesis started with the idea of improving predictions of wave characteristics using high resolutions atmospheric models. A problem that could benefit from improved wind field resolutions was found in short-fetch wave growth, investigated by Deltares [2013, 2015]. They reported that SWAN structurally under-predicted wave heights and wave periods by 15 % and 11 % for short fetches. One of their suggestions was to investigate the possibility of using high-resolution wind fields, produced by an atmospheric model, to improve these predictions. The underlying idea was that a more accurate representation of the wind field would lead to a better representation of the energy transfer from the wind to waves over the first hundreds of meters from the coast.

This study used the mesoscale NWP model WRF to investigate the possibility of simulating atmospheric processes—in particular wind—at high-resolutions. Two primary objectives were identified. First, to examine the limits of the atmospheric model (and the used parameterizations) regarding high horizontal resolutions. Second, to determine whether the higher resolution wind fields would lead to better wave prediction of SWAN for short fetches. The conclusions regarding the objective and other conclusions are treated in the first section of this chapter. Recommendations that followed from results of the research are given in the second section.

7.2. CONCLUSION

7.2.1. PERFORMANCE OF WRF FOR HIGH SPATIAL RESOLUTIONS

As part of the primary objective of the study, the possibility of using WRF at high resolutions was investigated. The first step towards an answer to this question was a theoretical approach. From literature, it was found that there are three parameterizations in the model of which the validity depends on the horizontal resolutions:

- Planetary boundary layer schemes are valid up to resolutions of ~1000 m; large eddies are sufficiently well resolved for resolutions higher than ~100 m. In between is a grey area where performance is unkown [Wyngaard, 2004].
- Cumulus parameterization schemes are valid up to resolutions of ~4000 m; convective processes are fully resolved explicitly for resolutions higher than of ~100 m. In between is a grey area where performance is unkown [Dudhia, 2014].
- Microphysics Parameterizations should contain at least six classes of hydrometeors for convection-resolving resolutions, roughly ~4000 m and higher [Dudhia, 2014].

The limitations of the planetary boundary layer scheme are the most important for this study, since these influence wind, and the other two mainly influence precipitation. Planetary boundary layers scheme can impose problems at high resolutions, mainly because turbulence will be resolved both implicitly—by the planetary boundary layer scheme—and explicitly—by resolving large eddies with the model. However, the

consequences do not have to be problematic, studies have shown good performances for resolutions higher than 1000 m [Hong and Dudhia, 2012].

During this study, the performance of WRF was tested using five different resolution grids—2700 m, 1500 m, 900 m, 500 m, 300 m. According to the theory, PBL schemes are valid up to resolutions of approximately 1000 m. Three of the simulations had resolutions within the grey area. Cumulus parameterizations were turned off for all simulations. For the 500-m resolution, the results of the uncalibrated model in terms of wind speed (around Lake IJssel; storm 1: rbias < 5%, SI ≈ 10%; storm 2: rbias 10%–20%, SI ≈ 20%) and wind direction (around Lake IJssel; storm 1: bias ≈ 3°, RMSE ≈ 10°; storm 2: bias 4°–15°, RMSE ≈ 20°) were in agreement with the measurements. The other simulations performed equally well for all resolutions regarding error statistics.

During periods of precipitation, deviations occurred in the wind field. These differences were related to the passage of fronts and precipitations. A specific event was investigated that turned out to be a convection cell. Interestingly, the simulations responded differently to the event; with increasing resolutions, higher velocities (horizontally and vertically), higher precipitation rates, and different locations for the convection cell were found. The coarser resolutions (Δx = 2700 m and Δx = 1500m) hardly showed any deviations in wind speed because of this cell, while the higher resolutions showed strong surface winds of up to 32 $\mathrm{m\,s^{-1}}$. No statements could be made about the accuracy of these predictions, but according to the theory, higher resolutions should be able ro resolve convective processes better than coarse resolutions. However, also other processes and variables are important. It was shown that also the domain size—which varied for the different resolutions—influences the triggering of convective processes.

Even though the results of the 300 m resolution are comparable to the other simulations, a numerical instability in the surface pressure was found for the second storm. It is not clear what triggered the instability, but the fact that this was only seen for the 300 m resolution and the fact that all other model parameters were equal, implies that the instability was caused as a result of the resolution. Thus, the high spatial resolution of 300 m let to numerical instabilities for the used combination of parameterization and settings.

All things considered, the results showed that the model was still able to produce results that were in agreement with observations, and simulations with other resolutions, without showing signs (in the variables: pressure, temperature, humidity, and wind) of instabilities. This suggests—in agreement with Hong and Dudhia [2012]— that the model indeed still produces reliable wind results for resolutions up to 500 m

7.2.2. PERFORMANCE OF SWAN FOR SHORT FETCHES USING HIGH-RESOLUTION WIND FIELDS

A SWAN model was set up for the Lake IJssel using calibrated settings (from WTI2011). Wind information was provided by WRF, using friction velocities. Because direct forcing of SWAN with friction velocities is not possible, an intermediate step was necessary. Pseudo wind fields were derived from the friction velocities using the inverse drag relation from SWAN. By applying these pseudo wind fields, the right friction velocities are used in the model physics of SWAN.

An analysis of the observations and the predictions shows that SWAN performed moderately well. For wind directions along the shore normal (239°N±20°), negative biases were found for the wave heights (H_{m0}; storm 1: −13%, −21% for location FL48 and FL49 respectively; storm 2: −18%, and −11% for location FL48 and FL49 respectively) and wave periods (T_{m-10}; storm 1: 10%, 7% for location FL48 and FL49 respectively; storm 2: –7%, –4% for location FL48 and FL49 respectively).

Further analysis of the data shows that both observed and predicted spectra contain more than one spectral peak during slanting fetch conditions. 2-D spectra from SWAN show that the low-frequency component is associated with the alongshore transport of wave energy and that the high-frequency peak is associated with wave energy propagating in the direction of the wind. The effects are further enhanced by the bended coastline, from where more wave energy is moving in. The qualitative agreement between the observed and predicted 1-D spectra suggest correct prediction of the situation by SWAN. If the predictions from SWAN are indeed correct, end if the measuring locations are disturbed by non-local energy, then the location might not be as useful for the assessment of wave growth as was first thought.

Additionally, interpolation of the pseudo wind field by SWAN resulted in significant deviations of the original wind field, due to interpolations across the land-water boundary. An extra preprocessing step was used in which land points were excluded from the wind field. Analysis of the results from SWAN regarding error

statistics for the different resolution wind fields showed equals performance for all resolutions. However, differences were found by comparing spatial plots. The patterns of the wind streaks were also present in the wave field; this resulted in differences up to ± 6% (0.02 m) near the coast.

7.2.3. THE ADDED VALUE OF HIGH-RESOLUTION ATMOSPHERIC MODELLING ON THE PREDICTION OF WAVE CHARACTERISTICS

In conclusion of the results of this study, it was shown that results from high-resolution simulations with WRF show more or less the same behaviour for the majority of the time. The difference for these periods were found in the wind streaks that were predicted and the better representation of the surface features (such as the land-water boundary, and land-use for the determination of the roughness).

There are still some uncertainties concerning the wind streaks since it not clear whether they are real or not. However, assuming that they are real, they would then result in local deviations of the wave characteristics; creating temporary smaller or larger wave heights. These features could for example, be used in port operations. If the aerodynamic roughness of the surrounding area is known around the port, one would be able to better predict operational time and downtime.

The higher resolution models are better capable of the capturing surface features such as the land-water boundary. This is especially interesting for small water bodies, such as rivers or harbour basins. Coarse resolutions larger than 10 km (e.g.HIRLAM) are not capable of predicting winds speeds for such small water bodies. The water fraction in the grid cell is simply too small for the model to notice it. It is shown that WRF can still function properly for horizontal resolutions of 500 m. Although this is probably still too coarse for most river and harbour basin, it is certainly an improvement.

These two examples illustrated the possible added value of the high-resolution models during calm periods. The simulations with WRF also showed that the resolution influences the convective processes in the model; this became clear from the example of the convection cell that was shown. While the coarsest resolution (Δx = 2700 and Δx = 1500) barely showed any influence of the convection cell in terms of horizontal wind speed, the higher resolutions showed a distinct gust front. This indicates that the ability of the model to correctly resolve convective processes (also squall-lines) could make a difference in operational warning systems.

7.3. RECOMMENDATIONS

7.3.1. GENERAL RECOMMENDATIONS

SWAN simulations have shown that there is alongshore and cross-shore directed energy at the measuring location FL48, and FL49 for slanting fetch conditions. The effects are enhanced by the asymmetry of the coastline. The prediction could not be confirmed since there is no directional data available. It is recommended to determine whether or not these predictions are correct. Because if this is the case, the location might not be such a good choice for studies concerning indealised wave growth.

7.3.2. MODELLING OF ATMOSPHERE

The set up of WRF used in this study was determined based on rules of thumb and literature. The influence of some settings was investigated, but this does not provide sufficient information for the best model set-up. For following studies with WRF, it is advised to investigate the influences of the different parameterizations. Especially different PBL and the surface layer parameterizations should be considered, since these are responsible for the wind in the ABL

The simulations showed a strong dependence of the wind on the local roughness. To reduce errors related to the incorrect land-use data or to increase the resolution of the land-use data, it is recommended tot use up-to-date local land-use maps in WRF.

The assessment of the stability predicted by WRF showed that there were large deviations for the water temperature in the model. It is recommended for further simulations that SSTs for inland water bodies are either updated manually or by a coupled lake model. So that no errors in the stability regime are expected.

WRF showed distinct wind streaks for all simulations, according to Kudryavtsev and Makin [1996] this is associated with stable conditions. However, surface and air temperatures were more or the less same during these simulations, suggesting neutral wind conditions. It is recommended to establish whether or not these wind streaks are real.

7.3.3. MODELLING OF WAVES

SWAN relates the wind to wave growth through the friction velocity $\boldsymbol{u}_*$. SWAN uses bulk relations to relate of $\boldsymbol{u}_*$ from to $\boldsymbol{u}_{10}$. These relations only apply for neutral conditions, moreover, while $\boldsymbol{u}_*$ is the coupling parameter in SWAN, it is not possible to use $\boldsymbol{u}_*$ directly as model input. It is also recommended to facilitate the direct use of $\boldsymbol{u}_*$ in SWAN. So that waves can also be modelled correctly during non-neutral conditions.

Moreover, the dependence of the surface roughness on the wind and the dependence of atmospheric stability on the water temperature makes coupled approaches between models an attractive option (e.g. Warner et al. [2010]). A coupled approach between wind and wave is recommended where possible.

BIBLIOGRAPHY

Wrf users page - modeling system overview, 2015. URL http://www2.mmm.ucar.edu/wrf/users/model.html. accessed: 2015-04-15.

A. Arakawa. The cumulus parameterization problem: Past, present, and future. *Journal of Climate*, volume 17(no. 13):2493–2525, July 2004.

F. Ardhuin, T.H.C. Herbers, G.Ph van Vledder, K.P. Watts, P. Jensen, and H.C. Graber. Swell and slanting-fetch effects on wind wave growth. *Journal of Physical Oceanography*, 37:908–931, 2006. doi: 10.1175/JPO3039.1.

P. Baas. Final report of wp1 of the wti2017-hb wind modelling project. KNMI Scientific Report WR 2014-02, KNMI, de Bilt, August 2014.

A.V. Babanin and V.K. Makin. Effects of wind trend and gustiness on the sea drag: Lake george study. *Journal of geophysical Research*, 113(C02015):1–18, 2008. doi: 10.1029/2007JC004233.

R. G. Barry and R.J. Chorley. *Atmosphere, Weather, and Climate*. Routledge, New York, United States, eighth edition, 2003.

Benschop. Windsnelheidsmetingen op zeestations en kuststations: herleiding waarden windsnelheid naar 10-meter niveau. Technical report TR-188, KNMI, De Bilt, The Netherlands, 1996. in Dutch.

P. Berens. Circstat: A matlab toolbox for circular statistics. *Journal of Statistical Software*, 31(11):1–21, 2009.

P. Berrisford, D. Dee, P. Poli, K. Brugge, R. Fielding, Feuntes, P. Kållberg, S. Kobayashi, S. Uppala, and A. Simmons. The era-interim archive. Technical report, European Centre for Medium Range Weather Forecasts (ECMWF), 2011.

N. Booij and H.L. Holthuijsen. *HISWA User manual*. Delft University of Technology, Delft, the Netherlands, 1985.

N. Booij, R.C. Ris, and L.H. Holthuijsen. A thrid-generation wave model for coastal regions part i model description and validation. *Journal of Geophysical Research*, vol 104(C4):7649–7666, April 1999.

M. Bottema. Measured wind-wave climatology lake ijssel (nl). Report rws riza 007.0 0, Rijkswaterstaat RIZA, 2007.

M. Bottema and G.Ph van Vledder. Effective fetch and non-linear four-wave interactions during wave growth in slanting fetch conditions. *Coastal Engineering*, 55:261–275, 2007.

C.L. Bretschneider. Revisions in wave forecasting: deep and shallow water. In *Proc. 6th Conf. Coastal Engineering*, pages 30–67, Richmond, California, US, 1958. Council on Wave Research, University of California.

W. A. Breugem and L. H. Holthuijsen. Generalized shallow water wave growth from lake george. *J. Waterway, Port, Coastal, and Ocean Engineering*, 133(3):173–182, 2007. URL http://dx.doi.org/10.1061/(ASCE)0733-950X(2007)133:3(173).

G.H. Bryan, J.C. Wyngaard, and J.M. Fritsch. Resolution requirements for the simulation of deep moist convection. *Monthly Weather Review*, vol 131:2394–2416, October 2003.

S. Caires, H. de Waal, G. Groen, N. Wever, and C. Geerse. Assessing the uncertainties of using land-based wind observations for determining extreme open-water winds. Technical report, Deltares, 2009.

F. Cassola, F. Ferrari, and A. Mazzino. Numerical simulations of mediterranean heavy percipitation events with the wrf model: A verification exercis using different approaches. *Atmospheric Research*, pages 210–225, 2015.

L. Cavaleri and P. Malanotte-Rizzoli. Wind wave prediction in shallow water: Theory and applications. *Journal of Geophysical Research: Oceans*, 86(C11):10961–10973, 1981. ISSN 2156-2202. doi: 10.1029/JC086iC11p10961. URL http://dx.doi.org/10.1029/JC086iC11p10961.

H. Charnock. Wave stress on a water surface. *Quarterly Journal of the Royal Meteorological Society*, vol 81: 639–640, 1955.

D. P. Dee, S. M. Uppala, A. J. Simmons, P. Berrisford, P. Poli, S. Kobayashi, U. Andrae, M. A. Balmaseda, G. Balsamo, P. Bauer, P. Bechtold, A. C. M. Beljaars, L. van de Berg, J. Bidlot, N. Bormann, C. Delsol, R. Dragani, M. Fuentes, A. J. Geer, L. Haimberger, S. B. Healy, H. Hersbach, E. V. Hólm, L. Isaksen, P. Kållberg, M. Köhler, M. Matricardi, A. P. McNally, B. M. Monge-Sanz, J.-J. Morcrette, B.-K. Park, C. Peubey, P. de Rosnay, C. Tavolato, J.-N. Thépaut, and F. Vitart. The era-interim reanalysis: configuration and performance of the data assimilation system. *Quarterly Journal of the Royal Meteorological Society*, 137(656):553–597, 2011. ISSN 1477-870X. doi: 10.1002/qj.828. URL http://dx.doi.org/10.1002/qj.828.

Deltares. Swan uncertainties for short fetches. Report 1207807-001-HYE-0008, Deltares, Delft, December 2013.

Deltares. Wave growth at short fetches. Report 1209433-007-hye-0010, Deltares, Delft, February 2015.

J. D'Errico. Surface fitting using gridfit. MATLAB Central File Exchange, 2010. URL http://www.mathworks.com/matlabcentral/fileexchange/8998-surface-fitting-using-gridfit. Retrieved december 17, 2015.

M. A. Donelan, B. K. Haus, N. Reul, W. J. Plant, M. Stiassnie, H. C. Graber, O. B. Brown, and E. S. Saltzman. On the limiting aerodynamic roughness of the ocean in very strong winds. *Geophysical Research Letters*, vol 31 (L18306), 2004.

M.A. Donelan. *The Sea: Ideas and Observations on Progress in the Study of the Seas*, volume Vol. 9: Ocean Engineering, chapter Air-Sea Interaction. Wiley-Intersience, 1990.

M.A. Donelan. On the dependence of sea surface roughness on wave development. *Journal of Physical Oceanography*, volume 23:2143–2149, September 1993.

Martin Dörenkämper, Michael Optis, Adam Monahan, and Gerald Steinfeld. On the offshore advection of boundary-layer structures and the influence on offshore wind conditions. *Boundary-Layer Meteorology*, 155(3):459–482, 2015. ISSN 0006-8314. doi: 10.1007/s10546-015-0008-x. URL http://dx.doi.org/10.1007/s10546-015-0008-x.

W.M. Drennan, H.C. Graber, D. Hauser, and C. Quentin. On the wave age dependence of wind stress over pure wind seas. *Journal of Geophysical Research*, vol 108(C3 8062), 2003.

J. Dudhia. Numerical study of convection observed during the winter monsoon experiment using a mesoscale two–dimensional model. *Journal of Atmospheric Science*, 46:3077–3107, 1989.

J. Dudhia. A history of mesoscale model development. *Asia-Pacific Journal of Atmospheric Sciences*, vol 50: 121–131, 2014. DOI:10.1007/s13143-014-0031-8.

J. Dudhia and W. Wang. Wrf advanced usage and best practices. Presentation Tutorial, 2014.

Dienst Weg-en Waterboukunde DWW, Rijksinstituut voor Integraal Zoetwaterbeheer en Afvalwaterbehandeling RIZA, and Rijksinstituut voor Kust en Zee RIKZ. Hydraulische randvoorwaarden primaire waterkeringen. Technical report, Ministerie van Verkeer en Waterstaat, August 2007. in dutch.

ECMWF. *IFS Documentation - Cy31r1*. ECMWF, 2007.

Y. Eldeberky. *Nonlinear Transformation of Wave Spectra in the Nearshore Zone*. Dissertation, Delft University of Technology, Delft, The Netherlands, 1996.

G.L. Gaile and J.E. Burt. *DIRECTIONAL STATISTICS*. CONCEPTS AND TECHNIQUES IN MODERN GEOGRAPHY No. 25. publisher, 1980.

M. García-Díez, J. Fernández, L. Fita, M. Menéndez, F. J. Méndez, and J.M. Gutiérrez. Using wrf to generate high resolution offshore wind climatologies. In *8º Congreso Internacional AEC*. IFCA and UC, 2012.

J.R. Garratt. Review of drag coefficients over oceans and continents. *Monthly Weather Review*, vol 105:915–929, July 1977.

J.R. Garratt. The stably stratified internal boundary layer for steady and diurnally varying offshore flow. *Boundary-Layer Meteorology*, 38(4):369–394, 1987. ISSN 0006-8314. doi: 10.1007/BF00120853. URL http://dx.doi.org/10.1007/BF00120853.

J.R. Garratt. The internal boundary layer - a review. *Boudnary Layer Meteorology*, vol 50:171–203, March 1990.

G.L. Geernaert, S.E. Larsen, and F. Hansen. Measurements of the wind stress, heat flux, and turbulence intensity during storm conditions over the north sea. *Journal of Geophysical Research*, Vol 92(C12):13127–13139, November 1987.

D. Gill and M. Pyle. Nesting in wrf. Presentation, 2012.

E.K. Gilliland and C.M. Rowe. A comparison of cumulus parameterization schemes in the wrf model. In *Proceedings of the 21th Conference on Hydrology*, San Antonio, Texas, USA, 2007.

A.A. Grachev and C.W. Fairall. Dependence of the monin-obukhov stability parameter on the bulk richardson number over the ocean. *Journal of Applied Meteorology*, 36:406–414, 1996.

J. Groeneweg, G. Burgers, S. Caires, and A. Feijt. Plan of approach sbw wind modelling. Technical Report 1202120-003, Deltares, Delft, 2011.

S.E. Gryning, E. Batchvarova, B. Brümmer, H. Jørgensen, and S. Larsen. On the extension of the wind profile over homogeneous terrain beyond the surface boundary layer. *Boundary-Layer Meteorology*, 124:251–268, 2007. doi: 10.1007/s10546-007-9166-9.

K. Hasselmann, T.P. Barnett, E. Bouws, H. Carlson, D. E. Cartwright, K. Enke, J.A. Ewing, H. Gienapp, D.E. Hasselmann, P. Kruseman, A. Meerburg, P. Muller, Olbers j., K. Richter, W. Sell, and H. Walden. Measurements of wind-wave growth and swell decay during the joint north sea wave project (JONSWAP). Technical report, Deutsches Hydrographisches Iinstitut Hambrug, 1973.

S. Hasselmann, K. Hasselmann, J.H. Allender, and T.P. Barnett. Computations and parameterizations of the nonlinear energy transfer in a gravity wave spectrum. part ii: Parameterizations of the nonlinear transfer for application in wave models. *Journal of Physical Oceanography*, 15(11):1378–1391, 1985. ISSN 0022-3670. doi: 10.1175/1520-0485(1985)015<1369:CAPOTN>2.0.CO;2. URL http://dx.doi.org/10.1175/1520-0485(1985)015<1369:CAPOTN>2.0.CO;2.

S. Hawkins. *High Resolution Reanalysis of Wind Speeds over the British Isles for Wind Energy Integration*. PhD thesis, University of Edinburgh, Edinburgh, July 2012.

D. Heinzeller, M. G. Duda, and H. Kunstmann. Towards convection-resolving, global atmospheric simulations with the model for prediction across scales (mpas) v3.1: an extreme scaling experiment. *Geoscientific Model Development*, 9(1):77–110, 2016. doi: 10.5194/gmd-9-77-2016. URL http://www.geosci-model-dev.net/9/77/2016/.

L.H. Holthuijsen. *Waves in Oceanic and Coastal Waters*. Cambridge University Press, 2007.

L.H. Holthuijsen, M.D. Powell, and J.D. Pietrzak. Wind and waves in extreme hurricanes. *Journal of Geophysical Research*, vol 117(C09003), September 2012.

S. Y. Hong, Y. Noh, and J. Dudhia. A new vertical diffusion package with an explicit treatment of entrainment processes. *Monthly Weather Review*, 134(9):2318–2341, 2006. ISSN 0027-0644. doi: 10.1175/MWR3199.1. URL http://dx.doi.org/10.1175/MWR3199.1.

S.Y. Hong and J. Dudhia. Next-generation numerical weather prediction - bridging parameterization, explicit clouds, and large eddies. *Bulletin of the American Meteorological Society*, vol 93:ES6–ES9, January 2012.

S. A. Hsu. An overwater stability criterion for the offshore and coastal dispersion model. *Boundary-Layer Meteorology*, 60(4):397–402, 1992. ISSN 1573-1472. doi: 10.1007/BF00155204. URL http://dx.doi.org/10.1007/BF00155204.

S.A. Hsu. A dynamic roughness equation and its application to wind stess determination at the air-sea interface. *Journal of Physical Oceanography*, vol 4:116–120, January 1974.

S.A. Hsu. On the correction of land-based wind measurements for oceanographic applications. In *Proceedings of the 17th Coastal Engineering Conference*, pages 708–724. ASCE, 1980.

S.A. Hsu. Correction of land-based wind data for offshore aplications: A further evaluation. *Journal of Physical Oceanography*, volume 16:390–394, February 1986.

S.A. Hsu. The relationship between the monin-obukhov stability parameter and the bulk richardson number at sea. *Journal of Geophysical Research*, 94(C6):8053–8054, 1989.

D. P. Hurdle and R. J. H. Stive. Revision of spm 1984 wave hindcast model to avoid inconsistencies in engineering applications. *Coastal Engineering*, 12:339–351, 1989.

P.A. Hwang. A note on the ocean surface roughness spectrum. *Journal of Atmospheric and Oceanic Technology*, vol 28:436–443, March 2011.

Z. Janjic, R. Gall, and M.E. Pyle. Scientific documentation for the nmm solver. Technical report, National Center for Atmospheric Research, Boulder, Colorado, USA, Februari 2010.

Z.L. Janjic. The step–mountain eta coordinate model: Further developments of the convection, viscous sublayer, and turbulence closure schemes. *Monthly Weather Review*, 117:231–257, 1994.

P.A. Jimenez, J. Dudhia, J.F. Gonzalez–Rouco, J. Navarro, J.P. Montavez, and E. Garcia–Bustamante. A revised scheme for the wrf surface layer formulation. *Monthly Weather Review*, 140:898–918, 2012.

K.K. Kahma and C.J. Calkoen. Reconciling discrepancies in the observed growth of wind-generated waves. *Journal of Physical Oceanography*, volume 22:1389–1405, December 1992a.

K.K. Kahma and C.J. Calkoen. Reconciling discrepancies in the observed growth of wind-generated waves,. *Journal of Physical Oceanography*, 22(12):1389–1405, 1992b.

J.S. Kain. The kain–fritsch convective parameterization: An update. *Journal of Applied Meteorology*, 43:170–181, 2003.

Kitaigorodskii. Applications of the theory of similarity to the analysis of wind generated wave motion as stochastic process. *Izvestia Academy of Sciences,USSR, Geophysics Series*, pages 106–117, 1962. [English edition translated and published by the American Geophysical Union of the National Academy of Sciences, April, 1962, 73–80.

M.A. Kleczek, G.J. Steeneveld, and A.M. Holtslag. Evaluation of the weather research and forecasting mesoscale model for gabls3: Impact of boundary-layer schemes, boundary conditions and spin-up. *Boundary-Layer Meteorology*, 152:213–243, 2014. doi: 10.1007/s10546-014-9925-3.

J.B. Klemp, W.C. Skamarock, and J. Dudhia. Conservative split-explicit time integration methods for the compressible nonhydrostatic equations. *Mon. Wea. Rev.*, 135(2897–2913), 2007. URL http://dx.doi.org/10.1175/MWR3440.1.

KNMI. Handbook for the meteorological observation. Technical report, KNMI, July 2001. in Dutch, chapter 1–6 are available in English.

G.J. Komen, L. Cavaleri, M. Donelan, K. Hasselmann, S. Hasselmann, and P.A.E.M. Janssen. *Dynamics and Modeling of Ocean Waves*. Cambridge University Press, August 1996.

V.N. Kudryavtsev and V.K. Makin. Transformation of wind in the coastal zone. Scientific Report WR 96-04, KNMI, de Bilt, 1996.

V.N. Kudryavtsev, V.K. Makin, A.M.G. Klein Tank, and J.W. Verkaik. A model of wind transformation over water-land surfaces. Scientific Report WR-2000-01, KNMI, March 2000.

J. Lo, N. Al-Madani, M.A. Tayfun, and D. Al-Ajmi. Estimation of winds over the sea from land-based measurements. *Ocean Engineering*, volume 21(No. 7):607–628, 1994.

N. Maat, C. Kraan, and W.A. Oost. The roughness of wind waves. *Boundary Layer Meteorology*, vol 54:89–103, 1991.

V.K. Makin. A note on the drag of the sea surface at hurricane winds. *Boudnary Layer Meteorology*, vol 115: 169–176, April 2005.

J. Miles. On the generation of surface waves by shear flows. *Journal of Fluid Mechanics*, vol 3:185–204, November 1957.

. J. Mlawer, S.J. Taubman, P.D. Brown, M.J. Iacono, and S.A. Clough. Radiative transfer for inhomogeneous atmospheres: Rrtm, a validated correlated–k model for the longwave. *Journal of Geophysical Research*, 102: 16663–16682, 1997.

MMM and NCAR. *ARW Version 3 Modeling System User's Guide*. Mesoscale & Microscale Meteorology Division and National Center for Atmospheric Research, January 2015.

A.S. Monin and A.M. Obukhov. Basic laws of turbulent mixing in the surface layer of the atmosphere. *Contrib. Geophys. Inst. Acad. Sci*, 151:163–187, 1954. in Russian.

NASA and NGA. Shuttle radar topography mission - the mission to map the world, 2015. URL `http://www2.jpl.nasa.gov/srtm/contact.htm`.

G.D. Nastrom and K.S. Gage. A climatology of atmospheric wavenumber spectra of wind and temperature observed by commercial aircraft. *Journal of Atmospheric Science*, 42:950–960, 1985. URL `http://dx.doi.org/10.1175/1520-0469(1985)042<0950:ACOAWS>2.0.CO;2`.

National Centers for Environmental Prediction NCEP, National Weather Service, NOAA, and U.S. Department of Commerce. Ncep fnl operational model global tropospheric analyses, continuing from july 1999, 2000. URL `http://dx.doi.org/10.5065/D6M043C6`.

A. M. Obukhov. Turbulence in an atmosphere with a non-uniform temperature. *Boundary-Layer Meteorology*, 2(1):7–29, 1971. ISSN 1573-1472. doi: 10.1007/BF00718085. URL `http://dx.doi.org/10.1007/BF00718085`.

M. Olabarrieta, J.C. Warner, B. Armstrong, J.B. Zambon, and R. He. Ocean–atmosphere dynamics during hurricane ida and nor'ida: An application of the coupled ocean–atmosphere–wave–sediment transport (coawst) modeling system. *Ocean Modeling*, 43–44:112–137, 2012.

W.A. Oost, G.J. Komen, C.M.J. Jacobs, and C. van Oort. New evidence for a relation between wind stress and wave age from measurements during asgamage. *Boundary-Layer Meteorology*, vol 103:409–438, 2002.

K. Ooyama. A thermodynamic foundation for modeling the moist atmosphere. *J. Atmos. Sci.*, 47:2580–2593, 1990. doi: http://dx.doi.org/10.1175/1520-0469(1990)047<2580:ATFFMT>2.0.CO;2.

C.A. Paulson. The mathematical representation of wind speed and temperature profiles in the unstable atmospheric surface layer. *Journal of Applied Meteorology*, 9:857–861, December 1970.

W. Perrie and B. Toulany. Relating friction velocity to spectral parameters. *Journal of Physical Oceanography*, 25:266–279, 1995.

H. Pettersson. *Wave Growth in a Narrow Bay*. PhD thesis, Finnish Institute of Marine Research, Helsinki, Finland, 2004.

O. M. Phillips. On the generation of waves by turbulent wind. *Journal of Fluid Mechanics*, 2:417–445, 7 1957. ISSN 1469-7645.

M.D. Powell, P.J. Vickery, and T.A. Reinhold. Reduced drag coefficient for high wind speeds in tropical cyclones. *Nature*, vol 422:279–283, March 2003.

D.A. Randall, M.F. Khairoutdinov, A. Arakawa, and W.W. W. W. Grabowski. Breaking the cloud parameterization deadlock. Bulletin of the American Meteorological Society, 2003.

P.J. Rasch, editor. *Climate Change Modeling Methodology*. Springer Science+Business Media, New York, 2012. ISBN 978-1-4614-5766-4.

E. Rogers, T. Black, B. Ferrier, Y. Lin, D. Parrish, and G. DiMego. Changes to the ncep meso eta analysis and forecast system: Increase in resolution, new cloud microphysics, modified precipitation assimilation, modified 3dvar analysis. Web document, 2012. URL `http://www.emc.ncep.noaa.gov/mmb/mmbpll/eta12tpb/`.

W.C. Rooy and K. Kok. A combined physical–statistical approach for the downscaling of model wind speed. *WEATHER AND FORECASTING*, 19:485–495, June 2004.

A. Sathe and W. Bierbooms. Influence of different wind profiles due to varying atmospheric stability on the fatigue life of wind turbines,. *Journal of Physics*, 75(012056), 2007. doi: 10.1088/1742-6596/75/1/012056.

W.C. Skamarock. Evaluating mesoscale nwp models using kinetic energy spectra. *Monthly Weather Review*, 132:3019–3031, December 2004.

W.C. Skamarock, J.B. Klemp, J. Dudhia, D.O. Gill, D.M. Barker, X. Huang, W. Wang, and J.G. Powers. A description of the advanced research wrf version 3. Technical report, National Center for Atmospheric Research, Boulder, Colorado, USA, June 2008.

S.D. Smith. Wind stress and heat flux over the ocean in gale force winds. *Journal of Physical Oceanography*, vol 10:709–726, May 1980.

S.D. Smith, R.J. Anderson, W.A. Oost, C. Kraan, N. Maat, J. Decosmo, K.B. Katsaros, K.L. Davidson, K. Bumke, L. Hasse, and H.M. Chadwick. Sea surface wind stress and drag coefficients: The hexos results. *Boundary Layer Meteorology*, vol 60:109–142, 1992.

R.L. Snyder, F.W. Dobson, J.A. Elliott, and R.B. Long. Array measurement of atmospheric pressure fluctuations above surface gravity waves. *Journal of Fluid Mechanics*, 102:1–59, 1981.

American Meteorologiacal Society. Meteorology glossary. `http://glossary.ametsoc.org/wiki/Main_Page`, 2015. accessed 2015-03-23.

R.B. Stull. *An Introduction to Boundary Layer Meteorology*. Number ISBN 978-94-009-3027-8. Kluwer Academic Publishers, Dordrecht, July 1988.

SVSD. Stormvloedflits 2012-01 west-zuidwesterstorm veroorzaakt hoge waterstanden langs de kust. Stormvloedflits, Stormvloedwaarschuwingsdienst/SVSD, Lelystad, January 2012a. in dutch.

SVSD. Stormvloedflits 2012-02 west-zuidwesterstorm veroorzaakt hoge waterstanden langs de kust. Stormvloedflits, Stormvloedwaarschuwingsdienst/SVSD, Lelystad, January 2012b. in dutch.

SVSD. Stormvloedflits 2013-07 sinterklaasstorm veroorzaakt zeer hoge waterstanden langs de kust. Stormvloedflits, Stormvloedwaarschuwingsdienst/SVSD, Lelystad, December 2013. in dutch.

SWAN team. Swan scientific and technical documentation - swan cycle iii version 40.72abcde. Technical report, Delft University of Technology, 2009a.

SWAN team. Swan user manual - swan cycle iii version 40.72abcde. Technical report, Delft University of Technology, 2009b.

Technische Adviescommissie voor de Waterkeringen TAW. Leidraad voor het ontwerp van rivierdijken; deel 1 - bovenrivierengebied. Technical report, Technische Adviescommissie voor de Waterkeringen, 1985.

P.A. Taylor and R.J. Lee. Simple guidlines for estimating wind speed variations due to small schale topographic features. *Climatological Bulletin*, volume 18:3–32, 1984.

P.K. Taylor and M.J. Yelland. The dependence of sea surface roughness on the height and steepness of the waves. *Journal of Geophysical Research*, vol 31:572–590, February 2000.

M.F. Tewari, F. Chen, W. Wang, J. Dudhia, M.A.. LeMone, K. Mitchell, M. Ek, G. Gayno, J. Wegiel, and R.H. Cuenca.

The MathWorks Inc. Matlab release 2014a, February 2014.

W. Uijttewaal. Turbulence in hydraulics. Lecture notes CT5312, 2014.

H. van der Brink, P. Baas, and G. Burgers. Towards an approved model set-up for harmonie contribution to wp 1 of the sbw-hb wind modelling project. Technical report, KNMI, 2013.

A.J. van der Westhuysen, M. Zijlema, and J.A. Battjes. Nonlinear saturation-based whitecapping dissipation in {SWAN} for deep and shallow water. *Coastal Engineering*, 54(2):151–170, 2007. ISSN 0378-3839. doi: http://dx.doi.org/10.1016/j.coastaleng.2006.08.006. URL `http://www.sciencedirect.com/science/article/pii/S037838390600127X`.

André J. van der Westhuysen. Modeling of depth-induced wave breaking under finite depth wave growth conditions. *Journal of Geophysical Research: Oceans*, 115(C1):n/a–n/a, 2010. ISSN 2156-2202. doi: 10.1029/2009JC005433. URL `http://dx.doi.org/10.1029/2009JC005433`. C01008.

G. Ph. van Vledder and F. Enet. Detaillering golfrandvoorwaarden nieuwe zeesluis ijmuiden. Technical report, BMT ARGOSS, November 2014.

A. Venkatram. A model of internal boundary-layer development. *Boundary-Layer Meteorology*, 11(4):419–437, 1977. ISSN 0006-8314. doi: 10.1007/BF02185869. URL `http://dx.doi.org/10.1007/BF02185869`.

H.J. Verhagen and B. Savov. Sea breeze generated waves on the coast of varna. In *2nd International Conference Port Development and Coastal Environment: PDCE 2000, 5-7 June 2000, Varna, Bulgaria*. Black Sea Coastal Association, 2000.

J.W. Verkaik. Evaluation of two gustiness models for exposure correction calculations. *Journal Applied Meteorology*, 39:1613–1626, 2000. doi: http://dx.doi.org/10.1175/1520-0450(2000)039<1613:EOTGMF>2.0.CO;2.

WAMDI Group. The wam model—a third generation ocean wave prediction model. *Journal of Physical Oceanography*, 18:1775–1810, 1988.

W. Wang. Considerations for designing an numerical experiment. Presentation, January 2015.

W. Wang and N.L. Seaman. A comparison study of convective parameterization schemes in a mesoscale model. *Monthtly Weather Review*, volume 125:252–277, February 1997.

J.C. Warner, B. Armstrong, R. He, and J.B. Zambon. Development of a coupled ocean–atmosphere–wave–sediment transport (coawst) modeling system. *Ocean Modeling*, vol 35: 230–244, July 2010.

T.T. Warner. Quality assurance in atmospheric modeling. *American Meteorological Society*, pages 1601–1610, December 2011. doi: 10.1175/BAMS-D-11-00054.1.

M.L. Weisman, W.C. Skamarock, and J.B. Klemp. The resolution dependence of explicitly modeled convective systems. *Monthtly Weather Review*, volume 125:527–548, April 1997.

J. Wieringa and P.J. Rijkoort. *Windklimaat van Nederland.* Number ISBN 90 12 044669. Staatsdrukkerij, 's-Gravenhage, 1983.

World Meteorological Organization WMO. Guide to wave analysis and forecasting. Technical Report WMO-No. 702, World Meteorological Organization, 1998.

World Meteorological Organization WMO. Guide to meteorological instruments and methods of observation. Technical Report 8, institution, 2008.

J. Wu. Froude number scaling of wind-stress coeficients. *Journal of Atmospheric Sciences*, vol 26:408–413, May 1969.

J. Wu. Wind-stress coefficients over sea surface near nutral conditions – a revisit. *Journal of Physical Oceanography*, vol 10(C12):9704–9706, November 1980.

J. Wu. Wind-stress coefficients over sea surface from breeze to hurricane. *Journal of Geophysical Research*, vol 87:727–740, May 1982.

J.C. Wyngaard. Toward numerical modeling in the "terra incognita". *Journal of Atmospheric Sciences*, volume 61:1816–1826, July 2004.

L. Yan. An improved wind input source term for third generation ocean wave modelling. Scientific report WR 87-8, Koninklijk Nederlands Meteorologisch Instituut (KNMI), De Bilt, 1987.

I.R. Young. An experimental investigation of the role of atmospheric stability in wind wave growth. *Coastal Engineering*, 34:23–33, 1998.

M. Zijlema, G.Ph. van Vledder, and L.H. Holthuijsen. Bottom friction and wind drag for wave models. *Coastal Engineering*, vol 66:19–26, 2012.

N.C. Zweers, V.K. Makin, J.W. de Vries, and G. Burgers. A sea drag relation for hurricane wind speeds. *Geophysical Research Letters*, vol 37(L21811), 2010.

A

METEOROLOGICAL PARAMETERS

Many parameters used in meteorology are not encountered on a daily basis by the average civil/ hydraulic engineer. This appendix is included to provide a quick reference on the meteorological parameters used in this report.

Potential temperature Potential temperature is the temperature a parcel of air will have if raised or lowered adiabatically to a certain reference height (often 100 hPa). The potential temperature is defined as [Stull, 1988]:

$$\theta = T\left(\frac{P_0}{P}\right)^{R/C_p} \tag{A.1}$$

in which:

θ	Potential temperature	[°K]
T	Absolute temperature	[°K]
P_0	Pressure at reference level (usually 100 hPa)	[hPa]
P	Pressure	[hPa]
R	Gas constant of dry air (= 287.04)	[J mol^{-1} K^{-1}]
C_p	Specific heat capacity of dry air at a constant pressure (=1004.67)	[J kg^{-1} K^{-1}]

Virtual temperature Virtual temperature is the temperature dry air would need to have in order to have de same density as moist air. According to Stull [1988]:

$$T_v = T\,(1 + 0.61\,r_{sat} - r_L) \tag{A.2}$$

in which:

T_v	Virtual temperature	[°K]
T	Absolute temperature	[°K]
r_{sat}	Saturated air mixing ratio	[g g^{-1}]
r_L	Liquid water mixing ratio	[g g^{-1}]

The formulation can be used analogously to potential temperature.

Equivalent potential temperature Equivalent potential temperature (often referred to as theta-e) is the temperature an air parcel will have if all of its water vapor is condensed (releasing all the latent heat), and if the parcel is raised or lowered adiabatically to a certain reference height (often 100 hPa). The equivalent potential temperature can be approximated with [Stull, 1988]:

$$\theta_e = \theta + \left(\frac{L_v \theta}{C_p T}\right) r \tag{A.3}$$

in which:

θ_e	Equivalent potential temperature	[°K]
θ	Potential temperature	[°K]
T	Absolute temperature	[°K]
L_v	latent heat of vaporization water	[J kg^{-1}]
C_p	Specific heat capacity of dry air at a constant pressure (=1004.67)	[J kg^{-1} K^{-1}]

Relative Humidity The relative humidity is a measure for the humidity of the atmosphere and is defined as the ratio of the vapour pressure to the saturation vapour pressure with respect to water. [Society, 2015]

$$RH = \frac{W}{WS}100\%$$

in which:

W	Vapour pressure	[Pa]
Ws	Potential temperature	[Pa]

Specific Humidity The specific humidity is a measure for the humidity of the atmosphere and ratio of the mass of water vapor to the total mass of the system. [Society, 2015]

$$q = \frac{r_v}{1 + r_v}100\%$$

in which:

r_v	mixing ratio	[g/g]

B

MODEL DESCRIPTION WRF

This Appendix provides a short overview of the WRF model. The information is based on the theory described in Skamarock et al. [2008] and Janjic et al. [2010]. For a more extensive description of the presented theory the reader is referred to original documents.

The Weather Research and Forecasting model (WRF) is an mesoscale numerical weather prediction system designed for both research and operational purposes. The development of WRF was initiated in the 1990's in a collaboration between National Center for Atmospheric Research (NCAR), the National Oceanic and Atmospheric Administration (represented by the National Centers for Environmental Prediction (NCEP) and the (then) Forecast Systems Laboratory (FSL)), the Air Force Weather Agency (AFWA), the Naval Research Laboratory, the University of Oklahoma, and the Federal Aviation Administration (FAA). Some of the applications for which WRF is used are:

- Meteorological investigations
- Real-time NWP
- Idealized atmospheric simulations
- Data assimilation studies and development
- Coupling with other earth system models

The model consists of two dynamical cores; the Advanced Research WRF (ARW) developed by MMM Division of NCAR [Skamarock et al., 2008], and the Nonhydrostatic Mesoscale Model (NMM) developed by The NOAA/NCEP and the Developmental Testbed Center (DTC) [Janjic et al., 2010]. The main differences between these cores are the grid definition and the integration method, also see Table B.1. The NMM is primarily used for operational weather forecasting, and the ARW is also used for research purposes. ARW also provides the opportunity to study idealized cases, which is not possible with NMM. This study will use the ARW core of WRF. Therefore, the remainder of this section will only discuss the features of ARW. A schematic overview of the model components is given in Figure B.1.

Table B.1: Main differences between two dynamical cores (ARW and NMM)in WRF

ARW	NMM
Terrain following hydrostatic-pressure vertical coordinate system	Sigma coordinate system
Arakawa C-grid	Arakawa E-grid
3rd order Runge-Kutta time-split differencing	Adams-Bashforth time differencing, time splitting
Conservation of mass, momentum, and scalars using fifth and sixth order spatial differencing	Conservation of kinetic energy, enstrophy, and momentum using second order spatial differencing equation

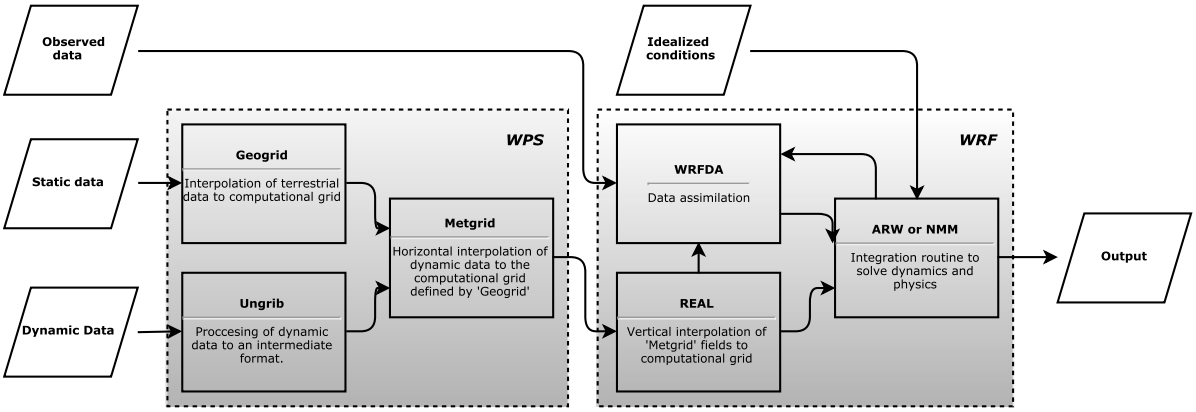

Figure B.1: Schematic overview of the WRF model, adapted from UCA [2015]

B.1. INITIAL AND BOUNDARY CONDITIONS

WRF can be used for the simulation of both real and idealized cases. For the simulation of idealized situations, WRF comes with a number of test cases that can be modified to construct a desired ideal case. The boundary conditions available for idealized simulations are:

- periodic lateral boundary conditions
- open lateral boundary conditions (absorbing)
- symmetric lateral boundary conditions
- specific lateral boundary conditions
- polar boundary conditions (when using a polar coordinate system in polar regions)

For the real-case simulations, a separate soft package is available to generate initial and lateral boundary conditions, the WRF Prepossessing System (WPS). WPS consists of three independent programs:

- Geogrid: used to construct the computational domain, and to interpolate static terrestrial data to the computational grid. The terrestrial data includes soil categories, land use category, terrain height, annual mean deep soil temperature, monthly vegetation fraction, monthly albedo and maximum snow albedo.
- Ungrib: responsible for the translation of different formats, variables, and data sets of time-varying meteorological fields to an intermediate format that can be read by the Metgrid.
- Metgrid: interpolates the time-varying meteorological data horizontally to the computational grid. It also combines the static data and the time-varying data in one file that can be read by WRF.

B.2. DOMAIN AND DISCRETIZATION

Domains in WRF can be made using four types of projections: the Lambert conformal, polar stereographic, Mercator, and latitude-longitude projections. In order to increase resolutions on a local scale, WRF provides a nesting option (one-way and two-way).

The domain is discretized horizontally using a staggered Arakawa C-grid. Velocity components of the wind are staggered one-half grid length from thermodynamic (and other scalar) variables. Vertically, terrain following η-coordinates are used. These are defined as:

$$\eta = \frac{p_{dh} - p_{dht}}{\mu_d} \tag{B.1}$$

where p_{dh} is the hydrostatic component of the pressure for dry air; μ_d is defined as $\mu_d = p_{dhs} - p_{dht}$, and represents the mass per unit area; and p_{dhs} and p_{dht} refer to hydrostatic pressure components for dry air along the surface and top boundaries, respectively. Again, velocity components are staggered one-half grid length from thermodynamic (and other scalar) variables. The staggered grid is illustrated in Figure B.2.

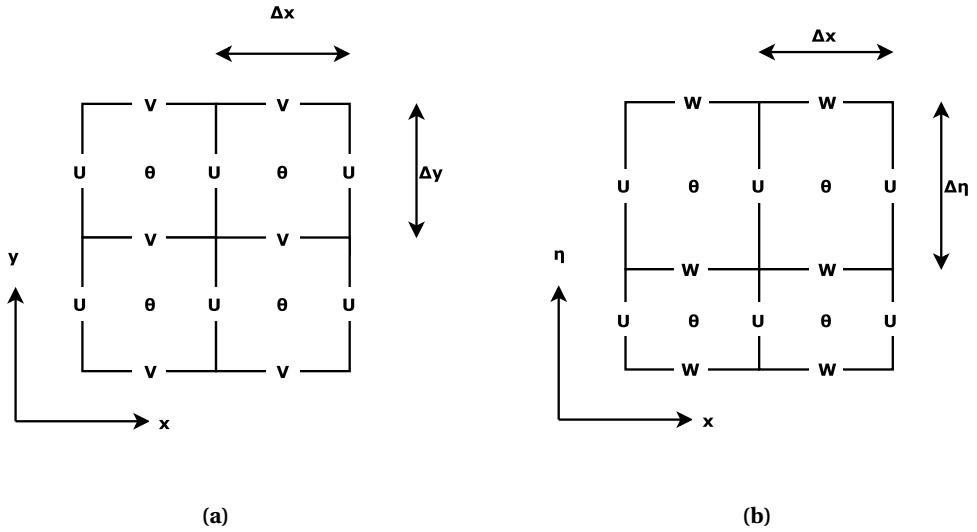

Figure B.2: Horizontal (a) and vertical (b) grids in ARW

B.3. PRIMITIVE EQUATIONS

The dynamical core of ARW integrates the compressible non-hydrostatic moist Euler equations following the philosophy of Ooyama [1990]. The moist Euler equations differ from the regular Euler equations in the treatment of moisture in the atmosphere. The density of air (ρ) is divided into three components, representing the density of dry air (ρ_d), the density of water vapour in air (ρ_v), and the density of water condensate in air (ρ_c):

$$\rho = \rho_d + \rho_v + \rho_c \tag{B.2}$$

The set of equations consists of prognostic equations for the conservation of mass, momentum, and energy [Skamarock et al., 2008]:

Conservation of mass (continuity)

$$\frac{\partial \mu_d}{\partial t} + \frac{\partial (\mu_d u)}{\partial x} + \frac{\partial (\mu_d v)}{\partial y} + \frac{\partial (\mu_d w)}{\partial z} = 0 \tag{B.3}$$

$$\frac{\partial (\mu_d q_m)}{\partial t} + \frac{\partial (\mu_d u q_m)}{\partial x} + \frac{\partial (\mu_d v q_m)}{\partial y} + \frac{\partial (\mu_d d w q_m)}{\partial z} = F_{q_m} \tag{B.4}$$

Conservation of momentum (equations of motion)

$$\frac{\partial (\mu_d u)}{\partial t} + \frac{\partial (\mu_d u^2)}{\partial x} + \frac{\partial (\mu_d uv)}{\partial y} + \frac{\partial (\mu_d uw)}{\partial z} + \mu_d \alpha \frac{\partial p}{\partial x} + \frac{\alpha}{\alpha_d}\frac{\partial p}{\partial \eta}\frac{\partial (\phi)}{\partial x} = F_u, \tag{B.5}$$

$$\frac{\partial (\mu_d v)}{\partial t} + \frac{\partial (\mu_d uv)}{\partial x} + \frac{\partial (\mu_d v^2)}{\partial y} + \frac{\partial (\mu_d vw)}{\partial z} + \mu_d \alpha \frac{\partial p}{\partial y} + \frac{\alpha}{\alpha_d}\frac{\partial p}{\partial \eta}\frac{\partial (\phi)}{\partial y} = F_v, \tag{B.6}$$

$$\frac{\partial (\mu_d w)}{\partial t} + \frac{\partial (\mu_d uw)}{\partial x} + \frac{\partial (\mu_d vw)}{\partial y} + \frac{\partial (\mu_d w^2)}{\partial z} - g\left[\frac{\alpha}{\alpha_d}\frac{\partial p}{\partial \eta} - \mu_d\right] = F_w \tag{B.7}$$

Conservation of energy (first law thermodynamics)

$$\frac{\partial (\mu_d \theta)}{\partial t} + \frac{\partial (\mu_d u\theta)}{\partial x} + \frac{\partial (\mu_d v\theta)}{\partial y} + \frac{\partial (\mu_d w\theta)}{\partial z} = F_\theta \tag{B.8}$$

in which q is the mixing ratio of moisture in the air, $\alpha_d = 1/\rho_d$ is the inverse density of dry air and $\alpha = 1/\rho$ the inverse density of air. F_u, F_v, F_w, F_θ represent forcing terms arising from model physics, turbulent mixing, spherical projections, and the earth's rotation. Together with the material derivative of the geopotential (Equation B.9), and diagnostic relations for the inverse density (Equation B.10) and pressure (Equation B.11) (equation of state) all variables can be solved.

$$\frac{\partial(\phi)}{\partial t} + \frac{1}{\mu_d}\frac{\partial(\mu_d u\phi)}{\partial x} + \frac{1}{\mu_d}\frac{\partial(\mu_d v\phi)}{\partial y} + \frac{1}{\mu_d}\frac{\partial(\mu_d w\phi)}{\partial z} - \frac{1}{\mu_d} g\mu w = 0 \tag{B.9}$$

Diagnostic relation for inverse density

$$\frac{\partial(\phi)}{\partial \eta} = -\alpha\mu \tag{B.10}$$

Equation of state

$$p = p_0\left(\frac{R_d\theta}{p_0\alpha}\right)^\gamma \tag{B.11}$$

in which R is the gas constant, and $\gamma = c_p/c_v = 1.4$ is the ratio of the heat capacities for dry air.

B.4. NUMERICAL TECHNIQUES

In ARW the time integration is split in two parts. The first part consists of the integration of the low-frequency modes with a third order Runge-Kutta scheme. The second part consists of high-frequency acoustic modes. These are not relevant for the meteorological purpose of the model, but do affect the overall stability. The high-frequency acoustic modes are integrated horizontally using a forward-backward time integration, and vertically using an implicit scheme. The whole routine is described in Klemp et al. [2007].

Spatially, the advection terms can be integrated using 2nd tot 6th order differencing schemes. The even-ordered schemes are spatially centred, and the odd-ordered schemes are upwind-biased, making them diffusive. A extensive description of the schemes is found in Skamarock et al. [2008].

B.5. TURBULENT MIXING

Turbulent mixing in WRF is accounted for using a first-order closure scheme, e.q.:

$$\overline{u'w'} = -K\frac{\partial u}{\partial z} \tag{B.12}$$

where K represents the turbulent eddy viscosity. The eddy viscosities can be determined in four different way:

- User specified constant values for K_h (horizontally) and K_v (vertically).
- 2-D Smagorinsky closure (only for the horizontal directions)
- 3-D Smagorinsky closure
- Prognotic TKE closure

The second method requires a PBL scheme for the vertical mixing. The third and the fourth methods are selected for LES simulations, and require the PBL scheme to be turned off.

B.6. PHYSICS

WRF uses several physics parameterizations. For each type of parameterization, several options are available, varying from simple models to more advanced models. A basic description of the parameterizations is given here, but for specific schemes the reader is referred to Skamarock et al. [2008].

- Microphysics: The microphysics parameterization scheme describes cloud and precipitation processes. This includes phase changes of moisture and the associated latent heat transport, evolution and interaction of water and ice particle, and fall-out of precipitating particles.

- Cumulus parameterization: the cumulus parameterization is responsible for the sub-grid scale effects of vertical latent-heat driven transport by updrafts and downdrafts within convective clouds (sometimes also shallow clouds).
- Surface Layer: the surface layer determines friction velocities and exchange coefficients that are used in the land-surface models and planetary boundary layer scheme for the determinations of the surface fluxes. Except for water surfaces, where the scheme calculates the fluxes itself.
- Land-Surface Model: the land-surface models used information, from all other physics parameterizations to determine surface fluxes.
- Planetary Boundary Layer: the planetary boundary layer parameterization accounts for vertical subgrid-scale fluxes due to transport by turbulent eddies in the whole atmospheric column (not only in the boundary layer).
- Atmospheric Radiation: the radiation parameterization handles heating of the atmosphere, and soil layers due to short and long wave radiation.

C

MODEL DESCRIPTION SWAN

This Appendix provides a short overview of the SWAN model [Booij et al., 1999] based on the description by SWAN team [2009a,b]. SWAN is a fully spectral third-generation wave model developed at the Delft University of Technology that is specifically designed for coastal applications. It is widely used for wave research and consultancy by scientists and engineers. A qualitative description of the model and its components is given. It is not intended to provide a full overview of all the possible options and methods in the model. For more details regarding the background of SWAN the reader is referred to SWAN team [2009a].

The model solves the wave action balance equation, incorporating state-of-the-art formulations for the deep water processes of wave generation, dissipation and the quadruplet wave-wave interactions. Specific shallow water formulations are used for dissipation due to bottom friction, triad wave-wave interactions and depth-induced breaking. By using implicit numerical schemes, SWAN is able to resolve evolution of the wave spectrum over a variety of spatial scales ranging from deep water to the surf zone.

C.1. ACTION BALANCE EQUATION

SWAN computation are carried out using either the stationary or the non-stationary mode. The core of the model is the wave action balance equation. Because the model accounts for wave-current interactions, a wave action ($N(\sigma,\theta) = E(\sigma,\theta)/\sigma$) balance is used rather than the wave energy (E) balance. The wave action balance is given for Cartesian coordinates by [Booij et al., 1999]:

$$\frac{\partial N}{\partial t} + \frac{\partial \left(c_{g;x} N\right)}{\partial x} + \frac{\partial \left(c_{g;y} N\right)}{\partial y} + \frac{\partial \left(c_\theta N\right)}{\partial \theta} + \frac{\partial \left(c_\sigma N\right)}{\partial \sigma} = \frac{S_{\text{tot}}}{\sigma} \tag{C.1}$$

where σ is the relative frequency ($\sigma = \omega - \boldsymbol{k} \cdot \boldsymbol{u}$), ω is the absolute frequency, and S_{tot} is the source term that represents the generation, dissipation, and redistribution of wave energy by physical processes. SWAN solves the whole wave action balance equation for non-stationary computations, for stationary computations the first term—representing the changed of wave action in time—is set to zero. Physical processes that are included in SWAN are the input of energy by the wind; dissipation by whitecapping, bottom friction and depth-induced breaking; and the redistribution of energy by non-linear wave-wave interactions. Different parameterizations are available in SWAN for these source terms.

C.2. NUMERICAL TECHNIQUES

The action balance equation is discretized using the finite differences method. The time derivative of the equation is discretized with the implicit Euler technique. For the spatial derivatives, three upwind schemes are available: first order upwind (resulting in BSBT), SORDUP, and the Stelling and Leendertse scheme. The first order upwind scheme is fully monotone, but give considerable numerical diffusion. The SORDUP scheme an alternative that is used for stationary computations that give less numerical diffusion. The alternative for non-stationary computations is the Stelling and Leendertse scheme. For the discretisation in spectral space a hybrid central/upwind scheme is used.

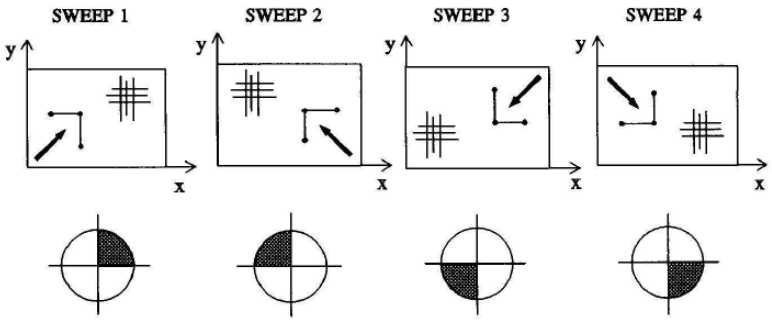

Figure C.1: The solution procedure for wave energy propagation in geographical space with the appropriate directional quadrant (indicated by shaded area) for each of four sweeps. Figure reproduced from SWAN team [2009a]

Upwind schemes can only handle the transport of energy in a specific direction. In order to predict the transport of energy in all directions, the directional space needs to be decomposed into four quadrants. Computations for each quadrant can then be carried out individually, and then all directions are covered; this process is illustrated in Figure C.1. However, energy exchange over the directional domain by refraction, diffraction, or the non-linear wave-wave interactions should remain possible; this requires the possibility of the energy to move one quadrant to another (within one timestep). To this extend, exchange of energy between quadrants is formulated in terms of boundary conditions at the first and last direction of each quadrant. Computations are then carried out iteratively for the solution to converge.

Finally, the large range of frequencies present in a wave field is a challenge for the spectral wave models. High-frequency components require smaller time step than the low-frequency components in order to maintain numerical stability. The interest often lies in the low-frequency components, since these contain the most energy. However, stability restrictions related to the time scales of the high-frequency components require timesteps to be much smaller than would be preferable. SWAN uses a so-called action density limiter to also guarantee numerical stability for larger time steps. This limiter limits the rate of change of the energy spectrum at each iteration, and thereby suppresses the development of numerical instabilities.

C.3. INITIAL AND BOUNDARY CONDITIONS

Boundary conditions are required to solve the wave action balance. Incoming wave components are specified by a two-dimensional wave spectrum at the boundaries. SWAN provides different options for the specification of the boundary conditions:

- parametric 1-D spectra with a certain imposed directional distribution (e.g. a JONSWAP spectrum).
- discrete 1-D spectra with a certain imposed directional distribution; this is often obtained from measurements.
- discrete 2-D spectra; this may be obtained from other SWAN runs or other models, such as WAM.

The boundaries in frequency and directional space (in case only a certain range of directions is used) are fully absorbent, allowing energy to move freely out of the domain. The boundaries in geographical space are either given by a land or a water boundary. No energy enters the domain from the land boundaries, and for the water boundaries one of the above-described boundary conditions can be used. Energy moving out of the domain is fully absorbed by SWAN.

For non-stationary computations, initial conditions are required (SWAN uses a first estimate by the second generation mode for stationary computations). These are either given by a previous computation (hot start) or by 2-D parametrized spectrum (e.g. JONSWAP) that are determined according to the initial wind conditions and the growth curves by Kahma and Calkoen [1992a].

Besides the wave boundary conditions, boundary conditions for the bathymetry, currents, water levels, bottom friction and the wind can be imposed on their original grids and time steps. SWAN automatically interpolates these conditions to the computational grid using tri-linear interpolation.

C.4. COMPUTATIONAL DOMAIN AND GRID

Computational domains need to be defined in SWAN for both the geographical space and spectral space. The spectral domain is simply defined by logarithmically ($\Delta f = 0.1 f$) spaced grid points between the frequency boundaries. For the geographical domain several options are available.

The geographical computational domain can be set up using different types of grid definitions, in both Cartesian and geographical coordinates. An important distinction between the grid types is the use of structured or unstructured grids. Structured grids in SWAN can be rectilinear and uniform or curvilinear. Unstructured grids are defined using triangular meshes. The unstructured grids provide the possibility to locally refine the grid where necessary; they provide a flexible way to model across different spatial scales. Alternatively, to model across different spatial scales using structural grids, nests can be used can be employed in SWAN.

D

KNMI STATIONS

Table D.1: Meta data KNMI stations

Name	Full name	Long. [°]	Lat. [°]	x (rd) [m]	y (rd) [m]	Height Wind Sensor [m]	Height station [m + NAP]	Standard Measurements	Potential Wind
'K210'	Valkenburg	4.4294	52.1703	88750	464425	10	-0.2	yes	yes
'K215'	Voorschoten	4.437	52.141	89933	461739	10	NaN	yes	no
'K225'	IJmuiden	4.555	52.4622	98450	497450	18.5	4.4	yes	yes
'K229'	Texelhors	4.72	52.995	110125	556875	10	1	no	yes
'K235'	De Kooy	4.7811	52.9269	114254	549042	10	0.6	yes	yes
'K240'	Schiphol	4.7903	52.3156	110750	482550	10	-4.4	yes	yes
'K242'	Vlieland	4.9208	53.24	123800	583850	10	0	yes	yes
'K248'	Wijdenes	5.1736	52.6325	140525	516175	10	-1.2	no	yes
'K249'	Berkhout	4.9789	52.6428	127350	517350	10	-2.5	yes	yes
'K251'	Hoorn Terschelling	5.3458	53.3911	152200	600600	10	0.5	yes	yes
'K252'	K13	3.2203	53.2178	10240	583356	73.8	0	no	yes
'K257'	Wijk aan Zee	4.603	52.506	101523	501543	10	8.5	yes	no
'K258'	Houtribdijk	5.4006	52.6481	155877	517729	17.25	NaN	no	yes
'K260'	De Bilt	5.1797	52.0989	140827	456835	20	2	yes	yes
'K265'	Soesterberg	5.274	52.13	147250	460075	10	11.9	yes	no
'K267'	Stavoren-AWS	5.3833	52.8967	154725	545250	10	-0.9	yes	yes
'K269'	Lelystad	5.5197	52.4572	164125	497125	10	-4	yes	yes
'K270'	Leeuwarden	5.7517	53.2231	178970	581970	10	1.5	yes	yes
'K273'	Marknesse	5.8875	52.7019	188850	523975	10	-3.1	yes	yes
'K275'	Deelen	5.8722	52.055	188330	451950	10	44.4	yes	yes
'K277'	Lauwersoog	6.1992	53.4117	209000	603125	10	3	yes	yes
'K278'	Heino	6.2589	52.4344	214550	494625	10	4	yes	yes
'K279'	Hoogeveen	6.5731	52.7489	235125	529750	10	15.6	yes	yes
'K280'	Eelde	6.5847	53.1236	235200	571350	10	3.5	yes	yes
'K283'	Hupsel	6.6567	52.0678	241400	454500	10	29	yes	yes
'K285'	Huibertgat	6.3983	53.5739	222037	621279	18	0	no	yes
'K286'	Nieuw Beerta	7.1492	53.1944	272775	580150	10	0.2	yes	yes
'K290'	Twenthe	6.8908	52.2731	257978	477076	10	34.5	yes	yes
'K308'	Cadzand	3.3792	51.38	15010	378610	17.1	0	no	yes
'K310'	Vlissingen	3.5958	51.4414	30475	385125	27	8	yes	yes
'K311'	Hoofdplaat	3.6722	51.3781	35636	377878	16.5	0	no	yes

Name	Full name	Long. [°]	Lat. [°]	x (rd) [m]	y (rd) [m]	Height Wind Sensor [m]	Height station [m + NAP]	Standard Measurements	Potential Wind
'K312'	Oosterschelde	3.6217	51.7667	32824	421369	16.5	0	no	yes
'K313'	Vlakte	3.2419	51.5036	6038	392714	16.5	0	no	yes
'K315'	Hansweert	3.9975	51.4458	58390	384990	16	0	no	yes
'K316'	Schaar	3.6939	51.6558	37852	408733	16.5	0	no	yes
'K319'	Westdorpe	3.8611	51.2247	48750	359596	10	1.68	yes	yes
'K320'	L.E.	3.67	51.9258	36662	437913	38.3	0	no	yes
'K321'	Europlatform	3.275	51.9978	10044	447580	29.1	0	no	yes
'K323'	Wilhelminadorp	3.8836	51.5258	51250	394325	10	0.7	yes	yes
'K324'	Stavenisse	4.0061	51.5956	59300	401630	16.5	0	no	yes
'K330'	Hoek van Holland	4.1217	51.9911	65550	445050	15	0	yes	yes
'K331'	Tholen	4.1925	51.4786	72030	388524	16.5	0	no	yes
'K340'	Woensdrecht	4.3419	51.4478	82820	384700	10	14.9	yes	yes
'K343'	Rotterdam	4.3125	51.8919	81025	434250	10	0	no	yes
'K344'	Zestienhoven	4.4469	51.9606	90125	441000	10	-4.8	yes	yes
'K348'	Cabauw	4.9258	51.9692	123350	442580	10	-0.7	yes	yes
'K350'	Gilze-Rijen	4.9353	51.565	123731	397594	10	11.1	yes	yes
'K356'	Herwijnen	5.1453	51.8578	138300	429900	10	0.9	yes	yes
'K370'	Eindhoven	5.3769	51.4497	156800	383950	10	20.3	yes	yes
'K375'	Volkel	5.7067	51.6583	177000	407500	10	21.1	yes	yes
'K377'	Ell	5.7625	51.1967	181300	356375	10	30	yes	yes
'K380'	Beek	5.7619	50.9053	182614	325240	10	125.6	yes	yes
'K391'	Arcen	6.1961	51.4972	211100	390150	10	19	yes	yes

E

STATISTICAL PARAMETERS

This appendix gives the definitions of the statistical parameters used throughout the report. Letting $O = (o_1, o_2, ..., o_N)$ be a set of N observed data points and letting $P = (p_1, p_2, ..., p_N)$ be a set of N predicted data points the following parameters can be determined:

Mean:

$$\overline{o} = \frac{1}{N}\sum_{i=1}^{N} o_i \tag{E.1}$$

$$\overline{p} = \frac{1}{N}\sum_{i=1}^{N} p_i \tag{E.2}$$

Standard deviation:

$$\sigma_o = \sqrt{\frac{1}{N-1}\sum_{i=1}^{N}(o_i - \overline{o})^2} \tag{E.3}$$

$$\sigma_p = \sqrt{\frac{1}{N-1}\sum_{i=1}^{N}(p_i - \overline{p})^2} \tag{E.4}$$

Correlation coefficient:

$$\mathrm{r} = \frac{1}{N-1}\sum_{i=1}^{N}\frac{(o_i - \overline{o})(p_i - \overline{p})}{\sigma_o \sigma_p} \tag{E.5}$$

Bias:

$$\mathrm{BIAS} = \overline{p} - \overline{o} \tag{E.6}$$

Relative bias:

$$\mathrm{RBIAS} = \frac{\mathrm{BIAS}}{\overline{o}} \tag{E.7}$$

Standard deviation of the error

$$\sigma_{p-o} = \sqrt{\frac{1}{N+1}\sum_{i=1}^{N}((p_i - o_i) - (\overline{o} - \overline{p}))^2} \tag{E.8}$$

Root-mean-square error:

$$\mathrm{RMSE} = \sqrt{\frac{1}{N}\sum_{i=1}^{N}(p_i - o_i)^2} = \sqrt{\frac{1}{N}\sum_{i=1}^{N}\mathrm{BIAS}^2 + \sigma_{p-o}^2} \tag{E.9}$$

Scatter index:

$$\mathrm{SI} = \frac{\mathrm{RMSE}}{\overline{o}} \tag{E.10}$$

For vectors also the directional statistics are calculated. Letting $\alpha_1, \alpha_2, ..., \alpha_N$ be a set of N observed directions with resultant vector $\mathbf{r}_\alpha$ and letting $\beta_1, \beta_2, ..., \beta_N$ be a set of N observed directions with resultant vector $\mathbf{r}_\beta$, and let be the resultant vector defined as:

$$\mathbf{r}_\alpha = \begin{pmatrix} \cos\alpha_i \\ \sin\alpha_i \end{pmatrix} \tag{E.11}$$

then the following statistical parameters can be determined:

Directional mean [Gaile and Burt, 1980]:

$$\overline{\alpha} = \arctan\left\{\frac{\sum_{i=1}^{N}[\sin(\alpha_i)]}{\sum_{i=1}^{N}[\cos(\alpha_i)]}\right\} \tag{E.12}$$

Directional bias:

$$\mathrm{BIAS} = \arctan\left[\frac{\sin\left(\overline{\alpha}-\overline{\beta}\right)}{\cos\left(\overline{\alpha}-\overline{\beta}\right)}\right] \tag{E.13}$$

Directional standard deviation [Berens, 2009]:

$$s = \sqrt{2(1-||\mathbf{r}||)} \tag{E.14}$$

Circular-circular correlation [Berens, 2009]:

$$\rho_{cc} = \frac{\sum_i \sin\left(\alpha_i-\overline{\alpha}\right)\sin\left(\beta_i-\overline{\beta}\right)}{\sqrt{\sum_i \sin^2\left(\alpha_i-\overline{\alpha}\right)\sin^2\left(\beta_i-\overline{\beta}\right)}} \tag{E.15}$$

F

VALIDATION WRF

F.1. STORM 1

Statistics wind direction

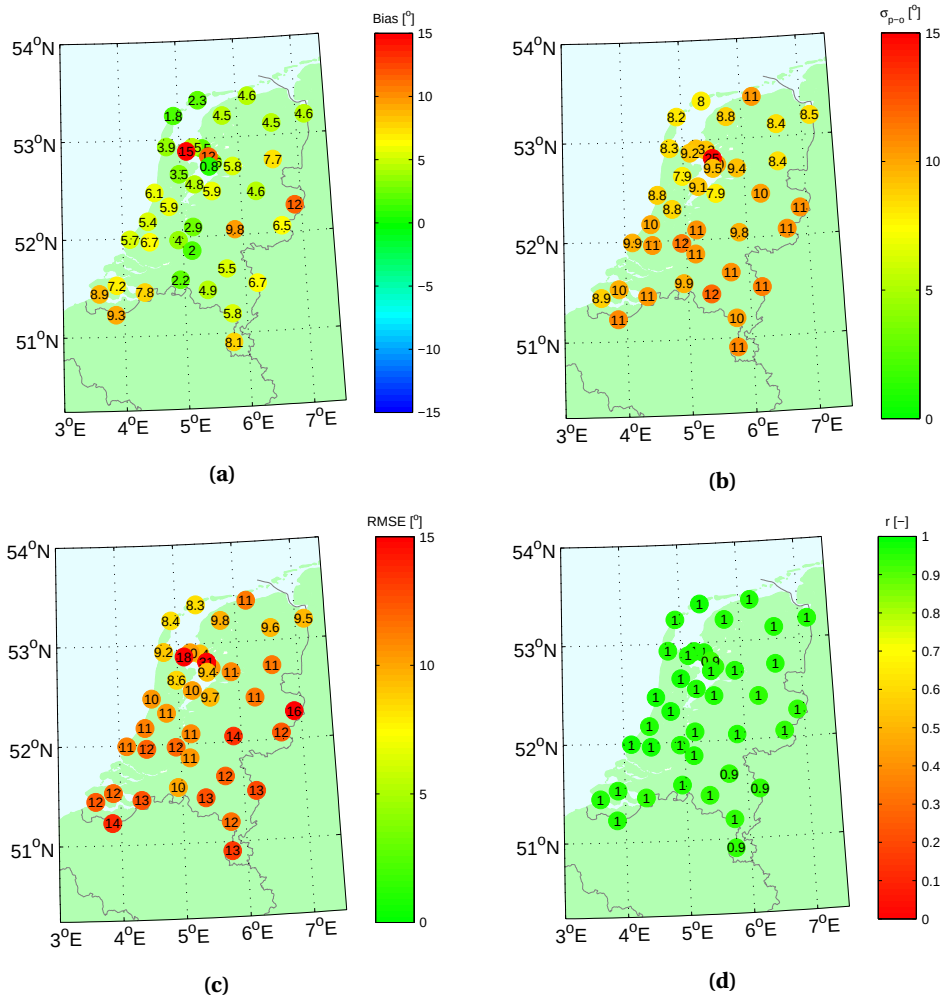

Figure F.1: Wind speed statistics for all stations during storm 1: (a) Bias, (b) Root-mean-square error, (c) Correlation coefficient

Statistics wind speed

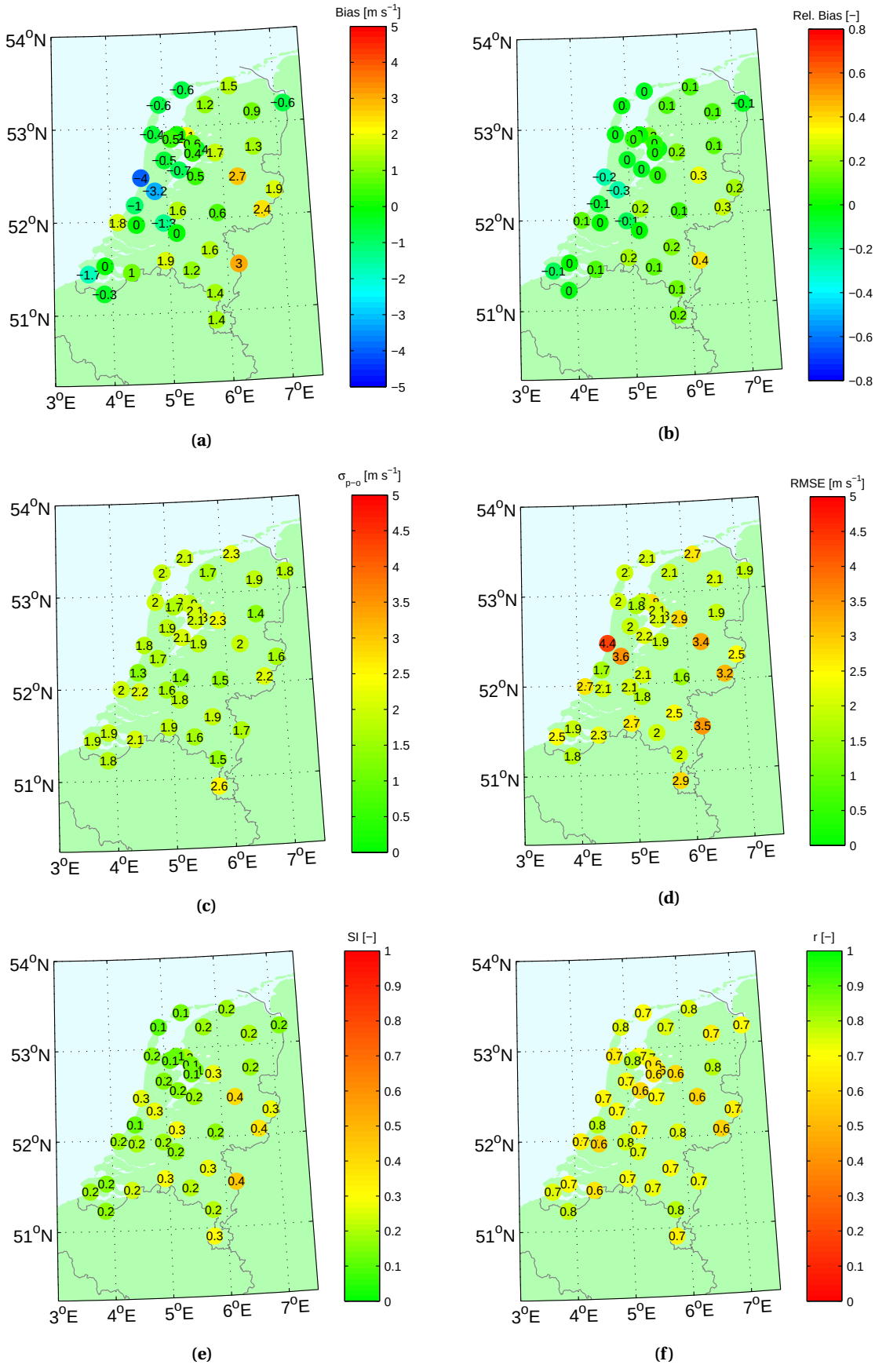

Figure F.2: Wind speed statistics for all stations during storm 1: (a) Bias, (B) Relative bias, (c) Root-mean-square error, (d) Scatter index, (e) Correlation coefficient

Statistics temperature

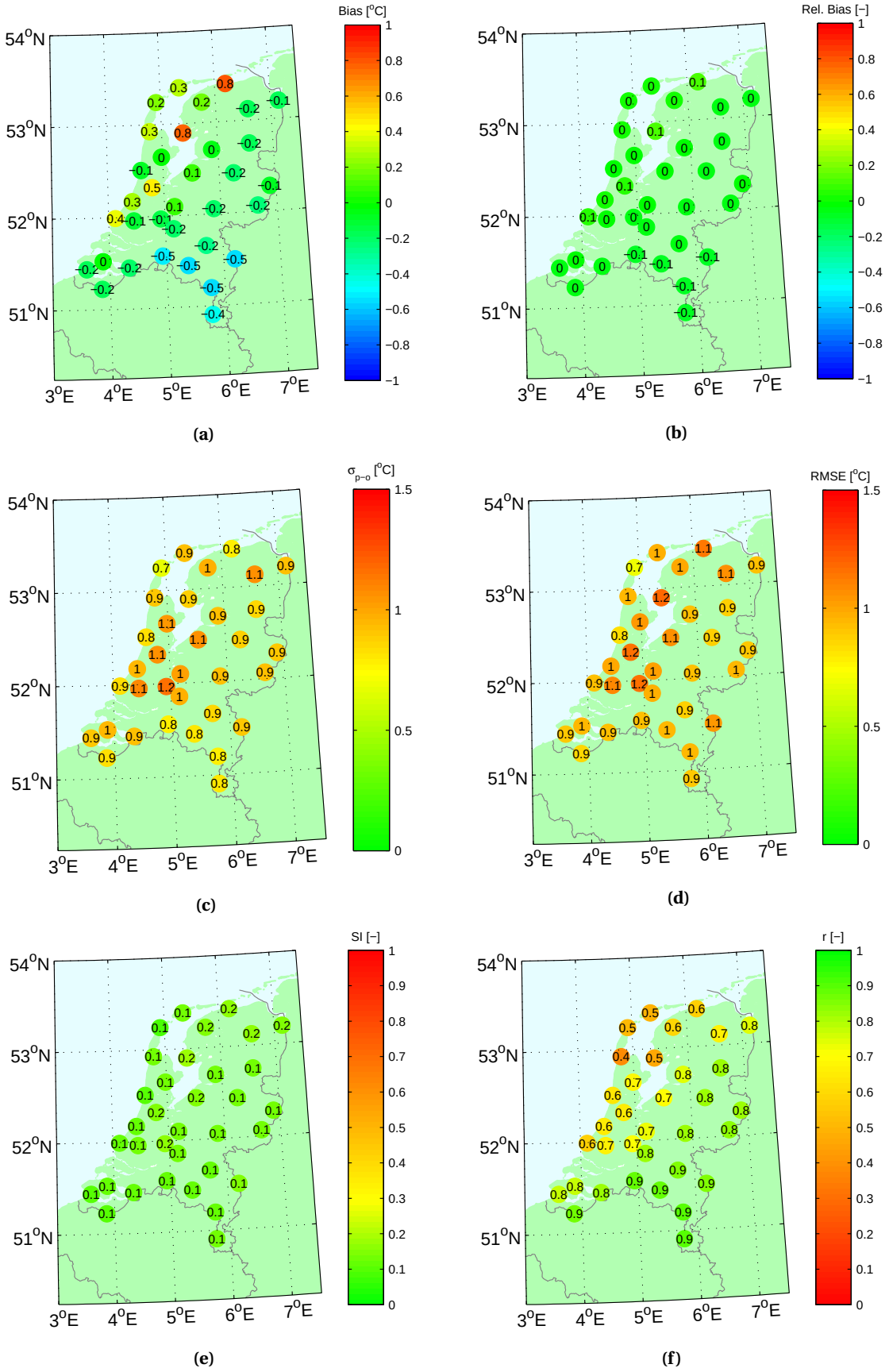

Figure F.3: Wind speed statistics for all stations during storm 1: (a) Bias, (B) Relative bias, (c) Root-mean-square error, (d) Scatter index, (e) Correlation coefficient

F.2. STORM 2

Statistics wind direction

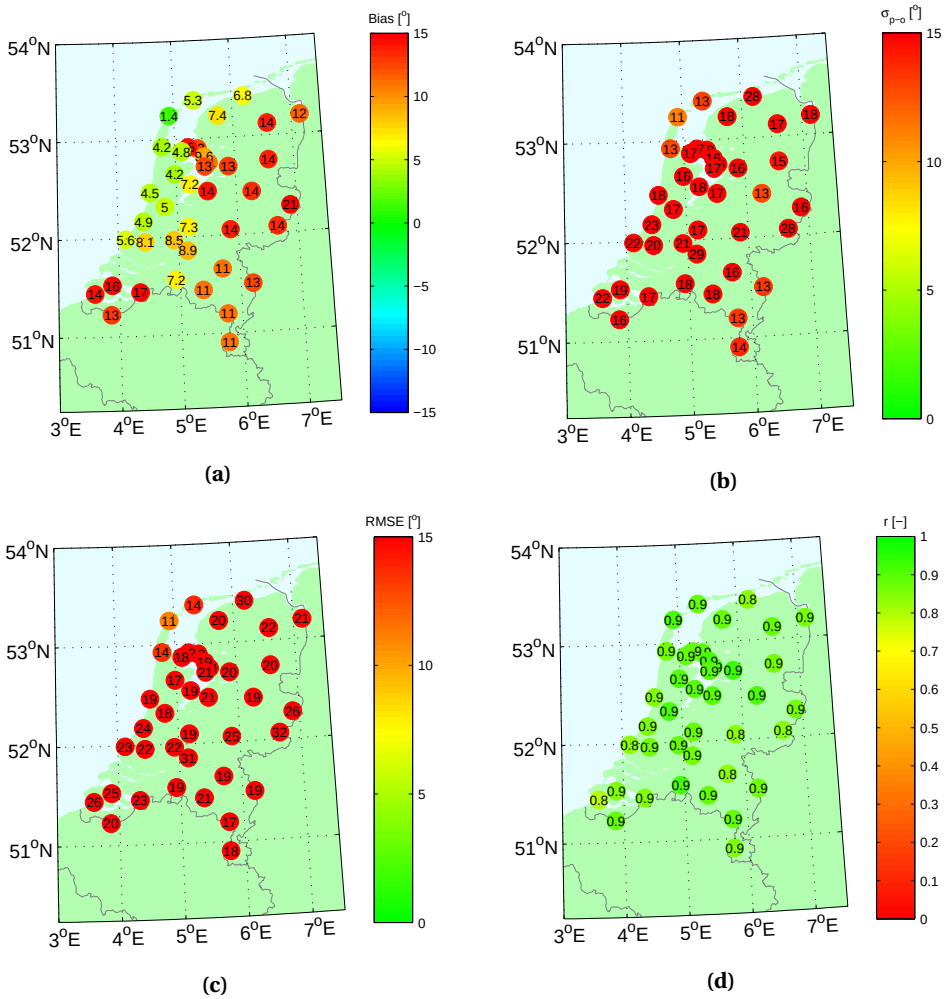

Figure F.4: Wind speed statistics for all stations during storm 2: (a) Bias, (b) Root-mean-square error, (c) Correlation coefficient

Statistics wind speed

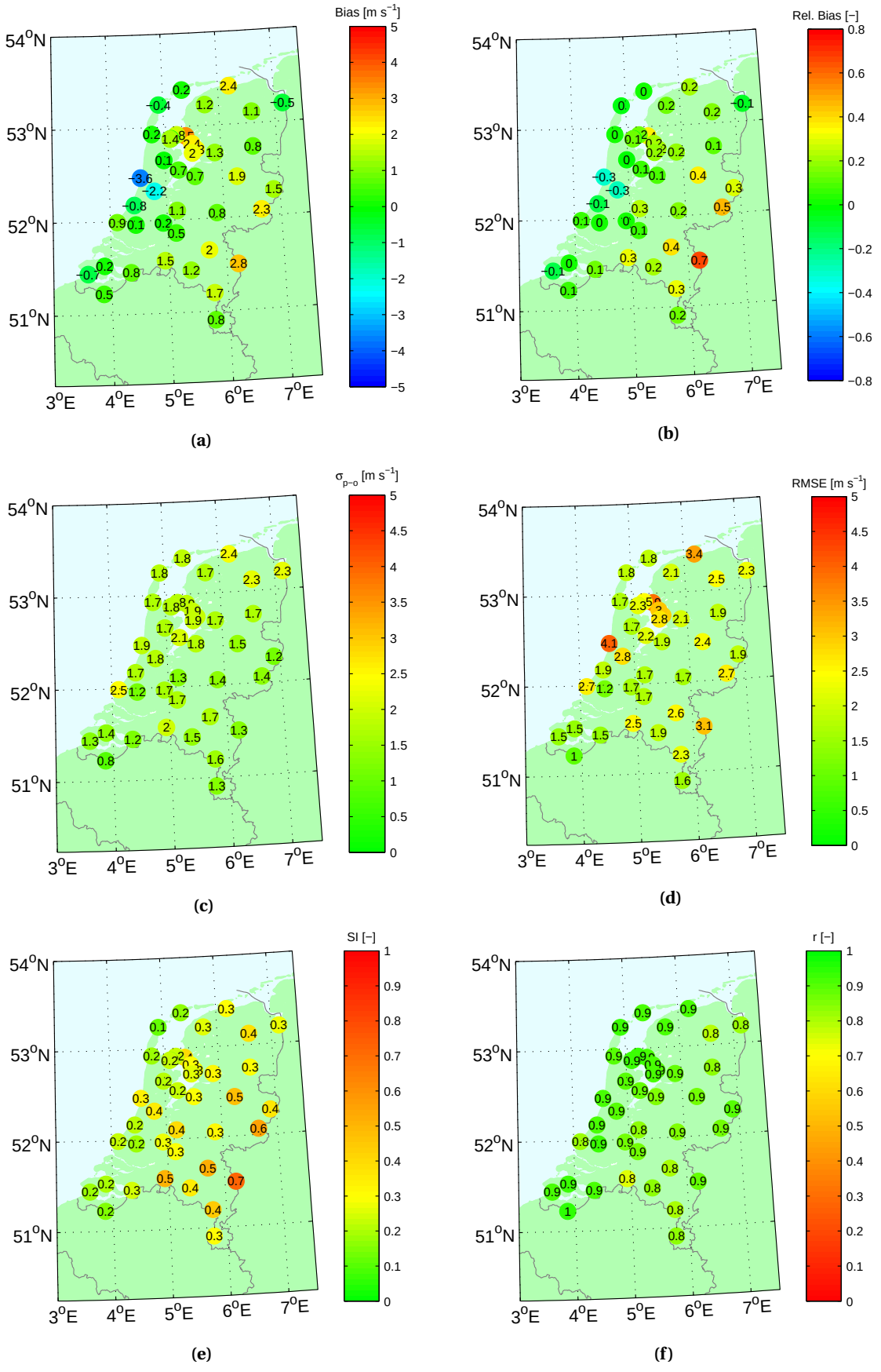

Figure F.5: Wind speed statistics for all stations during storm 2: (a) Bias, (B) Relative bias, (c) Root-mean-square error, (d) Scatter index, (e) Correlation coefficient

Statistics temperature

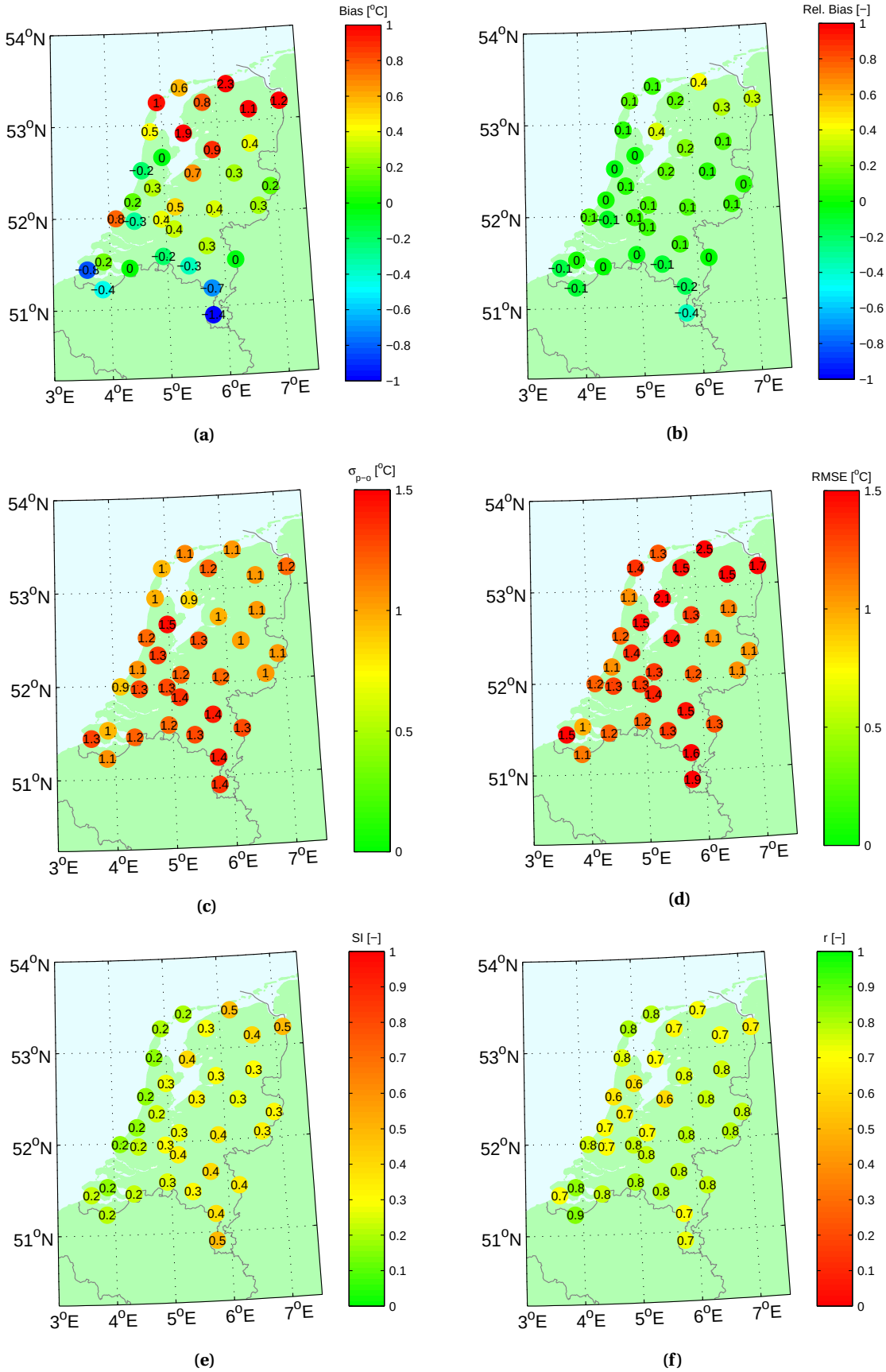

Figure F.6: Wind speed statistics for all stations during storm 2: (a) Bias, (B) Relative bias, (c) Root-mean-square error, (d) Scatter index, (e) Correlation coefficient

G

EFFECT SPATIAL RESOLUTIONS

G.1. WRF RESULTS

G.1.1. TIME SERIES

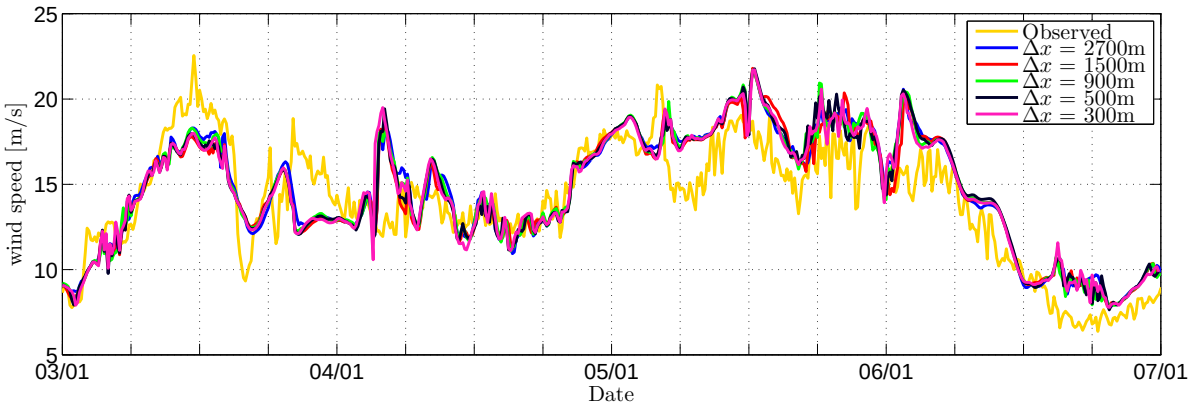

Figure G.1: Wind speed (10 minute averaged values) during storm 1 for station FL47

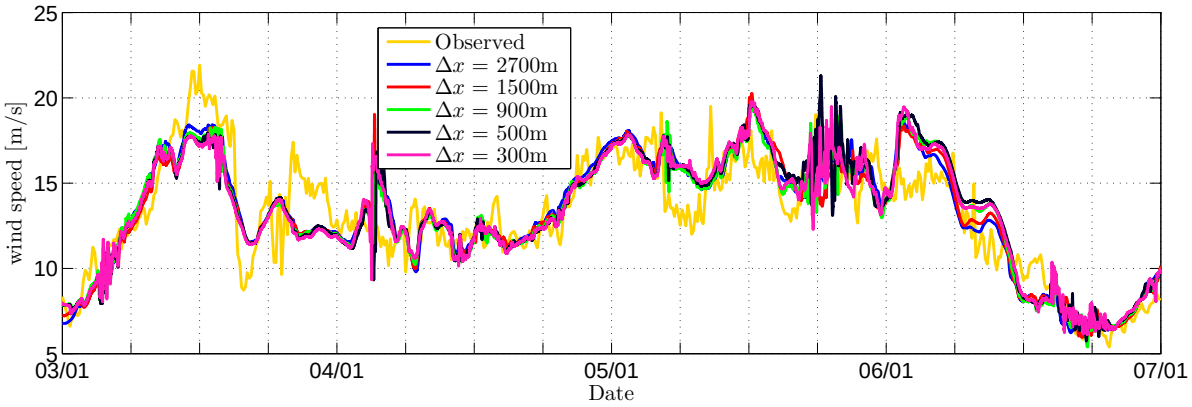

Figure G.2: Wind speed (10 minute averaged values) during storm 1 for station FL48

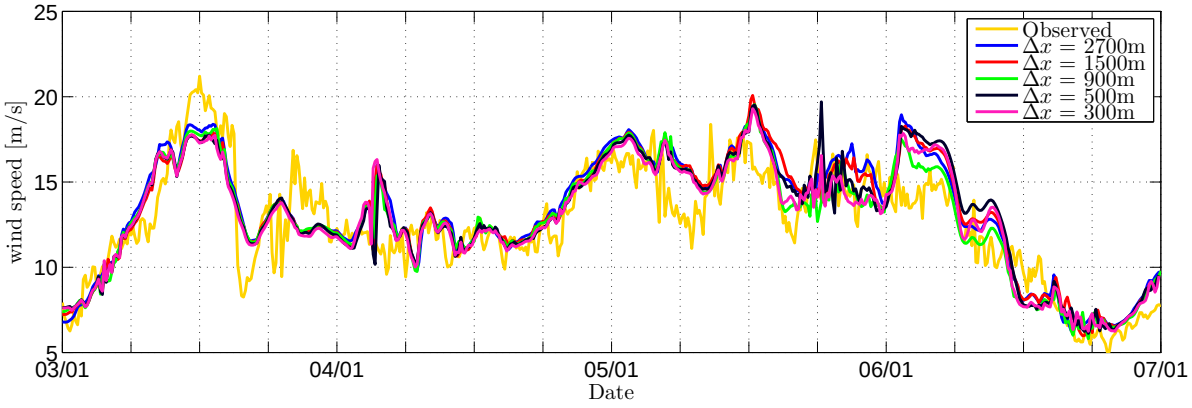

Figure G.3: Wind speed (10 minute averaged values) during storm 1 for station FL49

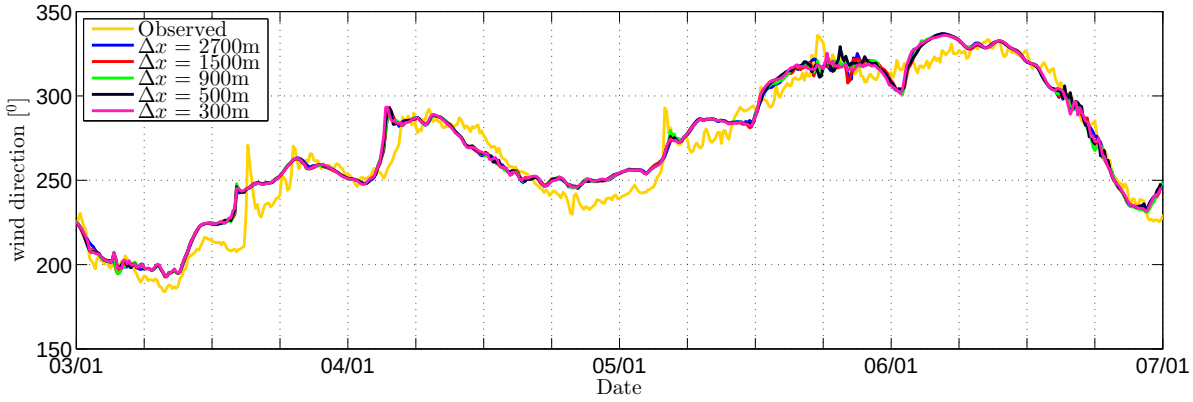

Figure G.4: Wind direction (10 minute averaged values) during storm 1 for station FL47

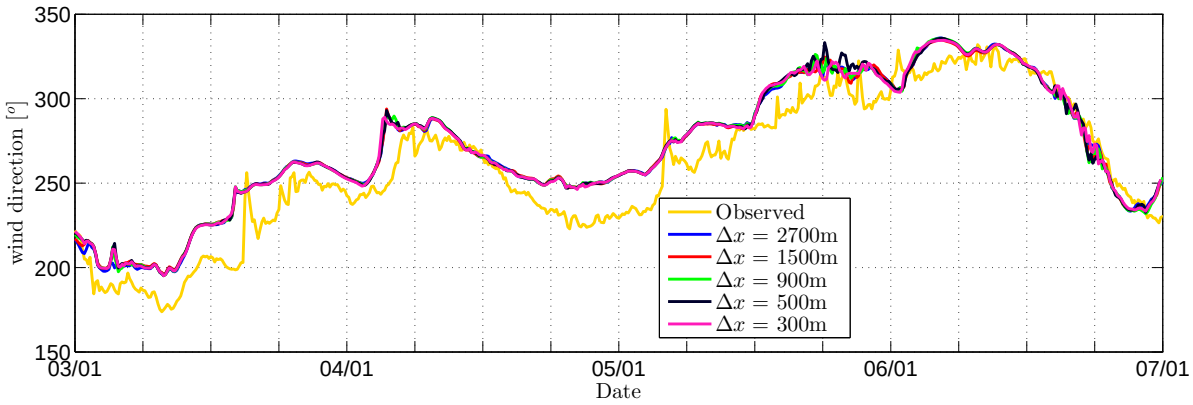

Figure G.5: Wind direction (10 minute averaged values) during storm 1 for station FL48

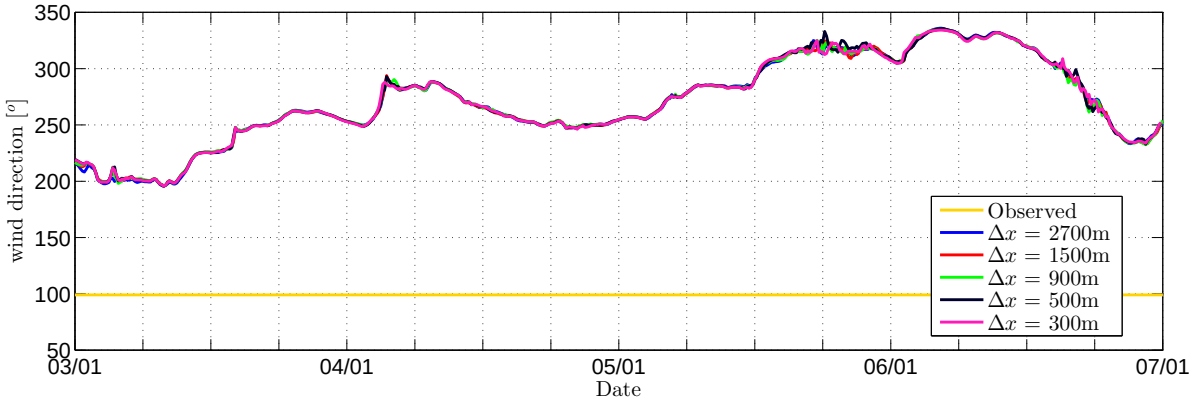

Figure G.6: Wind direction (10 minute averaged values) during storm 1 for station FL49

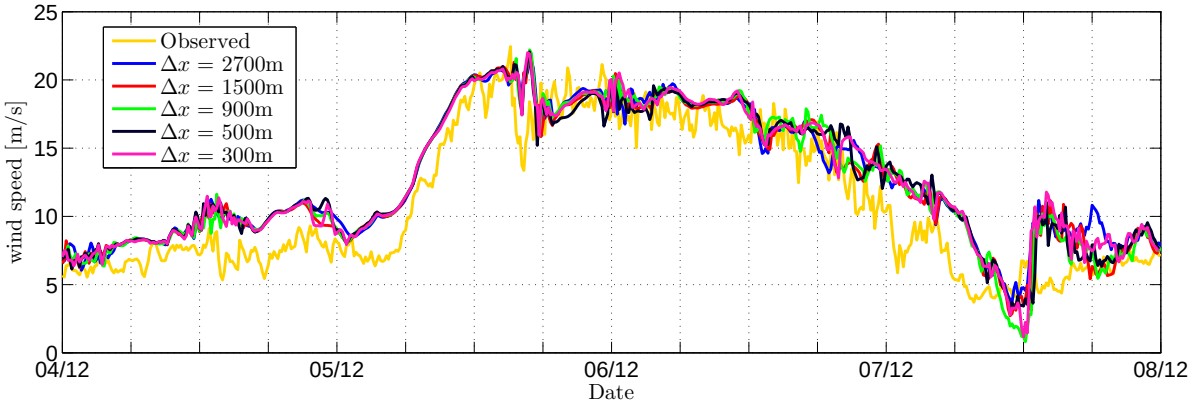

Figure G.7: Wind speed (10 minute averaged values) during storm 2 for station FL47

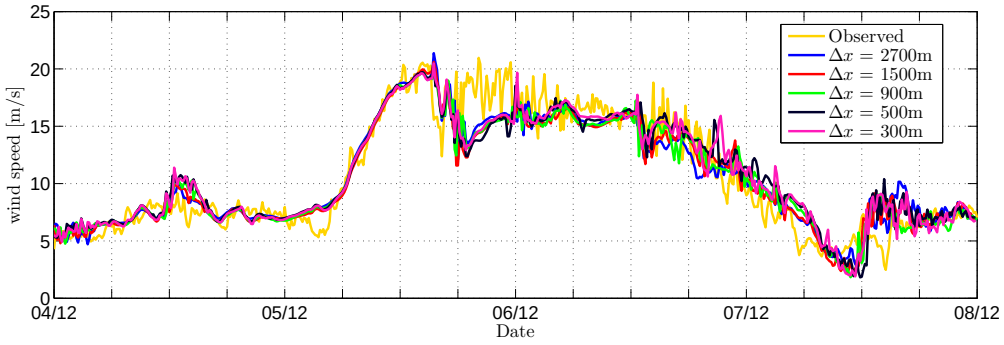

Figure G.8: Wind speed (10 minute averaged values) during storm 2 for station FL48

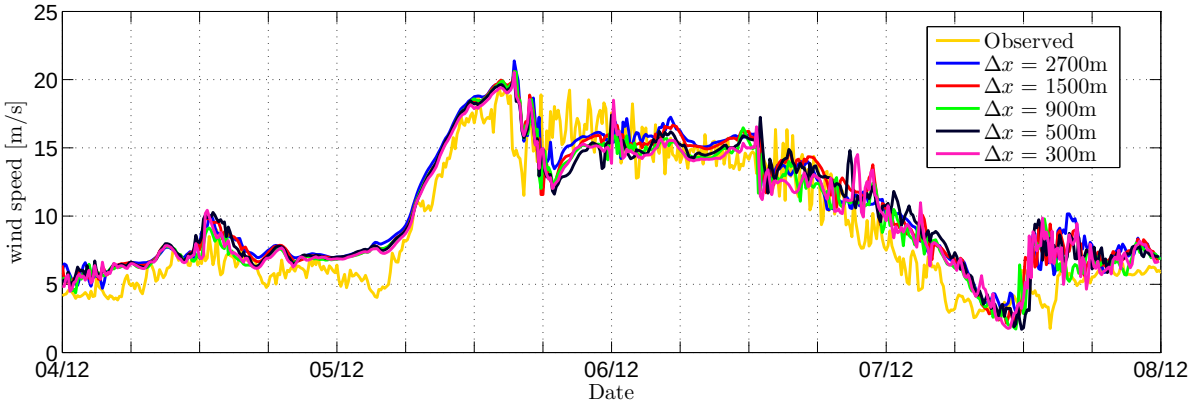

Figure G.9: Wind speed (10 minute averaged values) during storm 2 for station FL49

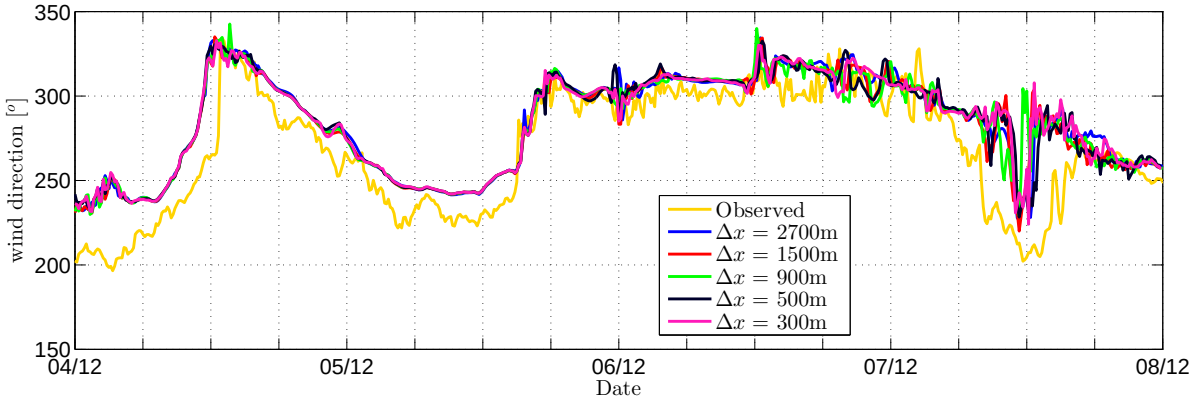

Figure G.10: Wind direction (10 minute averaged values) during storm 2 for station FL47

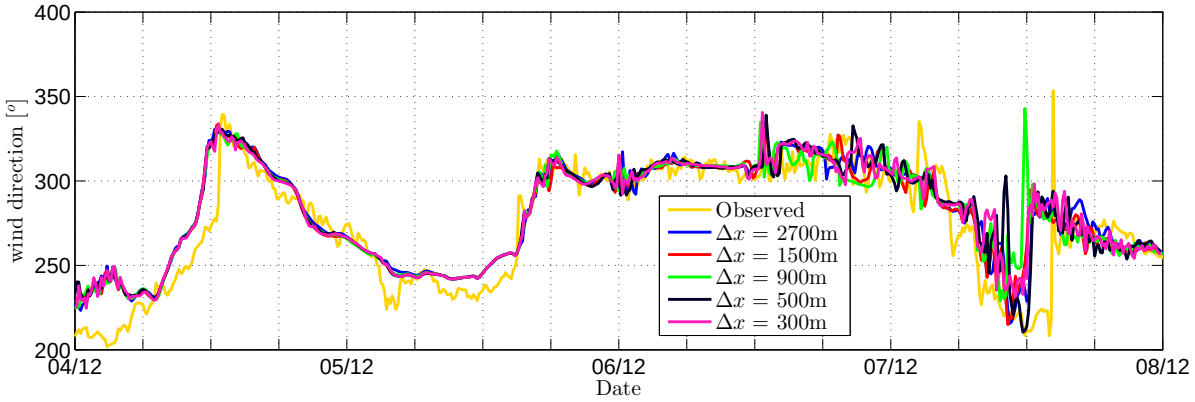

Figure G.11: Wind direction (10 minute averaged values) during storm 2 for station FL48

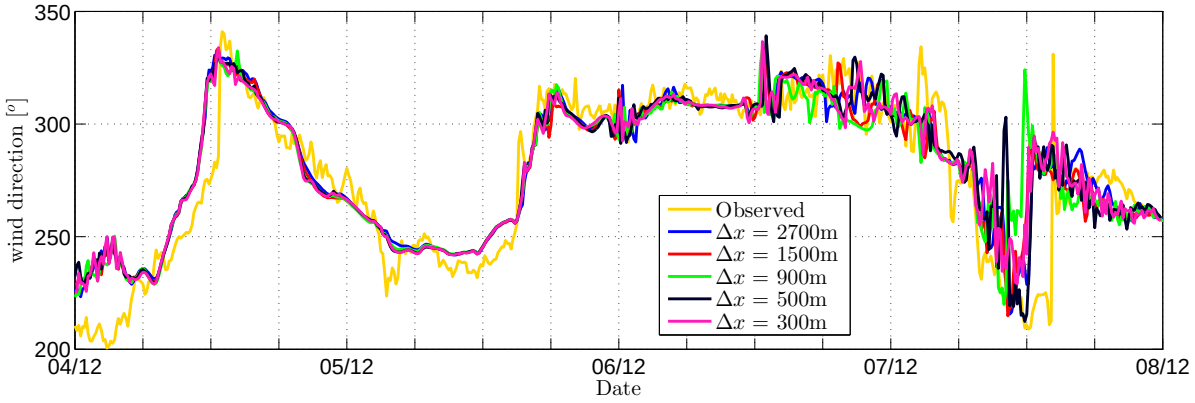

Figure G.12: Wind direction (10 minute averaged values) during storm 2 for station FL49

G.1.2. STATISTICS

Table G.1: Statistical quantities of the wind speed for the stations in lake IJssel, during storm 1

Station	Δx [m]	$\overline{o}$ [ms^{-1}]	$\overline{p}$ [ms^{-1}]	σ_o [ms^{-1}]	σ_p [ms^{-1}]	Bias [ms^{-1}]	RMSE [ms^{-1}]	r [-]	SI [-]
	2700	14.04	14.67	3.460	3.38	0.63	1.96	0.85	0.14
	1500		14.56		3.35	0.51	1.97	0.84	0.14
Fl47	900		14.62		3.40	0.58	1.98	0.85	0.14
	500		14.62		3.40	0.57	2.02	0.84	0.14
	300		14.61		3.36	0.56	2.02	0.84	0.14
	2700	13.16	13.30	3.330	3.33	0.15	1.64	0.88	0.12
	1500		13.23		3.27	0.06	1.70	0.87	0.13
Fl48	900		13.28		3.30	0.13	1.70	0.87	0.13
	500		13.39		3.35	0.23	1.82	0.85	0.14
	300		13.33		3.28	0.17	1.77	0.86	0.13
	2700	12.60	13.30	3.287	3.33	0.71	1.79	0.88	0.14
	1500		13.23		3.27	0.62	1.81	0.87	0.14
Fl49	900		12.95		3.21	0.35	1.64	0.88	0.13
	500		13.14		3.26	0.54	1.80	0.86	0.14
	300		12.96		3.18	0.35	1.72	0.87	0.14

Table G.2: Statistical quantities of the wind speed for the stations in lake IJssel, during storm 2

Station	Δx [m]	$\overline{o}$ [ms^{-1}]	$\overline{p}$ [ms^{-1}]	σ_o [ms^{-1}]	σ_p [ms^{-1}]	Bias [ms^{-1}]	RMSE [ms^{-1}]	r [-]	SI [-]
	2700	10.58	12.37	5.292	4.80	1.79	2.42	0.95	0.23
	1500		12.21		4.93	1.62	2.35	0.95	0.22
Fl47	900		12.20		5.09	1.62	2.38	0.94	0.22
	500		12.28		4.89	1.69	2.42	0.94	0.23
	300		12.33		4.93	1.74	2.45	0.95	0.23
	2700	10.27	10.24	5.162	4.45	-0.03	1.69	0.95	0.17
	1500		10.16		4.47	-0.11	1.76	0.94	0.17
Fl48	900		10.24		4.47	-0.03	1.78	0.94	0.17
	500		10.48		4.52	0.21	1.92	0.93	0.19
	300		10.45		4.56	0.18	1.81	0.94	0.18
	2700	8.90	10.24	4.899	4.45	1.33	2.03	0.95	0.23
	1500		10.16		4.47	1.25	2.04	0.95	0.23
Fl49	900		9.78		4.38	0.87	1.88	0.94	0.21
	500		10.07		4.33	1.16	2.13	0.93	0.24
	300		9.78		4.28	0.87	1.95	0.94	0.22

Table G.3: Statistical quantities of the wind direction for the stations in lake IJssel, during storm 1

Station	Δx [m]	$\overline{o}$ [ms^{-1}]	$\overline{p}$ [ms^{-1}]	σ_o [ms^{-1}]	σ_p [ms^{-1}]	Bias [ms^{-1}]	RMSE [ms^{-1}]	r [-]
Fl47	2700	268.18	271.19	38.929	37.02	3.01	9.50	0.98
	1500		271.15	38.930	37.00	2.89	9.63	0.97
	900		271.15	38.929	37.04	2.97	9.64	0.97
	500		271.45	38.930	37.05	3.19	9.72	0.97
	300		271.37	38.930	36.95	3.10	9.68	0.97
Fl48	2700	260.15	271.37	39.465	36.26	11.22	15.58	0.97
	1500		271.34	39.480	36.02	11.13	15.82	0.96
	900		271.39	39.465	36.23	11.24	15.87	0.96
	500		271.61	39.480	36.37	11.39	16.01	0.96
	300		271.41	39.480	36.15	11.20	15.75	0.97
Fl49	2700	No data	271.37	No data	36.26	No data	No data	No data
	1500		271.34		36.02			
	900		271.38		35.93			
	500		271.69		36.30			
	300		271.48		36.04			

Table G.4: Statistical quantities of the wind direction for the stations in lake IJssel, during storm 2

Station	Δx [m]	$\overline{o}$ [ms^{-1}]	$\overline{p}$ [ms^{-1}]	σ_o [ms^{-1}]	σ_p [ms^{-1}]	Bias [ms^{-1}]	RMSE [ms^{-1}]	r [-]
	2700	266.29	282.06	36.520	29.38	15.77	22.82	0.92
	1500		281.25		29.18	14.93	23.14	0.90
Fl47	900		281.50		28.63	15.21	23.70	0.90
	500		281.64		29.04	15.31	23.27	0.90
	300		282.15		28.70	15.82	24.12	0.89
	2700	271.60	278.87	36.385	30.25	7.27	17.49	0.92
	1500		277.99		29.92	6.35	17.78	0.92
Fl48	900		278.53		29.48	6.93	19.73	0.89
	500		279.03		30.27	7.39	18.43	0.91
	300		279.01		29.85	7.37	18.56	0.91
	2700	274.42	278.87	36.832	30.25	4.45	16.79	0.92
	1500		277.99		29.92	3.54	17.30	0.92
Fl49	900		278.10		29.30	3.67	19.14	0.89
	500		278.82		30.31	4.37	17.72	0.91
	300		278.74		29.77	4.28	17.67	0.91

Table G.5: Statistical quantities of the wind speed for the stations in lake IJssel, during storm 1 for wind from 239°N ± 20°

Station	Δx [m]	N [-]	$\overline{o}$ [ms^{-1}]	$\overline{p}$ [ms^{-1}]	σ_o [ms^{-1}]	σ_p [ms^{-1}]	Bias [ms^{-1}]	RMSE [ms^{-1}]	r [-]	SI [-]
	2700	202	14.16	13.76	3.716	3.04	-0.40	1.61	0.91	0.11
	1500	204	14.14	13.70	3.712	2.97	-0.44	1.77	0.89	0.13
Fl47	900	204	14.14	13.74	3.735	3.03	-0.40	1.67	0.90	0.12
	500	201	14.18	13.76	3.712	3.00	-0.42	1.69	0.90	0.12
	300	201	14.14	13.73	3.742	3.00	-0.41	1.69	0.90	0.12
	2700	184	13.38	13.31	4.013	3.42	-0.07	1.40	0.94	0.10
	1500	183	13.45	13.17	3.968	3.28	-0.28	1.49	0.94	0.11
Fl48	900	188	13.33	13.01	4.016	3.32	-0.33	1.47	0.94	0.11
	500	187	13.34	13.02	4.005	3.28	-0.33	1.53	0.94	0.11
	300	188	13.31	12.96	4.017	3.26	-0.35	1.55	0.93	0.12
	2700	184	12.83	13.31	4.025	3.42	0.48	1.48	0.94	0.12
	1500	183	12.89	13.17	3.984	3.28	0.28	1.50	0.94	0.12
Fl49	900	184	12.79	13.10	4.052	3.40	0.31	1.45	0.94	0.11
	500	185	12.81	12.98	4.017	3.28	0.17	1.49	0.94	0.12
	300	186	12.82	12.90	4.007	3.26	0.08	1.47	0.94	0.11

Table G.6: Statistical quantities of the wind speed for the stations in lake IJssel, during storm 2 for wind from 239°N ± 20°

Station	Δx [m]	N	$\overline{o}$ [ms^{-1}]	$\overline{p}$ [ms^{-1}]	σ_o [ms^{-1}]	σ_p [ms^{-1}]	Bias [ms^{-1}]	RMSE [ms^{-1}]	r [-]	SI [-]
	2700	191	9.01	10.39	5.281	5.24	1.38	1.79	0.98	0.20
	1500	189	8.93	10.29	5.228	5.34	1.36	1.83	0.97	0.20
Fl47	900	188	8.92	10.24	5.251	5.39	1.32	1.87	0.97	0.21
	500	187	8.97	10.32	5.234	5.33	1.35	1.89	0.97	0.21
	300	186	8.99	10.32	5.249	5.32	1.33	1.90	0.97	0.21
	2700	197	8.49	8.78	5.247	5.07	0.28	1.07	0.98	0.13
	1500	201	8.40	8.54	5.234	5.06	0.14	1.02	0.98	0.12
Fl48	900	202	8.45	8.70	5.197	4.98	0.25	1.12	0.98	0.13
	500	192	8.57	8.92	5.286	5.02	0.35	1.18	0.98	0.14
	300	198	8.46	8.71	5.245	5.03	0.24	1.19	0.98	0.14
	2700	197	7.29	8.78	5.089	5.07	1.49	1.79	0.98	0.25
	1500	201	7.19	8.54	5.079	5.06	1.35	1.67	0.98	0.23
Fl49	900	195	7.28	8.65	5.131	5.06	1.36	1.62	0.99	0.22
	500	189	7.39	8.77	5.168	5.05	1.38	1.72	0.98	0.23
	300	197	7.25	8.40	5.111	5.02	1.15	1.57	0.98	0.22

G.2. SWAN RESULTS

G.2.1. STATISTICS

Table G.7: Statistical quantities of the significant wave height [m] for the stations in lake IJssel, during storm 1

Station	Wind res. [m]	N [-]	$\overline{o}$ [m]	$\overline{p}$ [m]	σ_o [m]	σ_p [m]	r [-]	Bias [m]	RBias [-]	σ_{p-o} [m]	RMSE [m]	SI [-]
Fl47	2700		No data									
	1500											
	900											
	500											
Fl48	2700	129	0.59	0.52	0.179	0.13	0.8	-0.08	-0.13	0.11	0.13	0.22
	1500	130	0.6	0.52	0.18	0.13	0.8	-0.08	-0.14	0.11	0.14	0.23
	900	126	0.59	0.51	0.18	0.13	0.79	-0.09	-0.15	0.11	0.14	0.24
	500	129	0.6	0.51	0.179	0.13	0.79	-0.09	-0.15	0.11	0.14	0.24
Fl49	2700	127	0.45	0.43	0.162	0.13	0.82	-0.02	-0.04	0.09	0.09	0.21
	1500	130	0.46	0.43	0.165	0.13	0.82	-0.02	-0.05	0.09	0.1	0.21
	900	128	0.46	0.43	0.167	0.13	0.82	-0.02	-0.05	0.09	0.1	0.21
	500	129	0.46	0.43	0.166	0.13	0.82	-0.03	-0.05	0.09	0.1	0.21

Table G.8: Statistical quantities of the mean zero crossing period (T_{m01}) [s] for the stations in lake IJssel, during storm 1

Station	Wind res. [m]	N [-]	$\overline{o}$ [s]	$\overline{p}$ [s]	σ_o [s]	σ_p [s]	r [-]	Bias [s]	RBias [-]	σ_{p-o} [s]	RMSE [s]	SI [-]
Fl47	2700		No data									
	1500											
	900											
	500											
Fl48	2700	129	2.15	1.99	0.294	0.24	0.82	-0.16	-0.07	0.17	0.23	0.11
	1500	130	2.17	2	0.306	0.25	0.84	-0.17	-0.08	0.17	0.24	0.11
	900	126	2.15	1.98	0.296	0.24	0.82	-0.17	-0.08	0.17	0.24	0.11
	500	129	2.16	1.99	0.301	0.25	0.83	-0.17	-0.08	0.17	0.24	0.11
Fl49	2700	127	1.87	1.82	0.262	0.26	0.87	-0.05	-0.03	0.13	0.14	0.08
	1500	130	1.89	1.82	0.278	0.27	0.89	-0.06	-0.03	0.13	0.14	0.08
	900	128	1.88	1.82	0.28	0.28	0.89	-0.06	-0.03	0.13	0.15	0.08
	500	129	1.88	1.82	0.279	0.28	0.88	-0.06	-0.03	0.13	0.15	0.08

Table G.9: Statistical quantities of the mean zero crossing period (T_{m02}) [s] for the stations in lake IJssel, during storm 1

Station	Wind res. [m]	N [-]	$\overline{o}$ [s]	$\overline{p}$ [s]	σ_o [s]	σ_p [s]	r [-]	Bias [s]	RBias [-]	σ_{p-o} [s]	RMSE [s]	SI [-]
Fl47	2700		No data									
	1500											
	900											
	500											
Fl48	2700	129	2.02	1.86	0.259	0.2	0.79	-0.16	-0.08	0.16	0.22	0.11
	1500	130	2.04	1.87	0.268	0.21	0.8	-0.17	-0.08	0.16	0.23	0.11
	900	126	2.02	1.85	0.261	0.2	0.79	-0.17	-0.08	0.16	0.23	0.12
	500	129	2.03	1.86	0.265	0.21	0.79	-0.17	-0.08	0.16	0.23	0.12
Fl49	2700	127	1.77	1.7	0.233	0.22	0.84	-0.06	-0.04	0.13	0.14	0.08
	1500	130	1.78	1.71	0.245	0.23	0.86	-0.07	-0.04	0.13	0.15	0.08
	900	128	1.78	1.71	0.247	0.24	0.86	-0.07	-0.04	0.13	0.15	0.08
	500	129	1.78	1.71	0.246	0.23	0.85	-0.07	-0.04	0.13	0.15	0.08

Table G.10: Statistical quantities of the mean absolute period (T_{m-01}) [s] for the stations in lake IJssel, during storm 1

Station	Wind res. [m]	N [-]	$\overline{o}$ [s]	$\overline{p}$ [s]	σ_o [s]	σ_p [s]	r [-]	Bias [s]	RBias [-]	σ_{p-o} [s]	RMSE [s]	SI [-]
Fl47	2700		No data									
	1500											
	900											
	500											
Fl48	2700	129	2.35	2.2	0.345	0.3	0.87	-0.15	-0.07	0.17	0.23	0.10
	1500	130	2.37	2.2	0.362	0.31	0.88	-0.17	-0.07	0.17	0.24	0.10
	900	126	2.35	2.18	0.347	0.3	0.87	-0.17	-0.07	0.17	0.24	0.10
	500	129	2.37	2.19	0.357	0.31	0.87	-0.17	-0.07	0.17	0.24	0.10
Fl49	2700	127	2.06	2.01	0.308	0.32	0.91	-0.06	-0.03	0.13	0.15	0.07
	1500	130	2.08	2.02	0.331	0.34	0.92	-0.07	-0.03	0.13	0.15	0.07
	900	128	2.08	2.01	0.332	0.34	0.92	-0.07	-0.03	0.13	0.15	0.07
	500	129	2.08	2.01	0.332	0.34	0.92	-0.07	-0.03	0.13	0.15	0.07

Table G.11: Statistical quantities of the peak period (T_p) [s] for the stations in lake IJssel, during storm 1

Station	Wind res. [m]	N [-]	$\overline{o}$ [s]	$\overline{p}$ [s]	σ_o [s]	σ_p [s]	r [-]	Bias [s]	RBias [-]	σ_{p-o} [s]	RMSE [s]	SI [-]
Fl47	2700		No data									
	1500											
	900											
	500											
Fl48	2700	129	2.57	2.58	0.453	0.47	0.84	0	0	0.26	0.26	0.10
	1500	130	2.6	2.59	0.478	0.48	0.86	-0.01	0	0.25	0.25	0.10
	900	126	2.57	2.56	0.454	0.47	0.84	-0.01	-0.01	0.26	0.26	0.10
	500	129	2.59	2.58	0.472	0.49	0.85	-0.02	-0.01	0.26	0.26	0.10
Fl49	2700	127	2.21	2.35	0.477	0.56	0.71	0.14	0.06	0.4	0.42	0.19
	1500	130	2.24	2.37	0.511	0.57	0.75	0.13	0.06	0.39	0.41	0.18
	900	128	2.24	2.36	0.51	0.58	0.74	0.13	0.06	0.4	0.42	0.19
	500	129	2.24	2.36	0.512	0.58	0.75	0.12	0.05	0.4	0.41	0.18

Table G.12: Statistical quantities of the significant wave height [m] for the stations in lake IJssel, during storm 2

Station	Wind res. [m]	N [-]	$\overline{o}$ [m]	$\overline{p}$ [m]	σ_o [m]	σ_p [m]	r [-]	Bias [m]	RBias [-]	σ_{p-o} [m]	RMSE [m]	SI [-]
Fl47	2700	40	0.9	0.84	0.401	0.2	0.99	-0.06	-0.07	0.2	0.21	0.23
	1500	40	0.91	0.85	0.39	0.2	0.97	-0.06	-0.06	0.2	0.21	0.23
	900	41	0.9	0.85	0.392	0.2	0.98	-0.06	-0.06	0.2	0.21	0.23
	500	40	0.91	0.86	0.39	0.2	0.97	-0.06	-0.06	0.2	0.21	0.23
Fl48	2700	31	0.62	0.54	0.208	0.13	0.92	-0.08	-0.13	0.1	0.12	0.20
	1500	30	0.63	0.54	0.2	0.13	0.91	-0.09	-0.14	0.1	0.13	0.21
	900	30	0.63	0.54	0.2	0.13	0.91	-0.09	-0.14	0.1	0.13	0.21
	500	30	0.63	0.54	0.2	0.13	0.91	-0.09	-0.14	0.1	0.13	0.21
Fl49	2700	30	0.47	0.45	0.155	0.12	0.91	-0.02	-0.04	0.07	0.07	0.15
	1500	29	0.48	0.45	0.149	0.11	0.89	-0.02	-0.05	0.07	0.07	0.15
	900	29	0.48	0.45	0.149	0.11	0.89	-0.02	-0.05	0.07	0.07	0.15
	500	29	0.48	0.45	0.149	0.11	0.9	-0.03	-0.06	0.07	0.07	0.15

Table G.13: Statistical quantities of the mean zero crossing period (T_{m01}) [s] for the stations in lake IJssel, during storm 2

Station	Wind res. [m]	N [-]	$\overline{o}$ [s]	$\overline{p}$ [s]	σ_o [s]	σ_p [s]	r [-]	Bias [s]	RBias [-]	σ_{p-o} [s]	RMSE [s]	SI [-]
Fl47	2700	40	2.76	2.65	0.654	0.25	0.99	-0.12	-0.04	0.41	0.42	0.15
	1500	40	2.79	2.66	0.634	0.25	0.98	-0.13	-0.05	0.4	0.41	0.15
	900	41	2.77	2.65	0.635	0.25	0.98	-0.11	-0.04	0.39	0.4	0.15
	500	40	2.79	2.66	0.634	0.25	0.98	-0.12	-0.04	0.4	0.41	0.15
Fl48	2700	31	2.09	1.94	0.334	0.18	0.94	-0.16	-0.07	0.18	0.23	0.11
	1500	30	2.12	1.94	0.316	0.17	0.93	-0.17	-0.08	0.17	0.24	0.11
	900	30	2.12	1.94	0.316	0.17	0.93	-0.17	-0.08	0.17	0.24	0.11
	500	30	2.12	1.94	0.316	0.17	0.93	-0.18	-0.08	0.17	0.24	0.12
Fl49	2700	30	1.81	1.75	0.275	0.17	0.95	-0.06	-0.03	0.13	0.14	0.08
	1500	29	1.83	1.75	0.261	0.16	0.94	-0.08	-0.04	0.12	0.14	0.08
	900	29	1.83	1.75	0.261	0.16	0.93	-0.07	-0.04	0.13	0.14	0.08
	500	29	1.83	1.75	0.261	0.16	0.93	-0.08	-0.04	0.13	0.15	0.08

Table G.14: Statistical quantities of the mean zero crossing period (T_{m02}) [s] for the stations in lake IJssel, during storm 2

Station	Wind res. [m]	N [-]	$\overline{o}$ [s]	$\overline{p}$ [s]	σ_o [s]	σ_p [s]	r [-]	Bias [s]	RBias [-]	σ_{p-o} [s]	RMSE [s]	SI [-]
Fl47	2700	40	2.55	2.42	0.576	0.2	0.99	-0.13	-0.05	0.38	0.4	0.16
	1500	40	2.57	2.43	0.558	0.19	0.98	-0.14	-0.05	0.37	0.39	0.15
	900	41	2.55	2.43	0.559	0.2	0.98	-0.13	-0.05	0.37	0.38	0.15
	500	40	2.57	2.44	0.558	0.19	0.98	-0.13	-0.05	0.37	0.39	0.15
Fl48	2700	31	1.99	1.82	0.312	0.15	0.94	-0.17	-0.09	0.18	0.25	0.12
	1500	30	2.01	1.82	0.296	0.15	0.93	-0.19	-0.09	0.17	0.25	0.13
	900	30	2.01	1.82	0.296	0.15	0.92	-0.19	-0.09	0.17	0.25	0.13
	500	30	2.01	1.82	0.296	0.14	0.92	-0.19	-0.09	0.17	0.25	0.13
Fl49	2700	30	1.72	1.65	0.258	0.15	0.94	-0.08	-0.05	0.13	0.15	0.09
	1500	29	1.74	1.65	0.244	0.14	0.93	-0.09	-0.05	0.12	0.15	0.09
	900	29	1.74	1.65	0.244	0.14	0.92	-0.09	-0.05	0.13	0.15	0.09
	500	29	1.74	1.65	0.244	0.14	0.93	-0.09	-0.05	0.13	0.16	0.09

Table G.15: Statistical quantities of the mean absolute period (T_{m-01}) [s] for the stations in lake IJssel, during storm 2

Station	Wind res. [m]	N [-]	$\overline{o}$ [s]	$\overline{p}$ [s]	σ_o [s]	σ_p [s]	r [-]	Bias [s]	RBias [-]	σ_{p-o} [s]	RMSE [s]	SI [-]
Fl47	2700	40	3.07	2.98	0.748	0.33	0.99	-0.09	-0.03	0.42	0.43	0.14
	1500	40	3.09	2.99	0.728	0.33	0.98	-0.1	-0.03	0.41	0.42	0.14
	900	41	3.08	2.99	0.729	0.33	0.98	-0.09	-0.03	0.41	0.41	0.13
	500	40	3.09	3	0.728	0.33	0.98	-0.09	-0.03	0.41	0.42	0.14
Fl48	2700	31	2.26	2.13	0.346	0.21	0.95	-0.12	-0.05	0.16	0.2	0.09
	1500	30	2.28	2.14	0.327	0.2	0.94	-0.14	-0.06	0.16	0.21	0.09
	900	30	2.28	2.14	0.327	0.2	0.93	-0.14	-0.06	0.16	0.21	0.09
	500	30	2.28	2.14	0.327	0.2	0.94	-0.14	-0.06	0.16	0.21	0.09
Fl49	2700	30	1.96	1.92	0.28	0.19	0.95	-0.04	-0.02	0.11	0.12	0.06
	1500	29	1.98	1.92	0.266	0.18	0.95	-0.05	-0.03	0.11	0.12	0.06
	900	29	1.98	1.93	0.266	0.18	0.94	-0.05	-0.02	0.11	0.12	0.06
	500	29	1.98	1.92	0.266	0.18	0.94	-0.05	-0.03	0.11	0.12	0.06

Table G.16: Statistical quantities of the peak period (T_p) [s] for the stations in lake IJssel, during storm 2

Station	Wind res. [m]	N [-]	$\overline{o}$ [s]	$\overline{p}$ [s]	σ_o [s]	σ_p [s]	r [-]	Bias [s]	RBias [-]	σ_{p-o} [s]	RMSE [s]	SI [-]
Fl47	2700	40	3.46	3.65	0.871	0.56	0.98	0.19	0.06	0.34	0.39	0.11
	1500	40	3.5	3.68	0.846	0.56	0.97	0.18	0.05	0.33	0.37	0.11
	900	41	3.48	3.67	0.847	0.56	0.97	0.19	0.05	0.33	0.37	0.11
	500	40	3.5	3.69	0.846	0.56	0.97	0.19	0.06	0.33	0.38	0.11
Fl48	2700	31	2.4	2.42	0.359	0.3	0.93	0.02	0.01	0.14	0.14	0.06
	1500	30	2.42	2.43	0.337	0.3	0.91	0.01	0	0.14	0.14	0.06
	900	30	2.42	2.43	0.337	0.29	0.9	0	0	0.14	0.14	0.06
	500	30	2.42	2.42	0.337	0.29	0.91	0	0	0.14	0.14	0.06
Fl49	2700	30	2.07	2.12	0.3	0.27	0.94	0.05	0.02	0.1	0.11	0.05
	1500	29	2.09	2.13	0.28	0.27	0.93	0.04	0.02	0.1	0.11	0.05
	900	29	2.09	2.12	0.28	0.27	0.93	0.04	0.02	0.1	0.11	0.05
	500	29	2.09	2.11	0.28	0.27	0.93	0.03	0.01	0.1	0.1	0.05

G.3. TIME SERIES

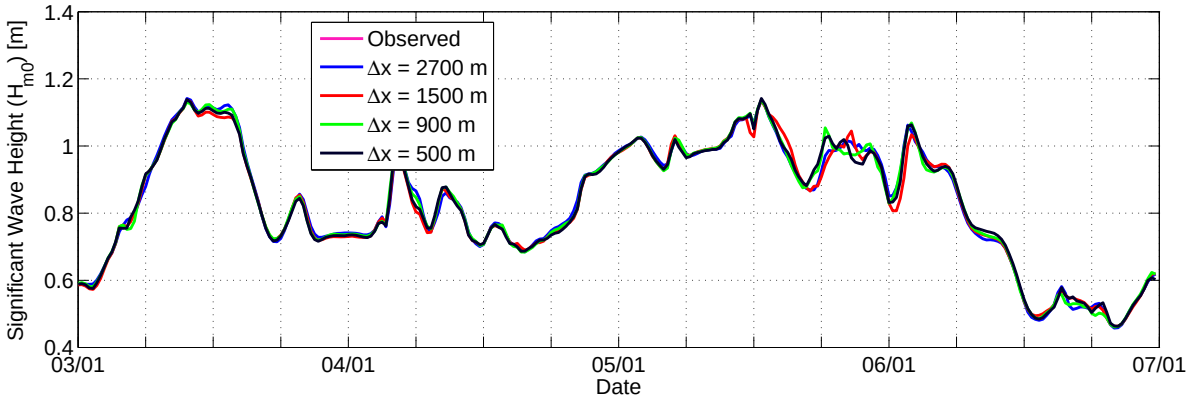

Figure G.13: Wave height (20 minute averaged values) during storm 1 for station FL47

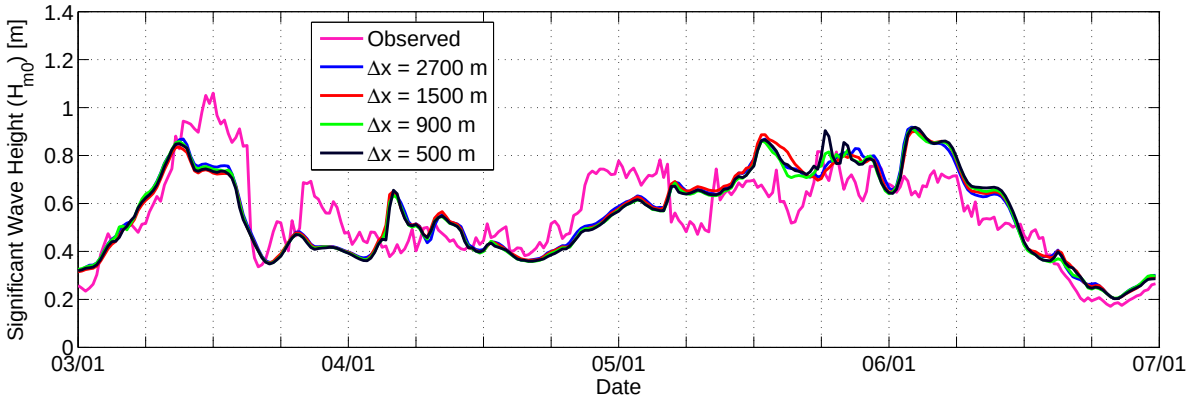

Figure G.14: Wave height (20 minute averaged values) during storm 1 for station FL48

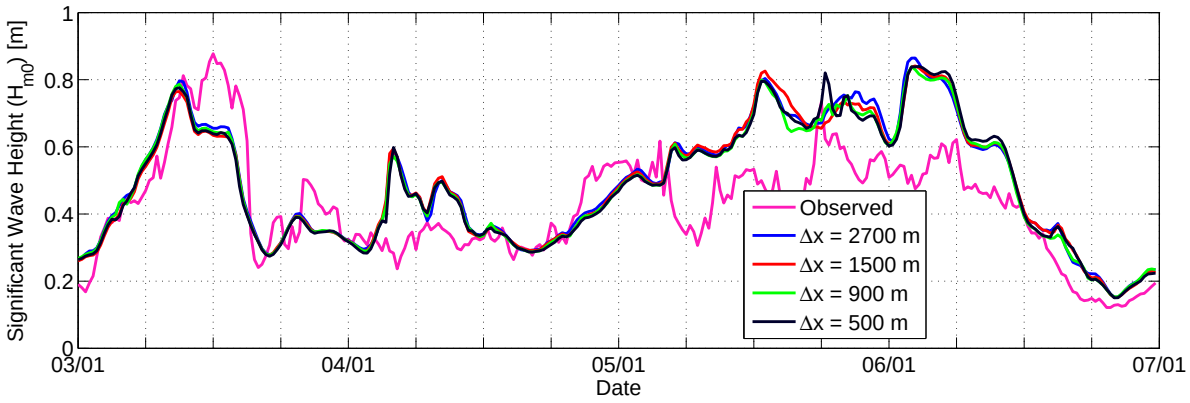

Figure G.15: Wave height (20 minute averaged values) during storm 1 for station FL49

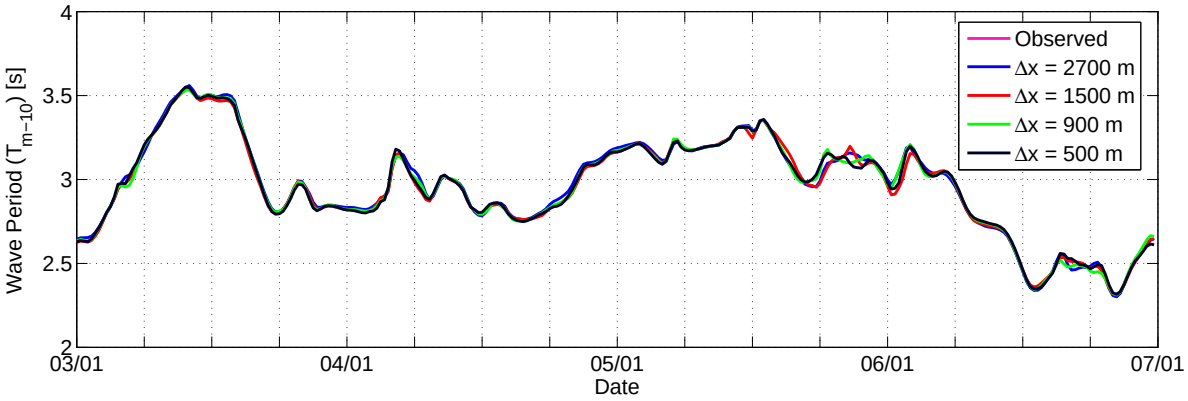

Figure G.16: Wave period (T_{m-10}) [s] (20 minute averaged values) during storm 1 for station FL47

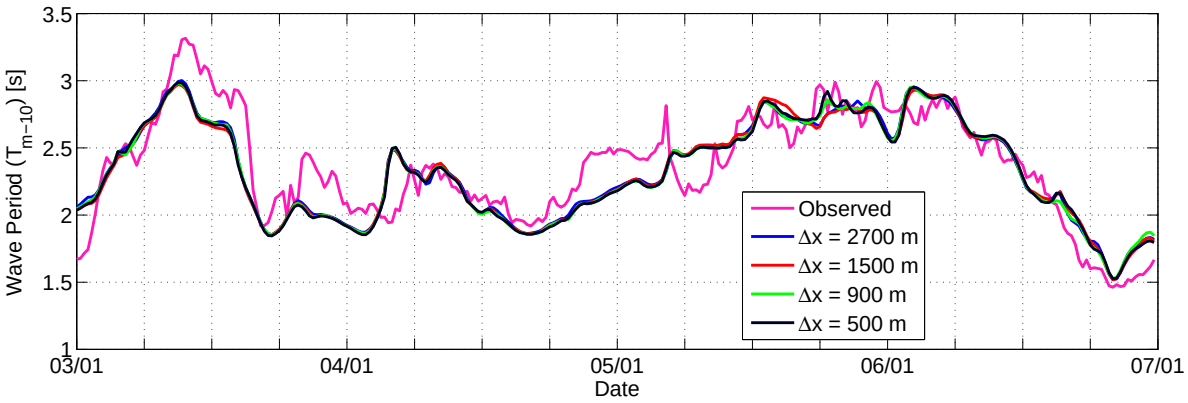

Figure G.17: Wave period (T_{m-10}) [s] (20 minute averaged values) during storm 1 for station FL48

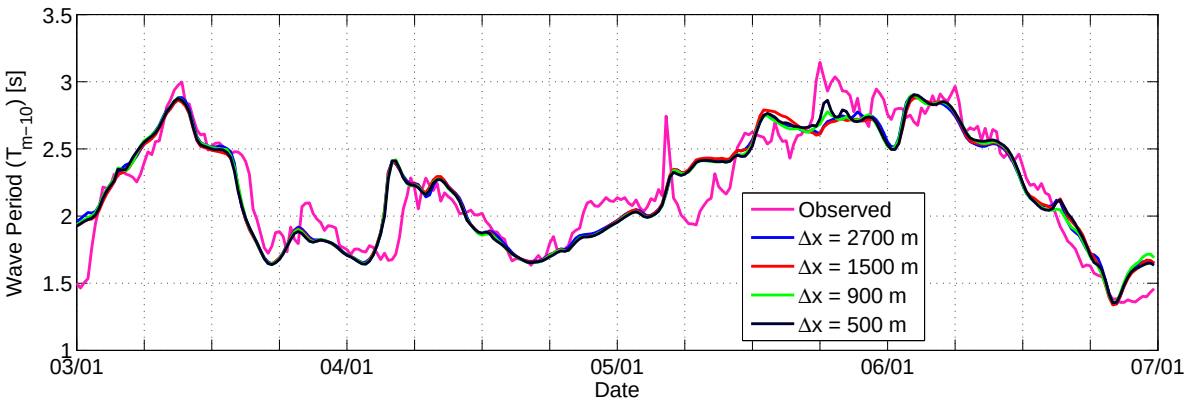

Figure G.18: Wave period (T_{m-10}) [s] (20 minute averaged values) during storm 1 for station FL49

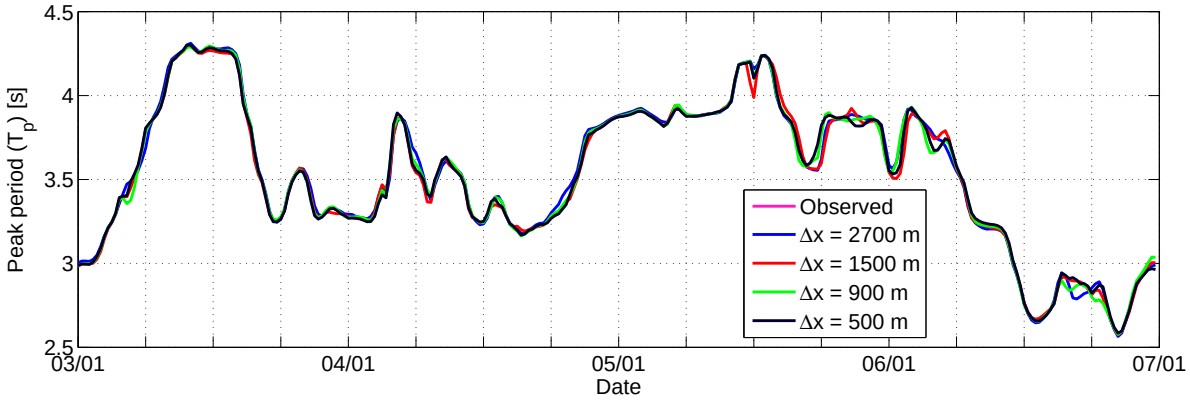

Figure G.19: Wave period (T_p) [s] (20 minute averaged values) during storm 1 for station FL47

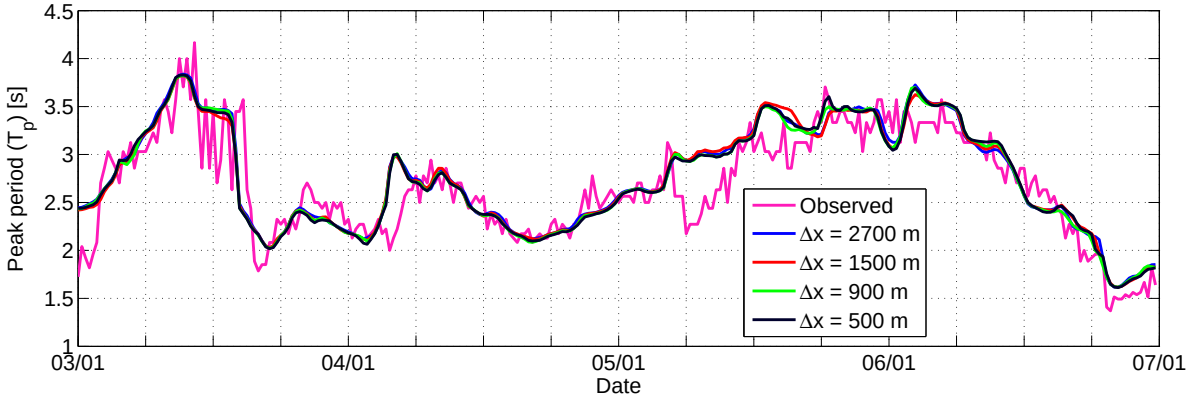

Figure G.20: Wave period (T_p) [s] (20 minute averaged values) during storm 1 for station FL48

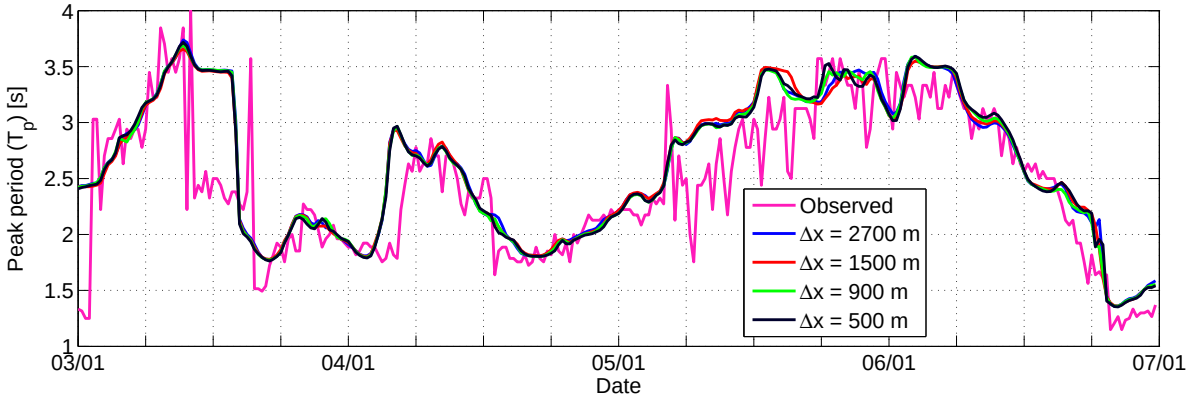

Figure G.21: Wave period (T_p) [s] (20 minute averaged values) during storm 1 for station FL49

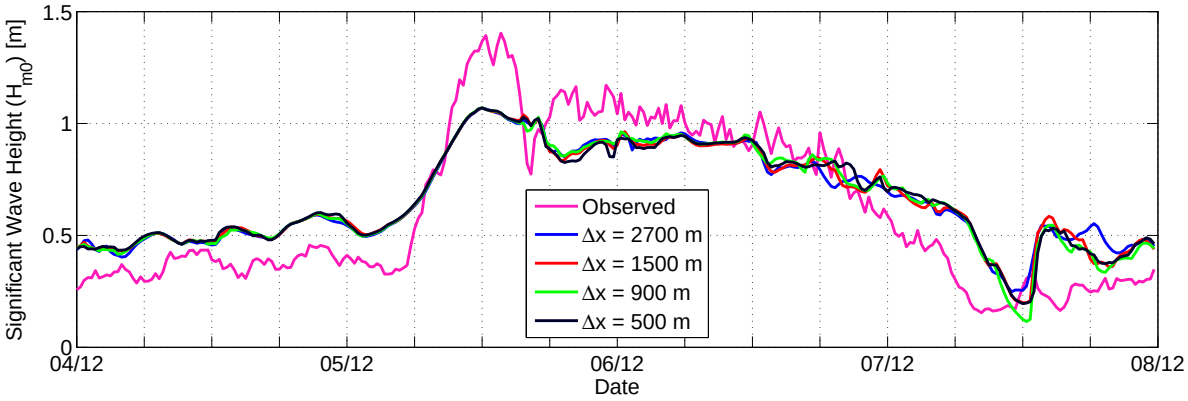

Figure G.22: Wave height (20 minute averaged values) during storm2 for station FL47

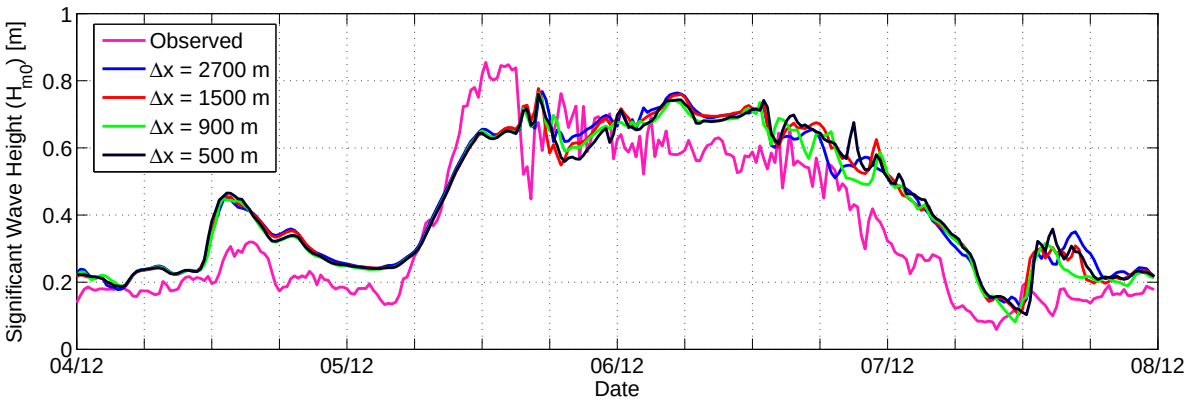

Figure G.23: Wave height (20 minute averaged values) during storm 2 for station FL48

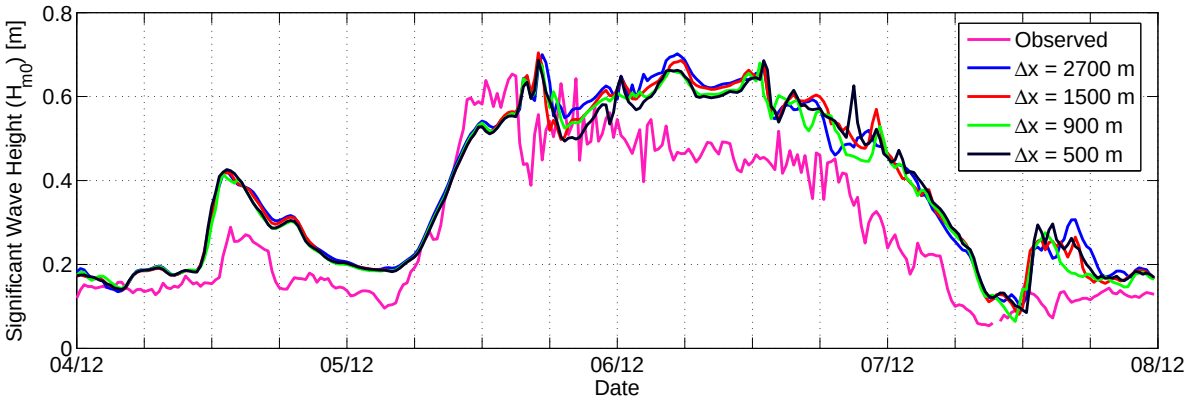

Figure G.24: Wave height (20 minute averaged values) during storm 2 for station FL49

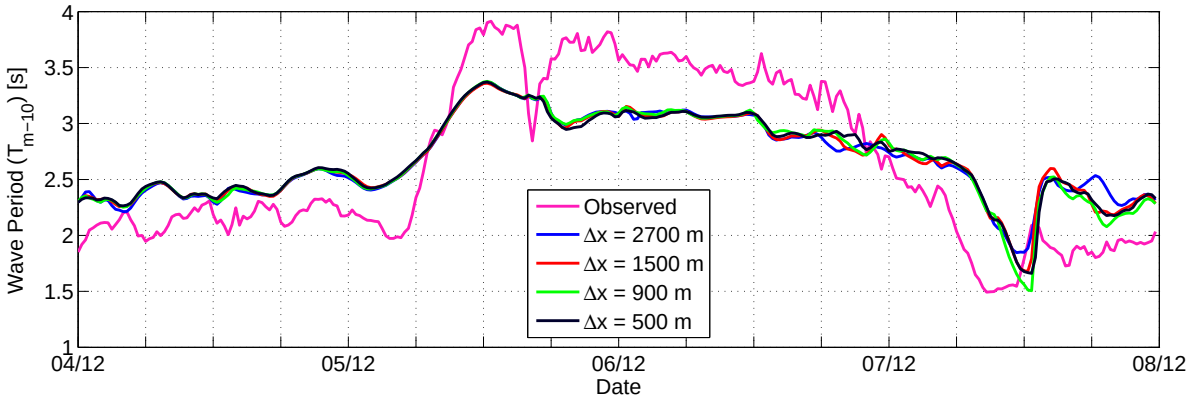

Figure G.25: Wave period (T_{m-10}) [s] (20 minute averaged values) during storm 2 for station FL47

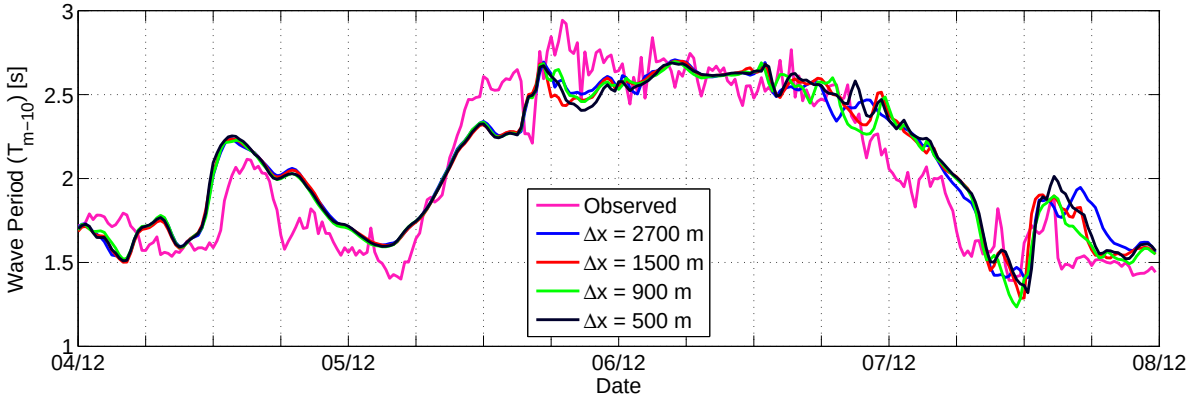

Figure G.26: Wave period (T_{m-10}) [s] (20 minute averaged values) during storm 2 for station FL48

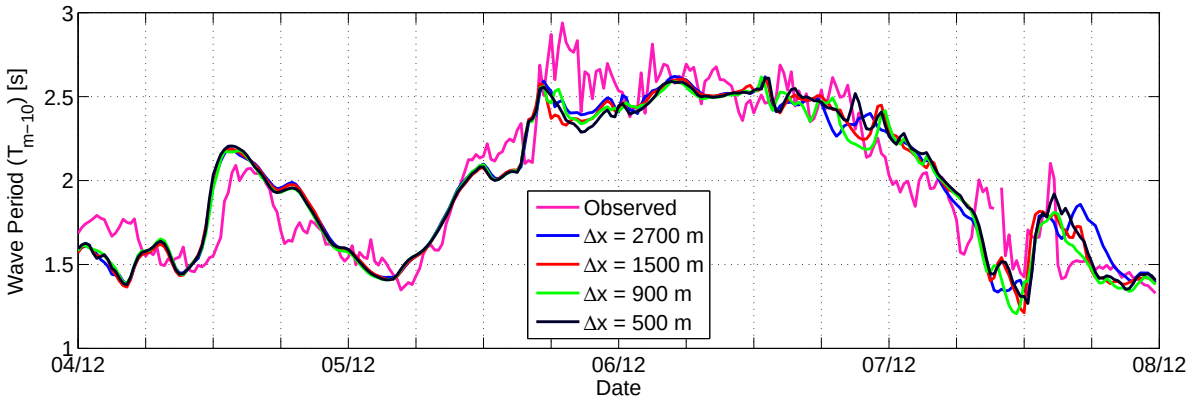

Figure G.27: Wave period (T_{m-10}) [s] (20 minute averaged values) during storm 2 for station FL49

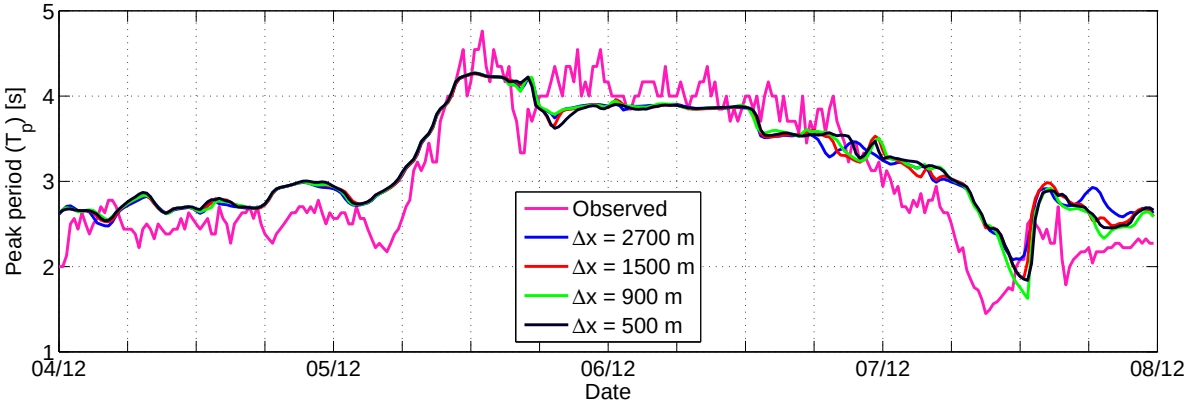

Figure G.28: Wave period (T_p) [s] (20 minute averaged values) during storm 2 for station FL47

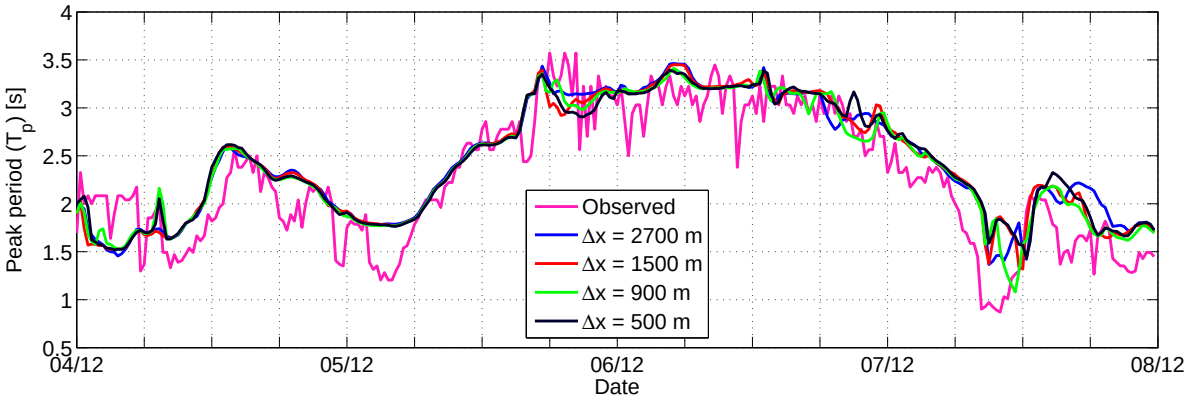

Figure G.29: Wave period (T_p) [s] (20 minute averaged values) during storm 2 for station FL48

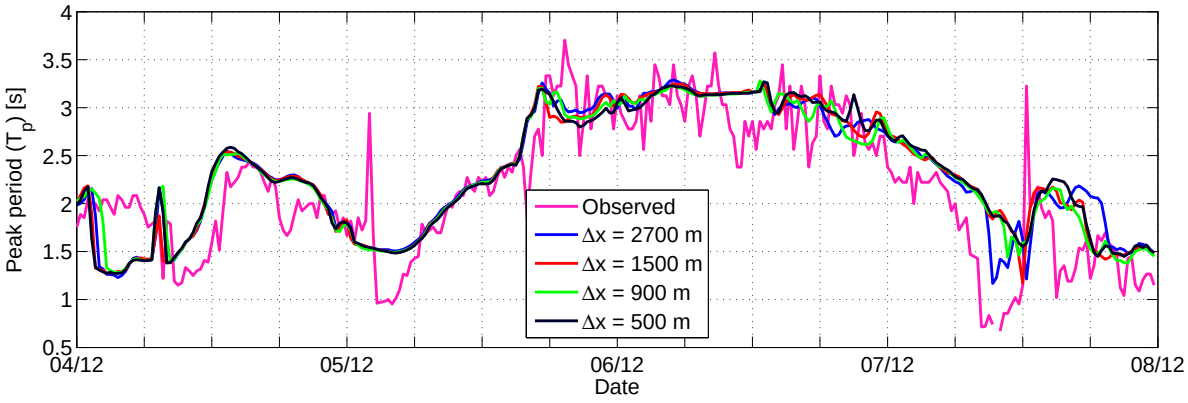

Figure G.30: Wave period (T_p) [s] (20 minute averaged values) during storm 2 for station FL49

G.4. ALONGSHORE PROFILES

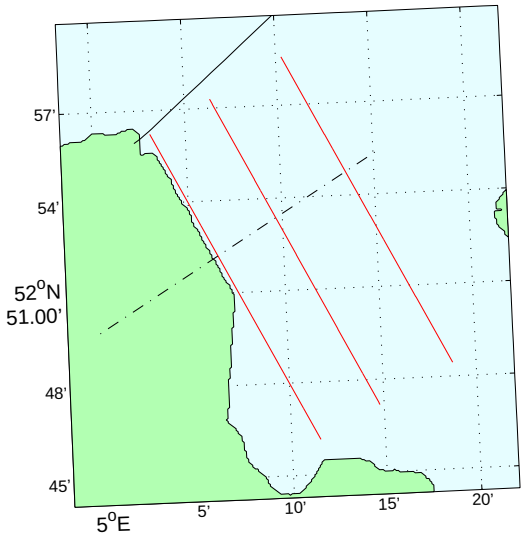

Figure G.31: Overview the locations, with the three profiles 1, 5, and 10 km from the coast (red lines), the dashed line represents the shore normal along the measuring stations.

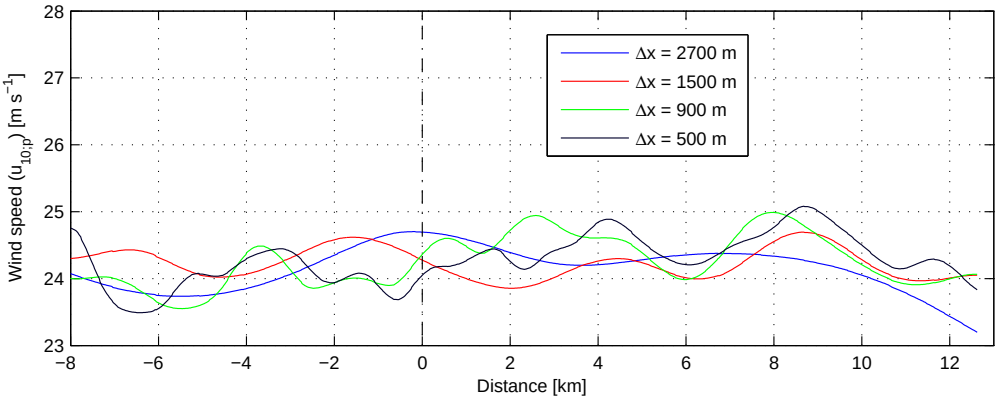

(a)

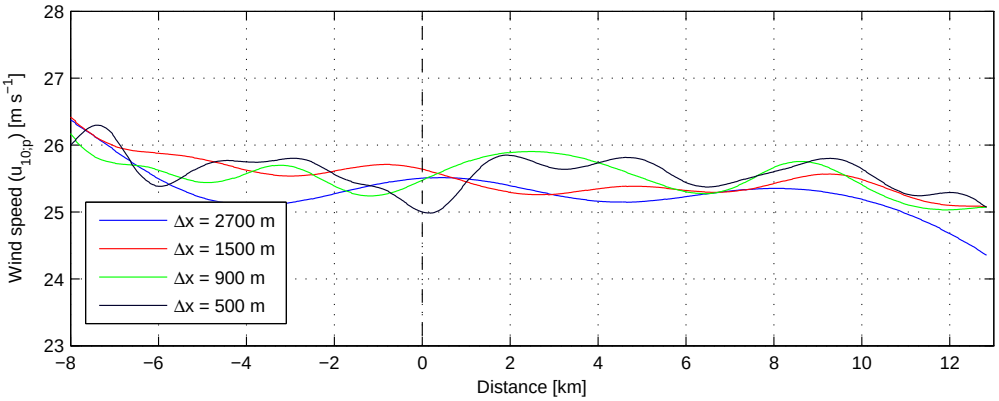

(b)

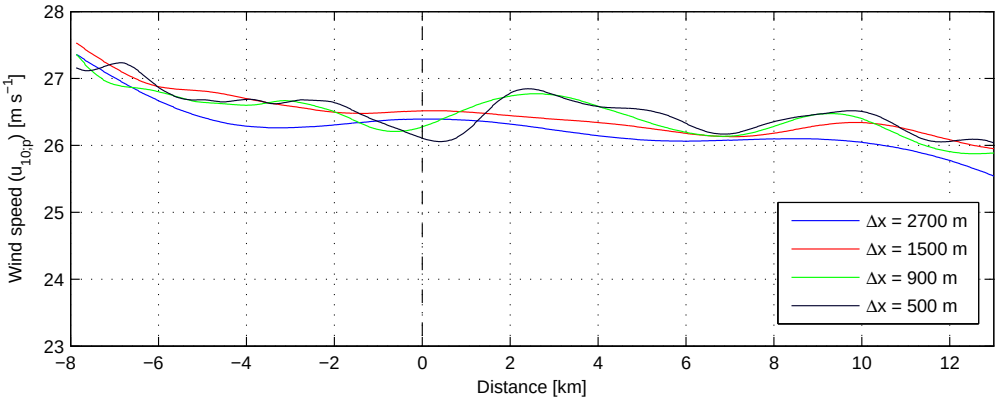

(c)

Figure G.32: Alongshore profiles of the wind ($u_{10;p}$) at December 5th 2013, 12:00 UTC+1, (a) 1 km offshore, (b) 5 km offshore, (c) 10 km offshore

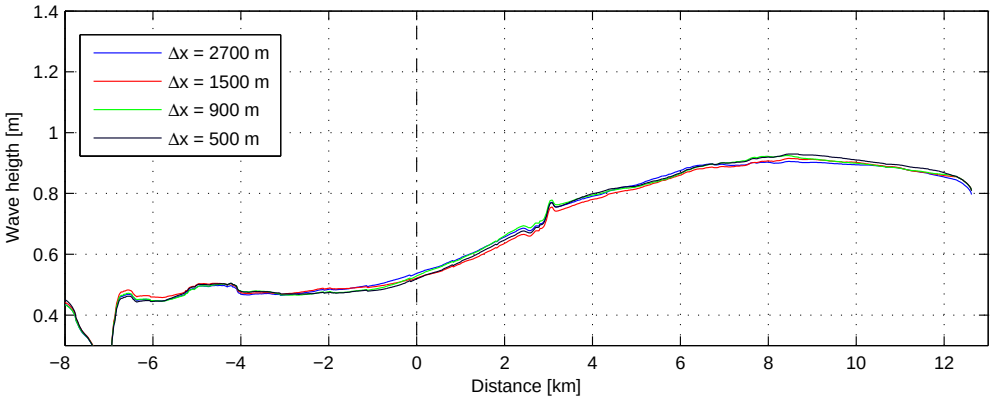

(a)

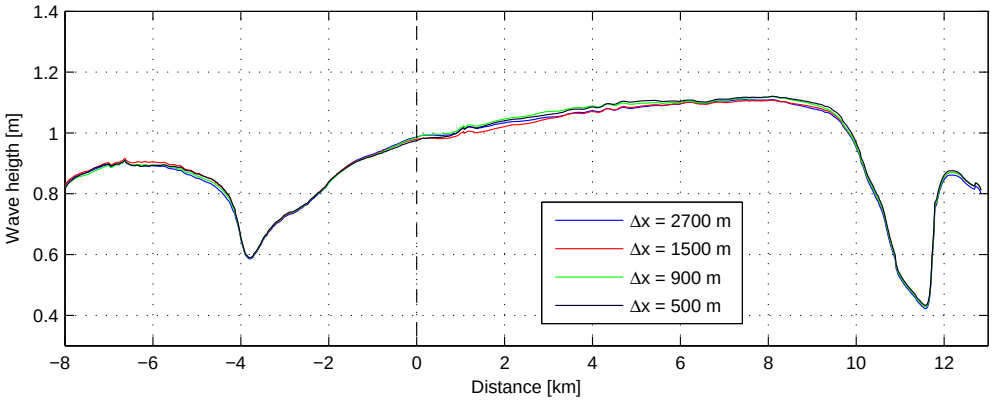

(b)

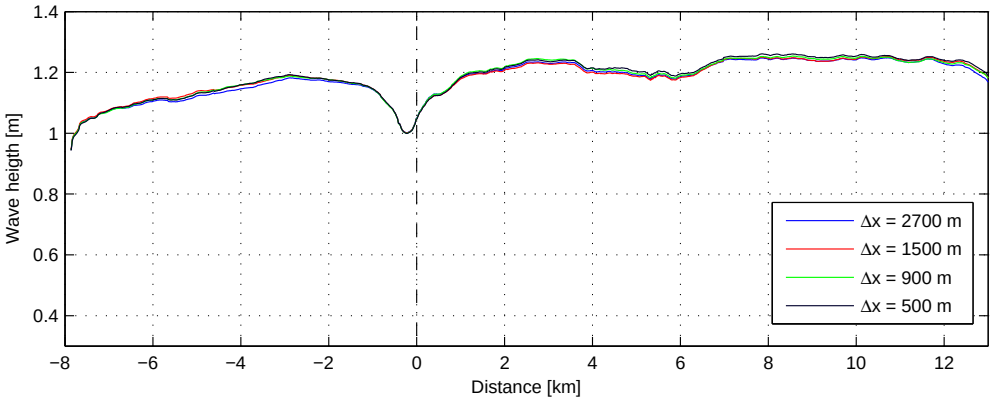

(c)

Figure G.33: Alongshore profiles of the significant wave height (H_{m0}) at December 5th 2013, 12:00 UTC+1, (a) 1 km offshore, (b) 5 km offshore, (c) 10 km offshore